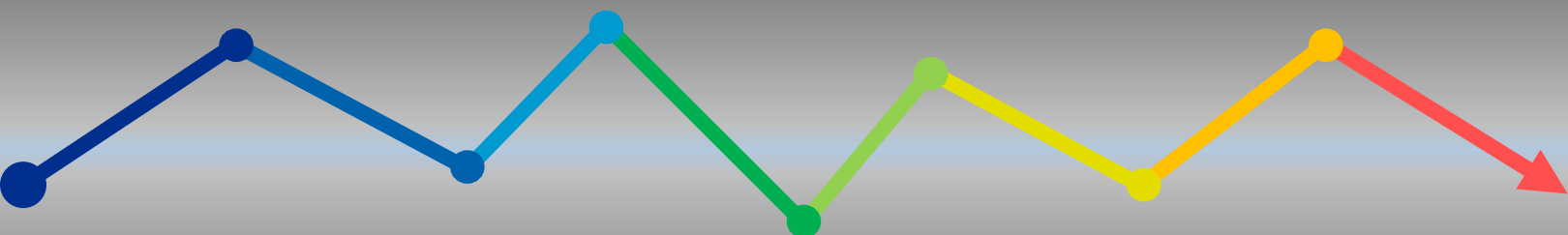


# Innovative Approaches for Light-Emitting Electrochemical Cells

Ph.D. Thesis  
Instituto de Ciencia Molecular  
Ph.D. program in Nanoscience and Nanotechnology



Lorenzo Pietro Mardegan

March 2023

Directors:

Prof. Dr. Hendrik J. Bolink

Prof. Dr. Daniel Tordera Salvador



VNIVERSITAT DE VALÈNCIA

# Innovative Approaches for Light-Emitting Electrochemical Cells

Ph.D. Thesis  
Instituto de Ciencia Molecular  
Ph.D. program in Nanoscience and Nanotechnology

Lorenzo Pietro Mardegan

March 2023

Directors:

Prof. Dr. Hendrik J. Bolink  
Prof. Dr. Daniel Tordera Salvador



VNIVERSITAT D VALÈNCIA

ICMOL



INSTITUTO DE  
CIENCIA MOLECULAR  
UNIVERSITAT DE VALÈNCIA



**Prof. Dr. Hendrik Jan Bolink** y **Prof. Dr. Daniel Tordera Salvador**, Profesor Titular del Departamento de Química Inorgánica y Profesor Ayudante Doctor del Departamento de Química Física, respectivamente, certifican que la memoria presentada por el estudiante de doctorado Lorenzo Pietro Mardegan con el título “Innovative Approaches for Light-Emitting Electrochemical Cells” corresponde a su Tesis Doctoral y ha sido realizada bajo su dirección, autorizando mediante este escrito la presentación de la misma.

En Valencia, a 2 de Febrero del 2023.

Prof. Dr. Hendrik Jan Bolink

Prof. Dr. Daniel Tordera Salvador



# Abstract

In the last two decades, light-emitting diodes (LEDs) and organic light-emitting diodes (OLEDs) have driven the development of lighting technology and systems in terms of efficiency, performance and new applications. The market for these technologies is expected to keep rising in the next decades as a result of the large energy and climate crisis that our modern society is facing. However, the possibilities of integration of LED sources are very limited, because OLEDs rely on an expensive fabrication process, consisting of multiple low-pressure and high-temperature sequential layers.

Light-emitting electrochemical cells (LECs) are another class of thin film light-emitting devices based on the same type of organic semiconductors as those used in OLEDs but with a fundamentally different working mechanism. The simultaneous presence of electronic and ionic charge carriers makes LECs independent of the work function of the electrodes and can consist, in their simplest form, in a single active layer sandwiched between two electrodes. Thanks to these properties, LECs truly represent a promising alternative as cost-effective sources for general lighting applications.

In this thesis, various novelties are introduced in LEC devices and in their fabrication such as a new ionic transporting polymer, new emitters, and finally the use of novel characterization methods new to the field of LECs, that give important insight in the functioning and shortcomings of these devices. In this Thesis, we demonstrate the introduction of a new ionic transporting polymer for polymer LECs. The concentration of the ionic transporting polymer and salt were optimized allowing to obtain state-of-the-art devices with long lifetime and brightness (over 1600 operational hours above 300 cd/m<sup>2</sup>). A new characterization tool was also used to probe the photoluminescence signal under electrical bias of a device. Thanks to this setup, it was possible to link the photoluminescence decay with the different phases of the turn-on and the recovery after turn-off.

Secondly, in the field of semitransparent optoelectronics, we also developed efficient semitransparent LECs with a unique SnO<sub>2</sub>/ITO-based top cathode fabricated with atomic layer deposition and pulsed laser deposition techniques. The high transparency of the cathode resulted in a peak transmission of 82% corresponding at the electroluminescence peak (563 nm). Interestingly, the two sides of the devices show a different luminance response to the electrical bias. The down side (anode side) shows higher luminance and longer lifetime than the up side (cathode side). We concluded that few possible reasons of this behavior can be associated with the different refractive indices of the substrate/anode and cathode, internal reflections and electroluminescence quenching. To prove this, photoluminescence measurements were done by irradiating either the down or up sides. The results indicate that the photoluminescence intensity is lower when measured exciting from the top side, suggesting that anode and cathode quench the photoluminescence by non-radiative recombination in different levels and that the additional damage might be caused by the cathode deposition techniques.

Finally, a series of copper(I) and platinum(II) complexes are used into working LECs. New emitters for light-emitting devices are necessary in order to mitigate the high costs of the most common iridium(III) compounds. In the last few years, Cu(I) complexes have rapidly grown in

interest inside the LEC field showing fast progresses, on the other hand, Pt(II) complexes have only found application in LECs only very recently. Here, first we focus on how different anions affects copper(I)-LECs and second, on the fine-tuning of the ligands to achieve for the first time blue/green electroluminescence from platinum(II)-LECs.

In summary, supported by comprehensive electrical device characterization and photoluminescence studies, this work demonstrates the applicability of these novelties to LECs and more in general to solid-state light-emitting devices.

# Table of Contents

Abstract	5
1. Introduction	9
1.1 Overview of Lighting Technologies	10
1.2 Light-Emitting Electrochemical Cells	13
1.3 Emitters for Light-Emitting Electrochemical Cells	16
1.4 Limitations of light-emitting electrochemical cells	19
1.5 Aim of the thesis	20
2. Experimental and methodology	22
2.1 Materials	23
2.2 Device Fabrication	25
2.2.1 Atomic Layer Deposition	26
2.2.2 Pulsed Laser Deposition	27
2.3 Photoluminescence Measurements	28
2.4 Electroluminescent Characterization of LECs	29
3. Stable Light-Emitting Electrochemical Cells using Hyperbranched Polymer Electrolyte	33
3.1 Introduction	34
3.2 Results and Discussion	35
3.3 Conclusions	42
4. Transparent Light-Emitting Electrochemical Cells	43
4.1 Introduction	44
4.2 Results and Discussion	45
4.3 Conclusion	52



5. New Emitters for Light-Emitting Electrochemical Cells: Cu(I) and Pt(II) Electroluminescent Complexes	53
5.1 Introduction	54
5.2 Results and Discussion	55
5.2.1 Photo-electrochemical properties of Cu1, Cu2, Cu3 and Cu4	56
5.2.2 Photophysical properties of Pt5, Pt6, Pt7, Pt8 and Pt9	56
5.2.3 Light Emitting Electrochemical Cells	57
5.3 Conclusion	67
6. Conclusion	69
7. Resumen en Español	72
8. References	83
9. Appendix	93
9.1 Index of Figures	94
9.2 Index of Tables	96
9.3 Index of Abbreviations	97
9.4 Author Contributions to this Thesis	99
9.5 Other Contributions during this Thesis	99

# 1. Introduction

# 1.1 Overview of Lighting Technologies

Lighting technologies have a huge impact on our lifestyle and in the progress of our society. Until the end of the 19th century the most common way of illumination was fire, discovered almost 400000 years ago. Then, driven by a great period of progress, came the discovery of electricity and the development and commercialization of light bulbs, which shaped the way of producing light. Today, the light bulb can be considered a true milestone that determined a change in our civilization towards a better and more practical way of living and interacting with the environment. This technology improved through the years giving us brighter, more compact, and lighter devices. However, the benefits brought by the latest discoveries have often been overshadowed by their defects which involve low energy management and are linked to the release of greenhouse gasses, such as CO<sub>2</sub>, into the atmosphere. Energetic efficiency and environmental pollution are relatively new aspects that have become prominent only in the last 40-50 years and, in particular, since the beginning of the 21<sup>st</sup> century, where there has been an increasing environmental awareness posed by the threat of climate change.

Lighting energy usage have gained attention in the last two decades for its approximate 20% share of global electric energy consumption and 5% of global greenhouse gas emissions. In this context, the advent of light-emitting diodes (LEDs) dictated a new era of super-efficient and more environmentally friendly devices. In fact, according to the EU commission, by switching to more energy-efficient lighting products Europe will be able to save up to 34 TWh of electricity per year by 2030 and will prevent around 7 million tonnes/year of CO<sub>2</sub> from being emitted (Source: EU commission: Energy labelling and ecodesign requirements). According to the International Energy Agency (IEA), LED use increased substantially from a 5% market share in 2010 to more than 50% in 2020, and is expected to reach 100% by 2025 to accomplish the net zero emission scenario (NZE) called for by the Paris Agreement (2015/2016), as can be seen in **Figure 1** (Source: IEA (2022), *Targeting 100% LED lighting sales by 2025*, IEA, Paris <https://www.iea.org/reports/targeting-100-led-lighting-sales-by-2025>, License: CC BY 4.0).

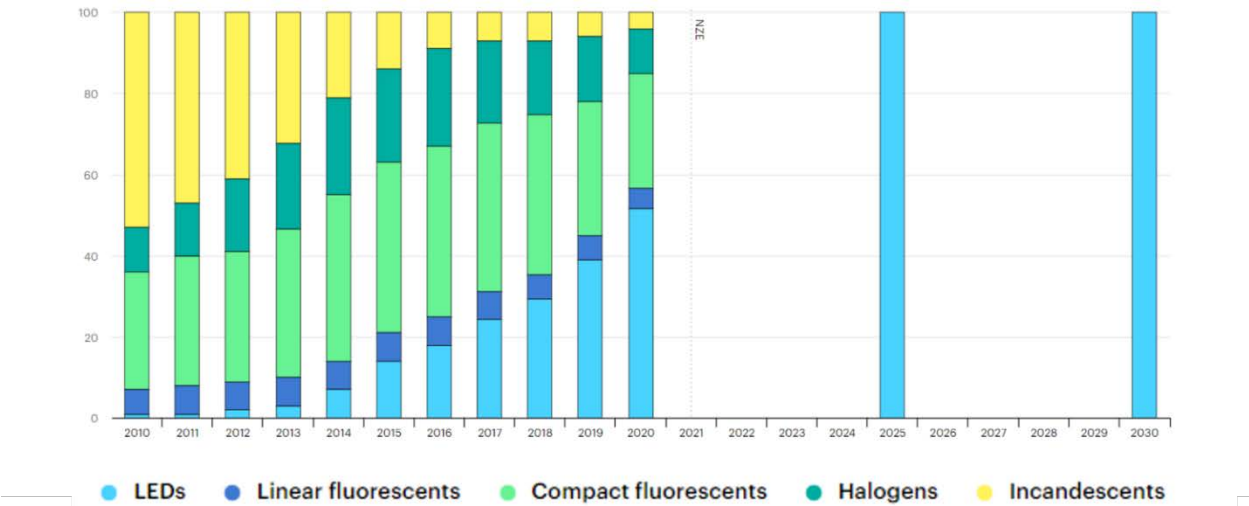


Figure 1. Market trend of different lighting technologies with particular emphasis on LEDs and their expected progression until 2030. (Source: International Energy Agency).

An LED is an electric component that emits light when an electric current is applied. The LED architecture is composed of two electrodes sandwiching a series of thin layers made of inorganic semiconductors, as shown in **Figure 2a** where a simple configuration is sketched. The process of light emission is called electroluminescence (EL) and takes place when a *p-n* junction is created and a forward bias is applied (Figure 2b). The chemical doping of such layers is adopted to improve their conductivity towards electrons ( $e^-$ ) or holes ( $h^+$ ) (n- and p-doping, respectively). First, when a p-doped material and an n-doped material are placed in contact electrons and holes diffuse towards the opposite polarity forming the, so-called, depletion region. This space charge separation produces a voltage called built-in voltage ( $V_0$ ). At this point this region is highly resistive and the only charge is given by the ionized donors and acceptors. Under the application of a bias the voltage drops across the depletion region. Specifically, under a forward bias, where  $h^+$  and  $e^-$  are injected in the region of opposite polarity, the depletion region shrinks ( $V_0 - V$ ) and the carriers diffuse into the region of opposite conductivity where they eventually recombine emitting a photon. LEDs are mainly based on p-n heterojunctions, in which the active layer acts as a trap for  $h^+$  and  $e^-$ . Ultimately, the chemical composition of the heterojunction barrier determines its band-gap ( $E_g$ ) and, therefore, the emitted light color across the spectra from UV to IR wavelengths. This technology has evolved rapidly since the past century and, in fact, LEDs have quickly found a wide selection of applications. The main advantages of LEDs are the long lifespan (up to 50000 hours), high efficiency, fast response to on-off switching, reduced dimensions and weight, better thermal management compared to conventional light sources, and extreme color tunability.<sup>[1-3]</sup> Nowadays, because of their reduced electrical consumption, LEDs represent the best alternative to incandescent and fluorescent light sources and their market is growing year by year, as already mentioned.

More recently, there has been intense development in the so-called organic light-emitting diodes (OLEDs) (Figure 2c). They represent an alternative energy-saving lighting technology, with processing and integration advantages over current inorganic LED systems. The semiconducting materials that constitute these devices are organic in nature, typically conjugated small molecules and polymers, but also neutral and ionic transition metal complexes (iTMCs). The conjugated feature of these materials determines their semiconductivity and the fine-tuning of their properties rely on their chemical structure, that is, the choice of their functional groups and heteroatoms. Similarly to LEDs, the EL process, occurs when electrons and holes meet in the semiconductor. Holes and electrons are injected into the conduction band (CB) or highest occupied molecular orbital (HOMO) and into the valence band (VB) or lowest unoccupied molecular orbital (LUMO), respectively. Pushed by the electric field the charge carriers drift in opposite directions until they recombine forming an exciton. The exciton is a localized hole-electron pair whose bond strength depends on the dielectric constant of the material. Depending on the nature of the emitter, excitons determine singlet and/or triplet electronic excited states which can eventually decay generating a photon or (undesired) heat. The wavelength of the emitted photon is dictated by the band-gap energy of the organic semiconductor layer.

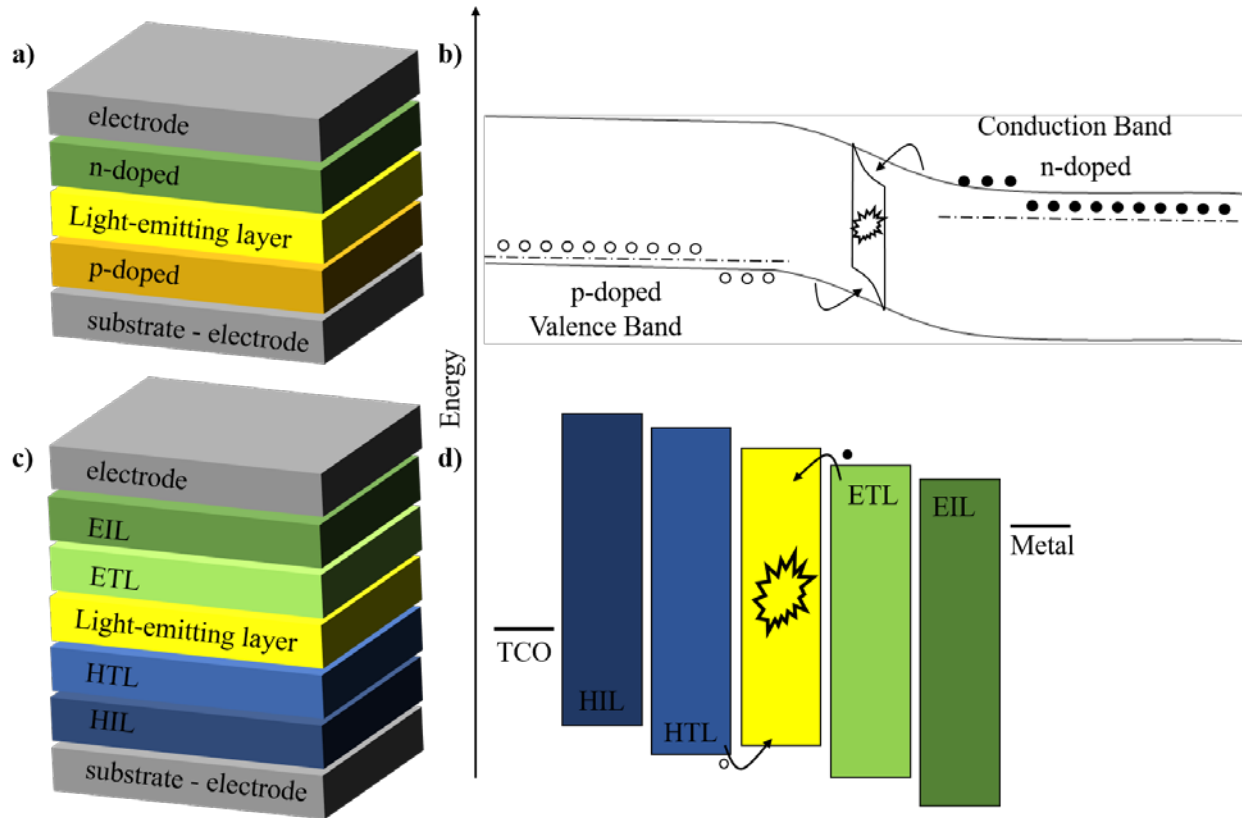


Figure 2. a) and b) show the stacked architecture of a LED and its energy band diagram, while c) and d) show the stacked architecture of an OLED and the energy levels for each layer.

The formation of the junction and the electrode work function (WF) is crucial to have energy alignment and working devices. This means that it is very difficult to have efficient electroluminescence from just the active layer sandwiched between two working electrodes and driven at low voltages. The large energy barriers between the active layer and the electrodes would allow charge injection only at high voltages causing overheating and high non-radiative recombination, implying a faster degradation and poor EL efficiency. Nowadays, the level of optimization of modern OLEDs allows for ohmic charge carrier injection, efficient recombination, and light extraction.<sup>[4]</sup> OLEDs are attractive because of their wide color gamut and high brightness, properties that are characteristic of the organic molecules used as light emitters. Moreover, they also allow for easier fabrication of foldable/flexible devices. Currently OLEDs are employed in TV, smartphone and smartwatch screens as they still need technological advances to become a competitor for indoor/outdoor lighting applications. This is due to their elevated production costs, as they consist of many layers processed via deposition techniques that require inert conditions, high vacuum and moderately high temperatures. In addition, the costs of the organic semiconductor materials are non-negligible.

More recently, a simpler form of OLED has been developed, the light-emitting electrochemical cell (LEC). LECs possess a very simple architecture in which a single organic active layer is deposited between two electrodes resulting in efficient light emission (**Figure 3**). This is possible

thanks to their unique operational mechanism, which combines charge carriers and ionic species displacement. This is advantageous since it reduces the fabrication costs and the total amount of resources used per device unit.

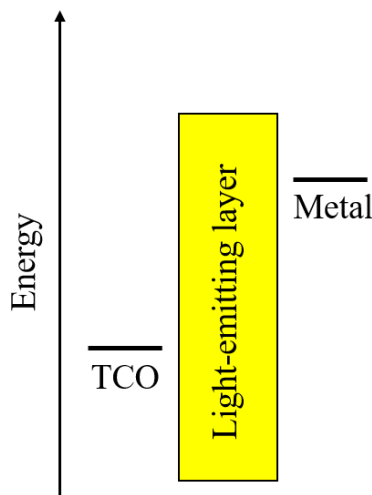


Figure 3. Single active layer sandwiched between two low work-function electrodes as archetypical LEC architecture.

## 1.2 Light-Emitting Electrochemical Cells

LECs are an emerging technology in the solid-state lighting field. In their simplest form, they comprise an organic electroluminescent semiconductor mixed with a solid electrolyte deposited as a thin active layer between two working electrodes.

The first example of a LEC was proposed in 1995 by Pei et al. who observed electroluminescence from a single emitting layer of MEH-PPV, a red conjugated copolymer, when a lithium salt was added into the layer.<sup>[5]</sup> One year later, in 1996, Lee et al. demonstrated the first emission in LECs from ionic transition metal complexes (iTMCs). In their work they showed that ionic ruthenium(II) complexes can give efficient electroluminescence when thin films are deposited between two electrodes.<sup>[6]</sup> These were the first two examples of the two most common families of LEC devices, polymer LECs (CP-LECs) and iTMC-LECs.

The simultaneous presence of charge carriers, mobile ions, and excitons within the same emitting layer of a LEC determines a complex working principle that has been the object of debate for a long time. After a certain voltage (or current) is applied to the device, the typical behavior over time shows an increase in luminance while the current (or voltage) increases (decreases). Generally, this is explained by the presence of mobile ions which, under an electric field, can reorganize in the active layer and migrate towards the electrodes, promoting charge carrier injection. Although this general explanation is commonly accepted, two different theories, the electrodynamical<sup>[7]</sup> and electrochemical<sup>[8]</sup> models, were developed to demonstrate how the electric field and the voltage distribute across the device. Both models agree on the formation of an electronic double layer (EDL) in close proximity to the electrodes which dissipates the applied

bias and allows for charge injection. However, the electrodynamical model (**Figure 4a**) assumes that the EDLs enable a sharp drop in the electric potential near the electrode interfaces. As a consequence, in the bulk of the material the vast majority of anion-cation pairs are still joined. Here, the electric field is absent and the light emission is thought to take place from this region. The electrochemical model (Figure 4b), on the other hand, assumes that the EDLs drop the potential only as it is needed to form ohmic contacts. The injected charge carriers represent uncompensated charge within the active layer which is being neutralized through further ionic redistribution. In fact, at the cathode side, electrons neutralized by cations constitute the n-doped zone. Similarly, at the anode side, holes neutralized by anions form the p-doped zone. The doped regions widen over time forming a  $p-i-n$  junction ( $i$  = intrinsic, undoped). Across the intrinsic region, the applied potential drops substantially and favors charge recombination and light emission. These operating regimes imply that their occurrence depends on the formation of ohmic contacts. When the injection is non-limited the LEC follows the electrochemical model. If the injection is limited, the doping becomes less pronounced and the ion redistribution increases the EDL formation until the bulk is field-free, following the electrodynamical model.<sup>[9]</sup> These models also differ in terms of device performance and degradation of the active layer, as the electrochemical model involves ohmic injection and a higher rate of electron-holes recombination.<sup>[9]</sup> The operational mechanism of LECs is a determining factor for key figures of merit, such as lifetime and turn-on time of these devices. It comes to no surprise that it has been thoroughly studied in the literature, including in this Thesis (Chapters 3 and 5).

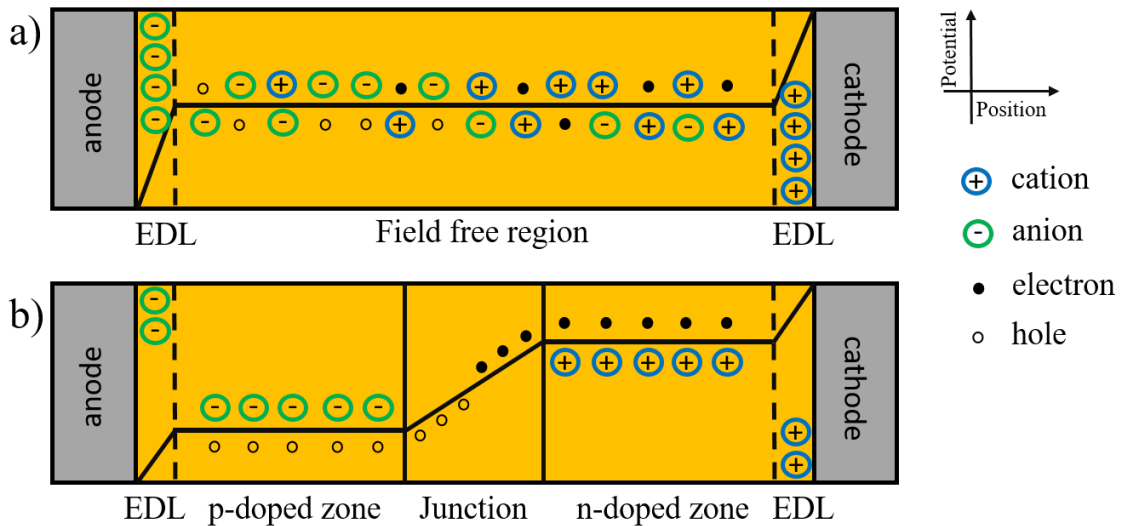


Figure 4. Simplified diagrams of a) the electrodynamical model and b) the electrochemical model.

For instance, a planar LEC configuration was used for in situ surface analysis, during the different phases of a device lifetime, such as Kelvin probe microscopy and FTIR (Fourier-transform infrared spectroscopy).<sup>[10]</sup> The planar configuration consists of an active layer deposited between two interdigitated electrodes. In the planar configuration, as the electrode spatial separation is in the micrometer scale, only high voltages are effective to drive the device, resulting in lower efficiency.

**Figure 5** shows Kelvin probe microscopy measurements performed on planar devices driven at 8 V, which demonstrate the two models predicted by theoretical calculations. In the electrochemical model (Figure 5a) the voltage slightly drops at the interfaces to form ohmic contacts and it is kept constant across the doped zones. A second abrupt voltage drop is then registered through the intrinsic zone where light emission occurs. Differently, for the electrodynamical model (Figure 5b) the voltage sharply drops at the electrodes interfaces and a constant value is kept across the film.<sup>[9]</sup>

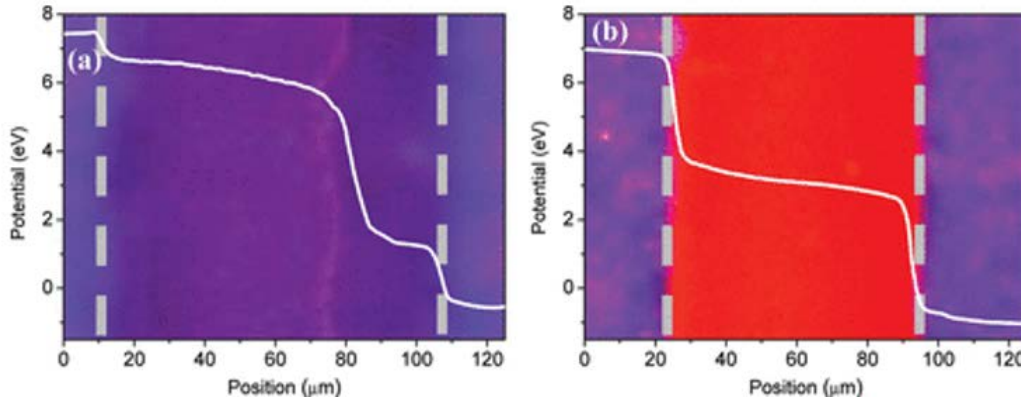


Figure 5. Electrostatic potential and light-emission profiles in planar LECs during operation and voltage dependence on the interfacial potential drop. Typical steady-state potential profiles of an LEC during operation at  $V = 8$  V in a), the noninjection-limited and b), the injection-limited regime. The pictures behind the graphs are UV/PL images in steady state, on the same horizontal scale. Figure taken from ref. 9.

The general operational mechanism of LECs can also be identified from a sandwiched device. This second configuration is more practical in view of real-life devices. This is because the closer separation of the electrodes (few hundreds of nanometers) facilitates efficient radiative recombination at lower voltages and the bottom transparent electrode allows for efficient light extraction. **Figure 6** shows the temporal evolution of the luminance and voltage when a current density is applied. The pristine state can be recognized by stage I where the device is contacted but no bias is applied. When a current (constant or pulsed) is applied to the electrodes the mobile ions begin to redistribute and form the EDL, in stage II. The EDL formation and the subsequent doping process determine the turn-on time of a device. This can range from a few seconds to hours.<sup>[11,12]</sup> Initially, the resultant voltage is high because the EDL and the doped zones are not yet completely formed. However, they quickly build up in time, and voltage decreases as result. At the same time, the luminance value increases until the maxim value is reached. In stage III, the device's lowest voltage and highest luminance are established and kept over time in its operational steady state. Finally, in stage IV, as the doped zones grow and the intrinsic zone shrinks, the luminance levels fall. This phase is often characterized by an increase in voltage as a result of possible degradation processes.

The mechanism of intrinsic degradation of the active layer is still something not fully understood but most certainly there is more than one effect causing it, such as degradation at the cathode



interface<sup>[13,14]</sup>, effect of self-heating<sup>[14,15]</sup> and irreversible redox reactions.<sup>[16–18]</sup> In Chapter 3, we introduce a novel technique to monitor the degradation by measuring the photoluminescence while biasing the device, in a simultaneous manner.<sup>[19]</sup> Similar results were obtained from previous studies in which the photoluminescence was measured at different times after turn-on.<sup>[20]</sup> The results illustrates that applying an electrical bias quenches the photoluminescence intensity. The devices are able to recover the photoluminescence in open-circuit conditions, although this recovery is only partial and bias-dependent. This implies that there exists an irreversible loss of light intensity after relaxation that increases with the driving time and magnitude of the electrical bias.

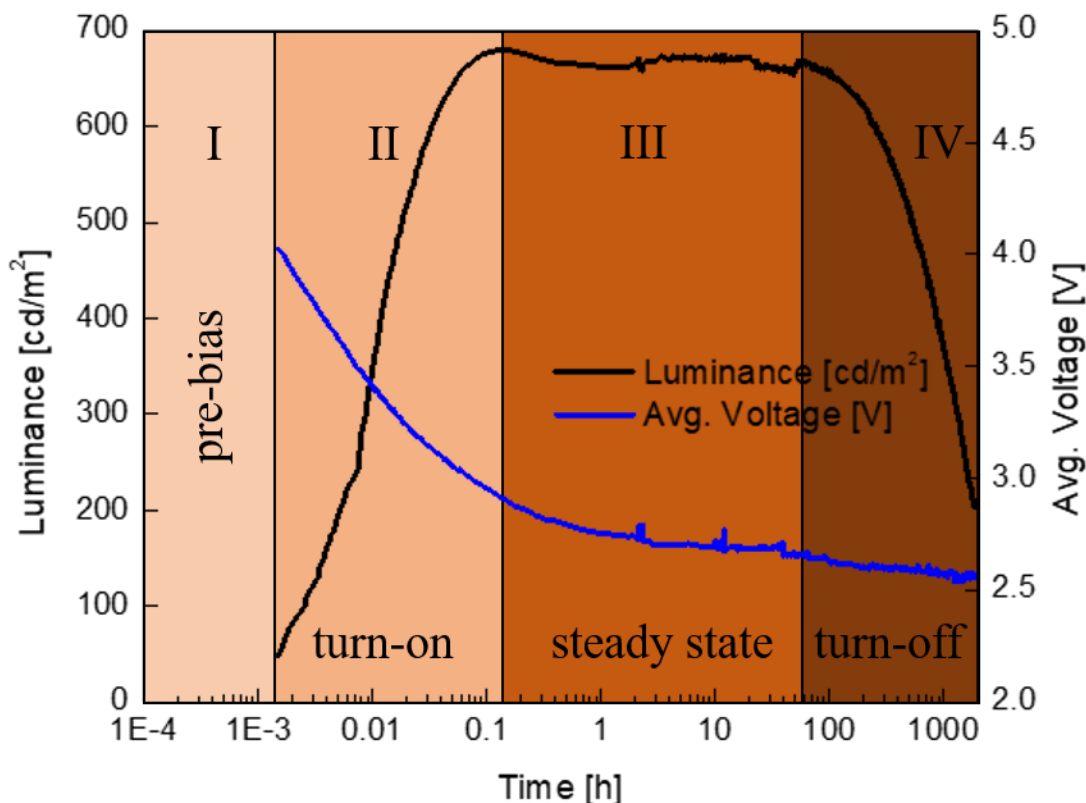


Figure 6. Temporal evolution of a LEC under pulsed current bias. When the time is expressed in logarithmic scale it is possible to observe each phase of the device lifetime.

### 1.3 Emitters for Light-Emitting Electrochemical Cells

The uniqueness and only requirements of LECs are the presence of mobile ions that drive the turn-on and govern the device behavior. A large variety of light-emitting molecules can be used when this condition is satisfied. Intensive research in the OLED and LEC fields produced a wide variety of emitters with fine-tuned photophysical properties and structures. The detailed review of all the emitters used in LECs is not the aim of this Thesis, instead, a summary will be presented highlighting the most important features of each category. The light-emitting components that first found application in LECs are fluorescent conductive polymers and iTMCs (in CP-LECs and

iTMC-LECs, respectively). However, more recently, driven by OLED and LED advancements new materials have been added to the list, such as small organic molecules (SM) and perovskites. As mentioned in paragraph 1.2, a red CP was used for the first LEC ever reported.<sup>[5]</sup> However, to guarantee ion conduction an additional component was added. Polyethylene oxide (PEO) was the first ion-conducting polymer to be used in LECs. The PEO ion conduction mechanism relies on the coordination of the cations by the oxygen atoms in the polymer chain.<sup>[21]</sup> At the same time, anions are poorly affected and only ionically bonded to the cations. In the pristine state, oxygen coordination competes with the ionic couple formation resulting in an equilibrium.<sup>[22]</sup> Only an external bias will drift apart these ions, and the cations displacement can be explained in sequential jumps within the coordinating matrix which can take place on the same chain or on a different chain of the ion-conducting polymer, depending on their distance.<sup>[23,24]</sup> Anions instead are not so hindered and typically move faster. For this reason, in CP-LECs the emitting zone is often closer to the cathode in the first stages of operation.<sup>[25]</sup> The disadvantage of PEO is its tendency to form crystalline phases, especially at high molecular weights, which limit ion conduction.<sup>[21]</sup> Nonetheless, it has been vastly used and efficient devices were reported since the early days of LECs.<sup>[5,7]</sup> More recently, new ion-conducting polymers have been introduced resulting in improved performances. In this context, the work of Edman et al. on CP-LECs resulted in one of the most efficient and long-lived devices using a phenyl-substituted poly(*p*-phenylene vinylene) copolymer, also known as SY-PPV or “super-yellow”, and trimethylolpropane ethoxylate (TMPE) as ion-conducting polymer.<sup>[26,27]</sup> The same group reported another efficient device composition in which star-branched oligocarbonates were introduced.<sup>[28]</sup> In Chapter 3 of this Thesis we introduced a new hyperbranched ionic conductive polymer in a state-of-the-art CP-LEC.

Even though the use of polymeric emitters demonstrated efficient devices, they are limited by their fluorescent nature which reduces the collection of electrically-generated excitons and results in a maximum external quantum efficiency (EQE) of about 25%.<sup>[29]</sup> Indeed, upon the application of an electrical bias singlet and triplet exciton are generated in a specific ratio of 25% to 75%. This is regulated by spin statistics, since for a singlet the spin quantum number, which is  $s = 0$ , equals to only one spin state with total spin angular momentum of 0, while for a triplet,  $s = 1$ , it equals to three spin states with a total spin angular momentum of 1. In organic molecules and polymers singlet excitons (25%) give rise to emissive excited states whereas triplet excitons (75%) are typically non-emissive at room temperature.

The second large category of emitters for LECs is represented by iTMCs.<sup>[30]</sup> They differ from polymeric materials in that they are ionic phosphorescent emitters. Being intrinsically ionic, they do not need in principle any additional free-moving ionic species (such as the copolymers used in CP-LECs). However, it was soon clear that adding small concentrations of ionic liquids (ILs) would improve the turn-on time and luminance levels.<sup>[31–33]</sup> Another advantage of iTMCs is that they can collect up to 75% of the electrically-generated excitons and, at the same time, harvest singlet excitons thanks to the inter-system crossing process. As a result, the EQE can theoretically be 100%. The first works on iTMC-LEC focused on substituted ruthenium(II) complexes.<sup>[34,35]</sup> Ru(II)-based devices have one important limitation regarding the color tuning, since the emission band is placed in the orange-red part of the visible spectra. Later on, the family of iridium(III) complexes gained more interest thanks to their much improved photochemical stability, very high emission quantum efficiencies and wide color tunability, which is key in order to obtain white

emission for lighting applications.<sup>[36]</sup> Today they represent by far the most used and efficient metal complex for LECs. Two Ir(III) complexes can be considered the archetype for LEC applications,  $[\text{Ir}(\text{ppy})_2(\text{bpy})]^+$  and  $[\text{Ir}(\text{ppy})_2(\text{phen})]^+$ .<sup>[36]</sup> Their photophysical and electroluminescent properties set a benchmark from which ligand design began. The design of new ligands is of great importance as it allows for tuning to virtually any color and directly affects the final device performance.<sup>[37]</sup> Important developments in iTMCs device performance were proven by many research groups, Bolink et al., Slinker et al. and Zysman-Colmann et al. to cite a few, whose efforts combined ligand design (e.g. facilitating supramolecular interactions) and alternative driving conditions (pulsed bias vs constant bias) to further improve luminance and lifetime.<sup>[38-42]</sup> An additional factor that proves the superior properties of Ir(III) is demonstrated in a recent study, which showed the improved thermal stability of Ir(III) complexes due to lower non-radiative recombination rates.<sup>[43]</sup> Although Ir(III)-complexes proved to have superior properties, its costs are still high due to its scarcity in the Earth's crust. In this regard, it is important to find alternative emitters to alleviate the potential costs of device fabrication based on iridium-based emitters. Recently, Cu(I)-based LECs have also proven to be promising emitting species. The same concepts of ligand design can be applied to these complexes and they are rapidly improving with respectable efficiencies and color tunability, including white emission, and also showing thermally activated delayed fluorescence (TADF) properties.<sup>[18,44,45]</sup> On the other hand, Pt(II) complexes for LECs have been scarcely explored with only few examples in the red region of the visible spectra.<sup>[46-48]</sup> In Chapter 5, we introduce a comparative study on new Cu(I) complexes and, for the first time, on blue and green emissive Pt(II) complexes.

Small organic molecules (SM), can also be used as emitters for LECs as they can rely on different photophysical processes to harvest excitons, including phosphorescence, TADF, triplet-triplet annihilation (TTA) and hybridized local and charge transfer (HLCT). Once again, molecular design plays a major role as the photophysical properties depend on the molecule's electronic excited states. Most of the SM used in LECs are either pure fluorescent or take advantage of the TDAF mechanism, and they are divided into two main subgroups: ionic SM and non-ionic SM.<sup>[49,50]</sup>

Finally, perovskites are a class of polycrystalline materials with tunable optoelectronic properties. Perovskites with the general formula  $\text{ABX}_3$  (where A is an inorganic cation, such as  $\text{Cs}^+$ , or an organic cation such as  $\text{CH}_3\text{NH}_3^+$  (MA) or  $\text{CH}(\text{NH}_2)_2^+$  (FA), B is  $\text{Pb}^{2+}$  or  $\text{Sn}^{2+}$  and X a halogen, such as  $\text{I}^-$ ,  $\text{Br}^-$  or  $\text{Cl}^-$ ) have been largely studied for LED applications.<sup>[51,52]</sup> The green emissive  $\text{CsPbBr}_3$  represents the standard for light-emitting perovskites and it has been used as active material in LECs. Although the ionic components forming the crystal structure, especially the A and X sites, are to some extent mobile, it was shown how the introduction of an IL helped improve the maximum luminance values.<sup>[53-55]</sup> Perovskites are still new in the field of LECs but they have already shown encouraging results and they will probably take over for the next generation of devices.

## 1.4 Limitations of light-emitting electrochemical cells

Since their discovery, LECs have always lacked behind the two most efficient solid-state light sources, LEDs and OLEDs. Four main shortcomings prevented LECs from meeting market requirements: 1) long turn-on time, 2) short lifetime 3) low efficiency, and 4) limited color emission/emitter band-gap. In addition to these, the lack of a standardized method to measure the device performance makes difficult to establish a direct comparison between different devices to objectively assess where LECs stand compared to OLEDs.

The first parameter is the turn-on time that quantifies the device's response to the electrical current. It is often referred to as the time employed to reach  $100 \text{ cd m}^{-2}$  or the maximum luminance value. The turn-on time is a direct consequence of the ionic motion in the active layer, hence ions and their concentration have a direct influence. These effects have been largely proven with different emitters and electrolytes.<sup>[56]</sup> In general, increasing the electrolyte concentration would decrease the turn-on time, but beyond a certain threshold the performance can be negatively affected. Applying a higher current density or voltage also decreases the turn-on time but again, it is important to not overdo it to prevent degradation that could affect the lifetime. The effects of the IL concentration and bias on the device performance are also shown in Chapter 3 of this Thesis.

The lifetime is maybe the most important aspect that needs to be improved in LECs. Everything in the device affects the lifetime, from the choice of the materials and their concentration to the choice of the applied bias. Moreover, it is not yet clear the degradation paths that the electroluminescent species undergo during operation. The proposed mechanism includes permanent oxidation/reduction and degradation at the electrode interfaces as mentioned in Section 1.2. As already mentioned, both turn-on time and lifetime depend directly on the operational mechanism of LECs and there are some ways to improve them, for example tuning the IL concentration or applying a pulsed driving current<sup>[38,39]</sup>.

Efficiency is another important aspect that needs improvement for this technology to reach the market. The efficiency is mainly limited by four factors: photoluminescence quantum yield (PLQY), nature of the emitter, non-selective contacts, and electroluminescence quenching. The PLQY is strictly related to the electroluminescence efficiency of the emitter, as it exists a direct correlation between the PLQY and the EQE of the device as explained in Section 2.3 of this Thesis.<sup>[31]</sup> In general, from a higher QY, higher efficiency is expected as well, however, fluorescent and phosphorescent emitters have a different electroluminescent response, as mentioned in Section 1.3. Ultimately, there can be electroluminescence quenching due to high emitter concentration, especially for iTMCs,<sup>[57,58]</sup> and due to the advancement of the doped zones. It has also been demonstrated how the choice of the top electrode can play a role in determining the efficiency and lifetime.<sup>[9,59]</sup>

Finally, although the emission spectra of a molecule or polymer can be fine-tuned by adjusting the functional groups and ligands, it is not yet trivial to obtain stable blue and red emitters. Particularly for blue emitters, due to the wide band gap ( $\sim 3 \text{ eV}$ ) and long exciton lifetime ( $\sim \mu\text{s}$ , for phosphorescent materials), excitons might accumulate giving rise to quenching interaction like TTA or triplet-polaron quenching (TPQ). In addition, it may also create hot excited states. This is due to the interaction of high energy excited states ( $S_n$  or  $T_n$  with  $n > 1$ ) with each other that generates a hot exciton (or hot polaron). If not controlled through molecular design and

dopants,<sup>[60,61]</sup> their relaxation follows a predisocciative path yielding radicals that result in defect states, thus causing intrinsic degradation.<sup>[62]</sup> Low band-gap organic materials suitable for red and NIR emission also suffer from significantly lower luminescence efficiency.<sup>[63]</sup> This can be understood when considering the so-called “band-gap” law which predicts a progressively greater likelihood of nonradiative deactivation of the excited states as the energy gap is reduced.<sup>[64]</sup> Finally, from a real-life application point of view, LECs are still in an initial stage when compared to OLEDs. OLEDs are already marketed and can be found in different architectures and novel designs, such as transparent, conformable or flexible devices, giving rise to a plethora of new applications.<sup>[4,65]</sup> In Chapter 4 of this Thesis we have also explored a different device configuration with the fabrication of semitransparent devices, hoping that it can motivate future research outcomes.

## 1.5 Aim of the thesis and Overview

LEC device prototypes, in the field of solid-state optoelectronics, are still in their early stages. On the one hand, the principles that dictate the working mechanism and performance are well known. On the other hand, efficient, long-lived and with a wide color gamut devices are still lacking. In this regard, the simplicity of the LEC device architecture is very advantageous but with many aspects to take into account, as mentioned in the previous sections.

The work of this Thesis focuses on the improvement of the LEC technology by introducing new materials, in particular iTMC emitters and an ionic conductive polymer, in order to improve the figures-of-merit of LECs and overcome their shortcomings, as well as the design and fabrication of novel architectures that can enable new applications for these devices.

In Chapter 3, it is shown how the introduction of a new hyperbranched ionic transporting polymer in the solution of the precursors favors the fabrication of state-of-the-art CP-LECs with an improved lifetime. By measuring the PL during EL operation we observe that the addition of such polymer reduces the PL quenching of the CP due to the interactions with the ionic species and stabilizes the steady state operation of the device under a driving pulsed current.

In Chapter 4, ALD and PLD techniques (atomic layer deposition and pulsed laser deposition, respectively) are used for the first time to achieve highly transparent iTMC-LECs. Here, a thin layer of SnO<sub>2</sub> deposited by ALD has a double function of buffer and charge transport layer while a thicker indium tin oxide (ITO), deposited by PLD, is used as a semitransparent top cathode. The effects of such techniques on the active layer are accounted by characterizing the performance and PL properties.

In Chapter 5, two new families of iTMCs based on copper(I) and platinum(II) are explored as alternative emitting materials to the more commonly used and costly Ir(III)-based complexes. In collaboration with the group of Prof. Dr. Edwin Constable and Prof. Dr. Catheryne Housecroft, Cu(I) complexes with different counterions are synthesized and characterized. Devices are fabricated and the effect of these counterions are investigated. Finally, in collaboration with the group of Prof. Dr. Violeta Sicilia, we also develop, for the first time, blue/green emissive LEC devices based on Pt(II) complexes. Here, devices are fabricated starting from solutions using different solvents, acetonitrile and dichloromethane. We observed that the performance changes according to the solvent used to cast the active layer. Overall, in this Chapter we demonstrate the

feasibility of such ionic metal complexes as future emitters in LECs and organic solid state light-emitting devices.

The main results shown in this Thesis are summarized in Chapter 6 and a brief Spanish resume is included in Chapter 7.

## 2. Experimental and methodology

## 2.1 Materials

Both CPs and iTMCs were used as emitters in this work. A summary of their chemical structures is shown in **Figure 7**. In Chapter 3 the so-called “Super yellow” (SY) conjugated copolymer was used.<sup>[19]</sup> SY is considered a reference emitter for CP-LECs and it is readily available for purchase. As ionic transporting polymer a hyperbranched polymer (Hybrane) was used. In Chapter 4, an archetypical yellow Ir(III) complex,  $[\text{Ir}(\text{ppy})_2(\text{dtb-bpy})][\text{PF}_6]$ , where ppy is 2-phenylpyridine and dtb-bpy is 4,4'-di-tert-butyl-2,2'-dipyridyl, was used to fabricate semitransparent iTMC-LECs. The use of this complex in LECs was previously reported by Slinker et al.<sup>[66]</sup> In Chapter 5, Cu(I) and Pt(II) complexes were introduced as novel emitters for iTMC-LECs. The Cu(I) complexes (Cu1, Cu2, Cu3 and Cu4), had the general formula  $[\text{Cu}(\text{P}^{\wedge}\text{P})(\text{N}^{\wedge}\text{N})]^+ [\text{A}]^-$ , where the ( $\text{P}^{\wedge}\text{P}$ ) is the bidentate xantphos (4,5-bis(diphenylphosphino)-9,9-dimethylxanthene) ligand, and the ( $\text{N}^{\wedge}\text{N}$ ) is the Me<sub>2</sub>bpy (6,6'-dimethyl-2,2'-bipyridine) ancillary ligand and where  $[\text{A}]^-$  is either  $[\text{PF}_6]^-$  (Cu1),  $[\text{BF}_4]^-$  (Cu2),  $[\text{BPh}_4]^-$  (Cu3) or  $[\text{Bar}^{\text{F}_4}]^-$  (Cu4) ( $[\text{Bar}^{\text{F}_4}]^- = \text{tetrakis}(3,5\text{-bis}(\text{trifluoromethyl})\text{phenyl})\text{borate}$ ). Complexes were synthesized and characterized by the group of Prof. Dr. Edwin Constable and Prof. Dr. Catherine Housecroft from the Chemistry Department at University of Basel (Switzerland). The five studied Pt(II) complexes were the following:  $[\text{Pt}(\text{Cbz-C}^{\wedge}\text{C}^*) (\text{PPh}_3)(\text{py})]^+$ ,  $[\text{Pt}(\text{Cbz-C}^{\wedge}\text{C}^*) (\text{P}^{\wedge}\text{N})]^+$  and  $[\text{Pt}(\text{Cbz-C}^{\wedge}\text{C}^*) (\text{P}^{\wedge}\text{P})]^+$  where Cbz-C<sup>∧</sup>C\* is a carbazole-modified cyclometallated ligand (1-(4-(9H-Carbazol-9-yl)phenyl)-3-methyl-1H-imidazole), py stands for pyridine (Pt5), ( $\text{P}^{\wedge}\text{N}$ ) stands for 2-(2-(diphenylphosphino)ethyl)pyridine (Pt6), and ( $\text{P}^{\wedge}\text{P}$ ) stands for 1,1-bis(diphenylphosphino)methane (Pt7), 1,1-bis(diphenylphosphino)ethane (Pt8) and 1,1-bis(diphenylphosphino)benzene (Pt9). The synthesis, purification and characterization were carried out by the group of Prof. Dr. Violeta Sicilia from the Homogenous Catalysis Department at the University of Zaragoza (Spain).



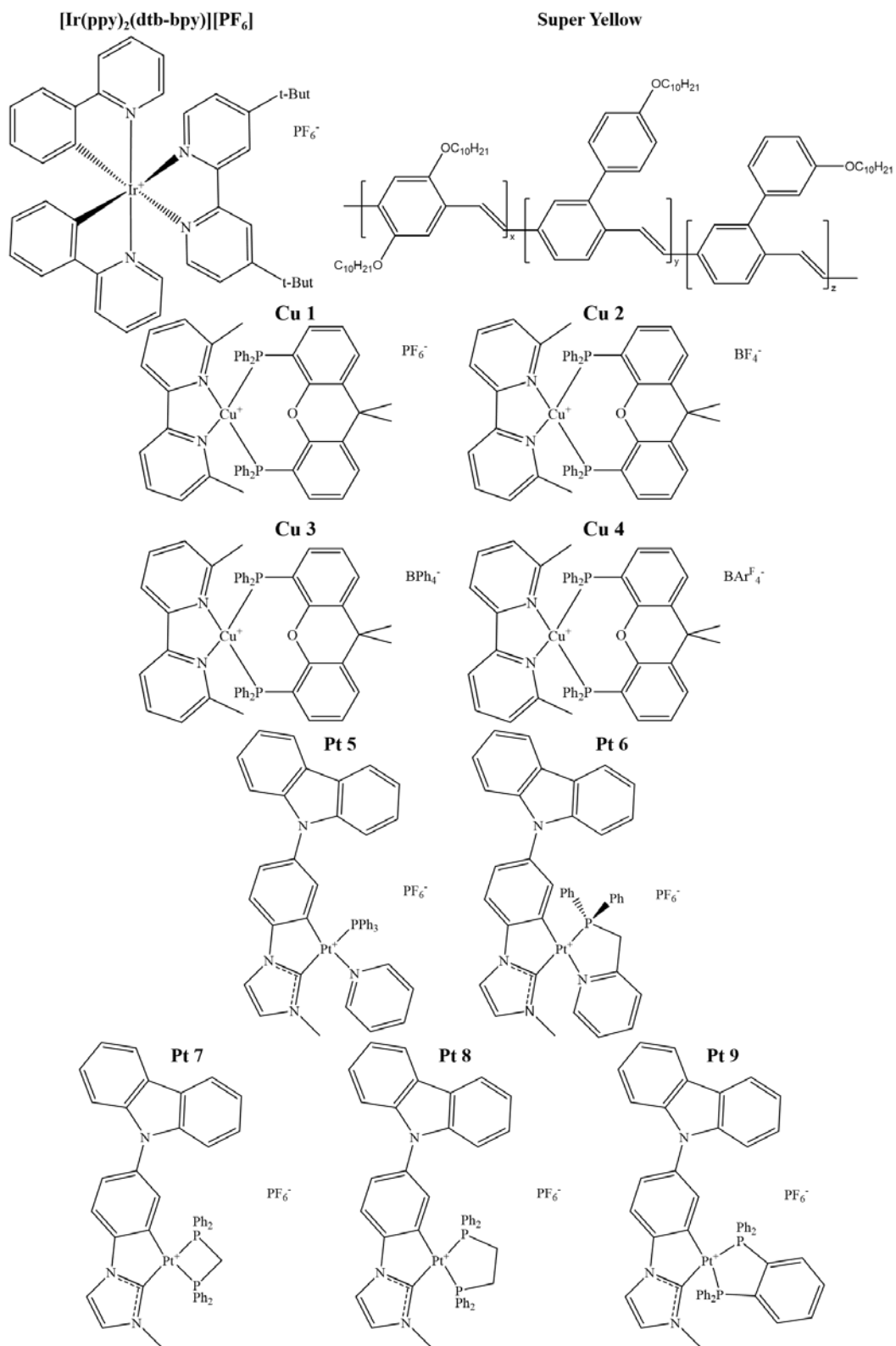


Figure 7. List of light-emitting materials used as active materials in LECs in this Thesis. The series of Cu1-4 present different counterions while the the series Pt5-9 different ancillary ligands.

## 2.2 Device Fabrication

The fabrication of LECs consists of several steps carried out in a  $N_2$  filled glovebox in a class 10000 clean room. Devices were fabricated as follows: cleaning of substrates, deposition of PEDOT:PSS (poly(3,4-ethylenedioxythiophene) polystyrene sulfonate) by spin-coating (only for iTMC-LECs), deposition of the active layer by spin-coating and deposition of the top metal cathode. For standard devices Al was thermally evaporated and for the semi-transparent iTMC-LECs  $SnO_2$  and ITO were deposited by ALD (atomic layer deposition) and PLD (pulsed layer deposition), respectively (see details in Chapter 4).

A vertical device architecture was used with the following stacks (**Figure 8**): glass/ITO/Active layer/Al for SY-LECs, glass/ITO/PEDOT:PSS/Active layer/ $SnO_2$ /ITO for semi-transparent Ir-LECs and glass/ITO/PEDOT:PSS/Active layer/Al for Pt-LECs and Cu-LECs.

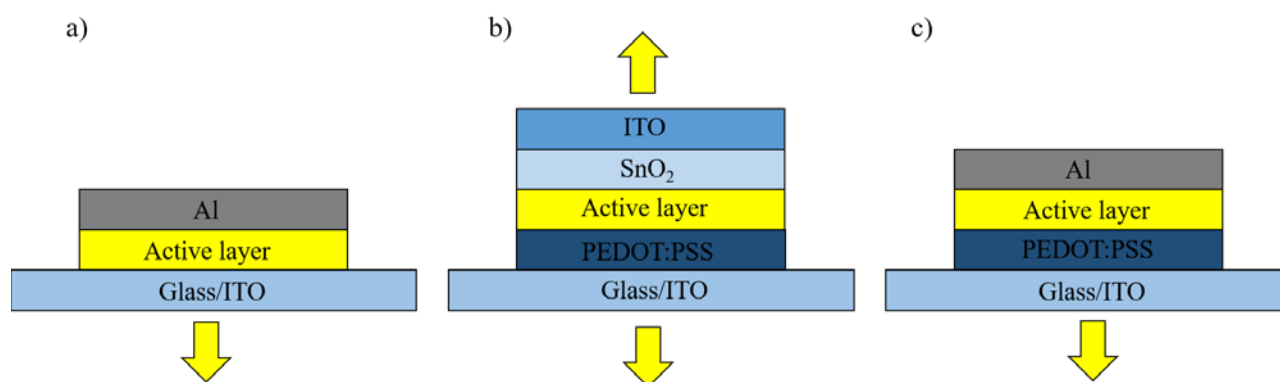


Figure 8. Schematic representation of the device architectures presented in this Thesis.

Pre-patterned ITO glass substrates were used for all devices. They were subsequently cleaned ultrasonically in water-soap, milliq water, and 2-propanol baths. After drying, the substrates were placed in a UV-ozone cleaner (Jelight 42-220) for 20 min. For iTMC-LECs, a PEDOT:PSS layer of 90-100 nm was spin coated on the substrates. This was done by dropping a commercial PEDOT:PSS CH8000 solution on the substrate and spun at 4000 rpm for 60 seconds. Subsequently, it was annealed at 150 °C for 10 minutes. This resulted in a thickness of 80 to 100 nm. PEDOT:PSS is used to help hole injection at the anode and to provide a smoother surface before the emitter deposition preventing pinholes.

Prior the deposition of the active layer, the emitter solution was prepared at the desired concentration. For iTMCs in acetonitrile (ACN) and dichloromethane (DCM) a solution concentration of 20 mg/mL was used and readily formed at ambient temperature. For the SY in cyclohexanone (CHN) a concentration of 7.5 mg/mL was used. The solution was left overnight on the stirrer at around 50 °C. The active layer consisted of the emitter and an ionic liquid, for iTMC-LECs, or a polymer electrolyte and a salt, for CP-LECs. Concentrations of the different components were optimized. For the active layer deposition it is important to tune the spinning speed as it controls the thickness. Thicknesses were optimized and measured using a profilometer (Ambios XP-1 profilometer). Speed rotations of 3000 rpm and 2000 rpm were used for SY- and iTMC-LECs, respectively. Solutions of highly volatile solvents (for example DCM) require

particular attention as they evaporate faster, resulting in a worse surface morphology. Therefore, in the case of DCM solutions, the substrates were covered in the first 10-15 seconds of spinning to mitigate this effect. In this Thesis this was done for the Pt-LECs of Chapter 5. For iTMCs the thickness of the active layer was between 80 nm and 90 nm from ACN solutions. For CP-LECs, the thin polymeric film thickness was in the range of 130-140 nm.

After the active layer the devices were transferred into a glovebox for annealing and cathode thermal deposition under ultra-high vacuum ( $10^{-6}$  mbar). Aluminum was used as top electrode (100 nm) using a shadow mask. The resulting active area was  $6 \text{ mm}^2$ . In the case of the semi-transparent iTMC-LECs, the top cathode consisted of  $\text{SnO}_2$  and ITO processed by ALD and PLD, respectively. These processes are described in detail in the following two Sections. The devices were generally measured in a  $\text{N}_2$  filled glovebox. However, for the particular characterization presented in Chapter 3, the devices were encapsulated and measured in a standard lab setting. The encapsulation consisted of an aluminum cover placed on top of the device using a photosensitive glue. The samples were then exposed for 1 minute to UV light to harden the glue.

## 2.2.1 Atomic Layer Deposition

Atomic layer deposition is a thin-film deposition technique that consists of a sequential use of chemicals in the vapor phase, also called precursors. As the precursors sequentially react with the surface of the sample, a thin film is grown layer-by-layer.<sup>[67]</sup> The choice of precursors is important for a successful ALD deposition. In fact, they should fulfill many requirements in terms of volatility, thermal stability, and reactivity with the substrates. Additionally, it is easier to produce the vapor phases if the precursors already are in their liquid phase at room temperature or if they are highly soluble in inert solvents. Other parameters should also be optimized for a correct film deposition, for example, the chamber temperature to which the substrates are exposed, the pulses of the precursors in terms of frequency and pressure, and the purging after every pulse.

For metal oxides deposition, such as  $\text{AlO}_x$  and  $\text{SnO}_x$ , an oxidizer (e.g.  $\text{H}_2\text{O}$  and  $\text{O}_3$ ) and a reactive compound of the metal of interest are used as precursors. The simplified sketch of **Figure 9** shows the principal steps of an ALD metal-oxide deposition. Initially, the metal precursor in its vapor phase is injected in the reaction chamber (step 1). After a delay, the chamber is purged to remove the precursor excess (step 2). In the same manner, in the second half cycle the oxidizer is first injected and purged (step 3 and 4). As a result, after every cycle a monolayer of the desired compound is formed on the substrate surface, This is repeated several times in order to achieve the desired thickness.

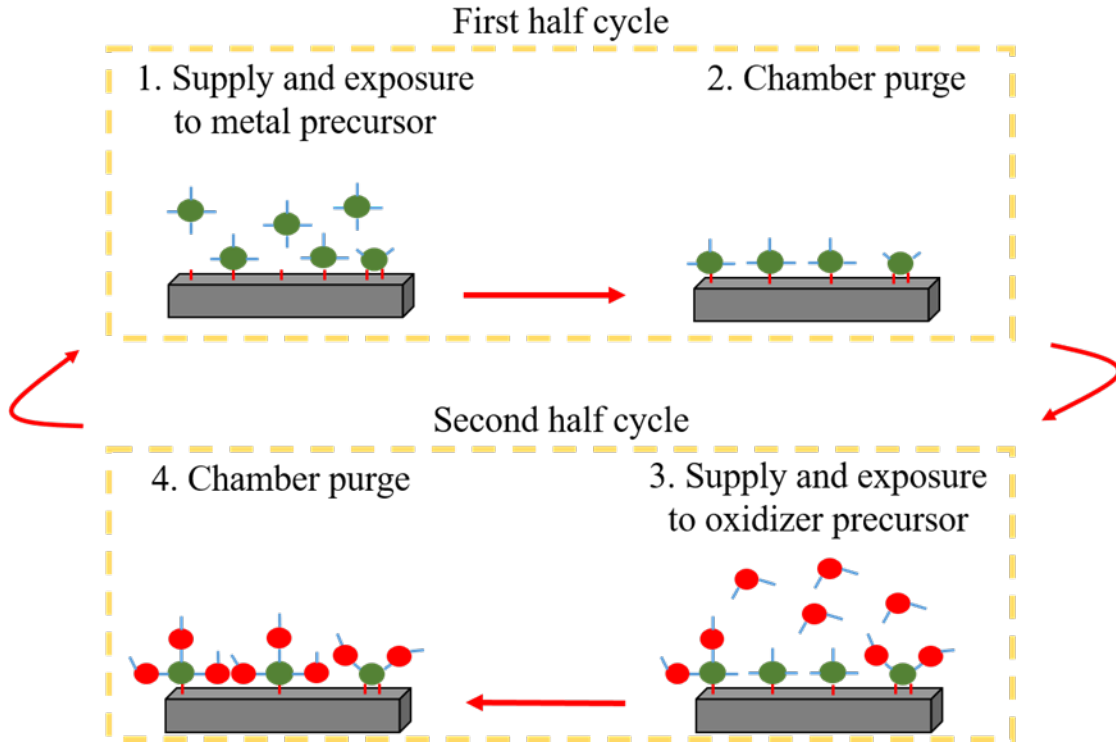


Figure 9. Simplified schematic illustration of an ALD cycle: first half cycle (metal precursor injection) and second half cycle (oxidizer precursor injection).

In Chapter 4, ALD was used to deposit 20 nm of SnO<sub>2</sub> at 90 °C. The SnO<sub>2</sub> was used both as a buffer and as an electron transport layer (ETL).

### 2.2.2 Pulsed Laser Deposition

The pulsed laser deposition is a physical vapor deposition technique that enables the depositing of thin films by utilizing a high-power pulsed laser focused onto the target material.<sup>[68,69]</sup> The laser beam locally vaporizes the target into a plasma plume that is then deposited on the substrate surface as a thin film (**Figure 10**). The process takes place in the presence of background gasses such as N<sub>2</sub>, O<sub>2</sub> and Ar depending on the composition of the thin film of interest. The deposition pressure is in the order of 10<sup>-3</sup> mbar. The PLD technique is mostly used for the deposition of transparent conductive oxides (TCO) and metal oxides, ITO, NiO<sub>x</sub> or SnO<sub>x</sub>. The PLD presents several advantages such as a high control over uniformity and stoichiometry of the deposited films, and high compatibility with a wide variety of different targets.

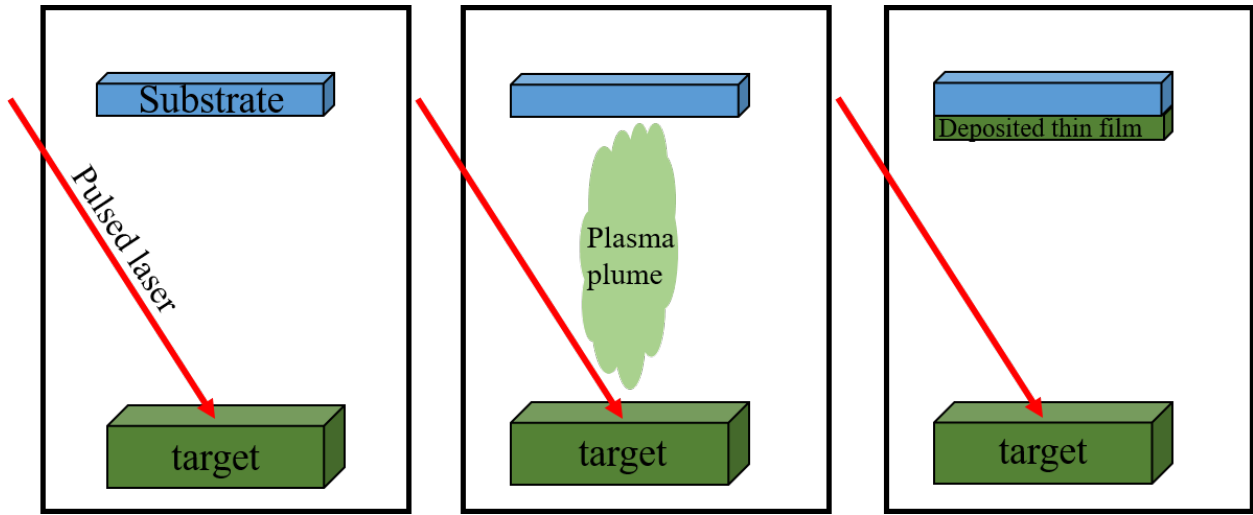


Figure 10. Simplified schematic illustration of a PLD cycle.

For PLD is extremely important to optimize the chamber pressure and the ratio between the background gasses in order to get the desired properties of the resultant thin film. In Chapter 4, PLD was used for ITO deposition as a transparent cathode for iTMC-LECs. The chamber parameters were previously optimized and used without further modification.<sup>[70]</sup>

## 2.3 Photoluminescence Measurements

Photoluminescence (PL) measurements involve the determination of the emission spectra and of the emission efficiency (photoluminescence quantum yield, PLQY) and they are a part of the fundamental characterization typically carried out on stand-alone thin films of light-emitting materials as well as these materials integrated into the final device configuration. The resulting PL characteristics allow us to predict their electroluminescence properties. Within the range of visible light, the PL spectra tells us about the color of emission of a certain luminescent molecule whereas the PLQY, determined as the ratio between the emitted and absorbed photons, dictates the efficiency of the photoluminescence process. The standard PL spectra and PLQY values presented in this Thesis were obtained with an N-M01 integrated sphere and an FLS1000 Edinburg Spectrometer.

For iTMCs, the PLQY is directly linked to the external quantum efficiency (EQE, eq. 1) of the device.<sup>[31]</sup> Since the light emission arises from excited triplet states and singlet states are also converted into triplets, the PLQY indicated as  $\varphi$  in eq. 1 should be in the same order or magnitude as the experimental PLQY value. In eq. 1, the  $b$  factor represents the recombination efficiency ( $b = 1$  for ohmic contacts) while the  $1/2n^2$  factor indicates the refractive index of glass ( $\sim 1.5$ ) and accounts for the light outcoupling.

$$EQE = \frac{b\varphi}{2n^2} \quad \text{eq. 1}$$

In this Thesis, PL measurements were also used as a valid tool to investigate the interaction that might be generated within the active layer or at the interfaces. For example, in Chapter 3, PL was used to study the interaction of the active material (SY) with the other components of the active layer, the ionic-transporting polymer (Hybrane) and the Li salt. In Chapter 4, a PL survey was conducted on the full device stack to evaluate the PL quench of the emitting layer due to the cathode deposition. Finally, in Chapter 3, a new PL measurement protocol is introduced. It consists of measuring the PL on the pixel active area while a current density is applied, *i.e.*, during electroluminescent operation. For this, a new setup was designed (**Figure 11**). Measuring the PL while driving the device allowed us to record in real-time the PL quench caused by the growth of the doped zones (see Section 1.2). This was achieved by using a lock-in amplifier and a picoammeter that allowed us to measure simultaneously the PL and the EL output. This technique is described in more detail in Chapter 3.

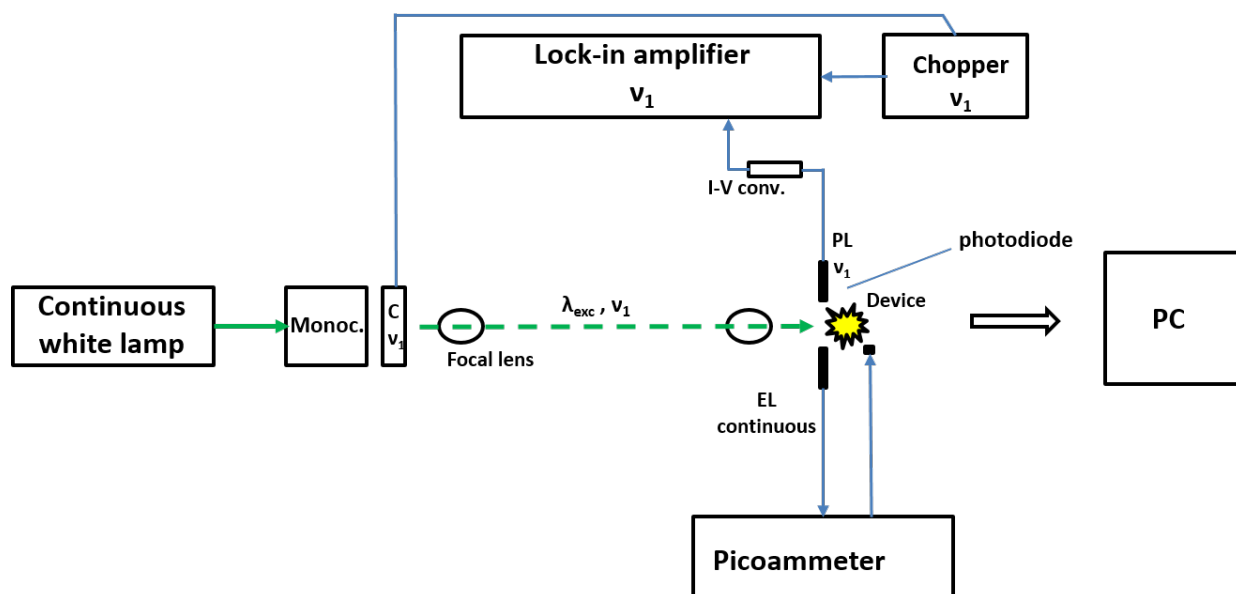


Figure 11. Experimental setup that allowed us to measure the PL of a pixel under an electrical bias.

## 2.4 Electroluminescent Characterization of LECs

As explained in Section 1.2, LECs are operated by applying a bias (either a voltage or a current). The devices presented in this thesis were always driven under pulsed current, with current densities between  $25 \text{ A m}^{-2}$  and  $100 \text{ A m}^{-2}$ . Under pulsed current bias conditions, the behavior of the LEC in the initial stages of operation shows a simultaneous decrease in voltage and an increase in luminance (Figure 11). This driving mode has been shown to improve the turn-on and lifetime of LECs.<sup>[39,71]</sup> The applied pulsed current consisted of block waves at a frequency of 1000 Hz with a duty cycle of 50%. As a result, the average current density and voltage were obtained by multiplying the values by the time-on (0.5 s) and dividing them by the total cycle time (1 s). Once

the current bias is applied, the devices are characterized by monitoring the voltage and luminance versus time by using a True Color Sensor MAZeT (MTCSiCT sensor) with a Botest OLT OLED Lifetime-Test system. In Chapter 3, the devices were also measured under constant current, to compare with the pulsed current bias. In Chapter 4, for the semitransparent LECs, the response was also measured from both sides and at the same time. For this, two equidistant photodiodes were placed at both sides of the same working pixel under a constant current density of  $50 \text{ A m}^{-2}$ . The output was measured in terms of photocurrent by two picoammeters.

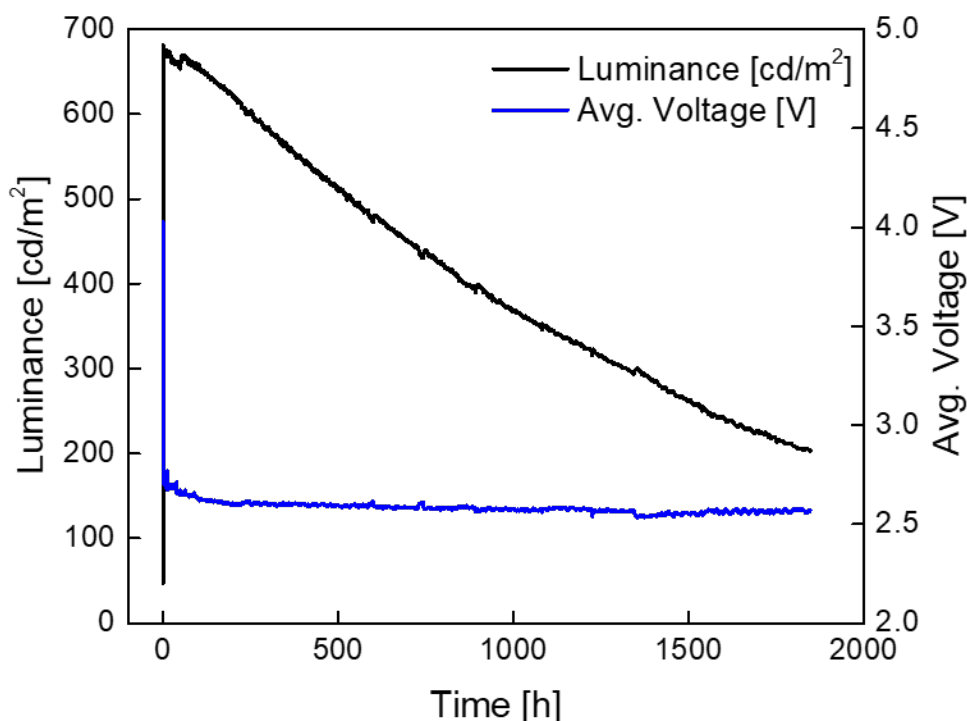


Figure 12. Typical temporal evolution of a LEC under a pulsed current bias.

The device performance is measured in terms of several figures of merit, however, as mentioned in the previous chapter, a standardized consensus is still lacking, so direct comparison between different devices and published reports is sometimes not straightforward. Here, we describe the most common figures of merit of a LEC.

- The EL spectra were measured with an optical fiber connected to an Avantes AvaSpec-2048L spectrometer while driving the cell with the Botest OLT OLED Lifetime-Test system. The EL indicates the region of the visible spectra where the device emits when an electrical bias is applied. It is often observed a small shift between the  $PL_{\max}$  and  $EL_{\max}$ . This is thought to be the result of a polarization of the molecular orbitals under electrical bias, a reduction of degree of freedom in the thin film solid state and the concentration of the emitter.<sup>[72–74]</sup>

- Luminance (Lum, black curve in **Figure 12**): The intensity of light measured per unit of surface expressed in [ $\text{cd m}^{-2}$ ]. It describes the quantity of light emitted by the device at a given moment.
- Current Density ( $J$ ): The intensity of current per unit of surface applied to a device. Usually expressed in [ $\text{A m}^{-2}$ ]. For a pulsed driving scheme, the value is averaged over the on and off time of the pulse.
- Voltage (V, blue curve in Figure 12): When a current density is applied, the voltage is monitored over time. Usually, a low voltage in the steady-state indicates long lifetimes and a facile charge carrier injection.
- Lifetime ( $t_{50}$ ): The time to reach half of the maximum luminance. It is the parameter most used to describe the stability of a LEC.
- Turn-on time ( $t_{\text{on}}$ ): The time needed to reach a determined value of luminance, usually  $100 \text{ cd m}^{-2}$ . Sometimes, it is also used as the time to reach the maximum luminance, regardless of its value, in particular for devices that do not reach  $100 \text{ cd m}^{-2}$ .
- Current Efficiency (CE): Represents the flux in candelas per electrical ampere [ $\text{cd A}^{-1}$ ]. It is obtained by dividing the luminance by the current density.
- Power Efficiency (PE): The flux of light described in lumens per electric watt [ $\text{lm W}^{-1}$ ] measured by an integrated sphere or assuming a Lambertian emission. In the case of pulsed-driven devices the duty cycle must be taken into account as well:

$$PE = \frac{Lum_{max} * \pi}{(V_{max} * J_{max}) * DC} \quad \text{eq. 2}$$

where  $V_{max}$  is the voltage value corresponding to  $Lum_{max}$ ,  $J_{max}$  is the current density value at the on phase of the current pulse and  $DC$  indicates the duty cycle.

- External Quantum Efficiency (EQE): The ratio of photons emitted per injected electron in a given device. Its relation to the PLQY has been described in the previous Section and it can be calculated by following eq. 1.
- Commission Internationale de l'Eclairage coordinates (CIE coordinates): The maximum wavelength of the EL spectra can only give a rough estimation of the true emission color. To fully define a color, the sensitivity of the photoreceptors in the human eye has to be considered. For that, the CIE coordinates are used. The coordinates can be calculated from the EL spectra and they give an exact definition of the emission color according to universally accepted international standards. The CIE coordinates are expressed in (x,y) coordinates and are placed in a 2D plot as shown in **Figure 13**.



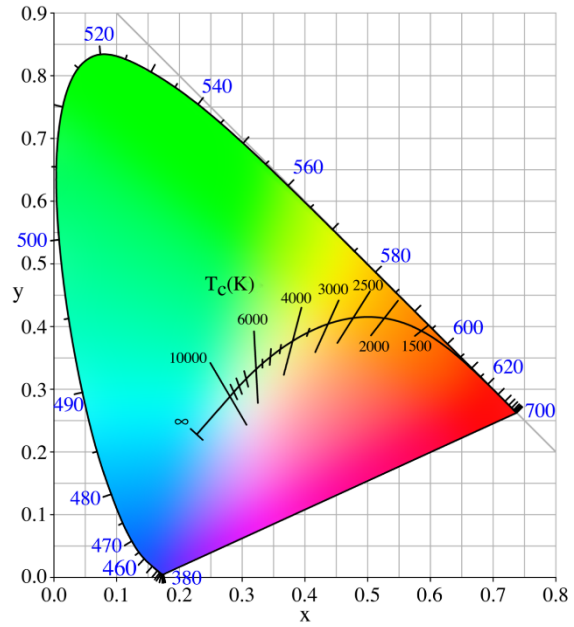


Figure 13. Commission Internationale de l'Eclairage coordinates (CIE coordinates) diagram that links the wavelengths of the visible spectra with the physiologically perceived colors in human vision.

### 3. Stable Light-Emitting Electrochemical Cells using Hyperbranched Polymer Electrolyte

### 3.1 Introduction

As mentioned in Section 1.2, LECs unique operation mechanism is based on the presence of both electronic and ionic conductors.<sup>[7]</sup> In the case of CP-LECs, the introduction of a polymer electrolyte<sup>[7]</sup> is a way to add ionic conductors and it plays a determining role in the overall performance. A polymer electrolyte consists of a salt and a coordinating polymer that dissolves and coordinates the ions thanks to its electron donor centers.<sup>[21]</sup> Since the early days, PEO has been one of the most commonly used ion conducting polymers LECs. However, especially at high molecular weights, PEO tends to form crystalline phases which hinder the ionic transport and limits its blending capacity with the emissive polymer. To this end, extensive research has been conducted on polymer electrolytes for LECs.

Recently, promising results have been attained on devices using Super Yellow (SY), a polyphenylenevinylene (PPV) based CP, as active material and branched polytrimethylene carbonate (PTMC) electrolytes derivatives, showing long operational lifetimes of 138 hours at  $> 300 \text{ cd m}^{-2}$  and a peak power efficiency (PE) of  $9.8 \text{ lm W}^{-1}$  at a constant current density driving bias of  $77 \text{ A m}^{-2}$ .<sup>[28]</sup> Previous works including SY and a star-branched trimethylolpropane ethoxylate (TMPE) derivatives as ion transporter showed exceptional lifetimes longer than 1200 hours over  $100 \text{ cd m}^{-2}$  and maximum PEs of  $18.1 \text{ lm W}^{-1}$ .<sup>[26,75]</sup>

In this Chapter, LECs based on the CP emitter SY combined with a novel hyperbranched ion solvating polymer, Hybrane® DEO750 8500 (Hy) and a lithium trifluoromethanesulfonate ( $\text{LiCF}_3\text{SO}_3$ , LiTf) salt were developed (**Figure 14**). The study is presented and divided into two parts: the first part focuses on the characterization of LECs using this novel active layer composition. The devices showed an extrapolated  $t_{50}$  of 2000 hours (at an initial luminance above  $480 \text{ cd/m}^2$ ) and peak power efficiencies of  $12.6 \text{ lm W}^{-1}$  with sub-minute turn-on times. These lifetime values are amongst the highest reported in the literature for fluorescent LECs. The second part focuses on the analysis of the interactions within the active layer, between the CP, the Hybrane and the Li salt. This was first achieved by performing steady state PL measurements which revealed that the introduction of Hybrane is beneficial as it decreases the quenching of the emitter by coordinating the  $\text{Li}^+$  atoms. Secondly, in an attempt to understand the effect of the doped zones formation on the stability, we performed a frequency modulated photoluminescence probing during steady state electroluminescence operation under a forward bias. This allowed to probe the evolution of the photoluminescence as a function of driving conditions in operating LECs, directly analyzing how the free ions interact with the polymer matrix in the different stages of operation of a LEC. Our results suggest that this method can be employed to model the operation mechanism of LECs and other ionic devices, correlate it with the composition of the active layer and improve the performance of these devices.

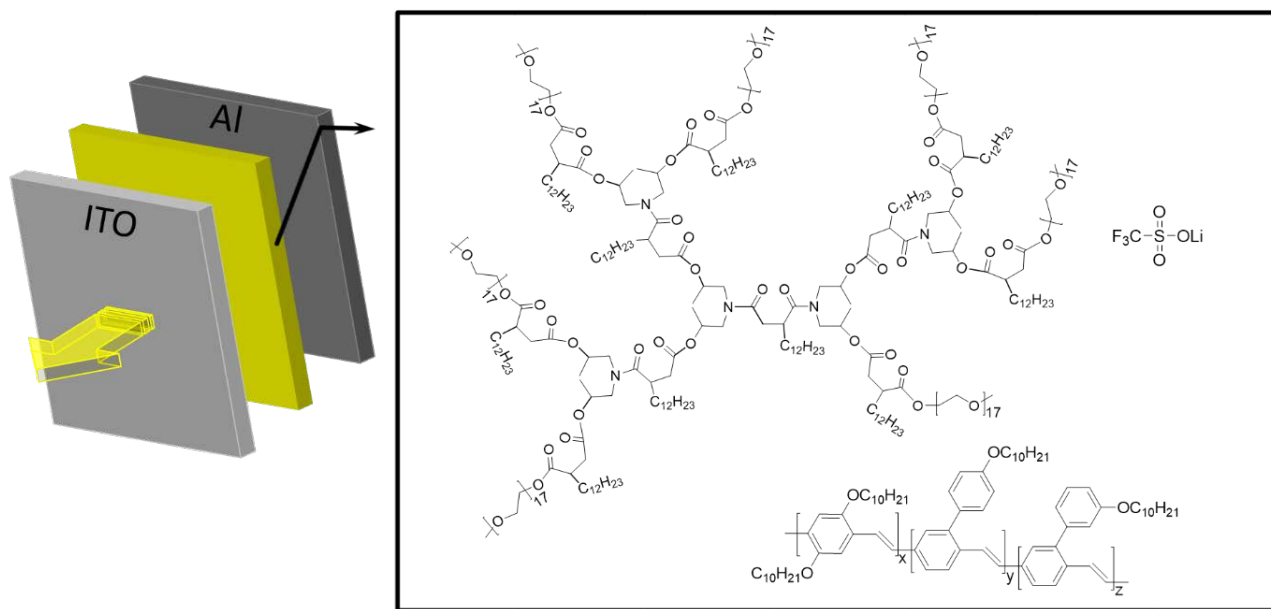


Figure 14. Scheme of the final device architecture and chemical structure of the components of the active layer: the ion dissolving hyperbranched polymer (Hybrane), the lithium trifluoromethanesulfonate salt and the semiconducting polymer Super Yellow (SY).

## 3.2 Results and Discussion

To successfully act as a host for free mobile ions, a polymer should have the following characteristics: 1) electron-donor groups or atoms able to coordinate cations; 2) high chain mobility and 3) suitable distance between the coordinating centers.<sup>[23,24,76]</sup> The Hybrane used in this work (Figure X) displays promising structural features for CP-LECs applications. At room temperature, the Hybrane is a dense liquid polymer and its backbone structure is constituted of ester and amide groups whereas the chains end with ethylene oxide units that are methoxy-terminated. In previous works, the ability of ester groups to coordinate and transport metal cations in CP-LECs has been shown.<sup>[28,77,78]</sup> Furthermore, a recent study showed that the methoxy (–OCH<sub>3</sub>) terminal groups provide enhanced mobility of the cations.<sup>[22]</sup> To ensure optimal device performance thin films should consist of a homogeneous blend between the polymer electrolyte and the semiconducting polymer.<sup>[79]</sup> When an optimum blend is provided one expects the most favorable salt dispersion over the active area and the most advantageous ion exchange between the ion-dissolving polymer and the CP.

The interaction between the two components has been investigated in the presence and absence of the lithium salt. Atomic Force Microscopy (AFM) has been used to establish whether the spin-casted solutions resulted in homogeneous thin films. In **Figure 15a** and **15b**, AFM images of pristine SY and blended SY+Hybrane+LiTf samples, deposited on a glass/ITO substrate, are shown, respectively. The AFM images reveal that both the pristine and blended films are very flat with an average roughness of 0.50 nm and an average height of 2.42 nm for SY (Figure 15a) and 0.43 nm and 2.97 nm for SY+Hybrane+LiTf (1:0.3:0.09 mass ratio, Figure 15b). The measured values are in line with recent literature data regarding pristine SY and SY+polymer electrolyte films.<sup>[28,80]</sup> As a result, both the pristine SY and the blend show very similar surface features

indicating that the mixed-polymer matrix appears in an amorphous state and that there is no sign of undesirable phase separation.

Subsequently, we determined the photoluminescence quantum yield (PLQY) of samples consisting of SY with and without Hybrane and the LiTf salt, deposited on a quartz substrate from a cyclohexanone solution. The maximum PLQYs obtained are 75%, 78%, 73% and 45% for the SY, SY+Hybrane, SY+Hybrane+LiTf and SY+LiTf samples, respectively (Figure 15c). The PL spectra were obtained using an excitation wavelength of 430 nm. From these results, it can be observed that the addition of solely the LiTf salt (SY+LiTf sample) decreases dramatically the PLQY when compared to the pristine SY polymer. We ascribe this decrease of PLQY as a result of the quenching of the excitons by the LiTf salt. This is in line with previous reports where it was found that additives, in particular, ionic species can act as interceptors of excitons through the generation of charge transfer non-emissive states and energy transfer processes and thus affect the PLQY.<sup>[81-83]</sup>

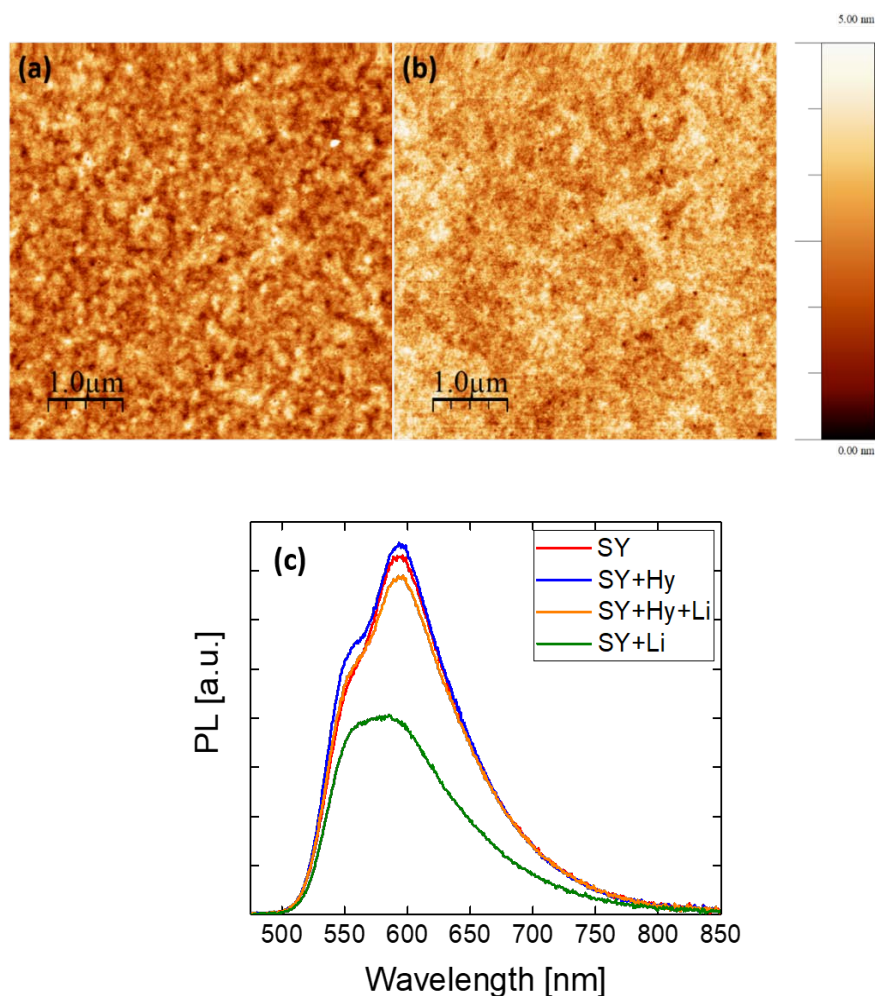


Figure 15. AFM images (5 μm x 5 μm) of a) pristine SY and b) SY + 30 % Hybrane + 9% LiTf coated on glass/ITO substrates. c) Photoluminescence spectra of SY and SY mixed with Hybrane, Hybrane+LiTf and LiTf only.

However, the addition of Hybrane recovers the PLQY of the sample, as it introduces coordinating sites for the salt. Finally, the SY+Hybrane sample does not show any quenching, as expected. In fact, the PLQY increases slightly compared to the pure SY sample up to 78% due to a slight dilution of the SY which reduces the excitons to migrate and encounter quenching sites. The Hybrane could in this case weaken the close packing of the SY chains and hence decrease the degree of  $\pi$ -interactions.<sup>[84]</sup>

Devices with three different LiTf concentrations (3%, 9% and 15%) and fixed Hybrane (30%) were fabricated by sandwiching the SY and Hybrane:LiTf salt blend in between ITO coated glass plates and Al cathodes and driven with a constant current bias. The mass ratio of 0.3:0.09 with respect to SY was then selected and driven with a pulsed current bias.

Device luminance and voltage were measured over time under a  $75 \text{ A m}^{-2}$  constant current density bias for the different SY:Hybrane:LiCF<sub>3</sub>SO<sub>3</sub> ratios (**Figure 16**). The starting voltage value for the three devices is around 3.6 V and the turn-on time at  $100 \text{ cd m}^{-2}$  is faster at higher salt concentrations, with values of 25.2 s, 7.2 s and 3.6 s for 3%, 9% and 15% of LiTf, respectively. However, a similar effect on the voltage curves is not directly observed as it decreases in the same manner independently from the LiTf amount. In fact, after the EDL is formed, generating an ohmic contact, the remaining ionic species will be used to compensate the charge carriers that start to electrochemically dope the CP.

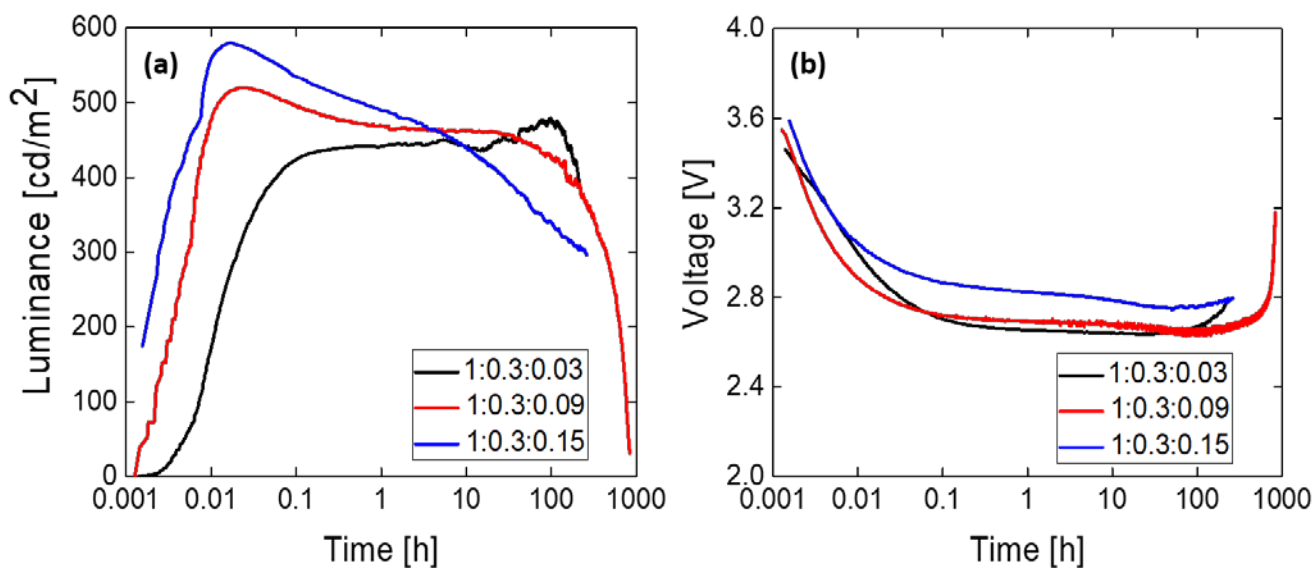


Figure 16. a) Luminance and b) driving voltage of the LECs driven at a constant current density of  $75 \text{ A m}^{-2}$ . Time is expressed in the log scale.

The maximum luminance values, 442, 520 and  $580 \text{ cd m}^{-2}$ , are proportional to the increase of salt content. This could be explained by the fact that, for this system, the amount of LiTf (at least up to 15%) can lead to brighter devices before the doping levels become too severe causing undesired exciton quenching.<sup>[85]</sup> At the steady state, the voltage keeps a constant value of around 2.7 V for the 3% and 9% LiTf salt concentration devices and a slightly higher value of 2.9 V for the 15% device. The current efficiency (CE) and power efficiency (PE) increase from  $5.9 \text{ cd A}^{-1}$  and  $6.9 \text{ lm W}^{-1}$  for 3% of LiTf to  $7.7 \text{ cd A}^{-1}$  and  $8.4 \text{ lm W}^{-1}$  for the device with 15% of LiTf content, as the voltage values are rather similar and the luminance increases along the device series.

One of the most important features of light-emitting devices is their lifetime. In this work, we report the lifetime using the most commonly used method in LEDs, the time it takes to reach 50%

of the initial luminance value. As LECs turn-on relatively fast it allows us to use the maximum luminance as the initial luminance value. Devices with 9% LiTf salt concentration show a measured  $t_{50}$  of 530 hours whereas the devices that have a LiTf salt concentration of 15% have a reduced lifetime of about 350 hours (estimated value). It is not easy to estimate  $t_{50}$  for the 1:0.3:0.03 mass ratio but we assume it to be within the interval between 400 and 500 hours. **Table 1** summarizes the principal performances of the above-described devices. Consequently, in order to improve the device performance, we selected the 1:0.3:0.09 ratio as it showed overall better performances when compared to 1:0.3:0.03 and 1:0.3:0.15 ratios.

Table 1. Main performances of LECs under a constant current bias of  $75 \text{ A m}^{-2}$ .

SY:Hybrane:LiCF <sub>3</sub> SO <sub>3</sub> mass ratio	Max Lum. (cd m <sup>-2</sup> )	t <sub>50</sub> (hours)	Peak CE (cd A <sup>-1</sup> )	Peak PE (lm W <sup>-1</sup> )
1:0.3:0.03	442	~400 - 500	5.9	6.9
1:0.3:0.09	520	530	6.9	7.8
1:0.3:0.15	580	~350	7.7	8.4

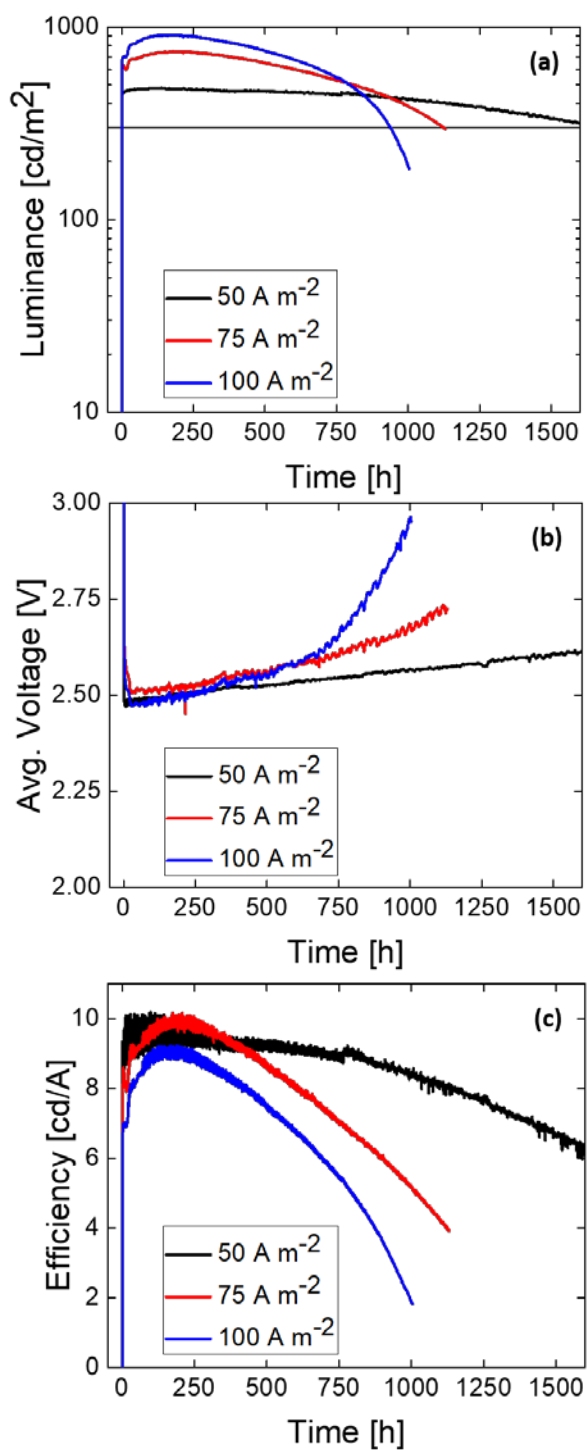


Figure 17. Performance of the 1:0.3:0.09 SY/Hybrane/LiTf ratio devices under an average pulsed current density of 50/75/100 A m<sup>-2</sup>. a) Luminance b) Avg. Voltage c) Current efficiency. Luminance is expressed in the log scale.



Devices were prepared with the selected 1:0.3:0.09 active layer ratio and driven under pulsed current biases of 50/75/100 A m<sup>-2</sup>. The applied pulsed current consisted in block waves at a frequency of 1000 Hz with a duty cycle of 50%. The benefits of a lower current density combined with a pulsed driving current have been demonstrated in previous works and consists in improved stabilities and efficiencies due to the presence of “off-states” that limit the growth of the doped zones and side reactions.<sup>[71,86,87]</sup> Under pulsed driving conditions the devices performance improve dramatically with respect to the constant current driving (**Figure 17**). Comparing the lifetime data recorded at the same current density it is possible to notice a 3-fold increase when a pulsed bias is applied. The most important performance parameters of the devices are highlighted in **Table 2**. Peak luminance of 900 cd m<sup>-2</sup> and 745 cd m<sup>-2</sup> are reached with average current densities of 100 and 75 A m<sup>-2</sup>, respectively. The t<sub>50</sub> for these rather high initial luminance values are impressive with 850 and about 1000 hours. When comparing the luminance over time curves for these higher average current density driven LECs it is clear that from an initially rather flat curve, the decline is increasing exponentially once it starts. This is the result of the combination of the degradation of the devices, as suggested by the dramatic voltage increase (especially in the 100 and 75 Am<sup>-2</sup> biased devices), and the continuous growth of the doped zones. As a result, the thickness of the intrinsic (non-doped) zone that is responsible for the light generation is reduced which leads to an increased quenching of emitting centers. At the same time, the driving voltage also starts to increase around the inflection point in the luminance time curve which implies that it is increasingly difficult to maintain the set current density. This is most likely the result of permanent degradation. Understanding the degradation of CP-LECs still remains a challenging task, however, irreversible redox reactions of the CP as well as changes at the polymer/cathode interface might be responsible of the progressively decrease of the cell performance.<sup>[13,88]</sup> At an average current density of 50 A m<sup>-2</sup> a peak luminance of about 480 cd m<sup>-2</sup> is reached and these luminance levels are maintained over a long period of time. An exact t<sub>50</sub> is not easy to extrapolate since near that point the luminance probably decays superlinearly. Nevertheless, we estimate a t<sub>50</sub> value in excess of 2000 hours. Moreover, the devices show sub-minutes turn-on times and excellent efficiencies throughout their lifetime. The peak current efficiencies (CE) and power efficiencies (PE) obtained for the three devices exceeds 9 cd A<sup>-1</sup> and 12 lm W<sup>-1</sup>, with values of 9.6 cd A<sup>-1</sup> and 12.6 lm W<sup>-1</sup> for the device biased with a 50 A m<sup>-2</sup> current density.

Table 2. Main performance parameters of representative LECs under pulsed current average bias of 50/75/100 A m<sup>-2</sup>.

Average Bias	Max Lum. (cd m <sup>-2</sup> )	t <sub>50</sub> (hours)	Peak CE (cd A <sup>-1</sup> )	Peak PE (lm W <sup>-1</sup> )
50 A m <sup>-2</sup>	480	2000	9.6	12.6
75 A m <sup>-2</sup>	745	1000	9.9	12.5
100 A m <sup>-2</sup>	900	850	9.2	12

To study in depth the effect of the doped zone formation on the stability of our devices, we developed a characterization method that measures the photoluminescence (PL) of the devices during electroluminescent operation. This is done by modulating the excitation light source and coupling this modulation to a lock-in amplifier. Hence, the frequency-modulated PL can be detected by the lock-in amplifier in the presence of a non-modulated (constant) EL signal. Using

this approach it was possible to extract at the same time the PL and EL profiles and their evolution in the critical first minutes of operation (**Figure 18**).

The intensity of the PL and EL signals followed over time are depicted in Figure 18a. At  $t=0$  the devices are driven at a constant current of  $50 \text{ A m}^{-2}$ . Prior to turn-on, the PL is stable and the intensity is normalized to this arbitrary value. Upon turning on the bias the PL rapidly decays followed by a more gradual decline. At the same time, the EL slowly rises, typical of the operation of a LEC. In figure 18b, the PL was recorded under different current densities applied to the device ( $25/50/100/200/500 \text{ A m}^{-2}$ ), and after the bias was removed. The drop in PL is more pronounced with increasing current density. We attribute this rapid decline in PL to the creation of doped regions that form by the dissociated ions and injected electronic charge carriers. A lower current density, for example,  $25 \text{ A m}^{-2}$  (black curve), corresponds to a less pronounced quenching when compared to a higher current density, for example,  $500 \text{ A m}^{-2}$  (green curve). This can be explained by the fact that higher current densities will generate more doping, reducing the intrinsic zone thickness and leaving less doping-free polymer to generate photoluminescence. The drop in PL intensity in the LEC is characterized by a first very fast step indicating the rapid ionic movement and doping as well as EDL formation. A second step then follows, 20-25 seconds after the bias is applied, in which the intensity decays at a slower rate, possible evidence of the slow growth of the doped zones. As the current is switched off (Figure 18b, blue region “no bias”), two steps can be observed again. The PL first recovers rapidly followed by a slower rate of recovery. The speed of PL recovery is proportional to the intensity of the applied bias, as expected. More detailed studies are needed to unravel the exact mechanism, in particular by probing at shorter timescales. However, the fast recovery of the PL signal must imply the removal of the species responsible for its quenching. The quenching of the PL in LECs is generally ascribed to the interaction with the radical cations and anions that form after injecting electrons and holes. Hence, after turning off the bias, these radical cations and anions, rapidly disappear to a large extent. In a timescale of 5 minutes, the PL signal has recovered to an extent between 96% for the LEC driven under  $25 \text{ A m}^{-2}$  and 86% for the LEC driven under  $500 \text{ A m}^{-2}$ . The cells driven at 25 and  $500 \text{ A m}^{-2}$  were also left to recover overnight for a total time of about 20 hours. We can notice that both curves regain PL intensity up to values of 98% and 97%, respectively. As most of the relaxation takes place in the first minutes after the bias for the  $25 \text{ A m}^{-2}$  current density (black curve) the additional recovery after 20 hours is low. On the other hand, for the  $500 \text{ A m}^{-2}$  current density, the relaxation is much slower. There is most likely almost no permanent degradation present in these devices, even at high current biases, as they have been driven for such a short time (5 minutes). These results might indicate that when the bias is removed the undoping process occurs on different time scales. The possibility to study the extent of the quenching as well as its decrease over time under bias provides useful insights about LECs doping and undoping mechanisms of different semiconducting materials,<sup>[20]</sup> ionic transport and to help assess the origin of undesired side reactions.

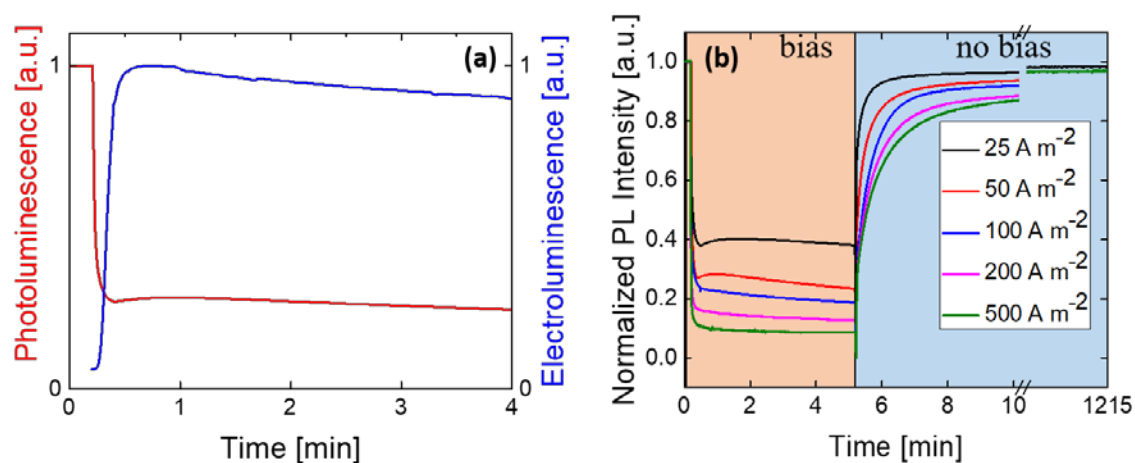


Figure 18. a) Photoluminescence (PL) and electroluminescence (EL) evolution in the first 4 minutes of device operation at  $50 \text{ A m}^{-2}$ . b) Normalized PL intensity, LEC devices biased with a constant current density of  $25/50/100/200/500 \text{ A m}^{-2}$ . The cells driven at  $25$  and  $500 \text{ A m}^{-2}$  were left to recover overnight for about 20 hours and measured again. Both measures were taken under a  $500 \text{ nm}$  light probe.

### 3.3 Conclusions

In conclusion, in this Chapter we have shown the effects of introducing a new hyperbranched polymer (Hybrane) as the ion dissolving and transporting material in an SY-based state-of-the-art CP-LEC device. The blending properties of the two polymers have been investigated by means of AFM and PLQY measurements. Our results confirm that SY and the Hybrane can form very homogeneous and smooth films without macro-phase separation. Devices were driven under constant and pulsed currents in order to evaluate the stability over time. At low pulsed current densities ( $50 \text{ A m}^{-2}$ ), the light-emitting devices showed outstanding lifetimes, maintaining a luminance in excess of  $300 \text{ cd m}^{-2}$  over 1600 operational hours (estimated  $t_{50}$  of over 2000 hours), and excellent current and power efficiencies of  $9.6 \text{ cd A}^{-1}$  and  $12.6 \text{ lm W}^{-1}$ , respectively. In addition, the effect of the doped zones formation on the performance of the devices was investigated. To do this, the PL signal of the pixels was simultaneously measured while EL operation. Our results indicate that the PL signal drops due to quenching induced by the operation of the LEC. After switching off, the PL is recovered. The transient PL values and degree of recovery are dependent on the current density applied. The ability to monitor both PL and EL in sandwiched LECs will provide new insights into the exact operation and allow for further improvement of the performance of these devices.

## 4. Transparent Light-Emitting Electrochemical Cells

## 4.1 Introduction

In recent years, new display technologies have emerged and with them, the need for the development of properties such as large area, stretchability or transparency in lighting devices such as OLEDs.<sup>[4,89]</sup> In particular, for semitransparent OLEDs, the requirements for the cathode are a high light transmittance (over 80%) and a low sheet resistance ( $R_s$ ).<sup>[90]</sup> The realm of transparent electrodes is vast and in continuous progress, nonetheless, the most common materials and structures are transparent conductive oxides (TCOs), very thin films of metals or alloys (*e.g.* Ag, Au, Ag:Al, Mg:Ag), multilayer metal thin film based cathodes (*e.g.* dielectric/metal/dielectric, metal/metal), nano arrays (*e.g.* carbon-based electrodes and metal NW electrodes) and conductive polymers (PEDOT:PSS).<sup>[91–93]</sup> TCOs are the preferred materials as transparent bottom electrodes, as they possess a high conductivity and there are barely any process limitations since they are often deposited on glass or plastic substrates that endure the harsh conditions during the TCO deposition via *e.g.* magnetron sputtering. The use of TCOs as transparent top electrodes on thin organic semiconductor-based devices requires, however, more attention. For example, the sputtering of TCO directly on top of device stacks can damage underlying charge transport layers or the active materials themselves, reducing their performances and lifetimes.<sup>[94]</sup> Additionally, the alignment of the TCO conduction band with the energy of the molecular orbitals of the organic semiconductor is important. These requirements have limited the widespread usage of TCOs as top electrodes in organic semiconductor devices.<sup>[92]</sup> The use of ITO as the top electrode in semitransparent devices has already been studied in LEDs and OLEDs.<sup>[95–100]</sup> One of the most efficient semitransparent and flexible devices was demonstrated by Han et al. reporting a white QD-LED with a maximum current efficiency of  $18.2 \text{ cd A}^{-1}$ , a maximum luminance value above  $10000 \text{ cd m}^{-2}$  and an EQE of 6.4%.<sup>[95]</sup> As already mentioned, LECs currently represent a promising alternative to LED and OLED technologies as in their simplest form they consist only of a light-emitting active layer sandwiched between two electrodes.<sup>[101]</sup> However, the literature is still relatively poor for semitransparent LECs with only a couple of examples reported, albeit using a top electrode that is either a conductive polymer or a nano-array.<sup>[102,103]</sup>

In this Chapter, semitransparent iTMC-LECs are developed in which ITO is used as both the top and bottom electrodes. ALD and PLD techniques are introduced, for the first time, in cathode fabrication for LECs. The top electrode was processed in a multilayer structure composed of an ALD-deposited tin oxide ( $\text{SnO}_2$ ) and a PLD-deposited indium-tin oxide (ITO). The cathode was directly deposited on top of the organic active layer based on a yellow iridium(III) iTMC emitter,  $[\text{Ir}(\text{ppy})_2(\text{dtb-bpy})][\text{PF}_6]$  (where ppy is 2-phenylpyridine and dtb-bpy is 4,4'-di-tert-butyl-2,2'-dipyridyl)<sup>[66]</sup> resulting in very high transparent devices, above 75% over the visible spectra region (380 to 750 nm). The possible harsh effects of the ALD and PLD during processing on the organic underlayers were examined by optical characterization including absorption, transmission, PL and EL output from both the top and bottom electrodes. The devices performance was recorded under a pulsed current bias showing a high electroluminescence above  $200 \text{ cd m}^{-2}$  which implies a very strong on/off contrast.

## 4.2 Results and Discussion

First, we developed the semitransparent top electrode for LEC devices. A fundamental condition for efficient light-emitting devices is to ensure the absence of shorts and leakage paths. For transparent top electrodes, TCOs represent the best choice because of their transparency combined with a high conductivity, tunable electronic properties and fabrication ease with several techniques. However, their deposition on organic thin films is not trivial as these materials are frequently deposited using harsh methods such as reactive ion sputtering or PLD. Even for ALD processes, the presence of reactive gasses and the needed temperatures can lead to undesired shorts. Additionally, it is important to have an energy matching interface between the light-emitting layer and the charge injection and electrode layers.<sup>[92,94]</sup> For PLD processes, the chamber pressure is a crucial factor because it determines how the particles pack during the layer formation and, therefore, affects its electrical properties. Generally, the lower the chamber pressure, the more conductive the TCO layer is, due to the enhanced bulk properties of the resultant film. However, it can also result in a higher number of shorts due to the higher kinetic energy of the TCO particles when impacting on the underlying layer. This effect has been recently demonstrated on perovskite solar cells where the ITO deposition pressure parameters were optimized.<sup>[70]</sup> Therefore, a higher chamber pressure must be used in the PLD process for the ITO deposition to minimize the damage to the samples. Based on this, we selected a chamber pressure of 0.042 mbar (with an O<sub>2</sub> partial pressure of 0.0076 mbar) for the deposition of the top ITO electrode via PLD. A 140 nm ITO layer deposited on glass under these conditions exhibited a sheet resistance of 140  $\Omega$ /sq. However, when deposited directly on the organic emitting layer in the LEC stack, it produced a considerable number of shorted devices.

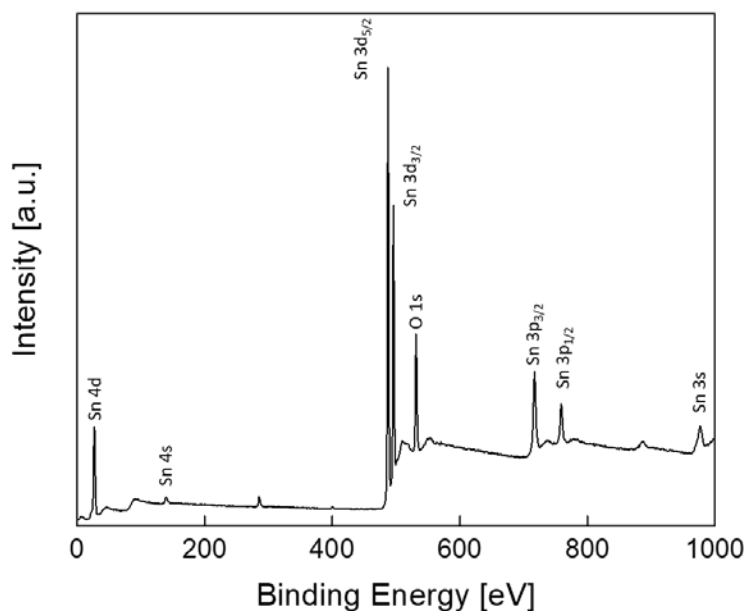


Figure 19. XPS survey of SnO<sub>2</sub> thin film on glass/ITO substrate.

To ensure there is no penetration of ITO in the thin film of the Ir(III) emitter, we employed an additional SnO<sub>2</sub> electron transport layer (ETL) via ALD. SnO<sub>2</sub> is gaining increased consideration for its use as a wide band gap semiconductor due to its high transmission and electrical properties combined with remarkable chemical stability and compatibility with several doping elements and fabrication techniques.<sup>[104]</sup> Regarding the ALD technique, the growth temperature and choice of the precursors are the key factors in order to achieve suitable film properties. However, for thermally sensitive materials, such as organics or organometallic semiconductors, it is imperative to reduce the growth temperature to a level at which this technique can be sustainably exploited. For our devices, we obtained SnO<sub>2</sub> films at a growth temperature of 90°C without further annealing using tetrakis(diethylamino) tin (TDAT) and water as precursors.<sup>[105]</sup> The SnO<sub>2</sub> films were characterized by means of Atomic Force Microscopy (AFM) and x-ray photoelectron spectroscopy (XPS). An AFM image of a thin SnO<sub>2</sub> film on a glass/ITO/PEDOT:PSS/Ir substrate (**Figure 20b**) reveals a very flat surface with an estimated mean roughness of 0.6 nm. Our results are in line with previous reports where SnO<sub>2</sub> was deposited at low temperature.<sup>[105–107]</sup> The XPS analysis (**Figure 19**) reveals the formation of SnO<sub>2</sub>,<sup>[105]</sup> with an element ratio close to 1:2 between Sn and O. Topographic AFM images were also collected for Ir deposited on glass/PEDOT:PSS and for ITO deposited on glass/PEDOT:PSS/Ir and glass/PEDOT:PSS/Ir/SnO<sub>2</sub> samples (Figure 20a, 20c and 20d respectively) showing flat surfaces in all cases with mean roughness below 1.5 nm.

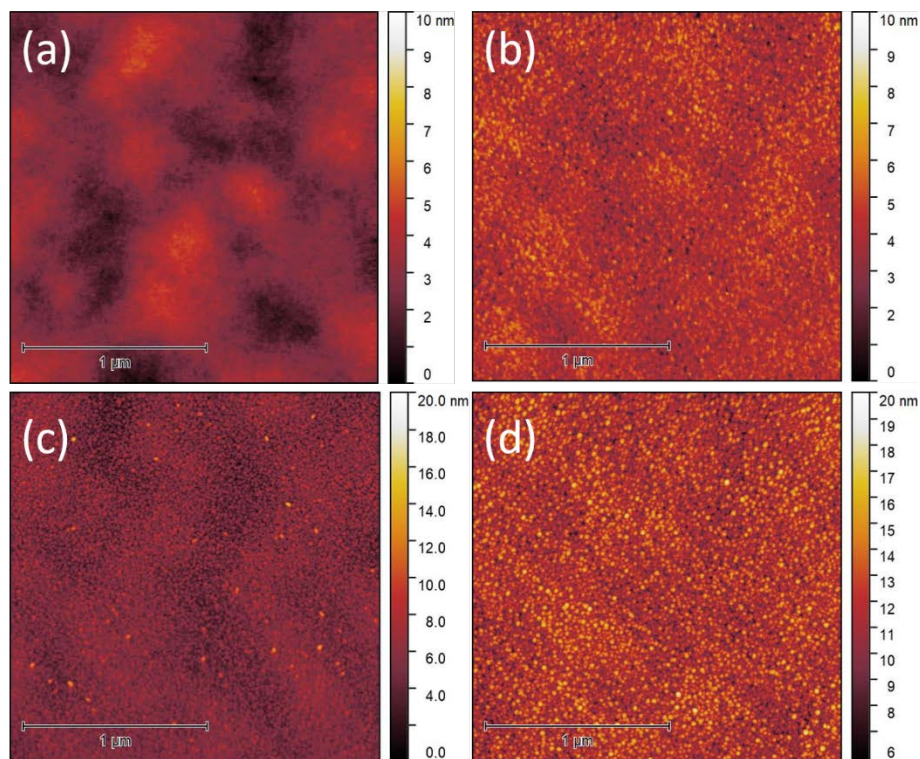


Figure 20. AFM images of a) glass/ITO/PEDOT:PSS/Ir, b) glass/ITO/PEDOT:PSS/Ir/SnO<sub>2</sub>, c) glass/ITO/PEDOT:PSS/Ir/ITO and d) glass/ITO/PEDOT:PSS/Ir/SnO<sub>2</sub>/ITO. They show a mean roughness of 0.6 nm, 0.6 nm, 1 nm, and 1.3 nm, respectively.

Thereafter, the effect of the deposited top electrode on the optical properties of the device stack was examined on samples with and without SnO<sub>2</sub> and ITO layers. The samples under examination were glass/ITO/PEDOT:PSS/Ir, glass/ITO/PEDOT:PSS/Ir/SnO<sub>2</sub>, glass/ITO/PEDOT:PSS/Ir/SnO<sub>2</sub>/ITO and glass/ITO/PEDOT:PSS/Ir/ITO, where Ir is the active layer composed of [Ir(ppy)<sub>2</sub>(dtb-bpy)][PF<sub>6</sub>] and 1-Butyl-3-methylimidazolium hexafluorophosphate [BMIM][PF<sub>6</sub>] in a molar ratio of 1:0.25. The thicknesses of SnO<sub>2</sub> and ITO were 20 and 140 nm, respectively. The absorbance and transmittance spectra of glass/ITO/PEDOT:PSS/Ir and glass/ITO/PEDOT:PSS/Ir/SnO<sub>2</sub> (Figure 21a-b, black and red curves, respectively) are superimposable and the addition of ITO slightly increases the absorption of light and consequently results in a decrease in transmission (Figure 21a-b, blue and pink curves, respectively). The full stack (blue curve) showed an average transmittance value of 75% within the visible spectrum range (380 to 750 nm) with a transmittance of 82% at the electroluminescence peak of 563 nm (discussed later and seen in Figure 23a). These measurements give important information about the features of the final device, however, they do not tell much about the intrinsic properties of the deposited layers because of the strong effect that the glass substrate has on the absorption. When glass and ITO from the substrate are not taken into consideration (Figure 21c-d), it is possible to observe that the SnO<sub>2</sub> and ITO deposition increases (decreases) the absorption (transmission), especially in the lower wavelength region between 300 nm and 400 nm of the spectra with respect to the Ir sample (black curve). This is in line with the absorption spectra measured for SnO<sub>2</sub> and ITO, green and orange curves, respectively (Figure 21a).

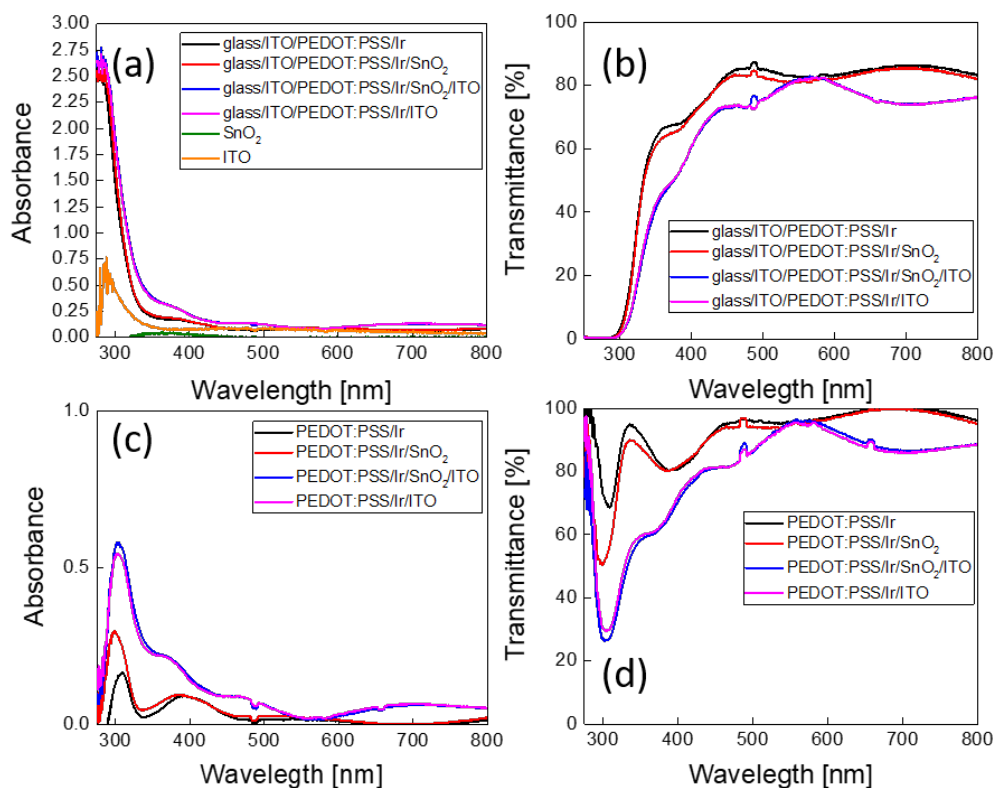


Figure 21. a) Absorbance and b) transmittance of the samples, before and after the SnO<sub>2</sub> and ITO layers deposition, as well as the absorbance of 20 nm SnO<sub>2</sub> deposited by ALD and the absorption of 140 nm of ITO deposited by PLD on a glass substrate. c) Absorbance and d) transmittance of



the same samples using a glass/ITO reference sample. The measurements were corrected for the absorption of the glass substrate.

Next, devices were fabricated in the following configuration: glass/ITO/PEDOT:PSS (80 nm)/[Ir(ppy)<sub>2</sub>(dtb-bpy)][PF<sub>6</sub>]:[BMIM][PF<sub>6</sub>] (1:0.25) (80 nm)/SnO<sub>2</sub> (20 nm)/ITO (140 nm) (**Figure 22a**). After the cathode deposition, gold was thermally evaporated at the edges to supply an additional low resistance path to facilitate effective charge injection from the ITO cathode. As mentioned before, the direct deposition of ITO resulted in a large number of shorts while SnO<sub>2</sub> effectively acted as a buffer layer preventing these shorts. For this reason, we will focus our discussion only on the device configuration that includes the SnO<sub>2</sub> buffer layer. The semitransparent devices were also compared with standard fully reflective Al-cathode (100 nm) LECs. The iridium complex, [Ir(ppy)<sub>2</sub>(dtb-bpy)][PF<sub>6</sub>], represented in Figure 22b, has been previously used as a yellow light-emitting material in iTMC-LECs and has displayed high stability and efficiency.<sup>[66,108]</sup> Images of the semitransparent device and the standard opaque device in their ON and OFF states are shown in Figure 22c-f showing the transparency of the transparent devices.

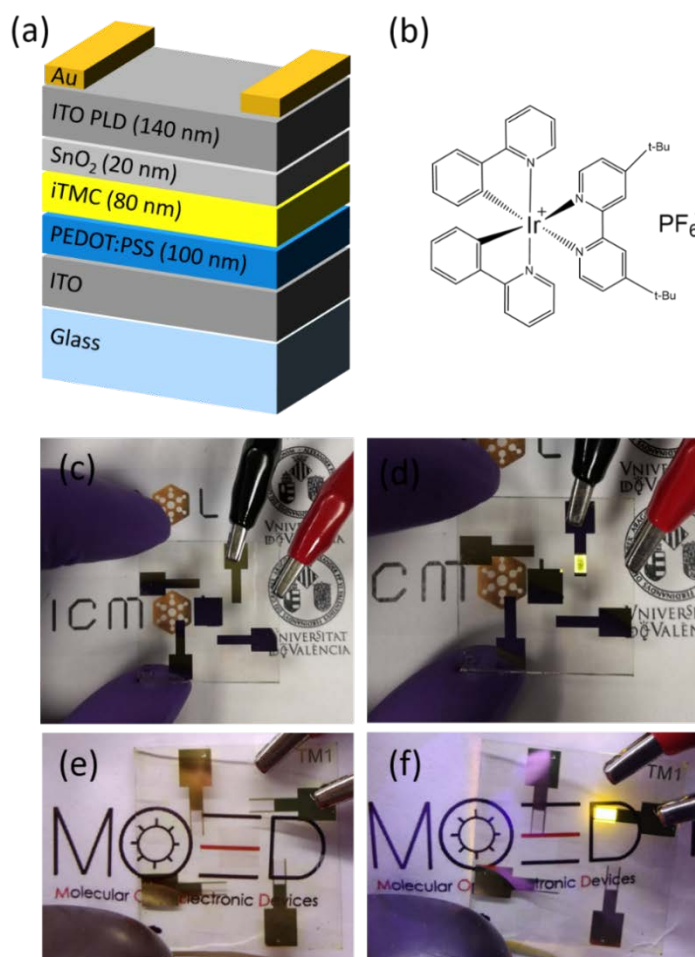


Figure 22. a) Architecture of the semitransparent devices, b) Chemical structure of the yellow Ir(III) emitter [Ir(ppy)<sub>2</sub>(dtb-bpy)][PF<sub>6</sub>] used in this work, OFF states of the c) reference and e) semitransparent devices and ON states of the d) reference and f) semitransparent devices.

Both the transparent and opaque devices were characterized by applying a pulsed driving current of  $100 \text{ A m}^{-2}$  (avg.  $50 \text{ A m}^{-2}$ ) and monitoring their luminance and voltage evolution over time. The pulsed bias consisted of a block wave current at a frequency of  $1000 \text{ Hz}$  with a duty cycle of  $50\%$ . The luminance of the transparent devices was measured from top ( $\text{SnO}_2/\text{ITO}$  side) and bottom (glass/ITO side). The electroluminescence spectra of the standard and semitransparent devices through the bottom substrate were rather similar. The EL peak from the semitransparent is slightly blue-shifted when compared to the opaque reference device, with maxima of  $563 \text{ nm}$  and  $571 \text{ nm}$ , respectively. The observed blue-shift could be the result of a different light outcoupling for the opaque and transparent devices, where the light-emitting layer acts as a cavity in which the position of the emissive non-doped zone is governed by the choice of the cathode. The main figures of merit of both the opaque and transparent LEC are summarized in **Table 3**.

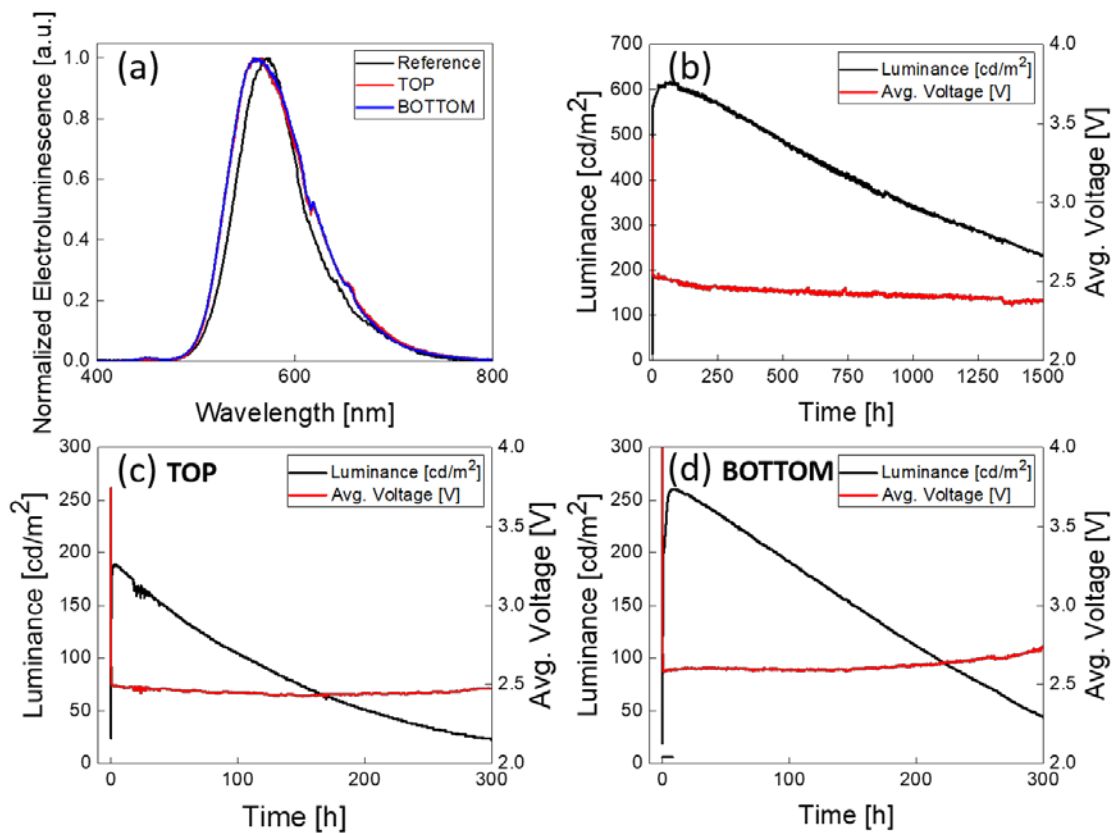


Figure 23. a) Electroluminescence of the standard Al-cathode and semitransparent devices, b) luminance and voltage over time of the standard Al-cathode device at an avg. current of  $50 \text{ A m}^{-2}$ , c) and d) luminance and voltage over time of the top and bottom sides of the transparent device driven at avg. current of  $50 \text{ A m}^{-2}$ .

The opaque device shows the evolution of luminance and voltage typical for LECs driven with a pulsed current (**Figure 23b**). The reference device reaches a maximum luminance value of  $620 \text{ cd m}^{-2}$  and a  $t_{50}$ , referred to as the time necessary to reach half of the maximum luminance, of  $1120 \text{ hours}$ . The high luminance and the low pulsed driving current density make this device very

efficient with a peak current efficiency (CE) value of 13.6 cd A<sup>-1</sup> and a power efficiency (PE) of 8.9 lm W<sup>-1</sup>. The semitransparent devices (Figure 23c-d), biased with the same average current density of 50 A m<sup>-2</sup> and maintaining the same electrode polarity, show a similar performance. When measured from the bottom side, the luminance reached a value of 260 cd m<sup>-2</sup> which is less than what is obtained for the opaque cells. This is primarily due to the loss of the reflecting electrode in the transparent devices. Indeed, when measured through the top ITO electrode a luminance value of 188 cd m<sup>-2</sup> is obtained. Even though the sum of these two values is still below what is obtained for the opaque cell, the difference is not very large. As a result of the lower luminance also the current efficacy and the power efficiency are lower in the transparent devices. The luminance values obtained from the bottom and top side are 260 cd m<sup>-2</sup> and 188 cd m<sup>-2</sup> which leads to CE and PE values of 5.2 cd A<sup>-1</sup> and 4.0 cd A<sup>-1</sup>, and 3.2 lm W<sup>-1</sup> and 2.5 lm W<sup>-1</sup>, for the bottom and top side, respectively. Finally, the t<sub>50</sub> for the bottom side is 176 hours while that for the top side is 118 hours.

Table 3. Figures of merit of the standard and transparent (T) cells driven at 50 A m<sup>-2</sup> average bias current.

	Peak Lum. [cd m <sup>-2</sup> ]	T <sub>50</sub> [h]	CE [cd A <sup>-1</sup> ]	PE [lm W <sup>-1</sup> ]
Standard	620	1120	13.6	8.9
T-Bottom side	260	176	5.2	3.2
T-Top side	188	118	4.0	2.5
T-overall	448	-	9.2	5.7

Several factors can contribute to the different luminance values observed for the bottom and top sides of the devices. The outcoupling of photons depends strongly on the refractive index of the layers the emitted light must pass through in order to escape from the device. With regard to SnO<sub>2</sub>, several reports show that its electrical as well as optical properties depend on the deposition temperature and precursors used.<sup>[105,109]</sup> The refractive index is reported to be close to 1.9/2.0 when SnO<sub>2</sub> is deposited from TDAT and water at low temperatures (below 100°C).<sup>[105]</sup> When driving the device and measuring from the bottom side (glass), the light is partially trapped because the glass substrate has a low refractive index of ~1.5. For commercial ITO on glass substrates the reported refractive index is generally 1.8 but the ITO optical properties are strictly related to its crystallinity, resistivity and surface morphology. For PLD deposition, these properties are controlled by changing chamber pressure and deposition temperature. It has been reported that room temperature depositions could lead to higher sheet resistance and refractive indices.<sup>[110,111]</sup> For our deposited ITO, due to the medium/high chamber pressure of 0.042 mbar (see experimental section) and room temperature, the final refractive index might be close to 2.0 or higher. The high refractive index of the top TCO electrode supports the outcoupling from the organic light emitting material into the TCO layers, however because of the large contrast in indices between the TCOs and air (~2 TCO:1 air) the light remains constrained within the outer TCOs layers. In order to exploit the advantage of using a high refractive index based outcoupling layer, nano arrays/lenses<sup>[112]</sup> would be required. In addition, internal reflections of the different layers of the stack and from the gold fingers evaporated around the device area could play an important role in

determining the final light output from the top and bottom side. This difference in luminance measured from the bottom and top sides has also been confirmed by the simultaneous measurement with two equidistant photodiodes of the generated photocurrent by the two sides of the same pixel under a constant current bias of  $50 \text{ A m}^{-2}$  (**Figure 24**). Although these results were obtained with a constant bias, they are in agreement with the luminance vs time data showed in Figure 23. Differences between top and bottom emission were also previously reported in transparent OLED and QD-LED and attributed to a difference in transparency between the top and bottom electrodes.<sup>[97,100]</sup> Finally, a rough estimation of the overall performance of the semitransparent device (obtained as the sum of the top and bottom measurements) can be made. The overall luminance is  $448 \text{ cd m}^{-2}$  with a CE and PE of  $9.2 \text{ cd A}^{-1}$  and  $5.7 \text{ lm W}^{-1}$ .

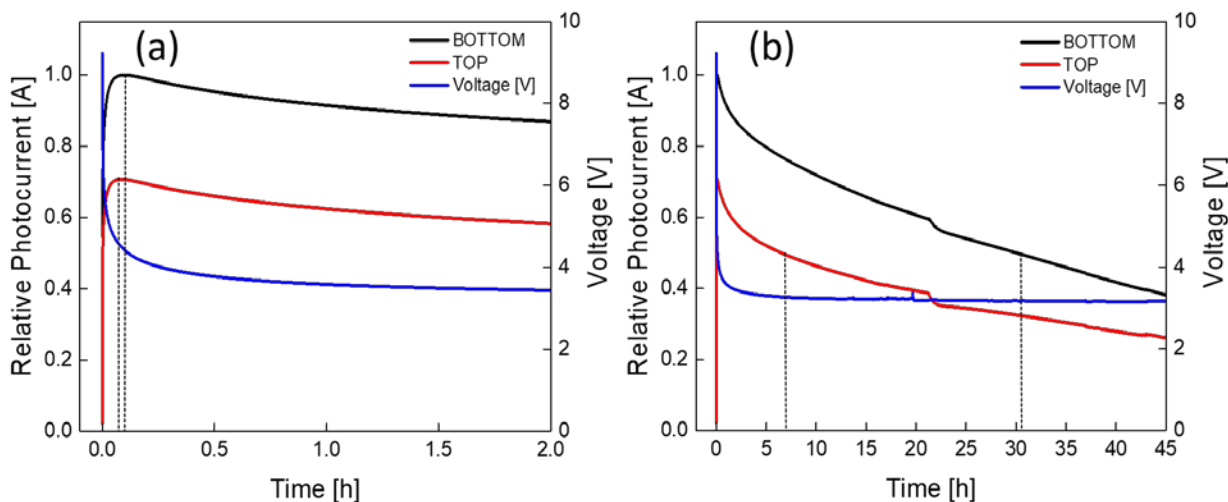


Figure 24. Normalized photocurrent from BOTTOM and UP side of a semitransparent device with the stack glass/ITO/PEDOT:PSS (80 nm)/ [Ir(ppy)<sub>2</sub>(dtb-bpy)][PF<sub>6</sub>]:[BMIM][PF<sub>6</sub>] (1:0.25) (80 nm)/SnO<sub>2</sub> (20 nm)/ITO (140 nm). The photocurrent was simultaneously measured for 45 hours. a) Until 2 hours, shows the difference in turn-on time between the BOTTOM and TOP side, which are 6 and 4 minutes respectively, and b) shows the complete measure and the difference in t<sub>50</sub> between the BOTTOM and TOP side, which are ~30 and ~6.5 hours.

Another factor that could play a role in the performance of the semitransparent LEC device is the photoluminescence (PL) quenching as a consequence of the cathode deposition. To study this, the photoluminescence was measured to understand the interactions between the Ir thin film and the SnO<sub>2</sub> and ITO deposited layers. The PL was measured from both sides of the samples using an excitation wavelength of 340 nm in an integrating sphere, where bottom indicates that the sample was excited from the glass substrate side and top from the PLD-ITO cathode side (Figures 25a-b). Analyzing the bottom orientation (**Figure 25a**) we observe that the PL intensity suffers from both the ALD and PLD depositions. In the first case, a drop of the PL intensity of 19% is observed by the ALD-deposited SnO<sub>2</sub> thin layer (red curve). It is well known the ability of SnO<sub>2</sub><sup>[113–116]</sup> and other metal oxides based ETLs<sup>[117,118]</sup> to quench the PL at the semiconductor/TCO interface through exciton trapping and non-radiative energy transfer. Furthermore, a degradation of the Ir complex by the action of the nucleophilic water molecules and temperature during the ALD deposition could play a critical role.<sup>[36,119]</sup> The ITO deposition directly on the active Ir material dramatically increases the quenching to about 52% (pink curve). Here, the ITO deposition could be too harsh for the organic active layer, as seen on the number of resulting shorted devices.

Surprisingly, we observe a remarkable decrease in the number of shorted cells upon SnO<sub>2</sub> insertion and, at the same time, the presence of an important interaction between the iTMC and the cathode as suggested by the intense PL quenching, around 48%, observed in the full-stack sample glass/ITO/PEDOT:PSS/Ir/SnO<sub>2</sub>/ITO (blue curve). Secondly, we measured the samples from the top side (Figure 25b). The samples showed the same degree of quenching after the SnO<sub>2</sub> deposition (red curve), as expected. The addition of ITO in the Ir/ITO and Ir/SnO<sub>2</sub>/ITO samples (pink and blue curves, respectively) follows the same trend as the bottom orientation, however with a higher degree of quenching of 74% and 65%, respectively.

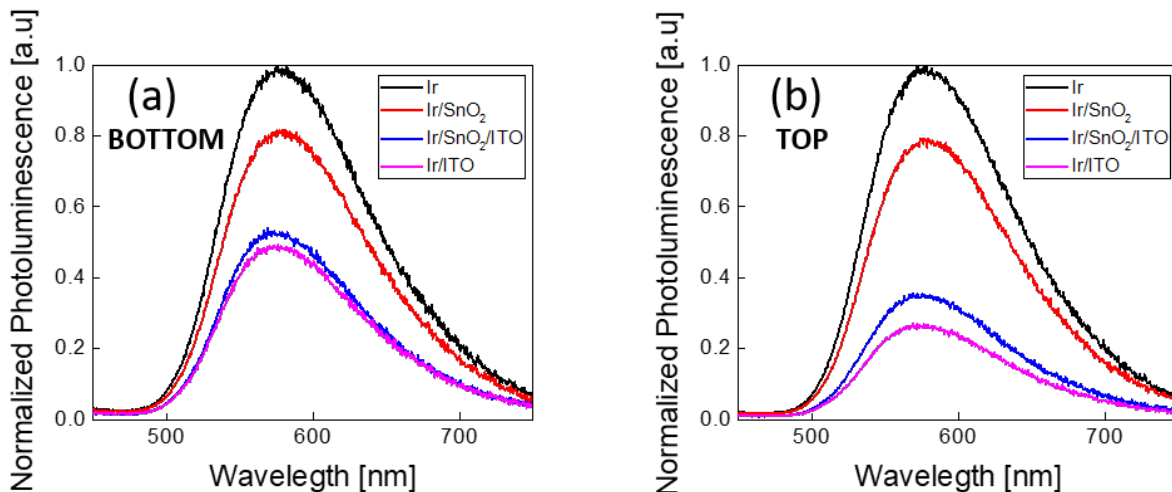


Figure 25. Photoluminescence from the a) BOTTOM side and b) TOP side obtained with an excitation wavelength of 340 nm of the iTMC film and with different metal oxide layers deposited on top of it (see legend).

### 4.3 Conclusion

In conclusion, in this Chapter we demonstrated the fabrication and characterization of iTMC-LECs by using a transparent top SnO<sub>2</sub>/ITO contact processed by ALD and PLD, respectively. Although the energy levels of SnO<sub>2</sub> and the active material in the light-emitting layer are not aligned, thanks to the operation mechanism of LECs involving ion migration to the electrode interface, this is not a problem. Furthermore, the combination of ALD and PLD offers the advantages of adjusting the deposition conditions, such as pressure and temperature, to provide a high-quality film, with precise control over thickness and composition. As a result, the devices had a full-stack transparency of 75% over the visible spectrum (380 to 750 nm) with a transmittance of 82% at the electroluminescence peak of 563 nm. A thorough optical characterization was carried out to evaluate the effects of the cathode deposition on the emitting layer, which included the luminance output from both sides. The devices performance showed excellent on/off ratio characterized by a high transmittance, and a luminance up to 260 cd m<sup>-2</sup> coupled to lifetimes up to 176 h, demonstrating the potential of these highly transparent light-emitting devices.

## 5. New Emitters for Light-Emitting Electrochemical Cells: Cu(I) and Pt(II) Electroluminescent Complexes

## 5.1 Introduction

Ionic transition metal complexes (iTMCs) are materials of great interest as active emitters in LECs as they are intrinsically ionic, so they do not need auxiliary charged species to drive the device, and they are phosphorescent triplet emitters, which allows for higher electroluminescence efficiencies compared to singlet emitters.

Early works on iTMC-LECs focused on substituted ruthenium(II) complexes, but they presented important color tuning limitations and only emit in the orange-red part of the visible spectra. Nowadays, the most versatile family of iTMCs is based on an iridium(III) core, which, thanks to a unique combination of physical and chemical properties, provides a huge variety of stable complexes, covering the visible spectrum from blue to red, and exhibiting high PLQY.<sup>[30]</sup> However, iridium is a rare and expensive metal, so it has become increasingly important to find alternatives as emitters for LEC devices. To this end, new metal centers such as copper(I) and, more recently, platinum(II) have been found to be interesting.

One of the most investigated families of copper(I)-based luminophores are  $[\text{Cu}(\text{P}^{\wedge}\text{P})(\text{N}^{\wedge}\text{N})]^+$  complexes, where  $\text{P}^{\wedge}\text{P}$  is a chelating bisphosphane, usually a derivative of POP (POP = oxydi(2,1-phenylene)]bis(diphenylphosphane)) or xantphos (xantphos = 9,9-dimethyl-9H-xanthene-4,5-diyl)(bis(diphenylphosphane)), and  $\text{N}^{\wedge}\text{N}$  is typically a derivative of bpy (bpy = 2,2'-bipyridine) or phen (phen = 1,10-phenanthroline).<sup>[120–126]</sup>  $[\text{Cu}(\text{P}^{\wedge}\text{P})(\text{N}^{\wedge}\text{N})]^+$  complexes have the advantage of being suitable scaffolds for systematic investigations and tuning of energy levels of the frontier molecular orbitals.<sup>[58,74,127]</sup> Moreover,  $[\text{Cu}(\text{P}^{\wedge}\text{P})(\text{N}^{\wedge}\text{N})]^+$  complexes often exhibit thermally activated delayed fluorescence (TADF).<sup>[128]</sup> This leads to theoretical internal quantum efficiency (IQE) values of up to 100%. In contrast, purely fluorescent emitters can only harvest 25% of the excitons.<sup>[129,130]</sup> On the other hand, platinum(II)-based LECs have seldom been explored, with just a few examples found in the literature which exhibit emission only in the red region of the visible spectra.<sup>[46,47,131,132]</sup> The chemistry of Pt(II) with cyclometallated N-heterocyclic carbenes (NHC; C<sup>^</sup>C) has proven to give elevated quantum efficiencies across the visible spectra.<sup>[133–141]</sup> In this regard, it is important to design rigid or semi-rigid scaffolds with chelating properties and strong donor atoms for having high PLQY.

With this in view, in this Chapter new iTMC emitters based on Cu(I) and Pt(II) are studied as active materials for LECs (**Figure 26**). First, we report a series of  $[\text{Cu}(\text{P}^{\wedge}\text{P})(\text{N}^{\wedge}\text{N})][\text{A}]$  complexes in which  $[\text{A}]^-$  is either  $[\text{PF}_6]^-$  (Cu1),  $[\text{BF}_4]^-$  (Cu2),  $[\text{BPh}_4]^-$  (Cu3) or  $[\text{Bar}^{\text{F}}_4]^-$  (Cu4) ( $[\text{Bar}^{\text{F}}_4]^-$  = tetrakis(3,5-bis(trifluoromethyl)phenyl)borate), ( $\text{P}^{\wedge}\text{P}$ ) is the bidentate xantphos ligand and ( $\text{N}^{\wedge}\text{N}$ ) is the Me<sub>2</sub>bpy (6,6'-Dimethyl-2,2'-bipyridine) ancillary ligand. We combined these iTMCs with different commonly-used ionic liquids, and study their time response and performance. Second, we explore the Pt(Cbz-C<sup>^</sup>C\*) system. Five complexes are investigated,  $[\text{Pt}(\text{Cbz-C}^{\wedge}\text{C}^*)(\text{PPh}_3)(\text{py})]^+$ ,  $[\text{Pt}(\text{Cbz-C}^{\wedge}\text{C}^*)(\text{P}^{\wedge}\text{N})]^+$  and  $[\text{Pt}(\text{Cbz-C}^{\wedge}\text{C}^*)(\text{P}^{\wedge}\text{P})]^+$ , where Cbz-C<sup>^</sup>C\* is a carbazole-modified cyclometallated ligand, namely 1-(4-(9H-Carbazol-9-yl)phenyl)-3-methyl-1H-imidazole, py stands for pyridine (Pt5), ( $\text{P}^{\wedge}\text{N}$ ) is 2-(2-(diphenylphosphino)ethyl)pyridine (Pt6) and ( $\text{P}^{\wedge}\text{P}$ ) is 1,1-bis(diphenylphosphino)methane (Pt7), 1,1-bis(diphenylphosphino)ethane (Pt8) and 1,1-bis(diphenylphosphino)benzene (Pt9). These complexes display a blue/green emission with high PLQY values.

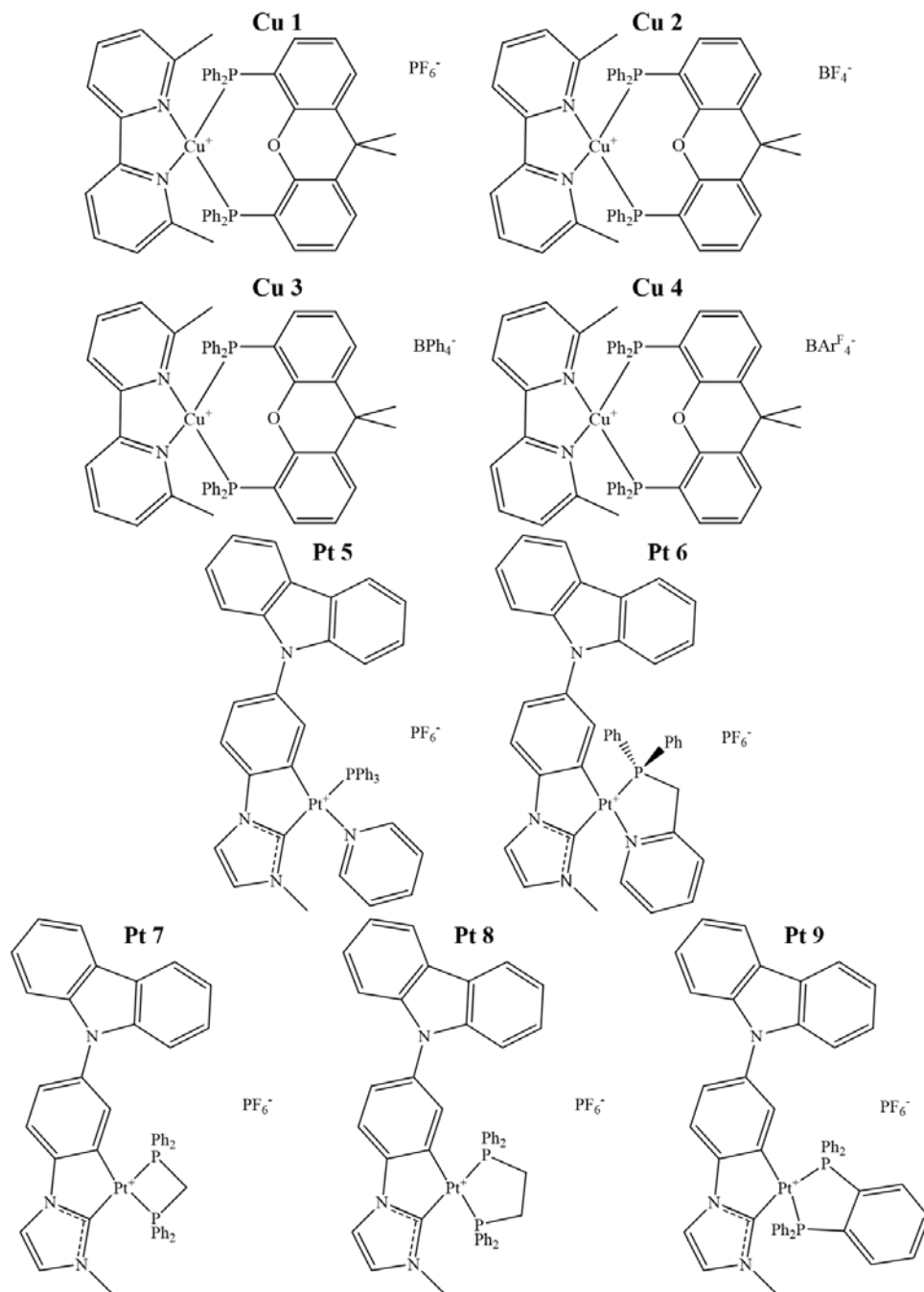


Figure 26: Chemical structure of the Cu(I) and Pt(II) complexes studied in this Chapter.

## 5.2 Results and Discussion

The synthesis, characterization and photophysical properties in solution and powder of the emitters, were carried out by the group of Prof. Dr. Edwin Constable and Prof. Dr. Catheryne Housecroft from the University of Basel (Cu(I)-complexes) and by the group of Prof. Dr. Violeta



Sicilia from the University of Zaragoza (Pt(II)-complexes). They are briefly reported in this Thesis, for more details we refer to the published works.<sup>[142,143]</sup>

### 5.2.1 Photo-electrochemical properties of Cu1, Cu2, Cu3 and Cu4

The redox properties of the complexes were investigated by cyclic voltammetry in dry propylene carbonate solution containing 0.1 mol dm<sup>-3</sup> [nBu<sub>4</sub>N][PF<sub>6</sub>] as supporting electrolyte. The Cu<sup>+</sup>/Cu<sup>2+</sup> oxidation is typically an irreversible process and the introduction of the Me<sub>2</sub>bpy ligand brings the oxidation potential to a higher value. As the copper center is formally oxidized from Cu(I) to Cu(II), the coordination geometry changes from tetrahedral to square planar. This can be rationalized by the two methyl substituents in Me<sub>2</sub>bpy preventing flattening of the Cu coordination sphere, resulting in a higher oxidation potential for the Me<sub>2</sub>bpy-containing compounds with a maximum value of +0.93 V for the case of Cu3.

The absorption spectra of solutions of the complexes in CH<sub>2</sub>Cl<sub>2</sub> exhibit intense high-energy absorption bands below *ca.* 330 nm arising from ligand-centered and, in the case of the [BPh<sub>4</sub>]<sup>-</sup> and [BAr<sup>F</sup><sub>4</sub>]<sup>-</sup> salts, counterion-centered  $\pi^* \leftarrow \pi$  transitions. Additionally, a lower intensity metal-to-ligand charge transfer (MLCT) band with  $\lambda_{\text{max}}$  in the range 373-381 nm.

The normalized solution emission spectra of the complexes were obtained in deaerated CH<sub>2</sub>Cl<sub>2</sub> solution with excitation wavelengths in the region of their MLCT band. The emission maxima of the complexes are around 560 nm which gives a yellow emission. In the solid-state, the emission maxima of the complexes is blue-shifted, lying between 520 and 530 nm, and thus, the complexes are green to yellowish emitters in powdered form.

The complexes have a high PLQY both in the solid state and solution which can be ascribed to the increased steric hindrance in the Cu(I) coordination sphere provided by the Me<sub>2</sub>bpy ligand. This impedes flattening of the tetrahedron upon excitation. Sterically protected copper centers are less accessible to, for example, solvent molecules. Exciton quenching by non-radiative intermolecular processes like collisional quenching, Förster resonance energy transfer and Dexter electron transfer are also expected to be reduced. The measured PLQY of the powders are 62%, 44%, 35% and 27% for Cu1, Cu2, Cu3 and Cu4, respectively.

### 5.2.2 Photophysical properties of Pt5, Pt6, Pt7, Pt8 and Pt9

The absorption spectra of the complexes was measured in a CH<sub>2</sub>Cl<sub>2</sub> solution. They exhibit very similar absorption profiles with relative intense bands around 290-350 nm that are normally attributed to intraligand transitions of the NHC ligand. Additionally, they show rather weak absorptions at  $\lambda > 370$  nm that appear slightly redshifted for the diphosphine derivatives (Pt7, Pt8 and Pt9).

From the theoretical calculations, the optimized HOMO is centered on the cyclometallating NHC ligand, almost entirely on the Cbz fragment, whereas the LUMO is distributed over the ancillary ligands and the Pt center. This indicates that the lowest energy absorption for both is attributed to a mixed transition LL'CT [ $\pi(\text{NHC}) \rightarrow \pi^*(\text{L}')$ ] / ILCT [(NHC)] and LMCT [ $\pi(\text{NHC}) \rightarrow d(\text{Pt})$ ]. The spin-density distributions in the optimized T<sub>1</sub> states are located on the C<sup>^</sup>C\* ligand and, to a minor extent, on the Pt center and the ancillary ligands. Therefore, the emission for all complexes would be attributed to metal-perturbed <sup>3</sup>IL [C<sup>^</sup>C\*] transitions.

The photoluminescent properties were examined in poly(methyl methacrylate) (PMMA) films at 5 wt% doping concentration of the Pt compounds. The two complexes Pt5 and Pt6 show blue emission centered around 480 nm, whereas the diphosphine derivatives (Pt7-9) display a green colour with maxima at around 510-520 nm. Their PLQY values reach very high values under Ar atmosphere, especially for the diphosphine derivatives. The final values of 47%, 49%, 76%, 77% and 83% were obtained for Pt5, Pt6, Pt7, Pt8 and Pt9, respectively. However, these values are much reduced when the complexes are measured in their solid state in air, obtaining 7%, 2%, 43%, 4% and 27%, respectively.

### 5.2.3 Light Emitting Electrochemical Cells

It has been previously reported the performances of LECs containing [Cu(POP)(Mebpy)][PF<sub>6</sub>], [Cu(POP)(Me<sub>2</sub>bpy)][PF<sub>6</sub>], [Cu(xantphos)(Mebpy)][PF<sub>6</sub>] and [Cu(xantphos)(Me<sub>2</sub>bpy)][PF<sub>6</sub>] in their active layers, but under different device driving conditions.<sup>[121,144]</sup> These compounds exhibit some of the highest PLQY values for [Cu(P<sup>^</sup>P)(N<sup>^</sup>N)]<sup>+</sup> complexes and are, therefore, good candidates for LECs. Here we study the electroluminescence properties of the series [Cu(xantphos)(Me<sub>2</sub>bpy)][PF<sub>6</sub>], [Cu(xantphos)(Me<sub>2</sub>bpy)][BF<sub>4</sub>], [Cu(xantphos)(Me<sub>2</sub>bpy)][BPh<sub>4</sub>] and [Cu(xantphos)(Me<sub>2</sub>bpy)][BAR<sup>F</sup><sub>4</sub>] (Cu1, Cu2, Cu3 and Cu4).

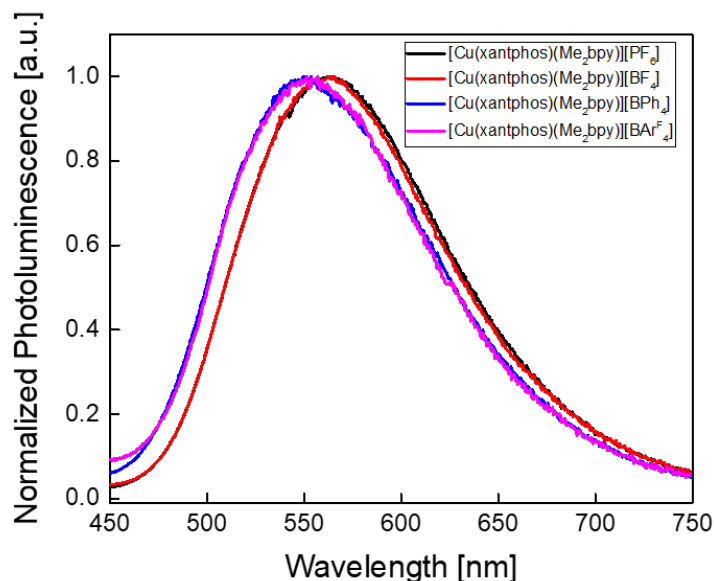


Figure 27. Normalized thin-film photoluminescence spectra of the [Cu(xantphos)(Me<sub>2</sub>bpy)]<sup>+</sup> complexes with different counterions.

The thin-film PL spectra and PLQY of complexes were measured and are shown in **Figure 27** and **Table 4**. The PL spectra reveal that the four complexes do not have exactly the same PL maximum, consistent with the solution and powder PL spectra. Both Cu1 and Cu2 show a PL maximum at 563 nm whereas thin-films of Cu3 and Cu4 have values of  $\lambda_{\max}^{\text{em}} = 548$  and 552 nm, respectively. The PLQYs of the thin films are 44, 45, 32 and 35%, respectively, for the [PF<sub>6</sub>]<sup>-</sup>, [BF<sub>4</sub>]<sup>-</sup>, [BPh<sub>4</sub>]<sup>-</sup> and [BAR<sup>F</sup><sub>4</sub>]<sup>-</sup> salts. The EL spectra of the LECs using the best performing complexes, Cu1 and Cu2, were also measured with values of  $\lambda_{\max}^{\text{em}}(\text{EL})$  of 546 and 550 nm, respectively (**Figure**

28a). The EL is blue-shifted with respect to the PL in solution and red-shifted with respect to the PL in solid state.<sup>[44]</sup> **Table 5** displays the active layers of the devices and LEC main figures of merit. The complexes were mixed with ILs (4:1 molar ratio complex : IL) containing the same and different counterions in order to study the behaviour of these complexes in LEC devices and the specific effect of the IL anion on the performance of the device. The cells were then driven under an average pulsed current of 50 A m<sup>-2</sup> while monitoring the luminance and voltage behaviour. Device performances of LECs containing Cu1 and Cu2 mixed with [EMIM]<sup>+</sup> (1-Ethyl-3-methylimidazolium) ILs using the same counterion as the copper(I) complex can be seen in Figure 28b (black and red curves, respectively). In both cases the cells have the typical LEC behaviour characterized by an initial high resistance and hence, a high initial voltage. As the electrochemical doping takes place over time, the film conductivity increases, and the voltage drops. The luminance increases following the electrochemical doping until a maximum value is reached. Then, a rapid loss of the EL intensity is observed, probably due to quenching caused by the growing doped zones as the voltage maintains a steady value, where smaller anions result in lower steady state voltage (Figure 28d). Both devices show a fast turn-on time of 58 s and 15 s (the time to reach a luminance of 100 cd m<sup>-2</sup>) with a maximum luminance of 173 cd m<sup>-2</sup> and 137 cd m<sup>-2</sup> respectively. Cu2 has a faster turn-on time, as the [BF<sub>4</sub>]<sup>-</sup> ion has smaller radius than [PF<sub>6</sub>]<sup>-</sup>, and thus is expected to have a higher mobility in the device. The LECs have a maximum current efficiency (CE) of 3.5 cd A<sup>-1</sup> and 2.7 cd A<sup>-1</sup>, respectively (Figure 28c). Recent works explored the electroluminescent properties of copper complexes with similar P<sup>^</sup>P and N<sup>^</sup>N ligands: [Cu(xantphos)(4,5,6-Me<sub>3</sub>bpy)][PF<sub>6</sub>]<sup>[44]</sup>, [Cu(xantphos)(Mebpy)][PF<sub>6</sub>]<sup>[144]</sup> and [Cu(BnN-xantphos)(Me<sub>2</sub>bpy)][PF<sub>6</sub>]<sup>[145]</sup>. When comparing the performances of these complexes with the LECs in the current investigation (Table 5) we notice similar luminance and current efficiencies (CE) with values of 190 cd m<sup>-2</sup> and 3.8 cd A<sup>-1</sup>, 90 cd m<sup>-2</sup> and 1.9 cd A<sup>-1</sup> and 179 cd m<sup>-2</sup> and 3.6 cd A<sup>-1</sup>, respectively, when operated under the same driving conditions. It is important to notice that the added IL was not always the same in all studies, and this can affect the performance of the device, as we show here. Additionally, the reported Cu1 was also previously studied<sup>[144]</sup> mixed with the IL [1-butyl-3-methylimidazolium][PF<sub>6</sub>] ([BMIM][PF<sub>6</sub>]). The devices show a slightly lower luminance of 145 cd m<sup>-2</sup> and CE of 3.0 cd A<sup>-1</sup>. The performances of devices using Cu1 and Cu2 with mixed counterions ([EMIM][BF<sub>4</sub>] and [EMIM][PF<sub>6</sub>]) can be seen in Figure 28b (blue and purple curves, respectively) and in Table 4. The addition of the IL with a different counterion seems to affect the luminance and the turn-on time of the LEC. Both the luminance of LECs containing Cu1 and Cu2 decrease to 132 cd m<sup>-2</sup> and 114 cd m<sup>-2</sup> at a maximum CE of 2.6 cd A<sup>-1</sup> and 2.3 cd A<sup>-1</sup>, respectively. The turn-on time (time to reach 100 cd m<sup>-2</sup>) increases to 47 s for Cu2, while Cu1 shows a similar turn-on time of 61 s (Table 4). The two complexes with larger aryl-substituted anions, Cu3 and Cu4, were also used in LECs. As before, two ILs with different anions were employed: one in which the anion in the IL ([EMIM][BPh<sub>4</sub>] and [EMIM][BAr<sup>F</sup><sub>4</sub>]) matched the anion in the complex, and another in which the anion in the IL is [PF<sub>6</sub>]<sup>-</sup> (IL = [EMIM][PF<sub>6</sub>]). In both cases the devices maintained a high voltage value of 9 V (limit of our setup) and did not turn-on after several minutes even at higher driving current density (avg. 100 A m<sup>-2</sup> and 200 A m<sup>-2</sup>) and with higher IL concentrations (2:1, Cu:IL). The failure to turn on is an indication of low charge injection/transport efficiency within the thin film. In the case of large counterions, the charge injection might be less efficient due to the lower ionic mobility. These results indicate that mixing counterions is not likely to produce a

beneficial change in performance, since it reduces all the figures of merit in LECs, as shown for Cu1 and Cu2 (Table 4). Moreover, using ILs with smaller counterion (*e.g.* [PF<sub>6</sub>]<sup>-</sup>) for devices using big aryl-substituted complexes, such as Cu3 and Cu4 is not sufficient to turn-on these LECs.

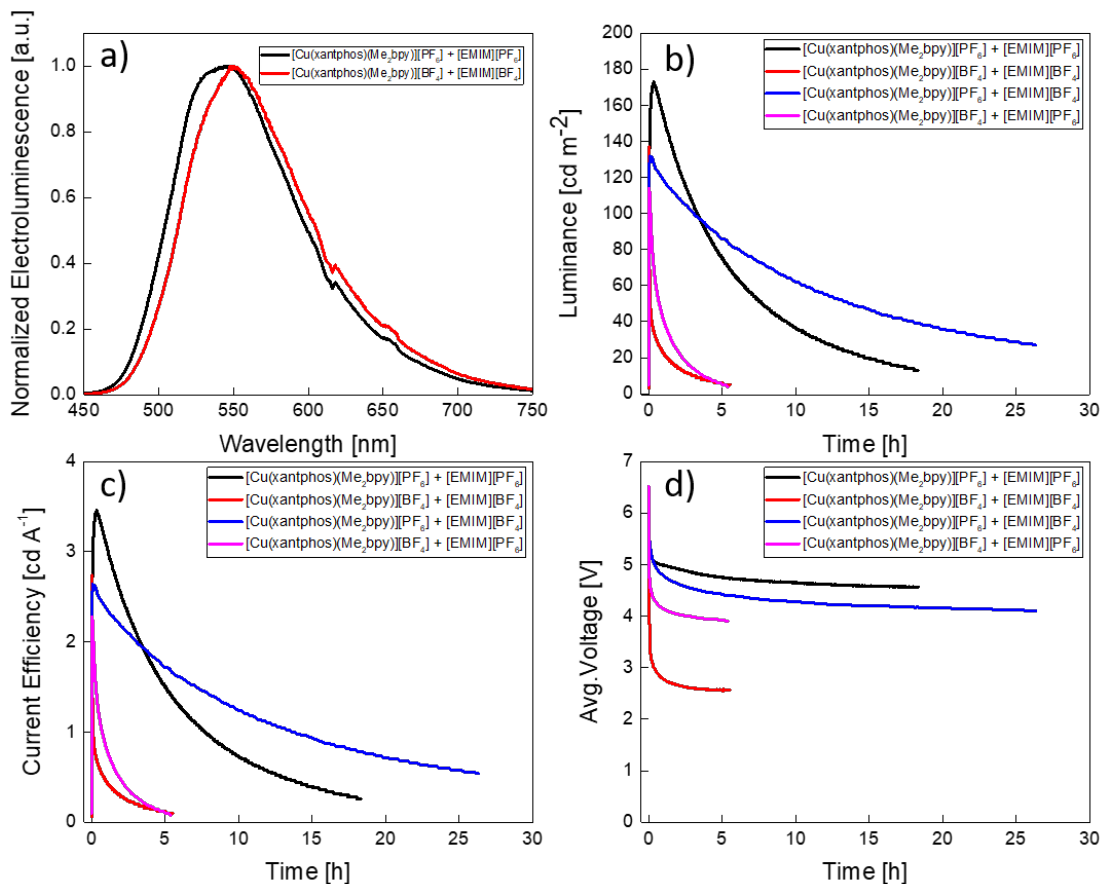


Figure 28. a) Normalized electroluminescence spectra of the two best performing complexes [Cu(xantphos)(Me<sub>2</sub>bpy)][PF<sub>6</sub>] (Cu1) and [Cu(xantphos)(Me<sub>2</sub>bpy)][BF<sub>4</sub>] (Cu2). b) luminance values and c) current efficiency and d) voltage of Cu1 and Cu2 LECs driven at an average current density of 50 A m<sup>-2</sup> with different IL counterions.

Table 4. Photoluminescence properties of thin films of the [Cu(xantphos)(Me<sub>2</sub>bpy)]<sup>+</sup> complexes.

Compound	$\lambda_{\max}^{\text{em}}$ [nm] ( $\lambda_{\text{exc}} = 365 \text{ nm}$ )	PLQY [%]
[Cu(xantphos)(Me <sub>2</sub> bpy)][PF <sub>6</sub> ]	563	44
[Cu(xantphos)(Me <sub>2</sub> bpy)][BF <sub>4</sub> ]	563	45
[Cu(xantphos)(Me <sub>2</sub> bpy)][BPh <sub>4</sub> ]	548	32
[Cu(xantphos)(Me <sub>2</sub> bpy)][BAr <sup>F</sup> <sub>4</sub> ]	552	35

Table 5. Performance of LECs with the  $[\text{Cu}(\text{xantphos})(\text{Me}_2\text{bpy})]^+$  series in the active layer; cell architecture ITO/PEDOT:PSS/ $[\text{Cu}(\text{xantphos})(\text{Me}_2\text{bpy})][\text{A}]:[\text{EMIM}][\text{A}]$  (4:1 molar ratio)/Al. LECs were measured using a pulsed current driving (average current density  $50 \text{ A m}^{-2}$ , 1 kHz, 50% duty cycle, block wave).

Complex	Max Luminance [ $\text{cd m}^{-2}$ ]	Max Current Efficiency [ $\text{cd A}^{-1}$ ]	Turn-on time [s] <sup>*</sup>
$[\text{Cu}(\text{xantphos})(\text{Me}_2\text{bpy})][\text{PF}_6]$ + $[\text{EMIM}][\text{PF}_6]$	173	3.5	58
$[\text{Cu}(\text{xantphos})(\text{Me}_2\text{bpy})][\text{BF}_4]$ + $[\text{EMIM}][\text{BF}_4]$	137	2.7	15
$[\text{Cu}(\text{xantphos})(\text{Me}_2\text{bpy})][\text{PF}_6]$ + $[\text{EMIM}][\text{BF}_4]$	132	2.6	61
$[\text{Cu}(\text{xantphos})(\text{Me}_2\text{bpy})][\text{BF}_4]$ + $[\text{EMIM}][\text{PF}_6]$	114	2.3	47

\*Turn-on-time is time to time to reach a luminance of  $100 \text{ cd m}^{-2}$ .

Light-emitting electrochemical cells using complexes Pt5-9 as active materials were also fabricated and characterized. Like for the Cu-complexes, the same fabrication methods were utilized: the complexes were mixed with the IL 1-butyl-3-methyl-imidazolium-hexafluorophosphate  $[\text{BMIM}]^+[\text{PF}_6]^-$  in a molar ratio of 4 to 1 (iTMC:IL). In the case of complexes Pt7, Pt8 and Pt9 they were dissolved in two different solvents, acetonitrile (ACN) and dichloromethane (DCM). Due to their low solubility in these solvents, complexes Pt5 and Pt6 were tested in dichloroethane (DCE) solutions. The active layers (iTMC:IL) were characterized by means of photoluminescence (PL) and quantum yield (PLQY). Devices were then fabricated from the solutions adopting the archetypical stack configuration: ITO/PEDOT:PSS (80 nm)/iTMC+IL (90-120 nm)/Al (100 nm). Devices were tested by measuring their performance over time and their electroluminescence (EL) spectra were reported. We will start the discussion focusing on the emitters Pt7, Pt8 and Pt9. The principal figures of merit are collected in **Table 6**. First, the PL and PLQY of the active layers prepared from ACN and DCM solutions of Pt7, Pt8 and Pt9 were measured ( $\lambda_{\text{ex}} = 340 \text{ nm}$ ), showing no significant solvent effect on either the  $\lambda_{\text{em}}$  and PLQY (**Figure 29** and Table 6).

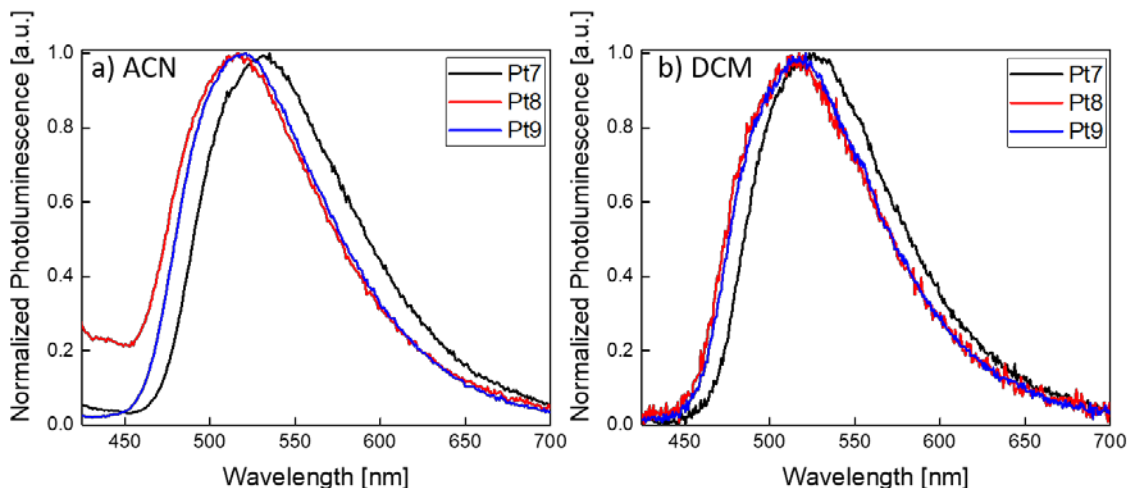


Figure 29. Photoluminescence of Pt7, Pt8 and Pt9 in ACN and DCM.

These PLQY values are far lower than the ones obtained in PMMA, most probably due to the higher concentration of iTMC in the active layer. In fact, it is often observed a self-quenching process, taking place in highly concentrated iTMC thin films.<sup>[72]</sup> These results are in agreement with the lower PLQYs of solid samples of compounds 7-9 compared to those obtained in PMMA. The QY values are generally a good indicator of the luminance performance of the iTMC when employed in a light-emitting device. In view of these results, a similar peak luminance is expected regardless of the solvent used.

Table 6. Figures of merits of the devices obtained from Pt7, Pt8 and Pt9 in ACN and DCM.

Emitter in ACN	PL $\lambda_{em}$ [nm]	PLQY [%]	EL [nm]	Peak Lum. [ $cd\ m^{-2}$ ]	$t_{50}$ [min]	CE [ $cd\ A^{-1}$ ]	PE [lm/W]
Pt7	531	11%	523	61	13	1.2	0.61
Pt8	516	8%	528	60	35	1.2	0.61
Pt9	521	14%	519	57	43	1.1	0.58
Emitter in DCM	PL $\lambda_{em}$ [nm]	PLQY [%]	EL [nm]	Peak Lum. [ $cd\ m^{-2}$ ]	$t_{50}$ [min]	CE [ $cd\ A^{-1}$ ]	PE [lm/W]
Pt7	525	12%	542	265	15	5.7	2.24
Pt8	517	6%	535	187	13	3.7	1.26
Pt9	517	11%	528	180	17	3.6	1.13

The LEC devices were operated under a pulsed current driving with an average current density of  $50 \text{ A m}^{-2}$  (1000 Hz block-wave, 50% duty cycle with a peak current of  $100 \text{ A m}^{-2}$ ) and, contrary to what was expected from the PLQY results, they behaved quite differently depending on the solvent used to process the active layers (**Figure 30**).

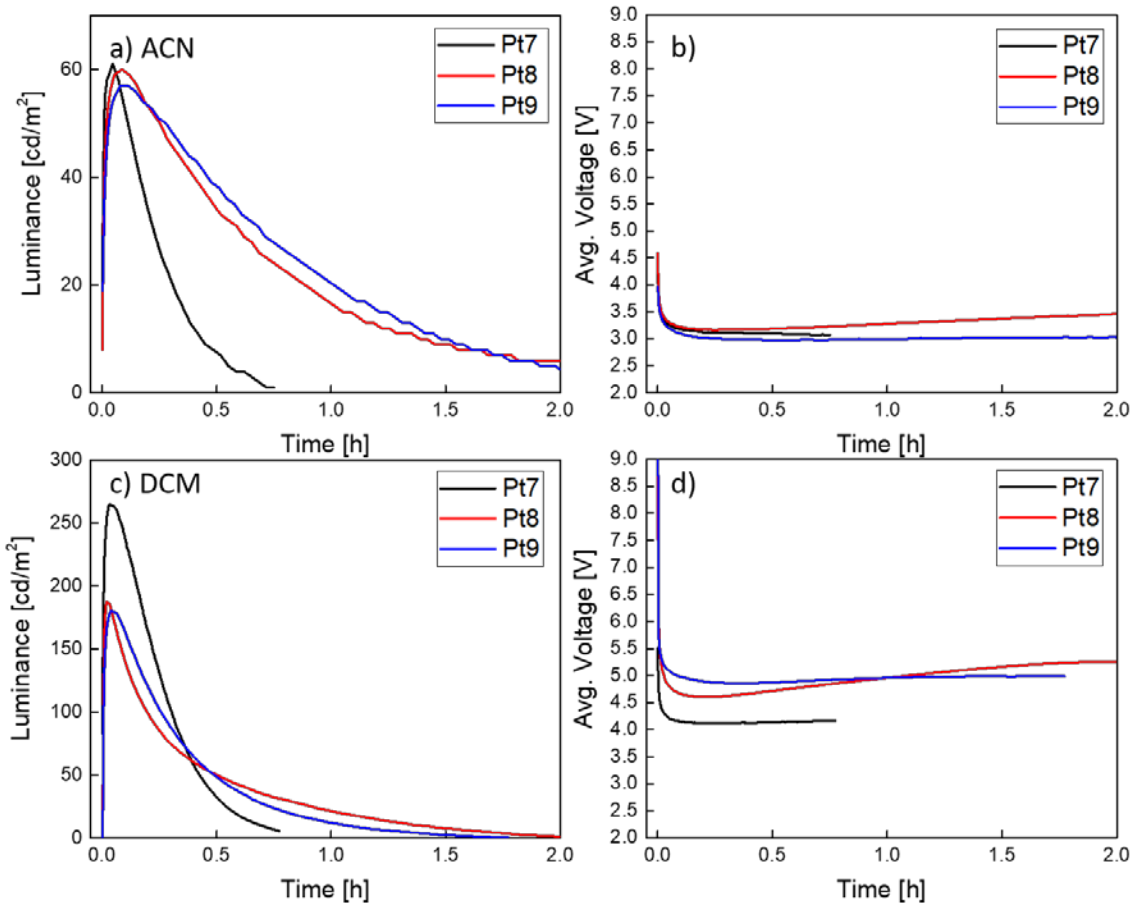


Figure 30: Time-dependence of the luminance [ $\text{cd/m}^2$ ] and average voltage [V] of LECs ITO/PEDOT:PSS/iTMC:IL(4:1)/Al, where iTMC are emitters Pt7 (black curve), Pt8 (red curve) and Pt9 (blue curve) in a)-b) ACN and c)-d) DCM. All the devices shown were driven with a pulsed current with an average current density of  $50 \text{ A m}^{-2}$ .

Devices made from ACN solutions (Figure 30a-b) showed in general lower efficiency with maximum luminance values of about  $60 \text{ cd m}^{-2}$  and current efficiency (CE) values of around  $1.2 \text{ cd A}^{-1}$ . When devices were fabricated from DCM instead, a three- to four-fold increase of the luminance and efficiency values were observed, achieving luminance values of  $265 \text{ cd m}^{-2}$ ,  $187 \text{ cd m}^{-2}$  and  $180 \text{ cd m}^{-2}$  with peak CEs of  $5.7 \text{ cd A}^{-1}$ ,  $3.7 \text{ cd A}^{-1}$  and  $3.6 \text{ cd A}^{-1}$  for compound Pt7, Pt8 and Pt9, respectively. Lower driving currents have been shown to improve LEC device efficiency.<sup>[146]</sup> We biased devices fabricated from DCM and ACN using emitter Pt7 with a pulsed current driving with average current densities of 25 and  $12.5 \text{ A m}^{-2}$  (**Figure 31**). The results show that, even using these lower biases, the efficiencies remain very similar, with peak efficiencies of 4.7 and  $5.2 \text{ cd A}^{-1}$  for current densities of 25 and  $12.5 \text{ A m}^{-2}$ , respectively, which indicates that phenomena such as self-heating of the device is not the limiting factor on the efficiency in these

devices, at least in the current density range studied.<sup>[15]</sup> Regarding the lifetime, devices made from ACN showed  $t_{50}$  of 13, 35 and 43 minutes, for emitters Pt7, Pt8 and Pt9, respectively, while those from DCM  $t_{50}$  were 15, 13 and 17 minutes, respectively.

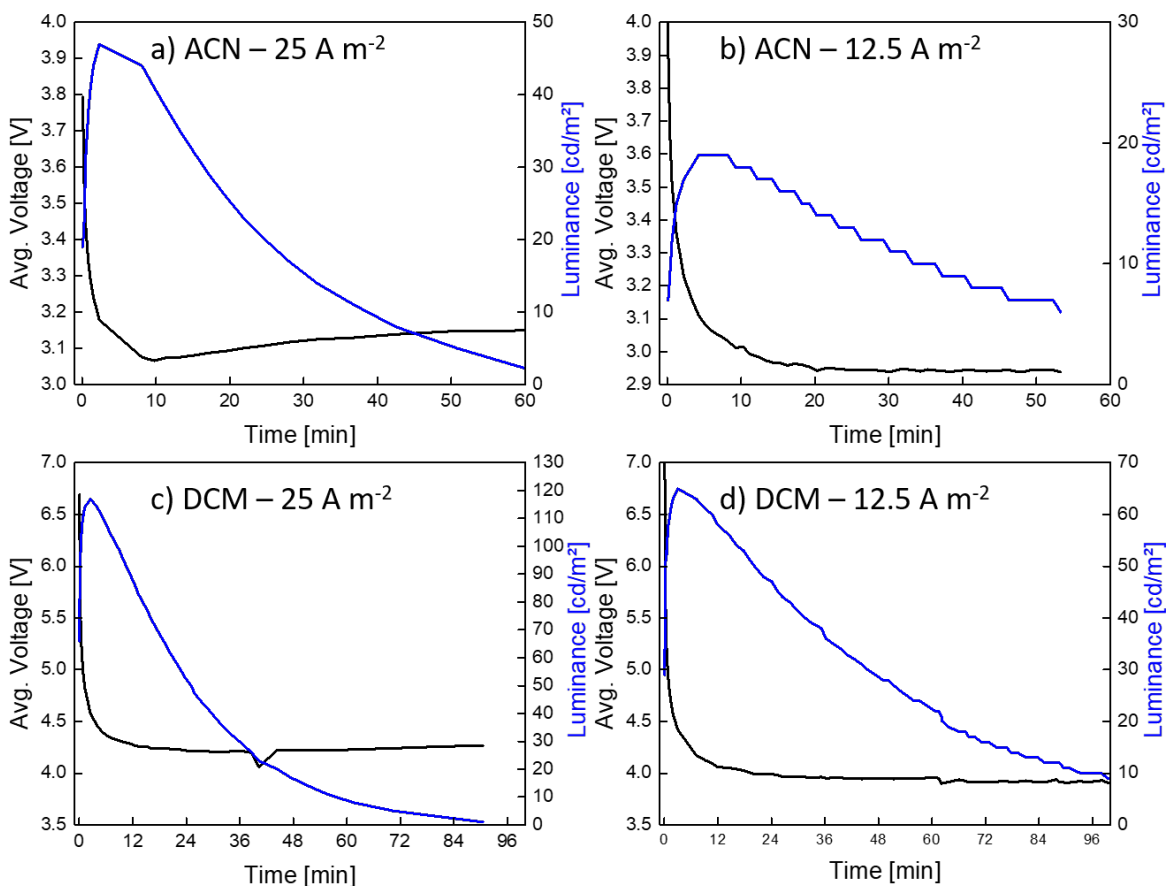


Figure 31: Time-dependence of the luminance [cd/m<sup>2</sup>] and average voltage [V] of LECs ITO/PEDOT:PSS/iTMC:IL(4:1)/Al, where the iTMC is Pt7. the devices shown were driven with a pulsed current with an average current density of 25 and 12.5 A m<sup>-2</sup>.

The increase in luminance together with the reduced  $t_{50}$  for DCM devices, despite the same PLQY values, could be explained by two main factors. The first point to take into consideration is the difference in boiling point of the two solvents, ~81°C for ACN and ~40°C for DCM and the temperature at which the films were annealed before the cathode vacuum deposition, 70°C for 15 min. These annealing conditions could allow all the DCM to evaporate and escape from the samples but in the case of the ACN residual solvent could remain in the active films. The effect of retained solvents has been reported in the past as detrimental for the devices as it can lead to degradation pathways or quenching.<sup>[147]</sup> In view of this, we increased the annealing conditions of devices prepared from ACN in terms of time and temperature. To do this, we prepared a device using emitter Pt7 with a longer annealing time (4 h) at the same temperature (70°C) as well as a device using emitter Pt9 with a higher temperature annealing process (90°C) and a longer time (1 h). The performance of the device processed at 70°C for 4h slightly improved with a maximum luminance of 75 cd m<sup>-2</sup> (vs 61 cd m<sup>-2</sup>), a CE of 1.5 cd A<sup>-1</sup> (vs 1.2 cd A<sup>-1</sup>) and a  $t_{50}$  of 11 min (vs 13 min) (**Figure 32a**). On the other hand, the device processed at higher annealing temperature not



only did not improve but it decreased, showing a maximum luminance of  $48 \text{ cd m}^{-2}$  (vs  $57 \text{ cd m}^{-2}$ ), a CE of  $0.96 \text{ cd A}^{-1}$  (vs  $1.1 \text{ cd A}^{-1}$ ) and a  $t_{50}$  of 7 min (vs 43 min) (Figure 32b).

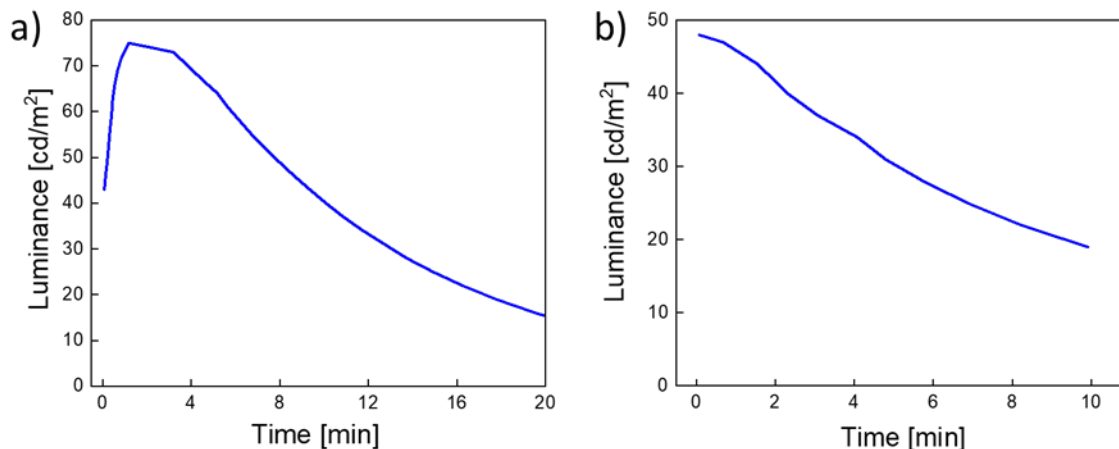


Figure 32. a) Time-dependence of the luminance of a LEC device ITO/PEDOT:PSS/Pt7:IL(4:1)/Al in ACN with a longer annealing time (4 h) at the same temperature ( $70^\circ\text{C}$ ). b) Time-dependence of the luminance of a LEC device ITO/PEDOT:PSS/Pt9:IL(4:1)/Al in ACN with a higher temperature annealing process ( $90^\circ\text{C}$ ) at a longer time (1 h).

These results, in particular the much lower  $t_{50}$ , could be an indication that the harsher annealing conditions are inducing a degradation of the emitter. The second aspect to be pointed out is the voltage during operation (Figure 30d). When compared, the voltage of the devices prepared from ACN is significantly lower than the DCM, with values between 3 V and 3.5 V for ACN and values between 4 V and 5 V for DCM. The origin of this effect can also be related to the residual solvent present on the active layer, where it has been seen that the presence of solvent decreases the resistance of the film, resulting in lower turn-on voltage.<sup>[147]</sup> Lower voltages notoriously allow for longer lifetimes, and therefore higher  $t_{50}$ , but at the expense of lower luminance levels. All in all, these results point that the origin of the difference in the performance of devices processed from ACN and from DCM might reside in their different morphology. Indeed, in previous works it has been seen that morphology can affect the performance of LEC devices.<sup>[148–150]</sup> However, Atomic Force Microscopy (AFM) images show no significant differences between active films using emitter Pt7 processed from different solvents (**Figure 33**). Both layers are very flat and homogeneous with no apparent phase separation or aggregation and with just small differences in the root mean square (RMS) roughness of the films (0.5 nm and 0.3 nm for ACN and DCM, respectively).

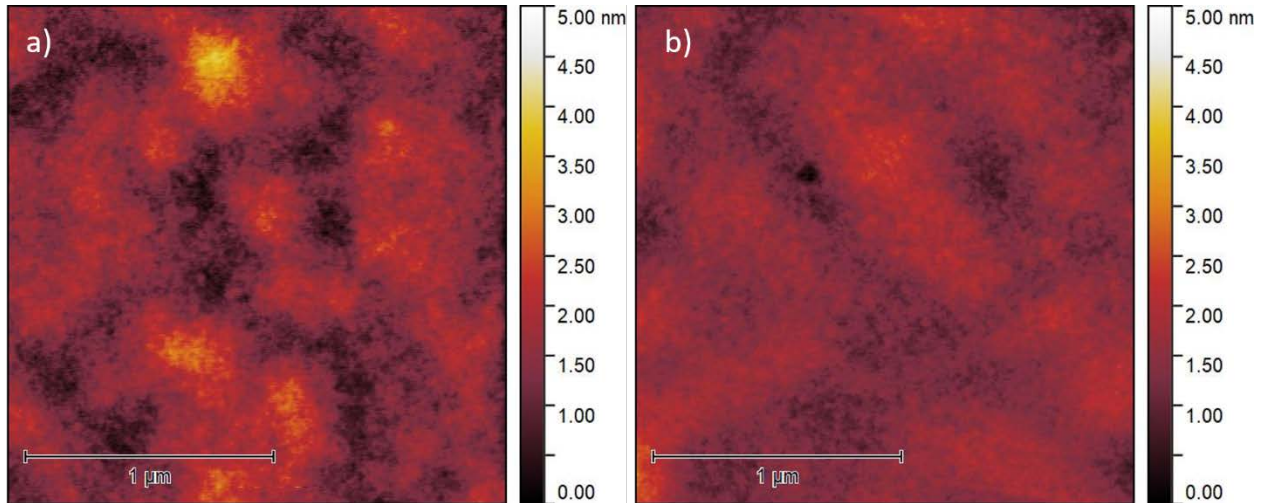


Figure 33. AFM images (2  $\mu\text{m}$  x 2  $\mu\text{m}$ ) of the active film using emitter Pt7 processed from a) ACN and b) DCM.

Finally, EL spectra were characterized both in ACN and in DCM (**Figure 34** and **Table 7**). In ACN the EL peaks of Pt7, Pt8 and Pt9 are centered at 523 nm, 528 nm and 519 nm while in DCM at 542 nm, 535 nm and 528 nm, respectively. The slight difference on the EL peaks between ACN- and DCM-processed devices is ascribed to optical effects arising from the differences in the thicknesses of the active layers (90 and 120 nm, respectively). The EL is very similar to the PL of the active layer films. In some cases, Pt8 from ACN and Pt7, Pt8 and Pt9 from DCM, a slight red-shift of the EL can be observed. A red-shift of the EL of iTMCs can be common and was also previously observed in LECs based on Ir(III) and Cu(I) complexes.<sup>[143,151]</sup> Notably, as seen by the EL spectra, the three devices emit in the green region. To our knowledge, these are the first reported green-emitting Pt(II)-based LECs. In spite of their simplicity, iTMC-LECs fabricated from DCM solutions of the carbazole-appended compounds, Pt7-9 showed improved performance than PhOLEDs based in similar complexes bearing R-C<sup>^</sup>C\* (R= H, CN), since the optimal OLED, based on compound [Pt(H-C<sup>^</sup>C\*)(dppbz)][PF<sub>6</sub>] achieved a maximum luminance of 200 cd m<sup>-2</sup> with a peak CE of 0.4, at 10 V.<sup>[133]</sup>

The PLQY values of the thin films and EL spectra offers two possible ways to estimate the external quantum efficiency (EQE) of the device.

$$EQE = \frac{CE * \lambda_{max} \pi * c}{lm \text{ radiant flux}} \quad \text{eq. 3}$$

$$EQE = \frac{b\phi}{2n^2} \quad \text{eq. 4}$$

In the first method, eq. 3, uses CE and EL spectra to derive the *lm radiant flux* factor, where  $\lambda_{max}$  is the maximum EL wavelength expressed in nanometers and  $c$  a constant. In the second method, eq. 4, EQE is obtained by approximating the IQE, referred to as  $\phi$ , to PLQY and where  $n$  is the refractive index of glass and  $b$  the recombination efficiency (equals to 1 for ohmic contacts). The EQE values were calculated and showed in Table 7 for the emitters in ACN and DCM respectively.

When the EQE is calculated from PLQY, it is assumed that the internal quantum efficiency (IQE), that is the ratio between the number of photons produced and number of electrons injected, is equal to the PLQY values as metal complexes can harvest both singlet and triplet energy. Thus the PLQY represents the maximum conversion rate of the electrical excitons into light. In the second case instead, assuming a Lambertian case where the emission only occurs in one half-plane, the EQE can be estimated from the CE value and the EL spectra of the device. It is possible to notice a considerable difference between the two results, in fact the EQE derived from the EL is substantially lower than the EQE derived from PLQY. The main reason behind this is due to a quench of the IQE or PLQY in the device during operation. A possible cause could be, for example, due to the electric field that the iTMC is experiencing because of the impartial screening by the mobile ions accumulated at the electrodes, which might also induce to an unbalanced current injection.<sup>[31,152]</sup> Another cause, as discussed above, is the effect of the concentration that eventually leads to a self-quench of the emission. For iTMC-LECs this is often remedied by incorporating an inert polymer matrix such as PMMA or using large ligands with a higher steric hindrance.<sup>[57,58,153]</sup>

Table 7. Calculated EQE from EL spectra and PLQY values of the thin films.

Emitter in ACN	EQE from EL [%]	EQE from PLQY [%]
Pt7	0.34	2.44
Pt8	0.33	1.77
Pt9	0.32	3.11
Emitter in DCM	EQE from EL [%]	EQE from PLQY [%]
Pt7	1.46	2.66
Pt8	0.97	1.33
Pt9	1.00	2.44

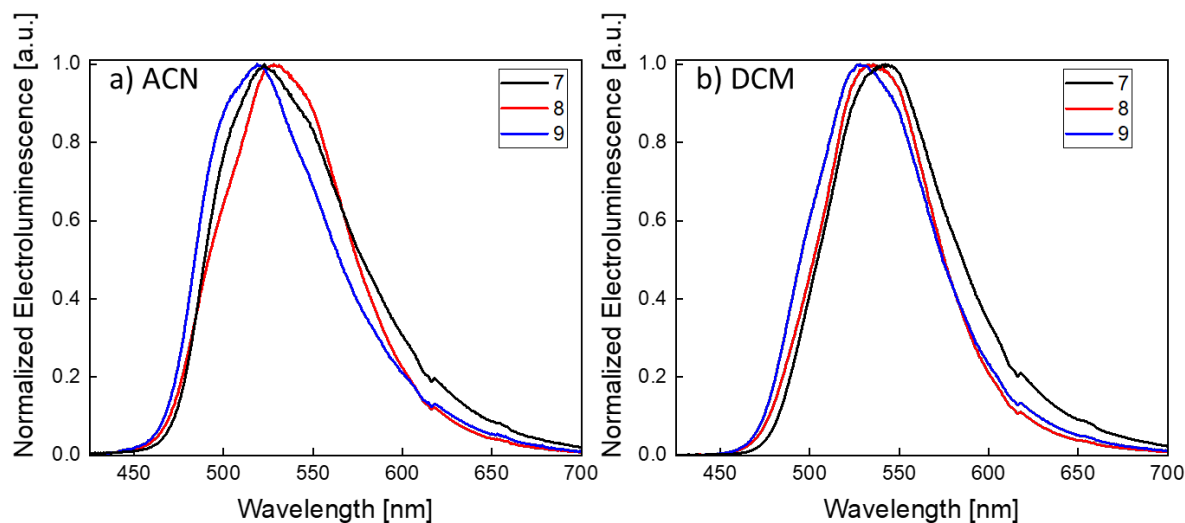


Figure 34: Normalized electroluminescence spectra of LEC devices ITO/PEDOT:PSS/iTMC:IL(4:1)/Al, where iTMC are emitters Pt7 (black curve), Pt8 (red curve) and Pt9 (blue curve) from a) ACN and b) DCM.

Similarly, devices made from compounds Pt5 and Pt6 were also fabricated. The active layers (iTMC:IL) showed very low PLQY with values of 1% for both emitters. Devices made with Pt5 and Pt6 turned-on, showing the classic voltage evolution over time of a LEC (Figure S24), however their performance was extremely poor. For emitter Pt6, the maximum observed luminance was  $4 \text{ cd m}^{-2}$  while for emitter Pt5 the luminance was lower than the sensitivity of our LEC lifetime characterization setup (less than *ca.*  $1 \text{ cd m}^{-2}$ ). For emitter Pt6 it was also possible to measure the EL spectra, which showed a blue emission centered at 491 nm. The very low QY of emitters Pt5 and Pt6 somewhat predicts the very low EL observed on these devices.

### 5.3 Conclusion

In this Chapter, we illustrated the photophysical and device properties of two families of iTMCs, based on Cu(I) and Pt(II). First, the effect of different counteranions ( $[\text{PF}_6]^-$ ,  $[\text{BF}_4]^-$ ,  $[\text{BPh}_4]^-$ ,  $[\text{BAr}^{\text{F}}_4]^-$ ) was studied for a family of Cu-complexes ( $[\text{Cu}(\text{xantphos})(\text{Me}_2\text{bpy})]^+$ ). The luminophores were mixed with  $[\text{EMIM}][\text{A}]$  ILs in which  $[\text{A}]^-$  was the same or a different counterion than in the copper(I) complex. LECs containing  $[\text{Cu}(\text{xantphos})(\text{Me}_2\text{bpy})][\text{BPh}_4]$  and  $[\text{Cu}(\text{xantphos})(\text{Me}_2\text{bpy})][\text{BAr}^{\text{F}}_4]$  failed to turn on under the LEC operating conditions, whereas those with the smaller  $[\text{PF}_6]^-$  or  $[\text{BF}_4]^-$  counterions had rapid turn-on times and exhibited maximum luminances of  $173$  or  $137 \text{ cd m}^{-2}$  and current efficiencies of  $3.5$  and  $2.6 \text{ cd A}^{-1}$ , respectively, if the IL contained the same counterion as the luminophore. Mixing the counterions ( $[\text{PF}_6]^-$  and  $[\text{BF}_4]^-$ ) in the active complex and the IL led to a reduction in all the figures of merit of the LECs. Second, platinum (II) complexes bearing a new carbazole-appended cyclometallated N-heterocyclic carbene were characterized. The presence of an electron donating group ( $\text{R} = \text{Cbz}$ ) in the  $\text{R-C}^{\wedge}\text{C}^*$  skeleton of these complexes, raised the energy of the HOMO bringing their emission into the green region. LECs were fabricated from ACN and DCM solutions of the carbazole-appended compounds, Pt7-9. The devices made from DCM gave the best performance, driven with an average pulsed current of  $50 \text{ A m}^{-2}$  and operating within 4-5 V. The luminance values were 265,

187 and 180  $\text{cd m}^{-2}$  with peak CEs of 5.7, 3.7 and 3.6  $\text{cd A}^{-1}$  for Pt7, Pt8 and Pt9, respectively. From the characterization, we noticed that the devices did not perform equally when prepared from different solvents. Our tests pointed out that a possible reason for this behavior is the remanence of solvent (in this case ACN) in the active layer, which does not completely evaporate. From supplementary AFM tests it was not possible to clarify the discrepancy in the luminance levels. We believe that the solvent coordination sphere might have affected how the complexes deposit to form the thin film, giving rise to distinct device behaviors. This is an important aspect that needs to be appointed for future device generations.

## 6. Conclusion

LECs have attracted a vast attention thank to their simple architecture and easy manufacture showing immediate aptness for being the next energy-saving and low-cost solid-state lighting source. While the fundamental physics of these devices is nowadays well understood and accepted, devices performance are low and still do not meet the market requirements. In this perspective, more efforts are needed to improve this technology. With this in mind, this Thesis demonstrates the efficacy of new materials for light emission and ionic transport in LECs as well as facile unique architectures for innovative applications.

Ultimately, the goal of this Thesis is also to motivate future research in the field for market-directed solutions.

In Chapter 3, a fast and stable CP-LEC is demonstrated using SY as emitter and introducing a hyperbranched ion conductive and solvating polymer (Hybrane) and a Li salt. The role of the Hybrane polymer is that of supplying good ion conduction within the active layer by coordinating the  $\text{Li}^+$  ions. Interestingly, this also helps to reduce the PL quenching. Maintaining the mass ratio between SY and Hybrane to 1:0.3, we fabricated devices with 9% of LiTf content and driven with averaged pulsed current densities of  $50 \text{ A m}^{-2}$ ,  $75 \text{ A m}^{-2}$ , and  $100 \text{ A m}^{-2}$ . As a result, we obtained bright devices with a maximum luminance value of  $480 \text{ cd m}^{-2}$  and an estimated  $t_{50}$  of over 2000 hrs (under a pulsed current bias of  $50 \text{ A m}^{-2}$ ). Finally, to better understand the doped zones formation in our devices, we performed a new characterization method which consisted in measuring the PL from a pixel under electrical bias over time (*i.e.* under EL operation). Our results indicate that the PL signal drops due to the quenching induced by the operation of the LEC. After switching off, the PL is recovered following different timescales. The transient PL values and degree of recovery were dependent on the current density applied.

In Chapter 4, a novel architecture for transparent LECs is presented, where the top electrode is composed of a  $\text{SnO}_2$  buffer layer and an ITO cathode, fabricated by ALD and PLD, respectively. To prevent damage and shorted cells due to the PLD technique, we deposited a  $\text{SnO}_2$  buffer layer at low temperature ( $90 \text{ }^\circ\text{C}$ ) between the active layer and the top ITO. Thanks to this, we achieved highly transparent working devices with a maximum transmission of 82% at the EL peak (563 nm). The devices were characterized by applying an averaged pulsed driving current of  $50 \text{ A m}^{-2}$  and monitoring their luminance and voltage over time. The performance of the transparent devices was measured from both sides, revealing a difference in efficiency and  $t_{50}$ . From the top side (through  $\text{SnO}_2/\text{ITO}$ ) a maximum luminance value of  $188 \text{ cd m}^{-2}$  was recorded ( $t_{50} = 118 \text{ h}$ ), while, from the bottom side (through glass/ITO) a luminance value of  $260 \text{ cd m}^{-2}$  was obtained ( $t_{50} = 176 \text{ h}$ ), resulting in efficiencies of  $4 \text{ cd A}^{-1}$  and  $5.2 \text{ cd A}^{-1}$  respectively. We ascribed the difference in performance between top and bottom illumination to three main reasons. Firstly, the light outcoupling dependence on the refractive index,  $n$ . Secondly, internal reflections caused by the Au fingers evaporated around the active area might have affected the final light output, promoting a higher luminance from the bottom side. Thirdly, as a consequence of the cathode deposition, a PL quench of the light-emitting layer was observed. This was further confirmed by the PL study conducted on device stacks and irradiating from the bottom and up side. Nevertheless, the figures of merit of these semitransparent devices are amongst the highest reported in the literature.

In Chapter 5, we studied the photophysical and device properties of two families of iTMCs, based on Cu(I) and Pt(II). First, the effect of different counteranions ( $[\text{PF}_6]^-$ ,  $[\text{BF}_4]^-$ ,  $[\text{BPh}_4]^-$ ,  $[\text{BAr}_4^{\text{F}}]^-$ ) was studied for the Cu-complexes and second, the effect of the introduction of carbazole-

substituted cyclometallating ligand and the use of two different solvents (ACN and DCM) for the Pt-complexes. In our work, [Cu(xantphos)(Me<sub>2</sub>bpy)][A] compounds were incorporated into the active layers of LECs. The luminophores were mixed with [EMIM][A] ILs in which [A]<sup>-</sup> was the same or a different counterion than in the copper(I) complex. LECs containing the smaller [PF<sub>6</sub>]<sup>-</sup> or [BF<sub>4</sub>]<sup>-</sup> counterions had rapid turn-on times and exhibited maximum luminances of 173 and 137 cd m<sup>-2</sup> and current efficiencies of 3.5 and 2.6 cd A<sup>-1</sup>, respectively. We also found that mixing the counterions ([PF<sub>6</sub>]<sup>-</sup> and [BF<sub>4</sub>]<sup>-</sup>) of the active complex and the IL led to a reduction in all the figures of merit of the LECs.

On the other hand, the chemistry of Pt(II) with cyclometallated N-heterocyclic carbenes (NHC; C<sup>^</sup>C) has proven to give elevated quantum efficiencies across the visible spectra. In this work, the Pt(Cbz-C<sup>^</sup>C\*) system was explored and green LECs were obtained and demonstrated for the first time. The devices made from DCM gave the best performance, driven with an average pulsed current of 50 A m<sup>-2</sup> and operating within 4-5 V. The maximum luminance value for the best emitter was 265 cd m<sup>-2</sup> with peak CE of 5.7. From the characterization, we noticed that the devices do not perform equally when prepared with different solvents. Our tests pointed out that a possible reason for this behavior is the remanence of acetonitrile solvent in the active layer, which does not completely evaporate. Here, the solvent coordination sphere might also affect how the complexes deposit to form the thin film, giving rise to distinct device behaviors. This is an important aspect that needs to be appointed for future device generations.

In conclusion, in this Thesis we have explored new approaches for the design of light-emitting electrochemical cells. The study of novel emitting materials based on Cu(I) and Pt(II) for iTMC-LECs, the incorporation of new ionic conducting polymers for CP-LECs and new electrode fabrication methods to obtain semitransparent LECs.



## 7. Resumen en Español

## 7.1 Introducción

Hoy en día, la iluminación consume el 20% de la energía eléctrica mundial e implica el 5% de las emisiones mundiales de gases de efecto invernadero. En este contexto, el uso de diodos emisores de luz (LEDs) como fuentes de iluminación puede ser una solución viable ya que se trata de dispositivos súper eficientes y más respetuosos con el medio ambiente. De hecho, según la Comisión Europea, con el cambio a productos de iluminación más eficientes Europa podrá ahorrar hasta 34 TWh de electricidad al año de aquí a 2030 y evitará la emisión de unos 7 millones de toneladas anuales de CO<sub>2</sub>. Según la Agencia Internacional de la Energía (AIE), el uso de LEDs ha aumentado sustancialmente, pasando de una cuota de mercado del 5% en 2013 a más del 50% en 2020, y se espera que llegue al 100% en 2025 para cumplir con el escenario de cero emisiones netas solicitado por el Acuerdo de París (2015/2016).

Un LED es un componente eléctrico que emite luz cuando se aplica una corriente eléctrica. La arquitectura del LED está compuesta por dos electrodos entre los que se intercalan una serie de capas finas de semiconductores inorgánicos, como se muestra en la Figura 2a (Capítulo 1). El proceso de emisión de luz, mostrado en la Figura 2b (Capítulo 1), se denomina electroluminiscencia (EL) y tiene lugar cuando se crea una unión *p-n* y se aplica una polarización positiva. La composición química del dispositivo determina su *bandgap* ( $E_g$ ) y, por tanto, el color de la luz emitida por el LED. Esta tecnología ha evolucionado rápidamente desde el siglo pasado y, de hecho, los LEDs han encontrado rápidamente una amplia selección de aplicaciones. Las principales ventajas de estos dispositivos son su larga vida útil (hasta 50000 horas), su alta eficiencia, su rápida respuesta al encenderse/apagarse, sus dimensiones y peso reducidos, su mejor gestión térmica en comparación con las fuentes de luz convencionales y su capacidad de emitir en todo el espectro visible e infrarrojo cercano.

Más recientemente se ha desarrollado la contrapartida orgánica de los LEDs, los diodos orgánicos emisores de luz (OLEDs). Los OLEDs son muy similares a los LEDs (Figura 2c, Capítulo 1). La diferencia radica en que los materiales semiconductores que constituyen los OLEDs son de naturaleza orgánica, normalmente moléculas pequeñas conjugadas y polímeros, pero también pueden utilizarse complejos metálicos de transición neutros e iónicos (iTMCs). Estos materiales son sistemas conjugados, lo que determina su semiconductividad. El ajuste de sus propiedades depende de su estructura química, es decir, de la elección de sus grupos funcionales y heteroátomos. La formación de la unión *p-n* y la función de trabajo (WF) de los electrodos son cruciales para tener una correcta alineación energética y, por tanto, dispositivos funcionales. Esto significa que, normalmente, no es posible tener una electroluminiscencia eficiente en los OLEDs sólo utilizando una capa activa entre dos electrodos cuando trabajamos a voltajes bajos (Figura 3, Capítulo 1). Las grandes barreras energéticas entre la capa activa y los electrodos permitirían la inyección de carga sólo a voltajes altos, causando un sobrecalentamiento y una alta recombinación no radiativa, lo que implicaría una degradación más rápida y una eficiencia de EL pobre. Es necesario, por tanto, el uso de capas adicionales para tener dispositivos eficientes.

Más recientemente, se ha desarrollado una forma más sencilla de OLED, la célula electroquímica emisora de luz (LEC). Los LECs poseen una arquitectura muy sencilla en la que una sola capa activa orgánica se deposita entre dos electrodos, lo que da lugar a una emisión de luz eficaz. Esto es posible gracias a su mecanismo de operación único, que combina portadores de carga eléctricos

y especies iónicas. Esto es, por supuesto, una ventaja, ya que reduce los costes de fabricación y la cantidad total de recursos utilizados por unidad. En su forma más sencilla, esta capa activa consiste en un semiconductor electroluminiscente orgánico mezclado con un electrolito. La presencia simultánea de portadores de carga eléctricos, iones móviles y excitones dentro de la misma capa emisora de un LEC determina un complejo principio de funcionamiento que ha sido objeto de debate durante mucho tiempo. Después de aplicar un determinado voltaje (o corriente) al dispositivo, el comportamiento típico en el tiempo muestra un aumento de la luminancia mientras la corriente (o voltaje) aumenta (disminuye). Generalmente, esto se explica por la presencia de iones móviles que, bajo un campo eléctrico, pueden reorganizarse en la capa activa y migrar hacia los electrodos, promoviendo la inyección de portadores de carga. Aunque esta explicación general es comúnmente aceptada, se describieron dos teorías diferentes, los modelos electrodinámico y electroquímico, para demostrar cómo se distribuyen el campo eléctrico y el voltaje a través del dispositivo. Clásicamente, los componentes emisores de luz que primero encontraron aplicación en los LECs son los polímeros conductores fluorescentes (CPs) y los iTMCs (en los llamados CP-LEC y los iTMC-LEC, respectivamente).

Desde su descubrimiento, los LECs siempre han estado por detrás de las dos fuentes de luz más eficientes, los LEDs y los OLEDs. Cuatro son las principales deficiencias que han impedido que los LECs cumplan los requisitos del mercado: 1) un largo tiempo de encendido, 2) una vida media corta, 3) una baja eficiencia y 4) una emisión de color limitada. Además, la falta de un método estandarizado para medir el rendimiento de los dispositivos dificulta la comparación directa entre los distintos dispositivos para analizar objetivamente dónde se encuentran los LECs en comparación con los OLEDs. En esta Tesis, exploramos diferentes enfoques para mejorar la tecnología LEC, con la esperanza de motivar futuras investigaciones en este campo.

## 7.2 Objetivos

El uso de nuevos materiales, como las moléculas emisoras de luz o los polímeros transportadores de iones, tiene una importancia fundamental a la hora de mejorar la vida útil o de conseguir altos niveles de luminancia en dispositivos de tipo LEC. Al mismo tiempo, los avances más recientes han llevado a la tecnología LED y OLED a una nueva clase de dispositivos con propiedades atractivas, como la flexibilidad o la transparencia, desarrollo que se ha llevado a cabo de forma muy limitada en los LECs.

Teniendo esto en cuenta, el trabajo de esta Tesis se centró en la implementación de nuevos materiales, en particular nuevos emisores iTMC y un polímero conductor iónico, y el diseño y fabricación de arquitecturas que puedan habilitar nuevas aplicaciones para estos dispositivos.

En los CP-LECs uno de los componentes esenciales de la capa es el polímero conductor iónico, de quien depende el rendimiento final de los dispositivos. En el Capítulo 3, se muestra cómo la introducción de un nuevo polímero transportador iónico híper-ramificado favorece la fabricación de CP-LECs con una vida media mucho más elevada. Hemos observado que la adición de dicho polímero reduce la disminución de la fotoluminiscencia (PL) del CP debido a las interacciones con las especies iónicas y estabiliza el estado estacionario del dispositivo operado bajo una corriente pulsada.

El concepto de dispositivo transparente ha sido, hasta ahora, estudiado principalmente en LEDs y OLEDs. En el Capítulo 4 se aplican por primera vez las técnicas ALD y PLD (respectivamente, deposición de capas atómicas y deposición por láser pulsado) para conseguir iTMC-LECs altamente transparentes. Aquí, se deposita una capa fina de SnO<sub>2</sub> por ALD, con una doble función de capa amortiguadora y de transporte de carga, mientras que otra capa de óxido de indio y estaño (ITO) más gruesa se deposita por PLD y se utiliza como cátodo.

La necesidad de nuevos materiales emisores de luz eficientes es crucial para reducir aún más los costes y disponer de una mayor variedad con la que fabricar dispositivos. En el Capítulo 5, se exploran dos nuevas familias de iTMCs basados en cobre(I) y platino(II) como materiales emisores alternativos a los complejos utilizados más comúnmente, pero más caros, basados en Ir(III).

### 7.3 Fabricación y caracterización de dispositivos: procedimientos generales

Los emisores utilizados en este trabajo pertenecen a las dos categorías de CPs y iTMCs. En el trabajo presentado en el Capítulo 3 se utilizó el copolímero conjugado "Super Yellow" (SY). El SY se considera un emisor de referencia para los CP-LECs y se puede adquirir fácilmente. En el Capítulo 4, se utilizó un complejo de Ir(III) para fabricar iTMC-LECs semitransparentes. En el Capítulo 5, se presentan nuevos complejos de Pt(II) y Cu(I) como emisores para los iTMC-LECs. La síntesis de los complejos de Pt(II) fue realizada por el grupo de la Prof. Dra. Violeta Sicilia del Departamento de Catálisis Homogénea de la Universidad de Zaragoza (España), mientras que la de los complejos de Cu(I) fue realizada por el grupo de los Prof. Dr. Edwin Constable y la Prof. Dra. Catherine Housecroft del Departamento de Química de la Universidad de Basilea (Suiza).

La fabricación de los LECs consta de varios pasos realizados en una sala limpia de clase 10000 y en una caja seca de N<sub>2</sub>. Para la fabricación de los dispositivos de esta tesis se aplicaron los siguientes procedimientos: limpieza de los sustratos, deposición de PEDOT:PSS (poly(3,4-ethylenedioxythiophene) polystyrene sulfonate)) por *spin-coating* (solo para los iTMC-LECs), deposición de los emisores por *spin-coating*, deposición del cátodo metálico por evaporación térmica y, para los iTMC-LECs semitransparentes, deposición de SnO<sub>2</sub> e ITO por ALD y PLD. Siempre se adoptó una arquitectura de dispositivo vertical con la siguiente configuración: sustrato de vidrio/ITO/SY/Al para los SY-LECs, sustrato de vidrio/ITO/PEDOT:PSS/iTMC/SnO<sub>2</sub>/ITO para los Ir-LECs semitransparentes y, finalmente, sustrato de /ITO/PEDOT:PSS/capa activa/Al para los Pt-LECs y Cu-LECs.

Las películas finas procesadas desde disolución se caracterizaron mediante perfilometría en muestras de control (capa activa sobre sustrato de vidrio). En los estudios presentados en esta tesis, el espesor del PEDOT:PSS se mantuvo siempre entre 90-100 nm. En el caso de los iTMCs, el espesor puede variar en función del disolvente utilizado. Sin embargo, siempre se ha garantizado un espesor mínimo de 80 nm a partir de disoluciones de acetonitrilo (ACN). En el caso de los CP-LECs, el grosor de la película polimérica se ha medido en el rango de los 130-140 nm. Tras la fabricación de las películas finas, los dispositivos se transfirieron a una caja de guantes para su recocido (*annealing*) y para la deposición térmica de un cátodo de aluminio bajo ultra alto vacío

( $10^{-6}$  mbar). Se utilizó una máscara de sombra para la deposición del electrodo superior, lo que dio como resultado un área activa de  $6 \text{ mm}^2$ .

En el Capítulo 4, se utilizó ALD para depositar 20 nm de  $\text{SnO}_2$ , con una doble función protectora y de capa de transporte de electrones. Para la deposición de óxidos metálicos, como el  $\text{AlOx}$  y el  $\text{SnOx}$ , se utilizan como precursores un oxidante (por ejemplo,  $\text{H}_2\text{O}$  y  $\text{O}_3$ ) y un compuesto reactivo del metal de interés. También deben optimizarse otros parámetros para una correcta deposición de la película, por ejemplo, la temperatura y presión de la cámara a la que se exponen los sustratos, la frecuencia de los pulsos de los precursores y las características de la purga después de cada pulso. Para ello, la cámara de ALD se calentó a  $90 \text{ }^\circ\text{C}$ , la botella del precursor de Sn (tetrakis(dimetilamino) estaño, TDAT) se calentó a  $60 \text{ }^\circ\text{C}$  mientras que la botella del oxidante (agua) no se calentó, y los colectores del precursor y del oxidante se calentaron a  $115$  y  $140 \text{ }^\circ\text{C}$ , respectivamente. Antes de la deposición, los tubos y las válvulas de los colectores se desgasificaron tres veces realizando una serie de 30 pulsos con las botellas cerradas manualmente. Los bordes de los contactos de ITO se protegieron con cinta Kapton de poliamida de Dupont y, a continuación, se introdujeron los sustratos en la cámara de ALD, que se evacuó. Un ciclo de ALD consistió en purgas consecutivas de TDAT durante 550 ms y de vapor de agua durante 200 ms, cada una de ellas seguida de purgas de  $\text{N}_2$  de 30 y 105 segundos, respectivamente, para asegurar la completa eliminación de los precursores de la cámara de ALD (crecimiento final por ciclo: 1.5 Angs).

La técnica de PLD se utiliza sobre todo para la deposición de óxidos conductores transparentes (TCO) y óxidos metálicos, tales como ITO,  $\text{NiOx}$  o  $\text{SnOx}$ . El proceso puede tener lugar en ultra alto vacío o en presencia de gases como  $\text{O}_2$  y Ar, dependiendo de la composición de la película fina de interés. Para un proceso de PLD es extremadamente importante optimizar la presión de la cámara y la proporción de gases de acuerdo con las propiedades deseadas de la película fina resultante. En el Capítulo 4, se utilizó la PLD para la deposición de ITO como cátodo para iTMC-LECs transparentes. Los parámetros de la cámara se optimizaron previamente. Se depositaron 140 nm de ITO con una presión de cámara de 0.042 mbar y una presión parcial de  $\text{O}_2$  de 0.0076 mbar, controladas por una inyección constante de una mezcla de gas de oxígeno/argón a temperatura ambiente. Esta herramienta de PLD está acoplada a una caja de guantes de  $\text{N}_2$ , para minimizar cualquier efecto perjudicial del  $\text{O}_2$  y de la humedad en el rendimiento de los dispositivos producidos. Se empleó un láser ( $\lambda = 248 \text{ nm}$ ), fijando la tasa de repetición en 25 Hz y un flujo de  $1.5 - 1.7 \text{ J cm}^{-2}$ . El material fuente para la deposición de ITO fue un blanco cerámico de  $\text{Sn:In}_2\text{O}_3$  con una proporción de 2:98 %p/p. Los sustratos se fijaron con cinta adhesiva a las máscaras de sombra para obtener un área activa de  $6 \text{ mm}^2$ .

Las medidas de fotoluminiscencia (PL) son cruciales, ya que proporcionan información adicional sobre los materiales emisores. Estas medidas implican la determinación de los espectros de emisión y de la eficiencia de emisión (rendimiento cuántico de fotoluminiscencia, PLQY) y forman parte de la caracterización fundamental que se suele llevar a cabo en materiales emisores de luz tanto en capas aisladas como integrados en la configuración final del dispositivo. Las características de PL resultantes permiten predecir sus propiedades de electroluminiscencia.

En esta tesis, las mediciones de PL se utilizan como una herramienta para investigar la interacción que puede generarse dentro de la capa activa o en las interfaces. Por ejemplo, en el Capítulo 3, se utilizó el PL para estudiar la interacción del SY con el polímero transportador de iones Hybrane y

la sal de litio. O en el Capítulo 4, se realizó un estudio del PL en la configuración completa del dispositivo para evaluar la disminución del PL de la capa emisora debido a la deposición del cátodo. Por último, también en el Capítulo 3, se introdujo un nuevo protocolo de medida del PL. Este consiste en medir el PL en el área activa del píxel mientras se aplica una corriente de diferentes intensidades. Para ello, se diseñó un nuevo montaje. La medición del PL mientras el dispositivo está funcionando nos permitió registrar en tiempo real la disminución del PL causado por el crecimiento de las zonas dopadas. Además, el uso de un amplificador de tipo lock-in y un picoamperímetro nos permitió medir simultáneamente el PL y la EL.

Los dispositivos presentados en esta tesis fueron siempre operados bajo corrientes pulsadas promediadas, desde  $25 \text{ A m}^{-2}$  hasta  $100 \text{ A m}^{-2}$ . Una vez aplicada la corriente, la caracterización de los dispositivos consistió en la monitorización del voltaje y la luminancia en función del tiempo. La corriente pulsada aplicada consistió en ondas de tipo bloque a una frecuencia de 1000 Hz con un ciclo de trabajo del 50%. Como resultado, la densidad de corriente y el voltaje medios se obtuvieron multiplicando los valores por el tiempo de encendido (0.5 s) y dividiéndolos por el tiempo de ciclo total (1 s).

El rendimiento del dispositivo se mide en función de varios parámetros. A continuación se muestran los parámetros medidos habitualmente en un LEC:

- El espectro de EL: al igual que en el caso del PL, el EL indica la región del espectro visible en la que el dispositivo emite cuando se aplica una polarización eléctrica.
- Luminancia (Lum): La intensidad de la luz medida por unidad de superficie expresada en  $[\text{cd m}^{-2}]$ . Describe la cantidad de luz emitida por el dispositivo en un momento dado.
- Densidad de corriente ( $J$ ): La intensidad de corriente por unidad de superficie expresada en  $[\text{A m}^{-2}]$ . Para un dispositivo operado bajo corriente pulsada el valor debe promediarse.
- Tiempo de vida media ( $t_{50}$ ): El tiempo para alcanzar la mitad de la luminancia máxima. Es el parámetro más utilizado para describir la estabilidad de un LEC.
- Tiempo de encendido ( $t_{\text{on}}$ ): El tiempo necesario para alcanzar un valor determinado de luminancia, generalmente  $100 \text{ cd m}^{-2}$ . A veces, también se expresa como el tiempo para alcanzar la luminancia máxima, independientemente de su valor.
- Eficiencia de corriente (CE): Representa el flujo en candelas por amperio eléctrico  $[\text{cd A}^{-1}]$ . Se obtiene dividiendo la luminancia por la densidad de corriente.
- Eficiencia de potencia (PE): Representa el flujo luminoso medido en lúmenes por vatio eléctrico  $[\text{lm W}^{-1}]$  medido en una esfera integrada o suponiendo una emisión lambertiana. En el caso de los dispositivos operados bajo corriente pulsada también hay que tener en cuenta el ciclo de trabajo.
- Eficiencia Cuántica Externa (EQE): Es la relación de fotones emitidos por cada electrón inyectado en un dispositivo determinado. Su relación con el PLQY se ha descrito anteriormente.
- Coordenadas de la Commission Internationale de l'Eclairage (coordenadas CIE): Las coordenadas pueden calcularse a partir de los espectros de EL y dan una definición exacta del color de emisión según los estándares internacionales. Las coordenadas CIE se expresan (x,y) y se colocan en un gráfico 2D.

## 7.4 Capítulo 3

Como se mencionó en la introducción, el mecanismo de funcionamiento de los LECs se basa en la presencia de conductores electrónicos e iónicos. En el caso de los CP-LECs, la introducción de un electrolito polimérico es una forma de añadir conductores iónicos, desempeñando un papel determinante en el rendimiento global. Un electrolito polimérico está formado por una sal y un polímero coordinador que disuelve y coordina los iones gracias a sus centros donantes de electrones.

En este Capítulo, se desarrollaron LECs basados en el emisor SY combinado con un nuevo polímero solvente de iones híper-ramificado, Hybrane DEO750 8500 (Hy) y con la sal trifluorometanosulfonato de litio ( $\text{LiCF}_3\text{SO}_3$ , LiTf).

El estudio se presenta y se divide en dos partes: la primera se centra en la caracterización de los LECs que utilizan esta nueva composición en su capa activa. Los dispositivos mostraron un  $t_{50}$  extrapolado de más de 2000 horas (con una luminancia inicial superior a  $480 \text{ cd m}^{-2}$ ) y una eficiencia de potencia máxima de  $12.6 \text{ lm W}^{-1}$  con tiempos de encendido inferiores al minuto. Estos valores se encuentran entre los más altos registrados en la literatura para CP-LECs. La segunda parte se centra en el estudio de las interacciones entre los materiales de la capa activa, el SY, el electrolito polimérico Hybrane y la sal de Li. Esto se llevó a cabo, en primer lugar, realizando mediciones de PL en estado estacionario que revelaron que la introducción del Hybrane en la capa activa disminuyó el *quenching* al ser capaz de coordinar los átomos de  $\text{Li}^+$ . En segundo lugar, en un intento de comprender el efecto de la formación de zonas dopadas en la estabilidad del dispositivo, realizamos mediciones de la fotoluminiscencia durante la operación eléctrica del dispositivo en estado estacionario. Esto permitió seguir la evolución de la fotoluminiscencia durante el funcionamiento del LEC, analizando directamente cómo los iones libres interactúan con la matriz polimérica en las diferentes etapas de funcionamiento de los LECs. Nuestros resultados sugieren que este método puede emplearse para modelar el mecanismo de funcionamiento de los LECs y otros dispositivos iónicos, correlacionarlo con la composición de la capa activa y mejorar el rendimiento de los dispositivos.

## 7.5 Capítulo 4

En los últimos años, impulsado por la aparición de nuevos productos, ha surgido la necesidad de desarrollar dispositivos OLED que presentan nuevas propiedades como superficies grandes, elasticidad o transparencia. En particular, para los OLEDs semitransparentes, los requisitos para el cátodo son una alta transmitancia de luz (más del 80%) y una baja resistencia de superficie ( $R_s$ ). Los materiales y estructuras más comunes en el uso como electrodos transparentes son los óxidos conductores transparentes (TCOs). Los TCOs son los materiales más utilizados ya que poseen una alta conductividad y apenas existen limitaciones al procesarlos, puesto que suelen depositarse sobre sustratos de vidrio o plástico que soportan las duras condiciones a las que se les somete durante la deposición de TCO mediante, por ejemplo, el *sputtering* de magnetrón. Sin embargo, el uso de TCOs como electrodos superiores transparentes en dispositivos basados en

semiconductores orgánicos finos requiere más cuidado, ya que, por ejemplo, la pulverización del TCO directamente sobre los dispositivos puede dañar las capas de transporte de carga o los propios materiales activos, reduciendo su rendimiento y su vida útil. Además, es importante la alineación de la banda de conducción del TCO con la energía de los orbitales moleculares del semiconductor orgánico. Estos requisitos han limitado el uso generalizado de los TCO como electrodos superiores en dispositivos semiconductores orgánicos. El uso de ITO como electrodo superior en dispositivos semitransparentes ya se ha estudiado en los LEDs y los OLEDs. Sin embargo, la bibliografía sobre los LECs semitransparentes sigue siendo relativamente escasa.

En este Capítulo se presentan iTMC-LECs semitransparentes en los que se utiliza ITO como electrodo superior e inferior y en los que, por primera vez, se introducen las técnicas de ALD y PLD en la fabricación de cátodos para LECs. El electrodo superior se procesó en una estructura multicapa compuesta por SnO<sub>2</sub> depositado por ALD e ITO depositado por PLD. El cátodo se depositó directamente sobre la capa activa orgánica basada en un emisor amarillo de iridio(III), [Ir(ppy)<sub>2</sub>(dtb-bpy)][PF<sub>6</sub>] (donde ppy es 2-fenilpiridina y dtb-bpy es 4,4'-di-tert-butil-2,2'-dipiridilo), dando lugar a dispositivos con una transparencia muy alta, superior al 75% en la región del espectro visible (380 a 750 nm). Los posibles efectos adversos del ALD y el PLD durante el procesamiento de las capas orgánicas inferiores se examinaron mediante caracterización óptica y eléctrica, incluyendo absorción, transmisión, PL y la respuesta de EL medida tanto desde el lado superior como el lado inferior de los dispositivos.

Aunque los niveles de energía del SnO<sub>2</sub> y del material activo en la capa emisora de luz no están alineados, esto no supone un problema en los LECs, gracias a su mecanismo de funcionamiento que implica la migración de iones a la interfaz del electrodo. Además, la combinación de ALD y PLD ofrece la posibilidad de ajustar las condiciones de deposición, como la presión y la temperatura, para obtener una película de alta calidad, con un control preciso del espesor y la composición. Como resultado, los dispositivos poseían una transparencia total del 75% en el espectro visible (380 a 750 nm) con una transmitancia del 82% en el pico de electroluminiscencia de 563 nm. Finalmente, el rendimiento de los dispositivos mostró una excelente relación de encendido/apagado caracterizada por una alta transmitancia, y una luminancia de hasta 260 cd m<sup>-2</sup> unida a tiempos de vida de hasta 176 h demostrando el potencial de estos dispositivos bifaciales emisores de luz altamente transparentes.

## 7.6 Capítulo 5

Los iTMCs son de gran interés en el campo de los LECs, ya que son intrínsecamente iónicos y no necesitan especies cargadas auxiliares para operar el dispositivo. Además, son emisores fosforescentes triplete, lo que permite mayores eficiencias de electroluminiscencia en comparación con los emisores singlete.

Los primeros trabajos sobre los iTMC-LECs se centraron en complejos de rutenio(II) sustituidos. Estos materiales poseen limitaciones importantes en el color de emisión, emitiendo tan solo en la parte naranja-roja del espectro visible. Hoy en día, la familia más versátil y más utilizada de iTMCs es la del iridio(III), que, gracias a una combinación única de propiedades físicas y químicas, proporciona una enorme variedad de complejos estables, cubriendo el espectro visible del azul al rojo, con una elevada PLQY. Esto ha sido posible gracias al diseño cuidadoso del ligando que ha permitido optimizar la energía de los orbitales moleculares y, al mismo tiempo, reducir las



interacciones intermoleculares que afectan negativamente al rendimiento cuántico. Sin embargo, el Ir es raro y caro, por lo que es importante encontrar alternativas para la fabricación de dispositivos. Con este fin, nuevos iTMCs basados en el cobre(I) y, más recientemente, el platino(II), son interesantes para los dispositivos emisores de luz.

En este Capítulo se presentan nuevos emisores iTMC basados en centros de Cu(I) y Pt(II) para dispositivos de tipo LEC. Entre los tipos más investigados de luminóforos basados en cobre(I) se encuentran los complejos  $[Cu(P^{\wedge}P)(N^{\wedge}N)]^{+}$  donde  $P^{\wedge}P$  es un bifosfano quelante, normalmente un derivado de POP (POP = oxidi(2,1-fenileno)]bis(difenilfosfano)) o xantphos (xantphos = 9,9-dimetil-9H-xanteno-4,5-diil)(bis(difenilfosfano)) y  $N^{\wedge}N$  suele ser un derivado de bpy (bpy = 2,2'-bipiridina) o phen (phen = 1,10-fenantrolina). Los complejos  $[Cu(P^{\wedge}P)(N^{\wedge}N)]^{+}$  tienen la ventaja de ser estructuras adecuadas para las investigaciones sistemáticas y para el ajuste de los niveles de energía de los orbitales moleculares frontera. Además, los complejos  $[Cu(P^{\wedge}P)(N^{\wedge}N)]^{+}$  presentan a menudo fluorescencia retardada activada térmicamente (TADF), lo que conduce a valores teóricos de eficiencia cuántica interna (IQE) de hasta el 100%. En este trabajo presentamos una serie de complejos  $[Cu(P^{\wedge}P)(N^{\wedge}N)][A]$  en los que  $[A]^{-}$  es  $[PF_6]^{-}$  (Cu1),  $[BF_4]^{-}$  (Cu2),  $[BPh_4]^{-}$  (Cu3) o  $[BarF_4]^{-}$  (Cu4) ( $[BarF_4]^{-}$  = tetrakis(3,5-bis(trifluorometil)fenil)borato), ( $P^{\wedge}P$ ) es el ligando xantphos bidentado y ( $N^{\wedge}N$ ) es el ligando auxiliar  $Me_2bpy$  (6,6'-Dimetil-2,2'-bipiridina). Combinamos estos iTMCs con diferentes líquidos iónicos, que se utilizan habitualmente en LECs, para estudiar sus diferentes características y rendimientos.

Por último, en este capítulo también se presenta un segundo grupo de complejos de Pt(II). Los LECs basados en platino han sido raramente explorados, con sólo unos pocos ejemplos encontrados en la literatura, que emiten en la región roja del espectro visible. La química del Pt(II) con carbenos N-heterocíclicos ciclometalizados (NHC;  $C^{\wedge}C$ ) ha demostrado dar elevadas eficiencias cuánticas en todo el espectro visible. En este sentido, es importante diseñar estructuras rígidas o semirrígidas con propiedades quelantes y átomos donantes fuertes para tener una PLQY elevada. Teniendo en cuenta esto, en este Capítulo también exploramos el sistema  $Pt(Cbz-C^{\wedge}C^*)$ , sus propiedades y su aplicación en dispositivos LECs. Se investigaron cinco complejos,  $[Pt(Cbz-C^{\wedge}C^*)(PPh_3)(py)]^{+}$ ,  $[Pt(Cbz-C^{\wedge}C^*)(P^{\wedge}N)]^{+}$  y  $[Pt(Cbz-C^{\wedge}C^*)(P^{\wedge}P)]^{+}$ , donde,  $Cbz-C^{\wedge}C^*$  es un ligando ciclometalado modificado con carbazol, 1-(4-(9H-Carbazol-9-il)fenil)-3-metil-1H-imidazol, py es piridina (Pt5), ( $P^{\wedge}N$ ) es 2-(2-(difenilfosfino)etil)piridina (Pt6), y ( $P^{\wedge}P$ ) es, para tres complejos diferentes, 1,1-bis(difenilfosfino)metano (Pt7), 1,1-bis(difenilfosfino)etano (Pt8) y 1,1-bis(difenilfosfino)benceno (Pt9). Estos complejos mostraron, por primera vez, una emisión azul/verde en LECs basados en complejos de Pt(II) con altos valores de PLQY.

## 7.7 Conclusiones

Los LEC han atraído una gran atención gracias a su sencilla arquitectura y fácil fabricación, mostrando una aptitud inmediata para ser la próxima fuente de iluminación de estado sólido de bajo coste y ahorro energético. Aunque hoy en día la física fundamental de estos dispositivos está bien entendida y aceptada, su rendimiento es bajo y aún no cumple los requisitos del mercado. Desde esta perspectiva, es necesario redoblar los esfuerzos para mejorar esta tecnología. Teniendo esto en cuenta, esta Tesis demuestra la eficacia de nuevos materiales para la emisión de luz o el transporte iónico en LECs y arquitecturas únicas para aplicaciones innovadoras.

En última instancia, el objetivo de esta Tesis es también motivar futuras investigaciones en este campo para obtener soluciones orientadas al mercado.

En el Capítulo 3 se demuestra un CP-LEC rápido y estable utilizando SY como emisor e introduciendo un polímero conductor y solvente de iones híper-ramificado (Hybrane) y una sal de Li. El papel del polímero es el de suministrar una buena conducción de iones dentro de la capa activa. Manteniendo la relación de masas entre SY e Hybrane en 1:0.3 fabricamos dispositivos con el contenido de la sal de LiTf al 9% en peso, que se operaron con una densidad de corriente pulsada media de  $50 \text{ A m}^{-2}$ ,  $75 \text{ A m}^{-2}$  y  $100 \text{ A m}^{-2}$ . Como resultado, obtuvimos dispositivos brillantes con una luminancia máxima de  $480 \text{ cd m}^{-2}$  y un  $t_{50}$  estimado de más de 2000 horas (bajo corriente pulsada de  $50 \text{ A m}^{-2}$ ). Finalmente, para tener una mejor idea de la formación de zonas dopadas en nuestros dispositivos, diseñamos un protocolo de caracterización que consistió en medir el PL de un píxel bajo operación eléctrica a lo largo del tiempo. Nuestros resultados indicaron que la señal de PL cae debido al *quenching* inducido por el funcionamiento del LEC. Tras dejar de operar el dispositivo, el PL se recupera siguiendo diferentes escalas de tiempo. Los valores de PL medidos y el grado de recuperación dependieron de la densidad de corriente aplicada.

En el Capítulo 4 se presenta una nueva arquitectura para LECs transparentes, donde el electrodo superior está compuesto por una capa de  $\text{SnO}_2$  y un cátodo de ITO, fabricados por ALD y PLD, respectivamente. Para evitar daños y cortocircuitos en los dispositivos, depositamos una capa amortiguadora de  $\text{SnO}_2$  a baja temperatura ( $90 \text{ }^\circ\text{C}$ ) entre la capa activa y el electrodo de ITO superior. Gracias a ello, conseguimos dispositivos altamente transparentes con una transmisión máxima del 82% en el pico de EL (563 nm).

Los dispositivos se caracterizaron aplicando una corriente pulsada promediada de  $50 \text{ A m}^{-2}$  y monitorizando su luminancia y voltaje a lo largo del tiempo. El rendimiento de los dispositivos transparentes se midió desde ambos lados, revelando una diferencia en la eficiencia. Desde la cara superior (a través del  $\text{SnO}_2/\text{ITO}$ ) se registró un valor máximo de luminancia de  $188 \text{ cd m}^{-2}$ , mientras que, desde la cara inferior (a través del sustrato de vidrio/ITO) se obtuvo un valor de luminancia de  $260 \text{ cd m}^{-2}$ , lo que dio lugar a eficiencias de  $4 \text{ cd A}^{-1}$  y  $5.2 \text{ cd A}^{-1}$  respectivamente. Finalmente, el  $t_{50}$  era de 118 h y 176 h para la cara superior e inferior, respectivamente. La diferencia de rendimiento entre la iluminación superior y la inferior se debe a tres razones principales. En primer lugar, del índice de refracción,  $n$ . En segundo lugar, las reflexiones internas causadas por los dedos de Au evaporados alrededor de la zona activa podrían haber afectado a la salida de luz final, promoviendo una mayor luminancia desde el lado inferior. En tercer lugar, como consecuencia de la deposición catódica, se observó una disminución del PL de la capa emisora de luz. Esto quedó confirmado por el estudio de PL realizado sobre muestras irradiando desde abajo y desde arriba. No obstante, el rendimiento de estos dispositivos semitransparentes se encuentra entre los más elevados de los reportados en la literatura.

En el Capítulo 5, ilustramos las propiedades fotofísicas y de dispositivo de dos familias de iTMCs, basadas en Cu(I) y Pt(II). En primer lugar, se estudió el efecto de diferentes contraaniones ( $[\text{PF}_6]^-$ ,  $[\text{BF}_4]^-$ ,  $[\text{BPh}_4]^-$ ,  $[\text{BArF}_4]^-$ ) para los complejos de Cu(I) y, en segundo lugar, el efecto de la introducción del ligando ciclometalante sustituido por carbazol y el uso de dos disolventes diferentes, acetonitrilo y diclorometano (ACN y DCM) para la fabricación de dispositivos basados en complejos de Pt(II).

Los luminóforos se mezclaron con líquidos iónicos  $[\text{EMIM}][\text{A}]$  (1-Ethyl-3-methylimidazolium) en los que  $[\text{A}]^-$  era el mismo o un contraanión diferente que en el complejo de cobre(I). Los LECs

que contenían [los contraiones más pequeños  $[\text{PF}_6]^-$  o  $[\text{BF}_4]^-$  se encendieron rápidamente y mostraron luminancias máximas de 173 o 137  $\text{cd m}^{-2}$  y eficiencias de corriente de 3.5 y 2.6  $\text{cd A}^{-1}$ , respectivamente. También se observó que la mezcla de los contraiones ( $[\text{PF}_6]^-$  y  $[\text{BF}_4]^-$ ) en el emisor y el IL conducía a una reducción del rendimiento de los LECs.

Por otro lado, para los complejos de Pt(II) se obtuvieron y caracterizaron por primera vez LECs verdes. Los dispositivos fabricados a partir de DCM ofrecieron el mejor rendimiento, operados con una corriente pulsada media de 50  $\text{A m}^{-2}$ . Los dispositivos alcanzaron valores de luminancia máxima de 265  $\text{cd m}^{-2}$  con CEs de 5.7  $\text{cd A}^{-1}$ , para el mejor emisor. A partir de la caracterización, observamos que los dispositivos no rinden igual cuando se preparan con distintos disolventes, obteniendo rendimientos peores al prepararlos desde ACN. Nuestras pruebas señalaron que una posible razón de este comportamiento es la permanencia de ACN en la capa activa, al no evaporarse completamente. En este caso, la esfera de coordinación del disolvente también podría afectar a la forma en que los complejos se depositan para formar la película fina, dando lugar a comportamientos distintos. Se trata de un aspecto importante que hay que tener en cuenta para el desarrollo de futuras generaciones de dispositivos.

En conclusión, en esta Tesis se han explorado nuevos enfoques para el diseño de LECs. El estudio de materiales emisores basados en Cu(I) y Pt(II) para iTMC-LECs, el uso de polímeros conductores iónicos para mejorar las propiedades en CP-LECs y nuevas técnicas de procesado de electrodos para la obtención de LECs semitransparentes.

## 8. References

- [1] B. F. Gerke, In *Technological Learning in the Transition to a Low-Carbon Energy System*, Elsevier, **2020**, pp. 233–256.
- [2] A. Nardelli, E. Deuschle, L. D. de Azevedo, J. L. N. Pessoa, E. Ghisi, *Renew. Sustain. Energy Rev.* **2017**, *75*, 368.
- [3] P. Morgan Pattison, M. Hansen, J. Y. Tsao, *Comptes Rendus Phys.* **2018**, *19*, 134.
- [4] R. Pode, *Renew. Sustain. Energy Rev.* **2020**, *133*, 110043.
- [5] A. J. H. Qibing Pei, Gang Yu, Chi Zhang, Yang Yang, *Science (80-. )*. **1995**, *269*, 1086.
- [6] J. -K. Lee, D. S. Yoo, E. S. Handy, M. F. Rubner, *Appl. Phys. Lett.* **1996**, *69*, 1686.
- [7] Q. Pei, Y. Yang, G. Yu, C. Zhang, A. J. Heeger, *J. Am. Chem. Soc.* **1996**, *118*, 3922.
- [8] J. C. deMello, *Phys. Rev. B* **2002**, *66*, 235210.
- [9] S. van Reenen, P. Matyba, A. Dzwilewski, R. A. J. Janssen, L. Edman, M. Kemerink, *J. Am. Chem. Soc.* **2010**, *132*, 13776.
- [10] M. J. Jafari, J. Liu, I. Engquist, T. Ederth, *ACS Appl. Mater. Interfaces* **2017**, *9*, 2747.
- [11] S. van Reenen, T. Akatsuka, D. Tordera, M. Kemerink, H. J. Bolink, *J. Am. Chem. Soc.* **2013**, *135*, 886.
- [12] R. D. Costa, A. Pertegás, E. Ortí, H. J. Bolink, *Chem. Mater.* **2010**, *22*, 1288.
- [13] F. AlTal, J. Gao, *Org. Electron.* **2015**, *18*, 1.
- [14] J. Fang, P. Matyba, N. D. Robinson, L. Edman, *J. Am. Chem. Soc.* **2008**, *130*, 4562.
- [15] J. Ràfols-Ribé, N. D. Robinson, C. Larsen, S. Tang, M. Top, A. Sandström, L. Edman, *Adv. Funct. Mater.* **2020**, *30*, 1908649.
- [16] J. C. Leprêtre, A. Deronzier, O. Stéphan, *Synth. Met.* **2002**, *131*, 175.
- [17] F. Zhang, L. Duan, J. Qiao, G. Dong, L. Wang, Y. Qiu, *Org. Electron.* **2012**, *13*, 2442.
- [18] E. Fresta, G. U. Mahoro, L. M. Cavinato, J. Lohier, J. Renaud, S. Gaillard, R. D. Costa, *Adv. Opt. Mater.* **2022**, *10*, 2101999.
- [19] L. Mardegan, C. Dreessen, M. Sessolo, D. Tordera, H. J. Bolink, *Adv. Funct. Mater.* **2021**, *31*, 2104249.
- [20] S. B. Meier, D. Hartmann, D. Tordera, H. J. Bolink, A. Winnacker, W. Sarfert, *Phys. Chem. Chem. Phys.* **2012**, *14*, 10886.
- [21] J. Mindemark, L. Edman, *J. Mater. Chem. C* **2016**, *4*, 420.
- [22] I. Gerz, E. M. Lindh, P. Thordarson, L. Edman, J. Kullgren, J. Mindemark, *ACS Appl. Mater. Interfaces* **2019**, *11*, 40372.
- [23] D. Devaux, R. Bouchet, D. Glé, R. Denoyel, *Solid State Ionics* **2012**, *227*, 119.
- [24] C. Poinsignon, *Mater. Sci. Eng. B* **1989**, *3*, 31.

- [25] M. Diethelm, A. Devižis, W. Hu, T. Zhang, R. Furrer, C. Vael, S. Jenatsch, F. Nüesch, R. Hany, *Adv. Funct. Mater.* **2022**, *32*, 2203643.
- [26] J. Mindemark, S. Tang, J. Wang, N. Kaihovirta, D. Brandell, L. Edman, *Chem. Mater.* **2016**, *28*, 2618.
- [27] S. Tang, J. Mindemark, C. M. G. Araujo, D. Brandell, L. Edman, *Chem. Mater.* **2014**, *26*, 5083.
- [28] J. Mindemark, S. Tang, H. Li, L. Edman, *Adv. Funct. Mater.* **2018**, *28*, 1801295.
- [29] S. B. Meier, D. Tordera, A. Pertegás, C. Roldán-Carmona, E. Ortí, H. J. Bolink, *Mater. Today* **2014**, *17*, 217.
- [30] R. D. Costa, E. Ortí, H. J. Bolink, F. Monti, G. Accorsi, N. Armaroli, *Angew. Chemie Int. Ed.* **2012**, *51*, 8178.
- [31] H. J. Bolink, E. Coronado, R. D. Costa, N. Lardiés, E. Ortí, *Inorg. Chem.* **2008**, *47*, 9149.
- [32] S. T. Parker, J. D. Slinker, M. S. Lowry, M. P. Cox, S. Bernhard, G. G. Malliaras, *Chem. Mater.* **2005**, *17*, 3187.
- [33] J. D. Slinker, C. Y. Koh, G. G. Malliaras, M. S. Lowry, S. Bernhard, *Appl. Phys. Lett.* **2005**, *86*, 173506.
- [34] H. Rudmann, S. Shimada, M. F. Rubner, *J. Am. Chem. Soc.* **2002**, *124*, 4918.
- [35] M. A. Baldo, D. F. O. an dY. You, A. Shoustikov, S. Sibley, M. E. Thompson, S. R. Forrest, *Nature* **1998**, *395*, 151.
- [36] C. E. Housecroft, E. C. Constable, *Coord. Chem. Rev.* **2017**, *350*, 155.
- [37] R. Bai, X. Meng, X. Wang, L. He, *Adv. Funct. Mater.* **2020**, *30*, 1907169.
- [38] N. M. Shavaleev, R. Scopelliti, M. Grätzel, M. K. Nazeeruddin, A. Pertegás, C. Roldán-Carmona, D. Tordera, H. J. Bolink, *J. Mater. Chem. C* **2013**, *1*, 2241.
- [39] D. Tordera, S. Meier, M. Lenes, R. D. Costa, E. Ortí, W. Sarfert, H. J. Bolink, *Adv. Mater.* **2012**, *24*, 897.
- [40] K. Hasan, L. Donato, Y. Shen, J. D. Slinker, E. Zysman-Colman, *Dalt. Trans.* **2014**, *43*, 13672.
- [41] L. Sun, A. Galan, S. Ladouceur, J. D. Slinker, E. Zysman-Colman, *J. Mater. Chem.* **2011**, *21*, 18083.
- [42] D. R. Martir, C. Momblona, A. Pertegás, D. B. Cordes, A. M. Z. Slawin, H. J. Bolink, E. Zysman-Colman, *ACS Appl. Mater. Interfaces* **2016**, *8*, 33907.
- [43] M. H. Bowler, T. Guo, L. D. Bastatas, M. D. Moore, A. V. Malko, J. D. Slinker, *Mater. Horizons* **2017**, *4*, 657.
- [44] S. Keller, A. Prescimone, M.-G. La Placa, J. M. Junquera-Hernández, H. J. Bolink, E. C. Constable, M. Sessolo, E. Ortí, C. E. Housecroft, *RSC Adv.* **2020**, *10*, 22631.

- [45] C. E. Housecroft, E. C. Constable, *J. Mater. Chem. C* **2022**, *10*, 4456.
- [46] K. T. Weber, K. Karikis, M. D. Weber, P. B. Coto, A. Charisiadis, D. Charitaki, G. Charalambidis, P. Angaridis, A. G. Coutsolelos, R. D. Costa, *Dalt. Trans.* **2016**, *45*, 13284.
- [47] M. Z. Shafikov, S. Tang, C. Larsen, M. Bodensteiner, V. N. Kozhevnikov, L. Edman, *J. Mater. Chem. C* **2019**, *7*, 10672.
- [48] K. J. Suhr, L. D. Bastatas, Y. Shen, L. A. Mitchell, G. A. Frazier, D. W. Taylor, J. D. Slinker, B. J. Holliday, *Dalt. Trans.* **2016**, *45*, 17807.
- [49] S. Kanagaraj, A. Puthanveedu, Y. Choe, *Adv. Funct. Mater.* **2020**, *30*, 1907126.
- [50] Q. Wei, N. Fei, A. Islam, T. Lei, L. Hong, R. Peng, X. Fan, L. Chen, P. Gao, Z. Ge, *Adv. Opt. Mater.* **2018**, *6*, 1800512.
- [51] S. Rakshit, P. Piatkowski, I. Mora-Seró, A. Douhal, *Adv. Opt. Mater.* **2022**, *10*.
- [52] W. Xiang, W. Tress, *Adv. Mater.* **2019**, *31*, 1902851.
- [53] M. Alahbakhshi, A. Mishra, R. Haroldson, A. Ishteev, J. Moon, Q. Gu, J. D. Slinker, A. A. Zakhidov, *ACS Energy Lett.* **2019**, *4*, 2922.
- [54] D. Gets, M. Alahbakhshi, A. Mishra, R. Haroldson, A. Papadimitratos, A. Ishteev, D. Saranin, S. Anoshkin, A. Pushkarev, E. Danilovskiy, S. Makarov, J. D. Slinker, A. A. Zakhidov, *Adv. Opt. Mater.* **2021**, *9*, 2001715.
- [55] A. Mishra, R. Bose, Y. Zheng, W. Xu, R. McMullen, A. B. Mehta, M. J. Kim, J. W. P. Hsu, A. V. Malko, J. D. Slinker, *Adv. Mater.* **2022**, *34*, 2203226.
- [56] M. H. Bowler, A. Mishra, A. C. Adams, C. L. D. Blangy, J. D. Slinker, *Adv. Funct. Mater.* **2020**, *30*, 1906715.
- [57] T. Hu, L. He, L. Duan, Y. Qiu, *J. Mater. Chem.* **2012**, *22*, 4206.
- [58] F. Brunner, A. Babaei, A. Pertegás, J. M. Junquera-Hernández, A. Prescimone, E. C. Constable, H. J. Bolink, M. Sessolo, E. Ortí, C. E. Housecroft, *Dalt. Trans.* **2019**, *48*, 446.
- [59] J. Xu, A. Sandström, E. M. Lindh, W. Yang, S. Tang, L. Edman, *ACS Appl. Mater. Interfaces* **2018**, *10*, 33380.
- [60] Y. Xu, P. Xu, D. Hu, Y. Ma, *Chem. Soc. Rev.* **2021**, *50*, 1030.
- [61] J. Lim, K. H. Lee, J. Kim, J. Y. Lee, *Adv. Opt. Mater.* **2022**, *10*, 2201575.
- [62] J. H. Lee, C. H. Chen, P. H. Lee, H. Y. Lin, M. K. Leung, T. L. Chiu, C. F. Lin, *J. Mater. Chem. C* **2019**, *7*, 5874.
- [63] A. Zampetti, A. Minotto, F. Cacialli, *Adv. Funct. Mater.* **2019**, *29*, 1.
- [64] R. Englman, J. Jortner, *Mol. Phys.* **1970**, *18*, 145.
- [65] Y. Huang, E.-L. Hsiang, M.-Y. Deng, S.-T. Wu, *Light Sci. Appl.* **2020**, *9*, 105.

- [66] J. D. Slinker, A. A. Gorodetsky, M. S. Lowry, J. Wang, S. Parker, R. Rohl, S. Bernhard, G. G. Malliaras, *J. Am. Chem. Soc.* **2004**, *126*, 2763.
- [67] R. W. Johnson, A. Hultqvist, S. F. Bent, *Mater. Today* **2014**, *17*, 236.
- [68] J. Schou, *Appl. Surf. Sci.* **2009**, *255*, 5191.
- [69] M. J. Aziz, *Appl. Phys. A* **2008**, *93*, 579.
- [70] K. P. S. Zaroni, A. Paliwal, M. A. Hernández-Fenollosa, P. Repecaud, M. Morales-Masis, H. J. Bolink, *Adv. Mater. Technol.* **2022**, *7*, 2101747.
- [71] N. M. Shavaleev, R. Scopelliti, M. Grätzel, M. K. Nazeeruddin, A. Pertegás, C. Roldán-Carmona, D. Tordera, H. J. Bolink, *J. Mater. Chem. C* **2013**, *1*, 2241.
- [72] J. D. Slinker, J. Rivnay, J. S. Moskowitz, J. B. Parker, S. Bernhard, H. D. Abruña, G. G. Malliaras, *J. Mater. Chem.* **2007**, *17*, 2976.
- [73] H. J. Bolink, L. Cappelli, S. Cheylan, E. Coronado, R. D. Costa, N. Lardiés, M. K. Nazeeruddin, E. Ortí, *J. Mater. Chem.* **2007**, *17*, 5032.
- [74] S. Keller, A. Prescimone, H. Bolink, M. Sessolo, G. Longo, L. Martínez-Sarti, J. M. Junquera-Hernández, E. C. Constable, E. Ortí, C. E. Housecroft, *Dalt. Trans.* **2018**, *47*, 14263.
- [75] S. Tang, L. Edman, *J. Phys. Chem. Lett.* **2010**, *1*, 2727.
- [76] K. Timachova, H. Watanabe, N. P. Balsara, *Macromolecules* **2015**, *48*, 7882.
- [77] H. Gao, S. Chen, J. Liang, Q. Pei, *ACS Appl. Mater. Interfaces* **2016**, *8*, 32504.
- [78] Z. Yu, M. Wang, G. Lei, J. Liu, L. Li, Q. Pei, *J. Phys. Chem. Lett.* **2011**, *2*, 367.
- [79] F. P. Wenzl, P. Pachler, C. Suess, A. Haase, E. J. W. List, P. Poelt, D. Somitsch, P. Knoll, U. Scherf, G. Leising, *Adv. Funct. Mater.* **2004**, *14*, 441.
- [80] S. Burns, J. MacLeod, T. Trang Do, P. Sonar, S. D. Yambem, *Sci. Rep.* **2017**, *7*, 40805.
- [81] J. M. Hodgkiss, G. Tu, S. Albert-Seifried, W. T. S. Huck, R. H. Friend, *J. Am. Chem. Soc.* **2009**, *131*, 8913.
- [82] O. V. Mikhnenko, M. Kuik, J. Lin, N. van der Kaap, T.-Q. Nguyen, P. W. M. Blom, *Adv. Mater.* **2014**, *26*, 1912.
- [83] S. van Reenen, M. V. Vitorino, S. C. J. Meskers, R. A. J. Janssen, M. Kemerink, *Phys. Rev. B* **2014**, *89*, 205206.
- [84] M. A. Summers, S. K. Buratto, L. Edman, *Thin Solid Films* **2007**, *515*, 8412.
- [85] M. Diethelm, Q. Grossmann, A. Schiller, E. Knapp, S. Jenatsch, M. Kawecki, F. Nüesch, R. Hany, *Adv. Opt. Mater.* **2019**, *7*, 1801278.
- [86] D. Tordera, J. Frey, D. Vonlanthen, E. Constable, A. Pertegás, E. Ortí, H. J. Bolink, E. Baranoff, M. K. Nazeeruddin, *Adv. Energy Mater.* **2013**, *3*, 1338.



- [87] D. Tordera, M. Lenes, H. J. Bolink, *J. Nanosci. Nanotechnol.* **2013**, *13*, 5170.
- [88] J. Fang, P. Matyba, N. D. Robinson, L. Edman, *J. Am. Chem. Soc.* **2008**, *130*, 4562.
- [89] C. S. Buga, J. C. Viana, *Adv. Mater. Technol.* **2021**, *6*, 2001016.
- [90] M. G. Song, K. S. Kim, H. I. Yang, S. K. Kim, J. H. Kim, C. W. Han, H. C. Choi, R. Pode, J. H. Kwon, *Org. Electron.* **2020**, *76*, 105418.
- [91] L. Liu, K. Cao, S. Chen, W. Huang, *Adv. Opt. Mater.* **2020**, *8*, 2001122.
- [92] M. Morales-Masis, S. De Wolf, R. Woods-Robinson, J. W. Ager, C. Ballif, *Adv. Electron. Mater.* **2017**, *3*, 1600529.
- [93] D. Li, W.-Y. Lai, Y.-Z. Zhang, W. Huang, *Adv. Mater.* **2018**, *30*, 1704738.
- [94] E. Aydin, C. Altinkaya, Y. Smirnov, M. A. Yaqin, K. P. S. Zanoni, A. Paliwal, Y. Firdaus, T. G. Allen, T. D. Anthopoulos, H. J. Bolink, M. Morales-Masis, S. De Wolf, *Matter* **2021**, *4*, 3549.
- [95] C. Y. Han, K. H. Lee, M. S. Kim, J. W. Shin, J. S. Kim, J. H. Hwang, T. Kim, M. S. Oh, J. Kim, Y. R. Do, H. Yang, *Org. Electron.* **2017**, *45*, 145.
- [96] J. H. Oh, J. W. Park, *Phys. Status Solidi - Rapid Res. Lett.* **2020**, *14*, 1.
- [97] J. H. Oh, J. W. Park, *Org. Electron.* **2021**, *96*, 106252.
- [98] Y. Yasuda, S. ichi Kobayashi, T. Uchida, Y. Hoshi, *Thin Solid Films* **2020**, *698*, 137868.
- [99] Y. J. Lee, J. H. Kim, J. N. Jang, I. H. Yang, S. N. Kwon, M. P. Hong, D. C. Kim, K. S. Oh, S. J. Yoo, B. J. Lee, W. G. Jang, *Thin Solid Films* **2009**, *517*, 4019.
- [100] W. Wang, H. Peng, S. Chen, *J. Mater. Chem. C* **2016**, *4*, 1838.
- [101] J. Xu, A. Sandström, E. M. Lindh, W. Yang, S. Tang, L. Edman, *ACS Appl. Mater. Interfaces* **2018**, *10*, 33380.
- [102] E. Auroux, A. Sandström, C. Larsen, P. Lundberg, T. Wågberg, L. Edman, *Org. Electron.* **2020**, *84*, 105812.
- [103] G. Qian, Y. Lin, G. Wantz, A. R. Davis, K. R. Carter, J. J. Watkins, *Adv. Funct. Mater.* **2014**, *24*, 4484.
- [104] G. K. Dalapati, H. Sharma, A. Guchhait, N. Chakrabarty, P. Bamola, Q. Liu, G. Saianand, A. M. Sai Krishna, S. Mukhopadhyay, A. Dey, T. K. S. Wong, S. Zhuk, S. Ghosh, S. Chakraborty, C. Mahata, S. Biring, A. Kumar, C. S. Ribeiro, S. Ramakrishna, A. K. Chakraborty, S. Krishnamurthy, P. Sonar, M. Sharma, *J. Mater. Chem. A* **2021**, *9*, 16621.
- [105] M. N. Mullings, C. Hägglund, S. F. Bent, *J. Vac. Sci. Technol. A Vacuum, Surfaces, Film.* **2013**, *31*, 061503.
- [106] J. Heo, A. S. Hock, R. G. Gordon, *Chem. Mater.* **2010**, *22*, 4964.
- [107] D. Choi, J.-S. Park, *Surf. Coatings Technol.* **2014**, *259*, 238.

- [108] E. Bandiello, M. Sessolo, H. J. Bolink, *J. Mater. Chem. C* **2016**, *4*, 10781.
- [109] J.-H. Lee, M. Yoo, D. Kang, H.-M. Lee, W. Choi, J. W. Park, Y. Yi, H. Y. Kim, J.-S. Park, *ACS Appl. Mater. Interfaces* **2018**, *10*, 33335.
- [110] H. Kim, J. S. Horwitz, A. Piqué, C. M. Gilmore, D. B. Chrisey, *Appl. Phys. A Mater. Sci. Process.* **1999**, *69*, S447.
- [111] A. Khodorov, M. Piechowiak, M. J. M. Gomes, *Thin Solid Films* **2007**, *515*, 7829.
- [112] R. Liang, J. Dai, L. Xu, J. He, S. Wang, Y. Peng, H. Wang, L. Ye, C. Chen, *IEEE Trans. Electron Devices* **2018**, *65*, 2498.
- [113] J. Mei, M. S. Bradley, V. Bulović, *Phys. Rev. B* **2009**, *79*, 235205.
- [114] H. Wang, H. Yu, W. Xu, Z. Yuan, Z. Yan, C. Wang, X. Liu, M. Fahlman, J. M. Liu, X. K. Liu, F. Gao, *J. Mater. Chem. C* **2018**, *6*, 6996.
- [115] V.-H. Tran, H. Park, S. H. Eom, S. C. Yoon, S.-H. Lee, *ACS Omega* **2018**, *3*, 18398.
- [116] L. Yan, Q. Xue, M. Liu, Z. Zhu, J. Tian, Z. Li, Z. Chen, Z. Chen, H. Yan, H.-L. Yip, Y. Cao, *Adv. Mater.* **2018**, *30*, 1802509.
- [117] J. M. Caruge, J. E. Halpert, V. Wood, V. Bulović, M. G. Bawendi, *Nat. Photonics* **2008**, *2*, 247.
- [118] V. Wood, M. J. Panzer, J. E. Halpert, J.-M. Caruge, M. G. Bawendi, V. Bulović, *ACS Nano* **2009**, *3*, 3581.
- [119] C. Zhang, R. Liu, D. Zhang, L. Duan, *Adv. Funct. Mater.* **2020**, *30*, 1907156.
- [120] R. D. Costa, D. Tordera, E. Ortí, H. J. Bolink, J. Schönle, S. Graber, C. E. Housecroft, E. C. Constable, J. A. Zampese, *J. Mater. Chem.* **2011**, *21*, 16108.
- [121] S. Keller, E. C. Constable, C. E. Housecroft, M. Neuburger, A. Prescimone, G. Longo, A. Pertegás, M. Sessolo, H. J. Bolink, *Dalt. Trans.* **2014**, *43*, 16593.
- [122] D. G. Cuttell, S.-M. Kuang, P. E. Fanwick, D. R. McMillin, R. A. Walton, *J. Am. Chem. Soc.* **2002**, *124*, 6.
- [123] N. Armaroli, G. Accorsi, M. Holler, O. Moudam, J.-F. Nierengarten, Z. Zhou, R. T. Wegh, R. Welter, *Adv. Mater.* **2006**, *18*, 1313.
- [124] M. D. Weber, C. Garino, G. Volpi, E. Casamassa, M. Milanese, C. Barolo, R. D. Costa, *Dalt. Trans.* **2016**, *45*, 8984.
- [125] A. A. Yaroshevsky, *Geochemistry Int.* **2006**, *44*, 48.
- [126] F. Brunner, S. Graber, Y. Baumgartner, D. Häussinger, A. Prescimone, E. C. Constable, C. E. Housecroft, *Dalt. Trans.* **2017**, *46*, 6379.
- [127] F. Brunner, L. Martínez-Sarti, S. Keller, A. Pertegás, A. Prescimone, E. C. Constable, H. J. Bolink, C. E. Housecroft, *Dalt. Trans.* **2016**, *45*, 15180.
- [128] R. Czerwieniec, M. J. Leidl, H. H. H. Homeier, H. Yersin, *Coord. Chem. Rev.* **2016**, *325*,

2.

- [129] M. Y. Wong, E. Zysman-Colman, *Adv. Mater.* **2017**, *29*, 1605444.
- [130] Z. Li, W. Li, C. Keum, E. Archer, B. Zhao, A. M. Z. Slawin, W. Huang, M. C. Gather, I. D. W. Samuel, E. Zysman-Colman, *J. Phys. Chem. C* **2019**, *123*, 24772.
- [131] W. Lu, M. C. W. Chan, N. Zhu, C.-M. Che, C. Li, Z. Hui, *J. Am. Chem. Soc.* **2004**, *126*, 7639.
- [132] L. M. Cinninger, L. D. Bastatas, Y. Shen, B. J. Holliday, J. D. Slinker, *Dalt. Trans.* **2019**, *48*, 9684.
- [133] V. Sicilia, L. Arnal, A. J. Chueca, S. Fuertes, A. Babaei, A. M. Igual Muñoz, M. Sessolo, H. J. Bolink, *Inorg. Chem.* **2020**, *59*, 1145.
- [134] S. Fuertes, A. J. Chueca, A. Martín, V. Sicilia, *J. Organomet. Chem.* **2019**, *889*, 53.
- [135] V. Sicilia, S. Fuertes, A. J. Chueca, L. Arnal, A. Martín, M. Perálvarez, C. Botta, U. Giovanella, *J. Mater. Chem. C* **2019**, *7*, 4509.
- [136] S. Fuertes, A. J. Chueca, M. Perálvarez, P. Borja, M. Torrell, J. Carreras, V. Sicilia, *ACS Appl. Mater. Interfaces* **2016**, *8*, 16160.
- [137] S. Fuertes, A. J. Chueca, L. Arnal, A. Martín, U. Giovanella, C. Botta, V. Sicilia, *Inorg. Chem.* **2017**, *56*, 4829.
- [138] S. Stipurin, T. Strassner, *Inorg. Chem.* **2021**, *60*, 11200.
- [139] H. Leopold, M. Tenne, A. Tronnier, S. Metz, I. Münster, G. Wagenblast, T. Strassner, *Angew. Chemie* **2016**, *128*, 16011.
- [140] P. Pinter, J. Soellner, T. Strassner, *Organometallics* **2021**, *40*, 557.
- [141] P. Pinter, J. Soellner, T. Strassner, *Eur. J. Inorg. Chem.* **2021**, *2021*, 3104.
- [142] S. Fuertes, L. Mardegan, I. Martínez, S. Ventura, I. Ara, D. Tordera, H. J. Bolink, V. Sicilia, *J. Mater. Chem. C* **2022**, *10*, 15491.
- [143] M. Meyer, L. Mardegan, D. Tordera, A. Prescimone, M. Sessolo, H. J. Bolink, E. C. Constable, C. E. Housecroft, *Dalt. Trans.* **2021**, *50*, 17920.
- [144] S. Keller, A. Pertegás, G. Longo, L. Martínez, J. Cerdá, J. M. Junquera-Hernández, A. Prescimone, E. C. Constable, C. E. Housecroft, E. Ortí, H. J. Bolink, *J. Mater. Chem. C* **2016**, *4*, 3857.
- [145] N. Arnosti, F. Brunner, I. Susic, S. Keller, J. M. Junquera-Hernández, A. Prescimone, H. J. Bolink, M. Sessolo, E. Ortí, C. E. Housecroft, E. C. Constable, *Adv. Opt. Mater.* **2020**, *8*, 1901689.
- [146] D. Tordera, J. Frey, D. Vonlanthen, E. Constable, A. Pertegás, E. Ortí, H. J. Bolink, E. Baranoff, M. K. Nazeeruddin, *Adv. Energy Mater.* **2013**, *3*, 1338.
- [147] W. Zhao, C.-Y. Liu, Q. Wang, J. M. White, A. J. Bard, *Chem. Mater.* **2005**, *17*, 6403.

- [148] Y. Cao, Q. Pei, M. R. Andersson, G. Yu, A. J. Heeger, *J. Electrochem. Soc.* **1997**, *144*, L317.
- [149] L. Edman, B. Liu, M. Vehse, J. Swensen, G. C. Bazan, A. J. Heeger, *J. Appl. Phys.* **2005**, *98*, 044502.
- [150] M. D. Weber, E. Fresta, M. Elie, M. E. Miehlich, J.-L. Renaud, K. Meyer, S. Gaillard, R. D. Costa, *Adv. Funct. Mater.* **2018**, *28*, 1707423.
- [151] H. J. Bolink, L. Cappelli, S. Cheylan, E. Coronado, R. D. Costa, N. Lardiés, M. K. Nazeeruddin, E. Ortí, *J. Mater. Chem.* **2007**, *17*, 5032.
- [152] J. D. Slinker, J. A. DeFranco, M. J. Jaquith, W. R. Silveira, Y.-W. Zhong, J. M. Moran-Mirabal, H. G. Craighead, H. D. Abruña, J. A. Marohn, G. G. Malliaras, *Nat. Mater.* **2007**, *6*, 894.
- [153] E. Fresta, G. Volpi, M. Milanesio, C. Garino, C. Barolo, R. D. Costa, *Inorg. Chem.* **2018**, *57*, 10469.

## Acknowledgments

I'll be honest, this is one of the hardest parts to write for me but I will do my best to express in words what I feel.

Some of you might know that the way I initially found this Ph.D. program and arrived in Valencia was kind of accidental, and at first, I would have never imagined anything that meant this experience. It has been a time of growth both as a person and as a scientist, I have been lucky enough to meet many people of different backgrounds, and cultures, to learn from the experience of others and visit incredible places. I am thankful to all of those who made my time during these years.

I wanted first to thank my parents for your sacrifices and always supporting me, although it means seeing each other only a few days a year.

Secondly, to my supervisors Henk and Dani. Henk, I'm grateful for the opportunities and time you dedicated to me; I first arrived not knowing what it meant to be part of a research group but the environment you created could not be better to learn science and work in a team. Dani, thank you for your precious advices and always positive mood, albeit my attraction to side experiments you could always keep me on track. The attention that you guys devote to the students, their needs, and projects is unique and make this process better in a way that hardly finds equals.

A huge, enormous, thanks to Jorge Ferrando. After all these years I still don't know if he is a LabView robot or "just" a very good engineer.

To my group, older and newer members that I met along this period, maybe my serious-looking face didn't show it enough but thank you all, for the time we spent together in and out of work. Being a Ph.D. student is not easy, sometimes it can be frustrating, exhausting, and a bit rough in the lab. but you guys were always smiling to me. A big big thank you for sharing your knowledge and happy moments with me.

To the Kaust group and Professor Stefaan de Wolf, I wanted to express my gratitude for having me as visiting student. It surely was an enriching time, I had a lot of fun and I learned a lot.

Finally, to Abhi, Cris, Renato and Isi; you deserve much more than just a line but I just wanted to let you know that you guys are the best and thank you for being always there.

## 9. Appendix

## 9.1 Index of Figures

Figure 1. Market trend of different lighting technologies with particular emphasis on LEDs and their expected progression until 2030. (Source: International Energy Agency)

Figure 2. a) and b) respectively show the stacked architecture of a LED and its energy band diagram, while c) and d) the stacked architecture of an OLED and the energy levels for each layer.

Figure 3. Single active layer sandwiched between two low work-function electrodes as archetypical LEC architecture.

Figure 4. Simplified diagrams of the a) electrodynamical model and b) electrochemical model.

Figure 5. Electrostatic potential and light-emission profiles in planar LECs during operation and voltage dependence on the interfacial potential drop. Typical steady-state potential profiles of an LEC during operation at  $V = 8 \text{ V}$  in a), the noninjection-limited and b), the injection-limited regime. The pictures behind the graphs are UV/PL images in steady state, on the same horizontal scale. Figure taken from ref. 9.

Figure 6. Temporal evolution of a LEC under pulsed current bias. When the time is expressed in logarithmic scale it is possible to observe each phase of the device lifetime.

Figure 7. List of light-emitting materials used as active materials in LECs in this Thesis.

Figure 8. Schematic representation of the device architectures presented in this Thesis.

Figure 9. Simplified schematic illustration of an ALD cycle: first half cycle (metal precursor injection) and second half cycle (oxidizer precursor injection).

Figure 10. Simplified schematic illustration of a PLD cycle.

Figure 11. Experimental setup that allowed us to measure the PL of a pixel under an electrical bias.

Figure 12. Typical temporal evolution of a LEC under a pulsed current bias.

Figure 13. Commission Internationale de l'Eclairage coordinates (CIE coordinates) diagram that links the wavelengths of the visible spectra with the physiologically perceived colors in human vision.

Figure 14. Scheme of the final device architecture and chemical structure of the components of the active layer: the ion dissolving hyperbranched polymer (Hybrane), the lithium trifluoromethanesulfonate salt and the semiconducting polymer Super Yellow (SY).

Figure 15. AFM images ( $5\ \mu\text{m} \times 5\ \mu\text{m}$ ) of a) pristine SY and b) SY + 30 % Hybrane + 9% LiTf coated on glass/ITO substrates. c) Photoluminescence spectra of SY and SY mixed with Hybrane, Hybrane+LiTf and LiTf only.

Figure 16. a) Luminance and b) driving voltage of the LECs driven at a constant current density of  $75\ \text{A m}^{-2}$ . Time is expressed in the log scale.

Figure 17. Performance of the 1:0.3:0.09 SY/Hybrane/LiTf ratio devices under an average pulsed current density of  $50/75/100\ \text{A m}^{-2}$ . a) Luminance b) Avg. Voltage c) Current efficiency. Luminance is expressed in the log scale.

Figure 18. a) Photoluminescence (PL) and electroluminescence (EL) evolution in the first 4 minutes of device operation at  $50\ \text{A m}^{-2}$ . b) Normalized PL intensity, LEC devices biased with a constant current density of  $25/50/100/200/500\ \text{A m}^{-2}$ . The cells driven at  $25$  and  $500\ \text{A m}^{-2}$  were left to recover overnight for about 20 hours and measured again. Both measures were taken under a  $500\ \text{nm}$  light probe.

Figure 19. XPS survey of  $\text{SnO}_2$  thin film on glass/ITO substrate.

Figure 20. AFM images of a) glass/ITO/PEDOT:PSS/Ir, b) glass/ITO/PEDOT:PSS/Ir/ $\text{SnO}_2$ , c) glass/ITO/PEDOT:PSS/Ir/ITO and d) glass/ITO/PEDOT:PSS/Ir/ $\text{SnO}_2$ /ITO. They show a mean roughness of  $0.6\ \text{nm}$ ,  $0.6\ \text{nm}$ ,  $1\ \text{nm}$ , and  $1.3\ \text{nm}$ , respectively.

Figure 21. a) Absorbance and b) transmittance of the samples, before and after the  $\text{SnO}_2$  and ITO layers deposition, as well as the absorbance of  $20\ \text{nm}$   $\text{SnO}_2$  deposited by ALD and the absorption of  $140\ \text{nm}$  of ITO deposited by PLD on a glass substrate. c) Absorbance and d) transmittance of the same samples using a glass/ITO reference sample. The measurements were corrected for the absorption of the glass substrate.

Figure 22. a) Architecture of the semitransparent devices, b) Chemical structure of the yellow Ir(III) emitter  $[\text{Ir}(\text{ppy})_2(\text{dtb-bpy})][\text{PF}_6]$  used in this work, OFF states of the c) reference and e) semitransparent devices and ON states of the d) reference and f) semitransparent devices.

Figure 23. a) Electroluminescence of the standard Al-cathode and semitransparent devices, b) luminance and voltage over time of the standard Al-cathode device at an avg. current of  $50\ \text{A m}^{-2}$ , c) and d) luminance and voltage over time of the top and bottom sides of the transparent device driven at avg. current of  $50\ \text{A m}^{-2}$ .

Figure 24. Normalized photocurrent from BOTTOM and UP side of a semitransparent device with the stack glass/ITO/PEDOT:PSS ( $80\ \text{nm}$ )/  $[\text{Ir}(\text{ppy})_2(\text{dtb-bpy})][\text{PF}_6]:[\text{BMIM}][\text{PF}_6]$  (1:0.25) ( $80\ \text{nm}$ )/ $\text{SnO}_2$  ( $20\ \text{nm}$ )/ITO ( $140\ \text{nm}$ ). The photocurrent was simultaneously measured for 45 hours. a) Until 2 hours, shows the difference in turn-on time between the BOTTOM and TOP side, which are 6 and 4 minutes respectively, and b) shows the complete measure and the difference in  $t_{50}$  between the BOTTOM and TOP side, which are  $\sim 30$  and  $\sim 6.5$  hours.



Figure 25. Photoluminescence from the a) BOTTOM side and b) TOP side obtained with an excitation wavelength of 340 nm of the iTMC film and with different metal oxide layers deposited on top of it (see legend).

Figure 26: Chemical structure of the Cu(I) and Pt(II) complexes studied in this Chapter.

Figure 27. Normalized thin-film photoluminescence spectra of the  $[\text{Cu}(\text{xantphos})(\text{Me}_2\text{bpy})]^+$  complexes with different counterions.

Figure 28. a) Normalized electroluminescence spectra of the two best performing complexes  $[\text{Cu}(\text{xantphos})(\text{Me}_2\text{bpy})][\text{PF}_6]$  (Cu1) and  $[\text{Cu}(\text{xantphos})(\text{Me}_2\text{bpy})][\text{BF}_4]$  (Cu2). b) luminance values and c) current efficiency and d) voltage of Cu1 and Cu2 LECs driven at an average current density of  $50 \text{ A m}^{-2}$  with different IL counterions.

Figure 29. Photoluminescence of Pt7, Pt8 and Pt9 in ACN and DCM.

Figure 30: Time-dependence of the luminance  $[\text{cd/m}^2]$  and average voltage  $[\text{V}]$  of LECs ITO/PEDOT:PSS/iTMC:IL(4:1)/Al, where iTMC are emitters Pt7 (black curve), Pt8 (red curve) and Pt9 (blue curve) in a)-b) ACN and c)-d) DCM. All the devices shown were driven with a pulsed current with an average current density of  $50 \text{ A m}^{-2}$ .

Figure 31: Time-dependence of the luminance  $[\text{cd/m}^2]$  and average voltage  $[\text{V}]$  of LECs ITO/PEDOT:PSS/iTMC:IL(4:1)/Al, where the iTMC is Pt7. the devices shown were driven with a pulsed current with an average current density of 25 and  $12.5 \text{ A m}^{-2}$ .

Figure 32. a) Time-dependence of the luminance of a LEC device ITO/PEDOT:PSS/Pt7:IL(4:1)/Al in ACN with a longer annealing time (4 h) at the same temperature ( $70^\circ\text{C}$ ). b) Time-dependence of the luminance of a LEC device ITO/PEDOT:PSS/Pt9:IL(4:1)/Al in ACN with a higher temperature annealing process ( $90^\circ\text{C}$ ) at a longer time (1 h).

Figure 33. AFM images ( $2 \mu\text{m} \times 2 \mu\text{m}$ ) of the active film using emitter Pt7 processed from a) ACN and b) DCM.

Figure 34: Normalized electroluminescence spectra of LEC devices ITO/PEDOT:PSS/iTMC:IL(4:1)/Al, where iTMC are emitters Pt7 (black curve), Pt8 (red curve) and Pt9 (blue curve) from a) ACN and b) DCM.

## 9.2 Index of Tables

Table 1. Main performances of LECs under a constant current bias of  $75 \text{ A m}^{-2}$ .

Table 2. Main performance parameters of representative LECs under pulsed current average bias of  $50/75/100 \text{ A m}^{-2}$ .

Table 3. Figures of merit of the standard and transparent (T) cells driven at 50 A m<sup>-2</sup> average bias current.

Table 4. Photoluminescence properties of thin films of the [Cu(xantphos)(Me<sub>2</sub>bpy)]<sup>+</sup> complexes.

Table 5. Performance of LECs with the [Cu(xantphos)(Me<sub>2</sub>bpy)]<sup>+</sup> series in the active layer; cell architecture ITO/PEDOT:PSS/[Cu(xantphos)(Me<sub>2</sub>bpy)][A]:[EMIM][A] (4:1 molar ratio)/Al. LECs were measured using a pulsed current driving (average current density 50 A m<sup>-2</sup>, 1 kHz, 50% duty cycle, block wave).

Table 6. Figures of merits of the devices obtained from Pt7, Pt8 and Pt9 in ACN and DCM.

Table 7. Calculated EQE from EL spectra and PLQY values of the thin films.

## 9.3 Index of Abbreviations

In order of appearance:

LED	Light-Emitting Diode
IEA	International Energy Agency
NZE	Net Zero Scenario
EL	Electroluminescence
OLED	Organic Light-Emitting Diode
iTMC	ionic Transition Metal Complex
CB	Conduction Band
HOMO	Highest Occupied Molecular Orbital
VB	Valence Band
LUMO	Lowest Unoccupied Molecular Orbital
WF	Work Function
LEC	Light-Emitting Electrochemical Cell
CP	Conductive Polymer
EDL	Electronic Double Layer
SM	Small Molecule
PEO	Polyethylene Oxide
TMPE	Trimethylpropane Ethoxylate
EQE	External Quantum Efficiency
TADF	Thermally Activated Delayed Fluorescence
TTA	Triplet-Triplet Annihilation
HLCT	Hybridized Local Charge Transfer
IL	Ionic Liquid
PLQY	Photoluminescence Quantum Yield
TPQ	Triplet-Polaron Quenching
ALD	Atomic Layer Deposition
PLD	Pulsed Laser Deposition
SY	Super Yellow
PEDOT.PSS	Poly(3,4-ethylenedioxythiophene) polystyrene sulfonate

ACN	Acetonitrile
DCM	Dichloromethane
CHN	Cyclohexanone
ETL	Electron Transport Layer
TCO	Transparent Conductive Oxide
ITO	Indium Tin Oxide
PL	Photoluminescence
Lum	Luminescence
$t_{50}$	Time at which half of the maximum luminance is reached
$t_{on}$	Turn-on time
CE	Current Efficiency
PE	Power Efficiency
CIE	Commission Internationale de l'Éclairage
PTMC	Polytrimethylene Carbonate
AFM	Atomic Force Microscopy
$R_s$	Sheet Resistance
QD-LED	Quantum Dot-LED
TDAT	Tetrakis(diethylamino) tin
XPS	X-ray Photoelectron Spectroscopy
BMIM PF <sub>6</sub>	1-Butyl-3-methylimidazolium Hexafluorophosphate
SSL	Solid State Lighting
POP	Oxydi(2,1-phenylene)]bis(diphenylphosphane)
Xantphos	9,9-dimethyl-9H-xanthene-4,5-diyl)(bis(diphenylphosphane)
Bpy	2,2'-bipyridine
Phen	1,10-phenanthroline
IQE	Internal Quantum Yield
Me <sub>2</sub> bpy	6,6'-Dimethyl-2,2'-bipyridine
NHC	N-heterocyclic carbene
Cbz	Carbazole
Py	Pyridine
MLCT	Metal to Ligand Charge Transfer
LLCT	Ligand to Ligand Charge Transfer
ILCT	Intra-Ligand Charge Transfer
LMCT	Ligand to Metal Charge Transfer
PMMA	Poly(methylmethacrylate)
EMIM	1-Ethyl-3-methylimidazolium
DCE	Dichloroethane
NMR	Nuclear Magnetic Resonance

## 9.4 Author Contributions to this Thesis

Article 1. *Stable Light-Emitting Electrochemical Cells Using Hyperbranched Polymer Electrolyte.* Advanced Functional Materials, **2021**, 31, 2104249.

Article 2. *Transparent Light-Emitting Electrochemical Cells.* Advanced Optical Materials, **2022**, 2201953.

Article 3. *A counterion study of a series of [Cu(P<sup>^</sup>P)(N<sup>^</sup>N)]/[A] compounds with bis(phosphane) and 6-methyl and 6,6'-dimethyl-substituted 2,2'-bipyridine ligands for light-emitting electrochemical cells.* Dalton Transactions, **2021**, 50, 17920.

Article 4. *Green light-emitting electrochemical cells based on platinum(II) complexes with a carbazole-appended carbene ligand.* Journal of Materials Chemistry C, **2022**, 10, 15491.

## 9.5 Other Contributions during this Thesis

Article 5. *Tunable luminescent lead bromide complexes.* Journal of Materials Chemistry C, **2020**, 8, 15996.

Article 6. *Polymer-Based Composites for Engineering Organic Memristive Devices.* Advanced Electronic Materials, **2022**, 2101192.

Article 7. *Ionic multiresonant thermally activated delayed fluorescence emitters for light emitting electrochemical cells.* Belstein Journal of Organic Chemistry, **2022**, 18, 1311-1321.

Article 8. *Efficient Semitransparent Perovskite Solar Cells Based on Thin Compact vacuum Deposited CH<sub>3</sub>NH<sub>3</sub>PbI<sub>3</sub> Films.* Advanced Materials Interfaces, **2022**, 9, 2201222.

Article 9. *Dimensionality Controls Anion Intermixing in Electroluminescent Perovskite Heterojunction.* ACS Photonics, **2022**, 9, 2483-2488.

## RESEARCH ARTICLE

## Stable Light-Emitting Electrochemical Cells Using Hyperbranched Polymer Electrolyte

Lorenzo Mardegan, Chris Dreessen, Michele Sessolo, Daniel Tordera, and Henk J. Bolink\*

The choice of an adequate electrolyte is a fundamental aspect in polymer light-emitting electrochemical cells (PLECs) as it provides the in situ electrochemical doping and influences the performance of these devices. In this study, a hyperbranched polymer (Hybrane DEO750 8500) blended with a Li salt is used as a novel electrolyte in state-of-the-art Super Yellow (a polyphenylenevinylene) based LECs. Due to the desirable properties of the hyperbranched polymer and the homogeneous and smooth films that it forms with the emitting polymer, PLEC with excellent electroluminescent properties are obtained using a pulsed current bias scheme. The devices are very stable, with lifetimes in excess of 2000 h with initial luminance values above  $450 \text{ cd m}^{-2}$ , a peak efficiency of  $12.6 \text{ lm W}^{-1}$ , and sub-minute turn-on times. The stability of the devices is also studied by measuring the photoluminescence (PL) of the semiconductor during electroluminescent operation. The findings suggest that it is possible to observe the quenching of the PL in vertically stacked devices due to the advancement of the doped fronts in the film and an immediate PL recovery when the bias is removed.


encapsulation to prevent degradation of the air-sensitive electrodes, and their processing consists of a large number of steps, most of which have to be done by evaporation techniques. In contrast to OLEDs, light-emitting electrochemical cells (LECs) have a much simpler layout consisting of an intimate blend of an electrolyte, that provides mobile ions, and a semiconducting electroluminescent material as the active layer, processed via solution techniques and sandwiched between two air-stable electrodes. LECs unique operation mechanism is based on the presence of both electronic and ionic conductors.<sup>[2]</sup> Upon the application of a bias the ions redistribute within the active layer allowing efficient electronic charge carrier injection at the electrodes, transport, and recombination.<sup>[2-7]</sup> Hence, the electrolyte plays a key role in determining the overall performance of LECs.

## 1. Introduction

Organic light-emitting diodes (OLEDs) are currently one of the preferred technologies for display applications in consumer electronics such as smartphones and TV screens. Their high image quality (e.g., contrast ratio and viewing angle), good power efficiency (PE), and fast response time, combined with the possibility to use lightweight and flexible plastic substrates make them an attractive solution for high-end products.<sup>[1]</sup> However, their fabrication costs limit their entry into the general lighting market where low-cost is a key parameter to compete with the existing lighting technologies. OLEDs are devices based on multilayer architectures that require a rigorous

The electroluminescent material can either be a conjugated polymer (CP),<sup>[2,8,9]</sup> a conjugated small molecule (SM),<sup>[10-14]</sup> or a transition metal complex (iTMC).<sup>[15-18]</sup> In LECs where the light-emitting material is a conjugated polymer (PLECs) one way to add ionic conductors is by using a polymer electrolyte which consists of a salt and a coordinating polymer that dissolves and coordinates the ions thanks to its electron donor centers.<sup>[19]</sup> LECs based on fluorescent CPs are attractive for their ease of processability, lower costs, and great compatibility with flexible substrates. However, CPs are limited as they can only harvest singlets which make them intrinsically less efficient than phosphorescent iTMCs that can harvest both singlets and triplets.<sup>[20]</sup> Improving the performance, in particular the stability, of LECs is challenging as the mechanism responsible for facile charge injection with air-stable electrodes also leads to an increased quenching of excited states over time, and thus to a decrease of the luminance levels.<sup>[4,21]</sup> Charge injection is facilitated by the build-up of ions at the electrode interfaces through an increase in the effective electric field. Upon electron injection at the cathode the uncompensated cations redistribute and stabilize the reduced segments on the CP chain. At the anode, the same occurs by uncompensated anions and oxidized segments on the CP. These interactions between electronic and ionic charges are generally referred to as doping, as it increases the effective charge density in the system, and as such increases the conductivity. However, as there is no physical separation between the area of exciton generation and the doped regions, part of the excitons are quenched due to the interaction with

L. Mardegan, C. Dreessen, M. Sessolo, D. Tordera, H. J. Bolink  
Instituto de Ciencia Molecular (ICMol)  
Universidad de Valencia  
C/Catedrático J. Beltrán 2 Paterna, Valencia 46980, Spain  
E-mail: henk.bolink@uv.es

 The ORCID identification number(s) for the author(s) of this article can be found under <https://doi.org/10.1002/adfm.202104249>.

© 2021 The Authors. Advanced Functional Materials published by Wiley-VCH GmbH. This is an open access article under the terms of the Creative Commons Attribution-NonCommercial-NoDerivs License, which permits use and distribution in any medium, provided the original work is properly cited, the use is non-commercial and no modifications or adaptations are made.

DOI: 10.1002/adfm.202104249

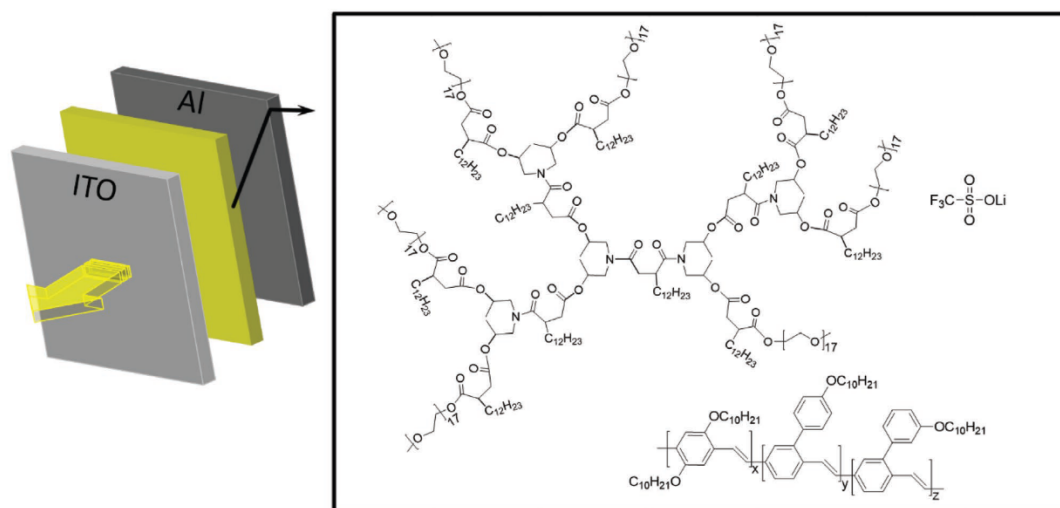


**Figure 1.** Scheme of the final device architecture and chemical structure of the components of the active layer: the ion dissolving hyperbranched polymer (Hybrane), the lithium trifluoromethanesulfonate salt, and the semiconducting polymer SY.

the radical cations and anions present in the doped regions.<sup>[6]</sup> Hence, to improve the performance of LECs one must be able to prevent as much as possible the interaction between the doped regions and the active intrinsic region where the excitons are generated. As doping leads to quenching of excitons, photoluminescence (PL) has been used in the past to probe the growth of the doped zones. This is difficult to do in operating devices, as it is not trivial to distinguish between electrically and photo-excited states. Recently, promising results have been attained on devices using Super Yellow (SY), a PPV-based CP, as active material and branched poly(trimethylene carbonate) (PTMC) electrolytes derivatives showing long operational lifetimes of 138 h at  $>300 \text{ cd m}^{-2}$  and a peak PE of  $9.8 \text{ lm W}^{-1}$  at a constant current density driving bias of  $77 \text{ A m}^{-2}$ .<sup>[22]</sup> Previous works including SY and a star-branched trimethylolpropane ethoxylate (TMPE) derivatives as ion transporter showed exceptional lifetimes longer than 1200 h over  $100 \text{ cd m}^{-2}$  and maximum PEs of  $18.1 \text{ lm W}^{-1}$ .<sup>[23,24]</sup> In this work, we develop LECs based on the archetype polyphenylenevinylene (PPV) CP SY and lithium trifluoromethanesulfonate ( $\text{LiCF}_3\text{SO}_3$ , LiTf) salt, combined with a novel hyperbranched ion solvating polymer, Hybrane DEO750 8500 (Hy) (Figure 1). The devices show an extrapolated  $t_{50}$  of 2000 h (at an initial luminance above  $480 \text{ cd m}^{-2}$ ) and peak power efficiencies of  $12.6 \text{ lm W}^{-1}$  with sub-minute turn-on times. These lifetime values are amongst the highest reported in the literature for fluorescent LECs. In an attempt to understand the effect of the doped zones formation on the stability we employ frequency-modulated PL probing during steady-state electroluminescence (EL) operation under a forward bias. This allows us to probe the evolution of the PL as a function of driving conditions in operating LECs. Our results suggest that this method could be employed to model how the free ions interact with the polymer matrix in the different stages of operation of a LEC.

## 2. Results and Discussion

Motivated by the recent advancements in the polymer electrolyte design for LECs we decided to introduce a hyperbranched polymer, Hybrane DEO750 8500, as ion-dissolving and transporting media. To successfully act as a host for free mobile ions, a polymer should have the following characteristics: 1) electron-donor groups or atoms able to coordinate cations; 2) high chain mobility and 3) suitable distance between the coordinating centers.<sup>[21,25,26]</sup> The Hybrane (Figure 1) displays promising structural features for PLECs applications. At room temperature, the Hybrane is a dense liquid and its backbone structure is constituted of ester and amide groups whereas the chains end with ethyleneoxide units that are methoxy-terminated. In previous works, the ability of ester groups to coordinate and transport metal cations in PLECs has been shown.<sup>[22,27,28]</sup> Furthermore, a recent study showed that the methoxy ( $-\text{OCH}_3$ ) terminal groups provide an enhanced mobility of the cations.<sup>[29]</sup> The anions, on the other hand, are less restricted by the polymeric host as the host is only able to coordinate the cations,<sup>[29,30]</sup> consequently they can move faster within the medium. As a result, the p-type doping in LECs is generally faster than the n-type doping. To ensure optimal device performance, thin films should consist of a homogeneous blend between the polymer electrolyte and the semiconducting polymer.<sup>[31]</sup> When an optimum blend is provided one expects the most favorable salt dispersion over the active area and the most advantageous ion exchange between the ion dissolving polymer and the CP. As stated above, the presence of oxygen coordinating groups mainly helps in the solvation and coordination of the cations, however, the presence of long carbon chains ( $-\text{C}_{12}\text{H}_{23}$ ) supports blending with the non-polar SY. Thus, its structure could result in a suitable option for a variety of semiconducting polymers.

The interaction between the two components has been investigated in the presence and absence of the lithium salt.

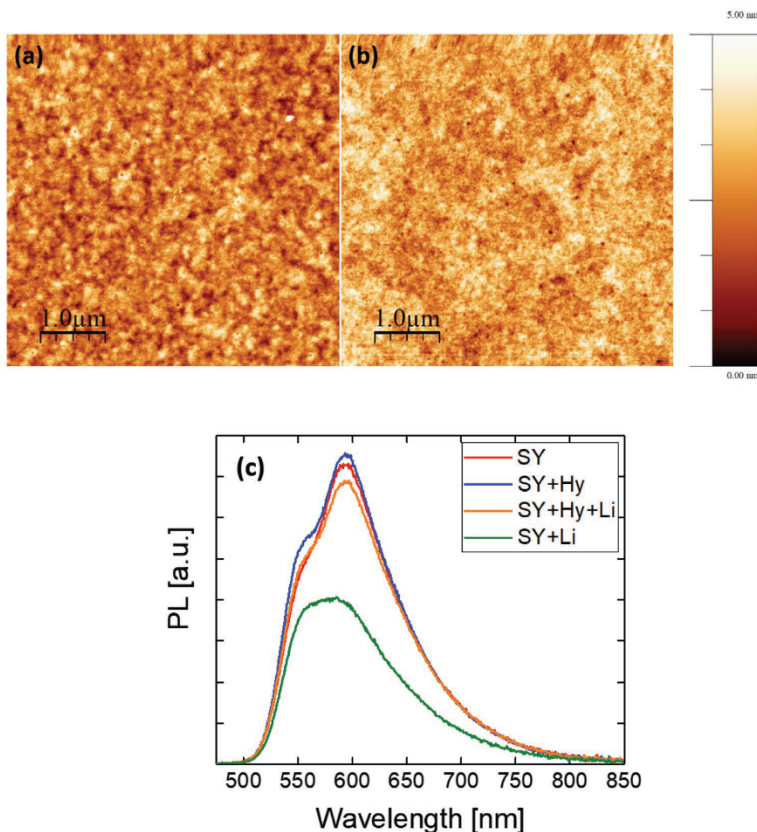


**Figure 2.** AFM images ( $5 \mu\text{m} \times 5 \mu\text{m}$ ) of a) pristine SY and b) SY + 30 % Hybrane + 9 % LiTf coated on glass/ITO substrates. c) PL spectra of SY and SY mixed with Hybrane, Hybrane+LiTf, and LiTf only.

Atomic Force Microscopy (AFM) has been used to establish whether the spin-casted solutions resulted in homogeneous thin films. In **Figure 2a,b** AFM images of pristine SY and blended SY+Hybrane+LiTf samples, deposited on a glass/ITO substrate, are shown, respectively. Details on the preparation of the samples are given in the Experimental Section. The AFM images reveal that both the pristine and blended films are very flat with an average roughness of 0.50 nm and an average height of 2.42 nm for SY (**Figure 2a**) and 0.43 and 2.97 nm for SY+ Hybrane+LiTf (1:0.3:0.09 mass ratio, **Figure 2b**). The measured values are in line with recent literature data regarding pristine SY and SY+polymer electrolyte films.<sup>[22,32]</sup> As a result, both the pristine SY and the blend show very similar surface features indicating that the mixed-polymer matrix appears in an amorphous state and that there is no sign of undesirable phase separation.

Subsequently, we determined the photoluminescence quantum yield (PLQY) of samples consisting of SY with and without Hybrane and the LiTf salt, deposited on a quartz substrate from a cyclohexanone solution. The maximum PLQYs

obtained are 75%, 78%, 73%, and 45% for the SY, SY+ Hybrane, SY+Hybrane+LiTf, and SY+LiTf samples, respectively (**Figure 2c**). The PL spectra were obtained using an excitation wavelength of 430 nm. From these results it can be observed that the addition of solely the LiTf salt (SY+LiTf sample) decreases dramatically the PLQY, when compared to the pristine SY polymer. We ascribe this decrease of PLQY as a result of the quenching of the excitons by the LiTf salt. This is in line with previous reports where it was found that additives, in particular ionic species, can act as interceptors of excitons through the generation of CT non-emissive states and energy transfer processes and thus affect the PLQY.<sup>[33–35]</sup> However, the addition of Hybrane recovers the PLQY of the sample, as it introduces coordinating sites for the salt. Finally, the SY+Hybrane sample does not show any quenching, as expected. In fact, the PLQY increases slightly compared to the pure SY sample up to 78% due to a slight dilution of the SY which reduces the excitons to migrate and encounter quenching sites. The Hybrane could in this case weaken the close packing of the SY chains and hence decrease the degree of  $\pi$ -interactions.<sup>[36]</sup>

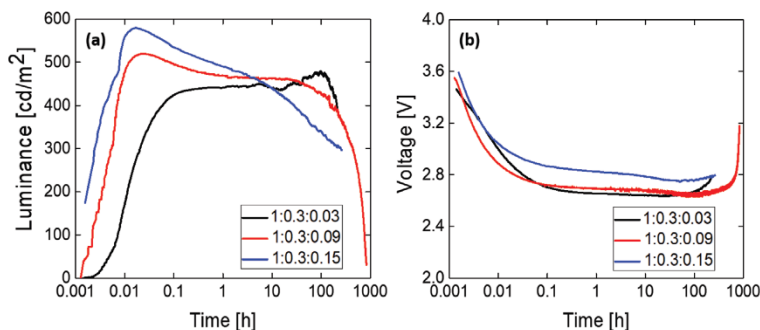


**Figure 3.** a) Luminance and b) driving voltage of the LECs driven at a constant current density of  $75 \text{ A m}^{-2}$ . Time is expressed in the log scale.

Devices with three different LiTf concentrations (3%, 9%, and 15%) and fixed Hybrane concentration (30%) were fabricated by sandwiching the SY and Hybrane:LiTf salt blend in between ITO coated glass plates and Al cathodes, and driven with a constant current. A mass ratio of 0.3:0.09 with respect to SY was then selected and driven with a pulsed current bias.

Device luminance and voltage were measured over time under a  $75 \text{ A m}^{-2}$  constant current density for the different SY:Hybrane:LiCF<sub>3</sub>SO<sub>3</sub> ratios (**Figure 3**). Over the reported time of 1000 h, it is possible to identify the typical transient states of a LEC. During the turn-on phase the applied voltage decreases. This is the phase where the EDLs are assembling at the interfaces.<sup>[37]</sup> We notice indeed that in the first instants of operation the voltage decreases as the luminance rises. The starting voltage value for the three devices is around 3.6 V and the turn-on time at  $100 \text{ cd m}^{-2}$  is faster at higher salt concentrations, with values of 25.2, 7.2, and 3.6 s for 3%, 9%, and 15% of LiTf, respectively. However, a similar effect on the voltage curves is not directly observed as it decreases in the same manner independently from the LiTf amount. In fact, after the EDL is formed, generating an ohmic contact, the remaining ionic species will be used to compensate the charge carriers that start to electrochemically dope the CP.

As a result, the luminance keeps increasing and the voltage decreasing until a maximum and a minimum are respectively reached. The maximum luminance values 442, 520, and  $580 \text{ cd m}^{-2}$  are proportional to the increase of salt content. This could be explained by the fact that, for this system, the amount of LiTf (at least up to 15%) can lead to brighter devices before the doping levels become too severe causing undesired exciton quenching.<sup>[38]</sup> At the steady-state, the voltage keeps a constant value of around 2.7 V for the 3% and 9% LiTf salt concentration devices and a slightly higher value of 2.9 V for the 15% device. The current efficiency (CE) and PE increase from  $5.9 \text{ cd A}^{-1}$  and  $6.9 \text{ lm W}^{-1}$  for 3% of LiTf to  $7.7 \text{ cd A}^{-1}$  and  $8.4 \text{ lm W}^{-1}$  for the device with 15% of LiTf content, as the voltage values are rather similar and the luminance increases along the device series. One of the most important features of light-emitting devices is their lifetime. There are several ways to express this, but mostly it is expressed as the time it takes to reach 50% of the initial luminance value, referred to as  $t_{50}$ . In OLEDs and inorganic LEDs, the initial luminance is easily adjusted by changing the

current density applied. In LECs, however, the initial luminance depends on a number of other parameters and therefore, its lifetime is expressed in more than one manner. Some state the overall luminance that is emitted over its lifetime, this is particularly important for slow starting LECs. Others, use the time it takes to reach a fixed luminance value. In this work, we will report the lifetime using the most commonly used method in LEDs, the time it takes to reach 50% of the initial luminance value. As LECs turn-on relatively fast it allows us to use the maximum luminance as the initial luminance value. Devices with 9% LiTf salt concentration show a measured  $t_{50}$  of 530 h whereas the devices that have a LiTf salt concentration of 15% have a reduced lifetime of about 350 h (estimated value). It is not easy to estimate  $t_{50}$  for the 1:0.3:0.03 mass ratio but we assume it to be within the interval between 400 and 500 h. We think the so-far best-reported stabilities ( $t_{50}$  lifetime) for an SY containing PLEC are 120 h driven by a constant current of  $77 \text{ A m}^{-2}$ .<sup>[22]</sup> This is lower than the  $t_{50}$  lifetime values we observe under  $75 \text{ A m}^{-2}$ , namely 530 h (for the 1:0.3:0.09 ratio device). It is worth mentioning that impressive lifetimes over 1000 h and  $100 \text{ cd m}^{-2}$  were also obtained from SY-LECs pre-biased at a constant current density of  $77 \text{ A m}^{-2}$  and then driven at  $19 \text{ A m}^{-2}$ .<sup>[23,24]</sup> It is, however, not straightforward to compare these data directly, as the previously reported devices showed higher maximum luminances and overall increased efficiency. Comparing the lifetime of devices that show different maximum luminances is not a trivial task, as there is a relation between both figures-of-merit and the exact driving conditions might be different. However, these results show that the use of the hyperbranched polymer leads to improvements in the stability of LEC devices. **Table 1** summarizes the principal performances of the above-described devices. Consequently, in order to improve the device performance, we selected the 1:0.3:0.09 ratio as it showed overall better performances when compared to 1:0.3:0.03 and 1:0.3:0.15 ratios.

Devices were prepared with the selected 1:0.3:0.09 active layer ratio and driven under pulsed current biases of  $50/75/100 \text{ A m}^{-2}$ . The applied pulsed current consisted of block waves at a frequency of 1000 Hz with a duty cycle of 50%. The benefits of a lower current density combined with a pulsed driving current have been demonstrated in previous works and consist in improved stabilities and efficiencies due to the



**Table 1.** Main performances of LECs under a constant current bias of  $75 \text{ A m}^{-2}$ .

SY:Hybrane:LiCF <sub>3</sub> SO <sub>3</sub> ratio	Max Lum. [ $\text{cd m}^{-2}$ ]	$t_{50}$ [h]	Peak CE [ $\text{cd A}^{-1}$ ]	Peak PE [ $\text{lm W}^{-1}$ ]
1:0.3:0.03	442	≈ 400–500	5.9	6.9
1:0.3:0.09	520	530	6.9	7.8
1:0.3:0.15	580	≈ 350	7.7	8.4

presence of “off-states” that limit the growth of the doped zones and side reactions.<sup>[39–41]</sup> Under pulsed driving conditions the device's performance improves dramatically with respect to the constant current driving (Figure 4). Comparing the lifetime data recorded at the same current density it is possible to notice a threefold increase when a pulsed bias is applied. The most important performance parameters of the devices are highlighted in Table 2. Peak luminances of 900 and  $745 \text{ cd m}^{-2}$  are reached with average current densities of 100 and  $75 \text{ A m}^{-2}$ , respectively. The  $t_{50}$  for these rather high initial luminance values are impressive with 850 and about 1000 h. When comparing the luminance over time curves for these higher average current density driven LECs it is clear that from an initially rather flat curve, the decline is increasing exponentially once it starts. This is the result of the combination of the degradation of the devices, as suggested by the dramatic voltage increase (especially in the 100 and  $75 \text{ A m}^{-2}$  biased devices), and the continuous growth of the doped zones. As a result, the thickness of the intrinsic (non-doped) zone that is responsible for the light generation is reduced which leads to an increased quenching of emitting centers. At the same time, the driving voltage also starts to increase around the inflection point in the luminance time curve which implies that it is increasingly difficult to maintain the set current density. This is most likely the result of permanent degradation. Understanding the degradation of PLECs still remains a challenging task, however, irreversible redox reactions of the CP, as well as changes at the polymer/cathode interface, might be responsible for the progressive decrease of the cell performance.<sup>[42,43]</sup> At an average current density of  $50 \text{ A m}^{-2}$  a peak luminance of about  $480 \text{ cd m}^{-2}$  is reached and these luminance levels are maintained over a long period of time. We have data for devices operated up to 1600 h where the average luminance obtained for the devices is still above  $300 \text{ cd m}^{-2}$ . An exact  $t_{50}$  is not easy to extrapolate since near that point the luminance probably decays superlinear. Nevertheless, we estimate a  $t_{50}$  value in excess of 2000 h. This is an order of magnitude higher than what was published previously for similar fluorescent polymer-based LECs.<sup>[22–24]</sup> Our results are, to the best of our knowledge, one of the most long-lived CP-based LEC in the literature.<sup>[9]</sup> Moreover, the devices show sub-minutes turn-on times and excellent efficiencies throughout their lifetime. The peak CE and PE obtained for the three devices exceeds  $9 \text{ cd A}^{-1}$  and  $12 \text{ lm W}^{-1}$ , with values of  $9.6 \text{ cd A}^{-1}$  and  $12.6 \text{ lm W}^{-1}$  for the device biased with a  $50 \text{ A m}^{-2}$  current density.

To study in depth the effect of the doped zone formation on the stability of our devices, we developed a characterization method that measures the PL of the devices during electroluminescent operation. This is done by modulating the excitation

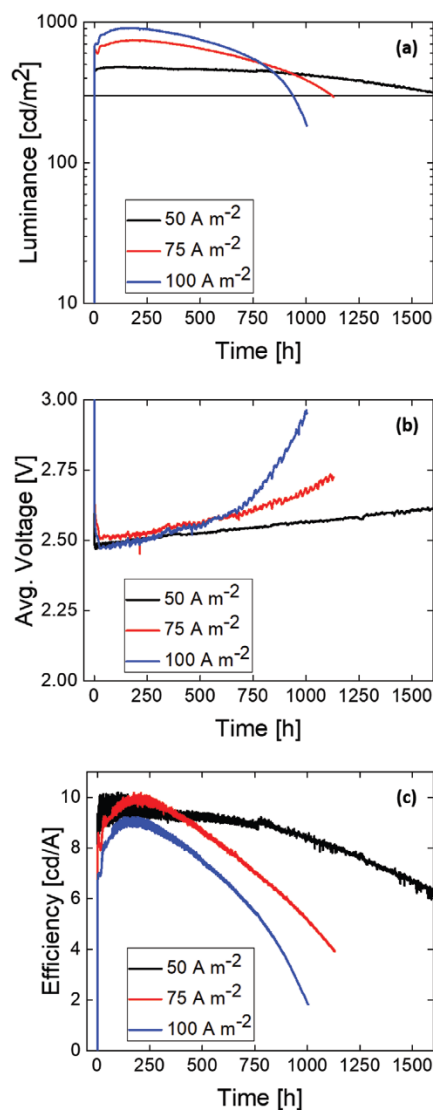


**Figure 4.** Performance of the 1:0.3:0.09 SY/Hybrane/LiTF ratio devices under an average pulsed current density of 50/75/100  $\text{A m}^{-2}$ . a) Luminance, b) Avg. Voltage, and c) CE. Luminance is expressed in the log scale.

**Table 2.** Main performance parameters of representative LECs under pulsed current average bias of 50/75/100  $\text{A m}^{-2}$ .

Average Bias	Max Lum. [ $\text{cd m}^{-2}$ ]	$t_{1/2}$ [h]	Peak CE [ $\text{cd A}^{-1}$ ]	Peak PE [ $\text{lm W}^{-1}$ ]
$50 \text{ A m}^{-2}$	480	2000	9.6	12.6
$75 \text{ A m}^{-2}$	745	1000	9.9	12.5
$100 \text{ A m}^{-2}$	900	850	9.2	12

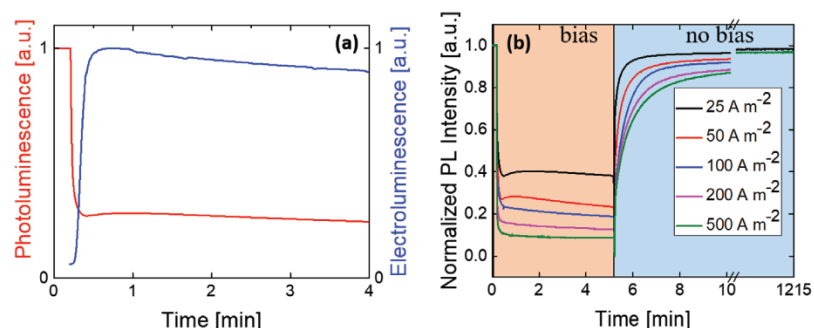


**Figure 5.** a) PL and EL evolution in the first 4 min of device operation at  $50 \text{ A m}^{-2}$ . b) Normalized PL intensity, LEC devices biased with a constant current density of  $25/50/100/200/500 \text{ A m}^{-2}$ . The cells driven at  $25$  and  $500 \text{ A m}^{-2}$  were left to recover overnight for about 20 h and measured again. Both measures were taken under a  $500 \text{ nm}$  light probe.

light source and coupling this modulation to a lock-in amplifier. Hence, the frequency-modulated PL can be detected by the lock-in amplifier in the presence of a non-modulated (constant) EL signal. Using this approach it was possible to extract at the same time the PL and EL profiles and their evolution in the critical first minutes of operation (Figure 5).

The intensity of the PL and EL signal followed over time are depicted in Figure 5a. At  $t = 0$  the devices are driven at a constant current of  $50 \text{ A m}^{-2}$ . Prior to turn-on, the PL is stable and the intensity is normalized to this arbitrary value. Upon turning on the bias the PL rapidly decays followed by a more gradual decline. At the same time, the EL slowly rises, typical of the operation of a LEC. In figure 5b, the PL was recorded under different current densities applied to the device ( $25/50/100/200/500 \text{ A m}^{-2}$ ), and after the bias was removed. In this graph we omitted to depict the EL for clarity, but it follows the same trend as already depicted in Figure 3. The drop in PL is more pronounced with increasing current density. We attribute this rapid decline in PL to the creation of doped regions that form by the dissociated ions and injected electronic charge carriers. A lower current density, for example,  $25 \text{ A m}^{-2}$  (black curve), corresponds to a less pronounced quenching when compared to a higher current density, for example,  $500 \text{ A m}^{-2}$  (green curve). This can be explained by the fact that higher current densities will generate more doping, reducing the intrinsic zone thickness and leaving less doping-free polymer to generate PL. The drop in PL intensity in the LEC is characterized by a first very fast step indicating the rapid ionic movement and doping as well as EDL formation. A second step then follows, 20–25 s after the bias is applied, in which the intensity decays at a slower rate, a possible evidence of the slow growth of the doped zones. As the current is switched off (Figure 5b, blue region “no bias”), two steps can be observed again. The PL first recovers rapidly followed by a slower rate recovery. The speed of PL recovery is proportional to the intensity of the applied bias, as expected. More detailed studies are needed to unravel the exact mechanism, in particular by probing at shorter time-scales. However, the fast recovery of the PL signal must imply the removal of the species responsible for its quenching. The quenching of the PL in LECs is generally ascribed to the interaction with the radical cations and anions that form after

injecting electrons and holes. Hence, after turning off the bias, these radical cations and anions, rapidly disappear to a large extent. In a timescale of 5 min, the PL signal has recovered to an extent between 96% for the LEC driven under  $25 \text{ A m}^{-2}$  and 86% for the LEC driven under  $500 \text{ A m}^{-2}$ . The cells driven at  $25$  and  $500 \text{ A m}^{-2}$  were also left to recover overnight for a total time of about 20 h. We can notice that both curves regain PL intensity up to values of 98% and 97%, respectively. As most of the relaxation takes place in the first minutes after the bias for the  $25 \text{ A m}^{-2}$  current density (black curve) the additional recovery after 20 h is low. On the other hand, for the  $500 \text{ A m}^{-2}$  current density the relaxation is much slower. There is most likely almost no permanent degradation present in these devices, even at high current biases, as they have been driven for such a short time (5 min). These results might indicate that when the bias is removed the undoping process occurs on different time scales.

The possibility to study the extent of the quenching as well as its decrease over time under bias provides useful insights about LECs doping and undoping mechanisms of different semiconducting materials,<sup>[7]</sup> ionic transport, and to help assess the origin of undesired side reactions.

### 3. Conclusion

In conclusion, we introduced a hyperbranched polymer (Hybrane) as the ion dissolving and transporting material in an SY-based state-of-the-art PLEC device. The blending properties of the two polymers have been investigated by means of AFM and PLQY measurements. Our results confirm that SY and Hybrane can form very homogeneous and smooth films without macro-phase separation. Devices were made and were driven under constant and pulsed currents in order to evaluate the stability over time. At low pulsed current densities ( $50 \text{ A m}^{-2}$ ), the light-emitting devices showed outstanding lifetimes maintaining a luminance in excess of  $300 \text{ cd m}^{-2}$  over 1600 operational hours (estimated  $t_{50}$  of 2000 h) and excellent current and power efficiencies of  $9.6 \text{ cd A}^{-1}$  and  $12.6 \text{ lm W}^{-1}$ , respectively. We measured the PL signal while EL operation of the devices. Our results indicate that the PL signal drops

due to quenching induced by the operation of the LEC. After switching off, the PL is recovered. The transient PL values and degree of recovery are dependent on the current density applied. The ability to monitor both PL/EL in sandwiched LECs will provide new insight into the exact operation and allow for further improvement of the performance.

#### 4. Experimental Section

**Materials:** All starting materials were obtained from commercial suppliers and used as received. The semiconducting polymer SY has been purchased from Merck, Hybrane DE0750 8500 from Polymer Factory, and  $\text{LiCF}_3\text{SO}_3$  and cyclohexanone from Sigma.

**Solution Preparation:** Solutions were prepared in an  $\text{N}_2$  controlled atmosphere. All the materials were dissolved in separate solutions of cyclohexanone at a concentration of  $10 \text{ mg mL}^{-1}$  for  $\text{LiCF}_3\text{SO}_3$  and Hybrane, and  $12 \text{ mg mL}^{-1}$  for SY which was left under continuous stirring and mild heating ( $50^\circ\text{C}$ ) overnight. Then the precursors were mixed following the mass ratios of 1:0.3:0.03, 1:0.3:0.09, and 1:0.3:0.15 (SY:Hybrane: $\text{LiCF}_3\text{SO}_3$ ). These solutions were left under stirring for 1 h. The final SY concentration was  $7.5 \text{ mg mL}^{-1}$ .

**Sample and Device Preparation:** Pre-patterned indium tin oxide (ITO)-coated glass plates were used as transparent conductive substrates both for AFM samples and for LEC devices. They were subsequently cleaned ultrasonically in water-soap, water, and 2-propanol baths. After drying, the substrates were placed in a UV-ozone cleaner (Jelight 42–220) for 20 min. The SY solution was then spun at 3000 rpm for 1 min. The as-coated films were annealed for 3 h at  $90^\circ\text{C}$  on a hotplate. A thickness of about 120 nm was obtained for all the three mass ratios. The thickness of the active layer was determined with an Ambios XP-1 profilometer. Finally, an Al electrode (100 nm) was thermally evaporated on top of the active layer using a shadow mask and resulting in multiple active areas of  $0.06 \text{ cm}^2$ . Similarly, for PLQY measurements the same solutions were spun at 3000 rpm on quartz substrates and annealed for 1 h at  $90^\circ\text{C}$ . The preparation of all the samples, devices, and thermal evaporation was conducted under an  $\text{N}_2$  filled atmosphere. Devices were then encapsulated with an Al protecting plate and the Ossila E132 encapsulation epoxy resin. A UV lamp (Hoenle UV Technology, UVACUBE 100) was used to initiate the polymerization reaction of the resin and the samples were left under irradiation for 1 min at a lamp output of  $100 \text{ W cm}^{-2}$ . The samples were left to rest for another 10 min to make sure that the polymerization reaction reached completion.

**Atomic Force Microscopy:** AFM measurements were collected in a Multimode atomic force microscope (Veeco instruments, Inc.). The images were obtained with a Si tip with frequency and K of ca. 300 kHz and  $40 \text{ N m}^{-1}$  respectively using the tapping-mode in air at room temperature. Images were recorded with a 0.5–1 Hz scan rate.

**LECs Characterization:** The devices were measured by applying a constant current density of  $75 \text{ A m}^{-2}$  and pulsed current density of 50, 75, and  $100 \text{ A m}^{-2}$  while monitoring the voltage and luminance versus time by using a True Color Sensor MAZeT (MTCsICT sensor) with a Botest OLT OLED Lifetime-Test system. The applied pulsed current consisted of block waves at a frequency of 1000 Hz with a duty cycle of 50%. As a result, the average current density and voltage were obtained by multiplying the values by the time-on (0.5 s) and dividing by the total cycle time (1 s). The reported data was the best data observed of at least 3 evaluated cells. There was less than 5% spreading between these cells.

**Photoluminescence Measures:** PL spectra and PLQY values were obtained using a Xe lamp and a monochromator as excitation source at 430 nm and an integrated sphere coupled to a spectrometer (Hamamatsu C9920-02 with a Hamamatsu PMA-11 optical detector). All the measurements were conducted under  $\text{N}_2$  atmosphere. The PL over time during device operation was measured using a Quartz Tungsten Halogen lamp (Newport model APEX2-QTH) and a monochromator (ORIEL 180) as a tunable excitation source. The excitation wavelength of 500 nm was selected. A silicon photodiode was positioned in close

proximity of the device pixel and connected to a lock-in amplifier (Standford Research System SR830 DSP) through a current-voltage converter (Oriel model 71 710) that transforms and amplifies the collected photocurrent into voltage. An optical chopper (New Focus 3502) was connected to the lock-in amplifier and set at a frequency of 327 Hz. The chopper was positioned in front of the light source for the lock-in amplifier to discriminate PL from EL since the former is collected as pulsed light and therefore generates a pulsed photocurrent signal. Finally, the devices were driven at different constant current biases (between 25 and  $500 \text{ A m}^{-2}$ ) using a Keithley 2612A controlled from a personal computer. These measurements were recorded in ambient atmosphere using encapsulated devices.

#### Acknowledgements

We acknowledge Jorge Ferrando for his help with the PL during EL setup. The research leading to these results has received funding from the European Research Council (ERC) under the European Union's Horizon 2020 research and innovation program Grant agreement No. 834431, the Spanish Ministry of Science, Innovation and Universities (MICIU, RTI2018-095362-A-I00, and EQC2018-004888-P), and the Comunitat Valenciana (IDIFEDER/2020/063 and PROMETEU/2020/077). C.D. acknowledges that the project that gave rise to these results received the support of a fellowship from "la Caixa" Foundation (ID 100010434, code LCF/BQ/DI19/11730020). M.S. acknowledges the MICIU for his RyC contract.

#### Conflict of Interest

The authors declare no conflict of interest.

#### Data Availability Statement

Research data are not shared.

#### Keywords

electroluminescence, hyperbranched polymers, lifetime, light-emitting electrochemical cells, photoluminescence, polymer electrolytes, solid-state lighting

Received: May 5, 2021

Revised: July 12, 2021

Published online:

- [1] N. Thejokalyani, S. J. Dhoble, *Renewable Sustainable Energy Rev.* **2014**, *32*, 448.
- [2] Q. Pei, Y. Yang, G. Yu, C. Zhang, A. J. Heeger, *J. Am. Chem. Soc.* **1996**, *118*, 3922.
- [3] D. L. Smith, *J. Appl. Phys.* **1997**, *81*, 2869.
- [4] S. van Reenen, P. Matyba, A. Dzwilewski, R. A. J. Janssen, L. Edman, M. Kemerink, *J. Am. Chem. Soc.* **2010**, *132*, 13776.
- [5] M. Lenes, G. Garcia-Belmonte, D. Tordera, A. Pertegás, J. Bisquert, H. J. Bolink, *Adv. Funct. Mater.* **2011**, *21*, 1581.
- [6] J. D. Slinker, J. A. DeFranco, M. J. Jaquith, W. R. Silveira, Y. W. Zhong, J. M. Moran-Mirabal, H. G. Craighead, H. D. Abrua, J. A. Marohn, G. G. Malliaras, *Nat. Mater.* **2007**, *6*, 894.
- [7] S. B. Meier, D. Hartmann, D. Tordera, H. J. Bolink, A. Winnacker, W. Sarfert, *Phys. Chem. Chem. Phys.* **2012**, *14*, 10886.
- [8] A. J. H. Qibing Pei, G. Yu, C. Zhang, Y. Yang, *Science* **1995**, *269*, 1086.

- [9] J. Gao, *ChemPlusChem* **2018**, *3*, 183.
- [10] Z. B. Hill, D. B. Rodovsky, J. M. Leger, G. P. Bartholomew, *Chem. Commun.* **2008**, 6594.
- [11] W.-C. Chen, C.-S. Lee, Q.-X. Tong, *J. Mater. Chem. C* **2015**, *3*, 10957.
- [12] S. Jenatsch, L. Wang, N. Leclaire, E. Hack, R. Steim, S. B. Anantharaman, J. Heier, B. Ruhstaller, L. Penninck, F. Nüesch, R. Hany, *Org. Electron.* **2017**, *48*, 77.
- [13] K. Shanmugasundaram, J. C. John, S. Chitumalla, J. Jang, Y. Choe, *Org. Electron.* **2019**, *67*, 141.
- [14] J. Choi, S. Kanagaraj, Y. Choe, *J. Mater. Chem. C* **2020**, *8*, 4580.
- [15] R. D. Costa, E. Ortá, H. J. Bolink, S. Graber, S. Schaffner, M. Neuburger, C. E. Housecroft, E. C. Constable, *Adv. Funct. Mater.* **2009**, *19*, 3456.
- [16] A. Pertegás, N. M. Shavaleev, D. Tordera, E. Ortí, M. K. Nazeeruddin, H. J. Bolink, *J. Mater. Chem. C* **2014**, *2*, 1605.
- [17] R. D. Costa, E. Ortí, H. J. Bolink, F. Monti, G. Accorsi, N. Armadori, *Angew. Chem., Int. Ed.* **2012**, *51*, 8178.
- [18] H. Xu, R. Chen, Q. Sun, W. Lai, Q. Su, W. Huang, X. Liu, *Chem. Soc. Rev.* **2014**, *43*, 3259.
- [19] J. Mindemark, L. Edman, *J. Mater. Chem. C* **2016**, *4*, 420.
- [20] S. B. Meier, D. Tordera, A. Pertegás, C. Roldán-Carmona, E. Ortí, H. J. Bolink, *Mater. Today* **2014**, *17*, 217.
- [21] C. Poinsignon, *Mater. Sci. Eng. B* **1989**, *3*, 31.
- [22] J. Mindemark, S. Tang, H. Li, L. Edman, *Adv. Funct. Mater.* **2018**, *28*, 1801295.
- [23] J. Mindemark, S. Tang, J. Wang, N. Kaihovirta, D. Brandell, L. Edman, *Chem. Mater.* **2016**, *28*, 2618.
- [24] S. Tang, L. Edman, *J. Phys. Chem. Lett.* **2010**, *1*, 2727.
- [25] D. Devaux, R. Bouchet, D. Glé, R. Denoyel, *Solid State Ionics* **2012**, *227*, 119.
- [26] K. Timachova, H. Watanabe, N. P. Balsara, *Macromolecules* **2015**, *48*, 7882.
- [27] H. Gao, S. Chen, J. Liang, Q. Pei, *ACS Appl. Mater. Interfaces* **2016**, *8*, 32504.
- [28] Z. Yu, M. Wang, G. Lei, J. Liu, L. Li, Q. Pei, *J. Phys. Chem. Lett.* **2011**, *2*, 367.
- [29] I. Gerz, E. M. Lindh, P. Thordarson, L. Edman, J. Kullgren, J. Mindemark, *ACS Appl. Mater. Interfaces* **2019**, *11*, 40372.
- [30] B. Sun, J. Mindemark, E. V. Morozov, L. T. Costa, M. Bergman, P. Johansson, Y. Fang, I. Furó, D. Brandell, *Phys. Chem. Chem. Phys.* **2016**, *18*, 9504.
- [31] F. P. Wenzl, P. Pachler, C. Suess, A. Haase, E. J. W. List, P. Poelt, D. Somitsch, P. Knoll, U. Scherf, G. Leising, *Adv. Funct. Mater.* **2004**, *14*, 441.
- [32] S. Burns, J. MacLeod, T. T. Do, P. Sonar, S. D. Yambem, *Sci. Rep.* **2017**, *7*, 40805.
- [33] J. M. Hodgkiss, G. Tu, S. Albert-Seifried, W. T. S. Huck, R. H. Friend, *J. Am. Chem. Soc.* **2009**, *131*, 8913.
- [34] O. V. Mikhnenko, M. Kuik, J. Lin, N. van der Kaap, T.-Q. Nguyen, P. W. M. Blom, *Adv. Mater.* **2014**, *26*, 1912.
- [35] S. van Reenen, M. V. Vitorino, S. C. J. Meskers, R. A. J. Janssen, M. Kemerink, *Phys. Rev. B* **2014**, *89*, 205206.
- [36] M. A. Summers, S. K. Buratto, L. Edman, *Thin Solid Films* **2007**, *515*, 8412.
- [37] S. Tang, L. Edman, *Top. Curr. Chem.* **2016**, *374*, 40.
- [38] M. Diethelm, Q. Grossmann, A. Schiller, E. Knapp, S. Jenatsch, M. Kawecki, F. Nüesch, R. Hany, *Adv. Opt. Mater.* **2019**, *7*, 1801278.
- [39] D. Tordera, J. Frey, D. Vonlanthen, E. Constable, A. Pertegás, E. Ortí, H. J. Bolink, E. Baranoff, M. K. Nazeeruddin, *Adv. Energy Mater.* **2013**, *3*, 1338.
- [40] N. M. Shavaleev, R. Scopelliti, M. Grätzel, M. K. Nazeeruddin, A. Pertegás, C. Roldán-Carmona, D. Tordera, H. J. Bolink, *J. Mater. Chem. C* **2013**, *1*, 2241.
- [41] D. Tordera, M. Lenes, H. J. Bolink, *J. Nanosci. Nanotechnol.* **2013**, *13*, 5170.
- [42] F. Alta, J. Gao, *Org. Electron.* **2015**, *18*, 1.
- [43] J. Fang, P. Matyba, N. D. Robinson, L. Edman, *J. Am. Chem. Soc.* **2008**, *130*, 4562.

# Transparent Light-Emitting Electrochemical Cells

Lorenzo Mardegan, Abhyuday Paliwal, Kassio P. S. Zanoni, Daniel Tordera, and Henk J. Bolink\*

Single layer light-emitting electrochemical cells (LECs) are amongst the simplest electroluminescent devices and operate with air-stable electrodes. Transparent light-emitting devices are of great interest as they can enable new applications in consumer electronics. In this work, a transparent ionic transition metal complex based LEC is fabricated by developing a transparent top contact based on tin (IV) oxide (SnO<sub>2</sub>) and indium-tin oxide, processed by low-temperature atomic layer deposition and pulsed laser deposition, respectively. The resulting devices present transparency in excess of 75% over the full visible spectrum (380–750 nm), with 82% transmission at the emission peak (563 nm). The devices emit from the front and the rear with high luminance (260 cd m<sup>-2</sup>) and long lifetime (176 h). These parameters place them among the highest performing single layer transparent electroluminescent devices.

## 1. Introduction

In recent years, new display technologies have emerged, and with them, the need for development of properties such as large area, stretchability, or transparency in organic light-emitting devices (OLEDs).<sup>[1,2]</sup> In particular, for semitransparent OLEDs, the requirements for the cathode are a high light transmittance (over 80%) and a low sheet resistance ( $R_s$ ).<sup>[3]</sup> The realm of transparent electrodes is vast and in continuous progress, nonetheless the most common materials and structures are transparent conductive oxides (TCOs), very thin films of metals or alloys (e.g., Ag, Au, Ag:Al, Mg:Ag), multilayer metal thin film based cathodes (e.g., dielectric/metal/dielectric, metal/metal), nano arrays (e.g., carbon based electrodes and metal nanowire electrodes) and conductive polymers (e.g., poly(3,4-ethylenedioxythiophene): polystyrenesulfonate (PEDOT:PSS)).<sup>[4–6]</sup> TCOs are the preferred materials as transparent bottom electrodes, as they


possess a high conductivity and there are barely any process limitations since they are often deposited on glass or plastic substrates that endure the harsh conditions during the TCO deposition via, for example, magnetron sputtering. The use of TCOs as transparent top electrodes on thin organic semiconductor based devices requires, however, more attention, particularly regarding the chemical and processing compatibility with the underlying thin (usually <500 nm) organic semiconductor layers. Additionally, the alignment of the TCO conduction band with the energy of the molecular orbitals of the organic semiconductor is important. These requirements have limited the widespread usage of TCO as top electrode in organic semiconductor devices.<sup>[5]</sup> For example, the

sputtering of TCO directly on top of device stacks can damage underlying charge transport layers or the active materials themselves, reducing their performances and lifetimes.<sup>[7]</sup> The use of indium-tin oxide (ITO) as top electrode in semitransparent devices has been studied in LEDs and OLEDs. Recent publications show that to avoid sputtering damage on the organic layers a buffer layer has to be included, usually ZnO nanoparticles or ultra-thin metal films, as well as carefully choosing the deposition conditions, taking into account the trade-off between the sheet resistance and the damage.<sup>[8–13]</sup> One of the most efficient semitransparent and flexible devices was demonstrated by Han et al. reporting a white quantum dot (QD) LED with a maximum current efficiency of 18.2 cd A<sup>-1</sup>, a maximum luminance value above 10 000 cd m<sup>-2</sup> and an external quantum efficiency of 6.4%.<sup>[8]</sup>

Light-emitting electrochemical cells (LECs) currently represent a promising alternative to LED and OLED technologies as in their simplest form they consist only of a light-emitting active layer sandwiched between two electrodes.<sup>[14]</sup> The active layer is composed of a blend of an electroluminescent semiconductor,<sup>[15–17]</sup> a salt and an electrolyte.<sup>[18,19]</sup> Over the years, numerous efforts have already been made to improve the properties of the blend of conjugated polymers (CP) and small molecules,<sup>[15,20–22]</sup> and ligand design in ionic transition metal complexes (iTMCs),<sup>[23,24]</sup> in pursuit of long-lived, efficient, and bright devices. However, the literature is still relatively poor for semitransparent LECs with only a couple of examples reported, albeit using a top electrode that is either a conductive polymer or a nano array.<sup>[25,26]</sup>

In this work, we developed semitransparent iTMC-LECs using a TCO as both the top and the bottom electrodes. The top electrode was processed in a multilayer structure

L. Mardegan, A. Paliwal, K. P. S. Zanoni, D. Tordera, H. J. Bolink  
 Instituto de Ciencia Molecular (ICMol)  
 Universidad de Valencia  
 C/Catedrático J. Beltrán 2, Paterna (Valencia) 46980, Spain  
 E-mail: henk.bolink@uv.es

 The ORCID identification number(s) for the author(s) of this article can be found under <https://doi.org/10.1002/adom.202201953>.

© 2022 The Authors. Advanced Optical Materials published by Wiley-VCH GmbH. This is an open access article under the terms of the Creative Commons Attribution-NonCommercial-NoDeriv License, which permits use and distribution in any medium, provided the original work is properly cited, the use is non-commercial and no modifications or adaptations are made.

DOI: 10.1002/adom.202201953

composed of tin oxide ( $\text{SnO}_2$ ) processed by atomic layer deposition (ALD) and ITO processed by pulsed laser deposition (PLD). The cathode was directly deposited on top of the organic active layer based on a yellow iridium(III) iTMC emitter,  $[\text{Ir}(\text{ppy})_2(\text{dtb-bpy})][\text{PF}_6]$  (where ppy is 2-phenylpyridine and dtb-bpy is 4,4'-di-tert-butyl-2,2'-dipyridyl).<sup>[27]</sup> The energy levels of  $\text{SnO}_2$  and the active material in the light-emitting layer are not aligned. Due to the operation mechanism of LECs involving ion migration to the electrode interface, this is not a problem. Furthermore, the combination of ALD and PLD offers the advantages of adjusting the deposition conditions, such as pressure and temperature, to provide a high-quality film, with precise control over thickness and composition. The possible harsh effects of the ALD and PLD during processing on the organic underlayers were examined. Transmittance, electroluminescence spectra (EL), and luminance output from both bottom and top side was measured. A very high transparency, above 75% over the visible spectra region (380 to 750 nm), was obtained in conjunction with a high electroluminescence above  $200 \text{ cd m}^{-2}$  which implies a very strong on/off contrast.

## 2. Results and Discussion

First, we developed the semitransparent top electrode for LEC devices. A fundamental condition for efficient light-emitting devices is to ensure the absence of shorts and leakage paths. TCOs represent the best choice in terms of transparency combined with a high conductivity, tunable electronic properties, and fabrication ease with several techniques. However, their deposition on organic thin films is not trivial as these materials are frequently deposited using harsh methods such as reactive ion sputtering or PLD. Even for ALD processes, the presence of reactive gasses and the needed temperatures can lead to undesired shorts. Additionally, it is important to have an energy matching interface between the light-emitting layer and the charge injection and electrode layers.<sup>[5,7]</sup> For PLD processes, the chamber pressure is a crucial factor because it determines the way the particles pack during the layer formation and, therefore, it affects its electrical properties. Generally, the lower the

chamber pressure, the more conductive the TCO layer is, due to the enhanced bulk properties of the resultant film. However, it can also result in a higher number of shorts due to the higher kinetic energy of the TCO particles when impacting on the underlying layer. This effect has been recently demonstrated on perovskite solar cells where the ITO deposition pressure parameters were optimized.<sup>[28]</sup> Therefore, a higher chamber pressure needs to be used in the PLD process for the ITO deposition in order to minimize the damage to the samples. Based on this, we selected a chamber pressure of 0.042 mbar (with an  $\text{O}_2$  partial pressure of 0.0076 mbar) for the deposition of the top ITO electrode via PLD. A 140 nm ITO layer deposited on glass under these conditions exhibited a sheet resistance of  $140 \Omega \text{ sq}^{-1}$ . However, when deposited directly on the organic emitting layer in the LEC stack, it produced a considerable number of shorted devices.

To ensure there is no penetration of ITO in the thin film of the Ir(III) emitter, we employed an additional  $\text{SnO}_2$  electron transport layer (ETL) via ALD.  $\text{SnO}_2$  is gaining increased consideration for its use as a wide band gap semiconductor due to its high transmission and electrical properties combined with remarkable chemical stability and compatibility with several doping elements and fabrication techniques.<sup>[29]</sup> Recent works describe the use of  $\text{SnO}_2$  as ETL in optoelectronic devices.<sup>[30–32]</sup> Regarding the ALD technique, the growth temperature and choice of the precursors are the key factors in order to achieve suitable film properties. However, for thermally sensitive materials, such as organics or organometallic semiconductors, it is imperative to reduce the growth temperature to a level at which this technique can be sustainably exploited. For our devices, we obtained  $\text{SnO}_2$  films at a growth temperature of  $90^\circ \text{C}$  without further annealing using tetrakis(diethylamino)tin (TDAT) and water as precursors.<sup>[33]</sup> The  $\text{SnO}_2$  films were characterized by means of atomic force microscopy (AFM) and X-ray photoelectron spectroscopy (XPS). An AFM image of a thin  $\text{SnO}_2$  film on a glass/ITO/PEDOT:PSS/Ir substrate (Figure 1a) reveals a very flat surface with an estimated mean roughness of 0.6 nm. Our results are in line with previous reports where  $\text{SnO}_2$  was deposited at low temperature.<sup>[33–35]</sup> The XPS analysis (Figure 1b) reveals the formation of  $\text{SnO}_2$ ,<sup>[33]</sup> with an element ratio close to

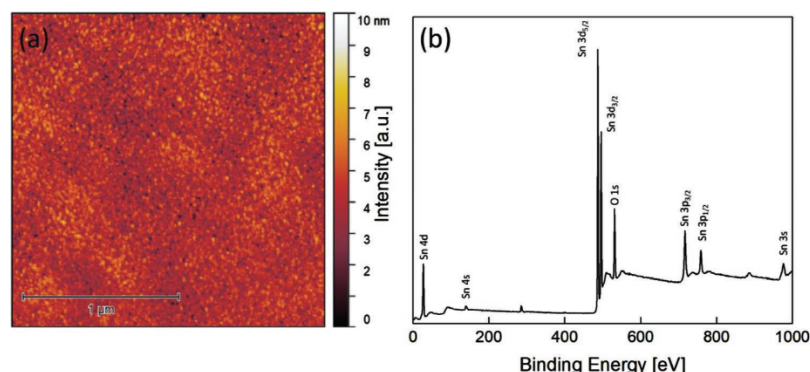


**Figure 1.** a) AFM topographic image of an ALD-deposited  $\text{SnO}_2$  thin film on glass/PEDOT:PSS/Ir substrate. b) XPS survey of  $\text{SnO}_2$  thin film on glass/ITO substrate.

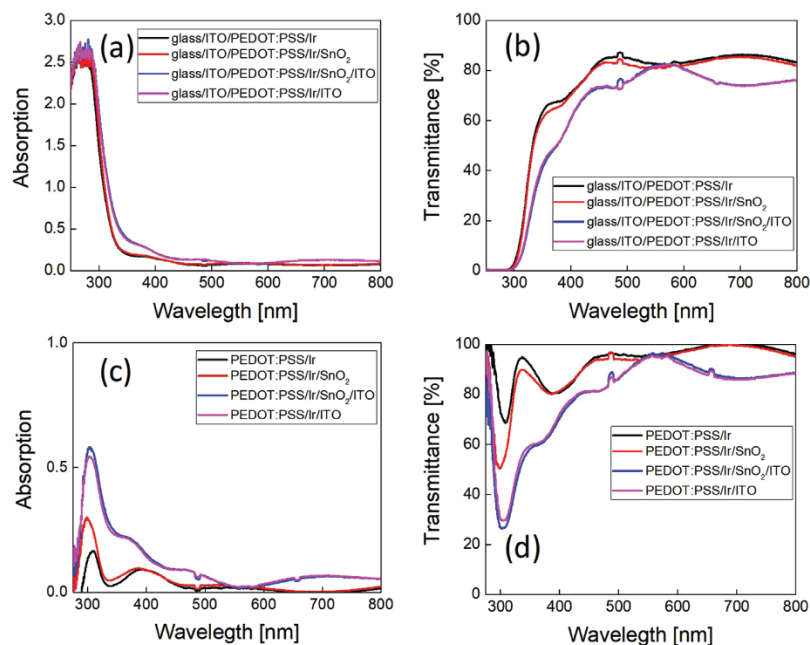


**Figure 2.** a) Absorbance and b) transmittance of the samples, before and after the SnO<sub>2</sub> and ITO layers deposition. c) Absorbance and d) transmittance of the same samples using a glass/ITO reference sample.

1:2 between Sn and O. Topographic AFM images were also collected for Ir deposited on glass/PEDOT:PSS and for ITO deposited on glass/PEDOT:PSS/Ir and glass/PEDOT:PSS/Ir/SnO<sub>2</sub> samples (Figure S1, Supporting Information) showing flat surfaces in all cases with mean roughness below 1.5 nm.

Thereafter, we proceeded to examine the effect of the deposited SnO<sub>2</sub> and ITO layers on the optical properties of the device stack. We prepared samples before and after the SnO<sub>2</sub> and ITO layers deposition, that is, glass/ITO/PEDOT:PSS/Ir, glass/ITO/PEDOT:PSS/Ir/SnO<sub>2</sub>, glass/ITO/PEDOT:PSS/Ir/SnO<sub>2</sub>/ITO, and glass/ITO/PEDOT:PSS/Ir/ITO, where Ir is the active layer composed of [Ir(ppy)<sub>2</sub>(dtb-bpy)][PF<sub>6</sub>] and 1-butyl-3-methylimidazolium hexafluorophosphate [BMIM][PF<sub>6</sub>] in a molar ratio of 1:0.25. The thicknesses of SnO<sub>2</sub> and ITO were 20 and 140 nm, respectively. The absorbance and transmittance spectra of glass/ITO/PEDOT:PSS/Ir and glass/ITO/PEDOT:PSS/Ir/SnO<sub>2</sub> (Figures 2a,b, black and red curves, respectively) are superimposable and the addition of ITO slightly increases the absorption of light and consequently results in a decrease in transmission (Figures 2a,b, blue and pink curves, respectively). The full stack (blue curve) showed an average transmittance value of 75% within the visible spectrum range (380 to 750 nm) with a transmittance of 82% at the electroluminescence peak of 563 nm (discussed later and seen in Figure 4a). These measurements give important information about the features of the final device, however, they do not tell much about the intrinsic properties of the deposited layers because of the strong effect that the glass substrate has on the absorption. When glass and ITO from the substrate are not taken into consideration

(Figure 2c,d), it is possible to observe that the SnO<sub>2</sub> and ITO deposition increases (decreases) the absorption (transmission), especially in the lower wavelength region between 300 and 400 nm of the spectra with respect to the Ir sample (black curve). This is in line with the absorption spectra measured for SnO<sub>2</sub> and ITO (Figure S2, Supporting Information).

Next, devices were fabricated in the following configuration: glass/ITO/PEDOT:PSS (80 nm)/[Ir(ppy)<sub>2</sub>(dtb-bpy)][PF<sub>6</sub>][BMIM][PF<sub>6</sub>] (1:0.25) (80 nm)/SnO<sub>2</sub> (20 nm)/ITO (140 nm) (Figure 3a). After the cathode deposition, gold was thermally evaporated at the edges to supply an additional low resistance path to facilitate effective charge injection from the ITO cathode. As mentioned before, the direct deposition of ITO resulted in a large number of shorts while SnO<sub>2</sub> effectively acted as a buffer layer preventing these shorts. For this reason, we will focus our discussion only on the device configuration that includes the SnO<sub>2</sub> buffer layer. The semitransparent devices were also compared with standard fully reflective Al-cathode (100 nm) LECs. The iridium complex, [Ir(ppy)<sub>2</sub>(dtb-bpy)][PF<sub>6</sub>], represented in Figure 3b, has been previously used as a yellow light-emitting material in iTMC-LECs and has displayed high stability and efficiency.<sup>[27,36]</sup> Images of the semitransparent device and the standard opaque device in their ON and OFF states are shown in Figure 3c–f showing the transparency of the transparent devices. To further highlight the transparency of these samples, pictures of transparent devices without the Au fingers were also taken and are shown in Figure S3, Supporting Information.

Both the transparent and opaque devices were characterized by applying a pulsed driving current of 100 A m<sup>-2</sup>

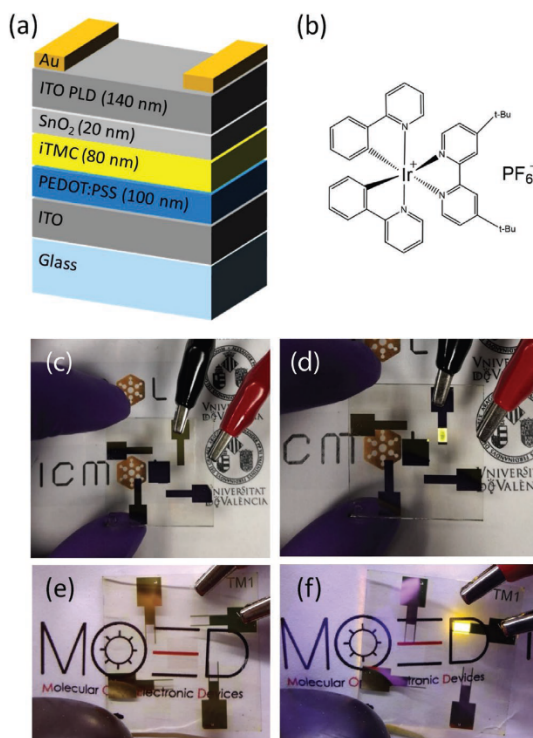


**Figure 3.** a) Architecture of the semitransparent devices. b) Chemical structure of the yellow Ir(III) emitter  $[\text{Ir}(\text{ppy})_2(\text{dtb-bpy})][\text{PF}_6]$  used in this work. OFF states of the c) reference and e) semitransparent devices, and ON states of the d) reference and f) semitransparent devices.

(avg.  $50 \text{ A m}^{-2}$ ) and monitoring their luminance and voltage evolution over time. The pulsed bias consisted of a block wave current at a frequency of 1000 Hz with a duty cycle of 50%. The luminance of the transparent devices was measured from top ( $\text{SnO}_2/\text{ITO}$  side) and bottom (glass/ITO side). The electroluminescence spectra of the standard and semitransparent devices through the bottom substrate were rather similar (Figure 4a). The EL peak from the semitransparent device is slightly blue-shifted when compared to the opaque reference device, with maxima of 563 and 571 nm, respectively. The observed blue-shift could be the result of a different light outcoupling for the opaque and transparent devices, where the light-emitting layer acts as a cavity in which the position of the emissive non-doped zone is governed by the choice of the cathode. The main figures of merit of both the opaque and transparent LEC are summarized in Table 1. The opaque device shows the evolution of luminance and voltage typical for LECs driven with a pulsed current (Figure 4b). In the first stages after applying the bias, the high resistance causes a high starting voltage. As the ionic species migrate within the thin film creating the electronic double layers (EDLs) the voltage quickly decreases while the luminance increases. The reference device reaches a maximum luminance value of  $620 \text{ cd m}^{-2}$  and a  $t_{50}$ , referred to as the time necessary to reach half of the maximum luminance, of 1120 h.

The high luminance and the low pulsed driving current density make this device very efficient with a peak current efficiency (CE) value of  $13.6 \text{ cd A}^{-1}$  and a power efficiency (PE) of  $8.9 \text{ lm W}^{-1}$ . The semitransparent devices (Figure 4c,d), biased with the same average current density of  $50 \text{ A m}^{-2}$  and maintaining the same electrode polarity, show a similar performance. When measured from the bottom side, the luminance reached a value of  $260 \text{ cd m}^{-2}$  which is less than what is obtained for the opaque cells. This is primarily due to the loss of the reflecting electrode in the transparent devices. Indeed, when measured through the top ITO electrode, a luminance of  $188 \text{ cd m}^{-2}$  is obtained. Even though the sum of these two values is still below what is obtained for the opaque cell, the difference is not very large. We will comment on the possible origin of this difference in the next section. As a result of the lower luminance also the current efficacy and the power efficiency are lower in the transparent devices. The luminance values obtained from the bottom and top side are  $260$  and  $188 \text{ cd m}^{-2}$  which leads to CE and PE values of  $5.2$  and  $4.0 \text{ cd A}^{-1}$ , and  $3.2$  and  $2.5 \text{ lm W}^{-1}$ , for the bottom and top side, respectively. Finally, the  $t_{50}$  for the bottom side is 176 h while that for the top side is 118 h.

Several factors can contribute to the different luminance values observed for the bottom and top sides of the devices. The outcoupling of photons depends strongly on the refractive index of the layers the emitted light must pass through in order to escape from the device. With regard to  $\text{SnO}_2$ , several reports show that its electrical as well as optical properties depend on the deposition temperature and precursors used.<sup>[33,37]</sup> The refractive index is reported to be close to 1.9/2.0 when  $\text{SnO}_2$  is deposited from TDAT and water at low temperatures (below  $100 \text{ }^\circ\text{C}$ ).<sup>[33]</sup> When driving the device and measuring from the bottom side (glass), the light is partially trapped because the glass substrate has a low refractive index of  $\approx 1.5$ . For commercial ITO on glass substrates the reported refractive index is generally 1.8 but the ITO optical properties are strictly related to its crystallinity, resistivity, and surface morphology. For PLD deposition, these properties are controlled by changing chamber pressure and deposition temperature. It has been reported that room temperature depositions could lead to higher sheet resistance and refractive indices.<sup>[38,39]</sup> For our deposited ITO, due to the medium/high chamber pressure of 0.042 mbar (see Experimental Section) and room temperature, the final refractive index might be close to 2.0 or higher. The high refractive index of the top TCO electrode supports the outcoupling from the organic light-emitting material into the TCO layers, however because of the large contrast in indices between the TCOs and air ( $\approx 2 \text{ TCO}:1 \text{ air}$ ) the light remains constrained within the outer TCOs layers. In order to exploit the advantage of using a high refractive index based outcoupling layer, nano arrays/lenses<sup>[40]</sup> would be required. In addition, internal reflections of the different layers of the stack and from the gold fingers evaporated around the device area could play an important role in determining the final light output from the top and bottom side. This difference in luminance measured from the bottom and top sides has also been confirmed by the simultaneous measurement with two equidistant photodiodes of the generated photocurrent by the two sides of the same pixel under a constant current bias of  $50 \text{ A m}^{-2}$  (Figure S4, Supporting Information). Although these results were obtained with a constant



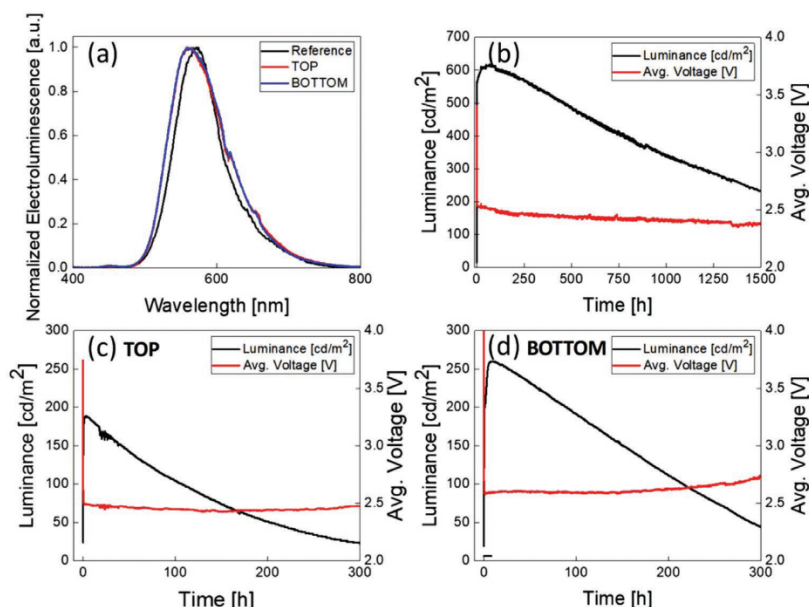


**Figure 4.** a) Electroluminescence of the standard Al-cathode and semitransparent devices, b) luminance and voltage over time of the standard Al-cathode device at an avg. current of  $50 \text{ A m}^{-2}$ . c,d) Luminance and voltage over time of the top and bottom sides of the transparent device driven at avg. current of  $50 \text{ A m}^{-2}$ .

bias, they are in agreement with the luminance versus time data showed in Figure 4. Differences between top and bottom emission were also previously reported in transparent OLED and QD-LED, and attributed to a difference in transparency between the top and bottom electrodes.<sup>[10,13]</sup>

Finally, a rough estimate of the overall performance of the semitransparent device (obtained as the sum of the top and bottom measurements) can be made. The overall luminance is  $448 \text{ cd m}^{-2}$  with a CE and PE of  $9.2 \text{ cd A}^{-1}$  and  $5.7 \text{ lm W}^{-1}$ . Another factor that could play a role in the performance of the semitransparent LEC device is the photoluminescence (PL) quenching as a consequence of the cathode deposition. To study this, the photoluminescence was measured to understand the interactions between the Ir thin film and the  $\text{SnO}_2$  and ITO deposited layers. The PL was measured from both sides of the samples using an excitation wavelength of  $340 \text{ nm}$  in an integrating sphere, where bottom indicates that the sample was excited from the glass substrate side and top from the PLD-ITO cathode side (Figure 5a,b). Analyzing the bottom orientation (Figure 5a) we observe that the PL intensity suffers from both

the ALD and PLD depositions. In the first case, a drop of the PL intensity of 19% is observed by the ALD-deposited  $\text{SnO}_2$  thin layer (red curve). It is well known the ability of  $\text{SnO}_2$ <sup>[31,41–43]</sup> and other metal oxides based ETLs<sup>[44,45]</sup> to quench the PL at the semiconductor/TCO interface through exciton trapping and non-radiative energy transfer. Furthermore, a degradation of the Ir complex by the action of the nucleophilic water molecules and temperature during the ALD deposition could play a critical role.<sup>[23,24]</sup> The ITO deposition directly on the active Ir material dramatically increases the quenching to about 52% (pink curve). Here, the ITO deposition could be too harsh for the organic active layer, as seen on the number of resulting shorted devices. Surprisingly, we observe a remarkable decrease in the number of shorted cells upon  $\text{SnO}_2$  insertion and, at the same time, the presence of an important interaction between the iTMC and the cathode as suggested by the intense PL quenching, around 48%, observed in the full-stack sample glass/ITO/PEDOT:PSS/Ir/ $\text{SnO}_2$ /ITO (blue curve). Second, we measured the samples from the top side (Figure 5b). The samples showed the same degree of quenching after the  $\text{SnO}_2$  deposition (red curve), as expected. The addition of ITO in the Ir/ITO and Ir/ $\text{SnO}_2$ /ITO samples (pink and blue curves, respectively) follows the same trend as the bottom orientation, however with a higher degree of quenching of 74% and 65%, respectively.

**Table 1.** Figures of merit of the standard and transparent (T) cells driven at  $50 \text{ A m}^{-2}$  average bias current.

	Peak lum. [ $\text{cd m}^{-2}$ ]	$t_{50}$ [h]	CE [ $\text{cd A}^{-1}$ ]	PE [ $\text{lm W}^{-1}$ ]
Standard	620	1120	13.6	8.9
T-bottom side	260	176	5.2	3.2
T-top side	188	118	4.0	2.5
T-overall	448	—	9.2	5.7

### 3. Conclusion

In conclusion, in this work we have fabricated semitransparent iTMC-LECs by using a transparent top  $\text{SnO}_2$ /ITO contact processed by ALD and PLD, respectively. The devices had

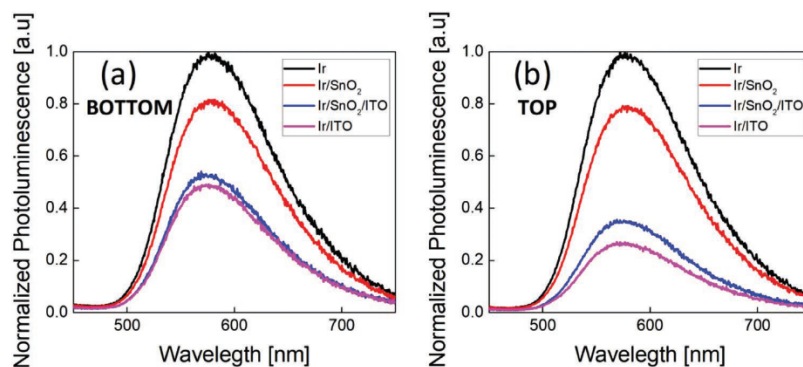


**Figure 5.** Photoluminescence from the a) BOTTOM side and b) TOP side obtained with an excitation wavelength of 340 nm of the iTMC film and with different metal oxide layers deposited on top of it.

a full-stack transparency of 75% over the visible spectrum (380 to 750 nm) with a transmittance of 82% at the electroluminescence peak of 563 nm. We were able to characterize the devices by measuring them from both sides. The devices showed excellent on/off ratio characterized by a high transmittance, and a luminance up to 260 cd m<sup>-2</sup> coupled to lifetimes up to 176 h demonstrating the potential of these highly transparent light-emitting devices.

#### 4. Experimental Section

**Materials:** Anhydrous acetonitrile (ACN) and 1-butyl-3-methylimidazolium hexafluorophosphate [BMIM][PF<sub>6</sub>] were obtained from Sigma-Aldrich and stored under N<sub>2</sub> filled atmosphere. The Ir(III) complex, [Ir(ppy)<sub>2</sub>(dtb-bpy)][PF<sub>6</sub>], was synthesized following a previously reported procedure.<sup>[27]</sup>

**Solution Preparation:** [Ir(ppy)<sub>2</sub>(dtb-bpy)][PF<sub>6</sub>] solutions were made in ACN at a final concentration of 20 mg mL<sup>-1</sup> and a molar ratio of 1:0.25 of [Ir(ppy)<sub>2</sub>(dtb-bpy)][PF<sub>6</sub>]:[BMIM][PF<sub>6</sub>] was used. The ionic liquid (IL) solution was previously prepared in anhydrous ACN at a concentration of 10 mg mL<sup>-1</sup> under inert atmosphere. The solvation of both the iTMC and IL in ACN as well as the final mixed solution were instantaneous and no further heating and stirring were needed.

**Samples and Device Preparation:** Pre-patterned indium tin oxide (ITO)-coated glass plates were used as transparent conductive substrates. They were subsequently cleaned ultrasonically in water-soap, water, and 2-propanol baths. After drying, the substrates were placed in a UV-ozone cleaner (Jelight 42-220) for 20 min. The ITO substrates were first coated with PEDOT:PSS and then with the iTMC-IL solution. Thicknesses of 100 and 80 nm were obtained, respectively. Before coating with the iridium complex, the PEDOT:PSS layers were annealed at 150 °C for 10 min. The iridium complex thin films were then annealed, instead, on a hotplate at 90 °C for 1 h under N<sub>2</sub> atmosphere. A 20 nm layer of SnO<sub>2</sub> was deposited by ALD using an Arradience's GEMStar XT Thermal ALD system integrated into a nitrogen-filled glovebox. For that, the ALD chamber was heated to 90 °C, the bottle containing the Sn precursor (tetrakis(dimethylamino) tin, TDAT) was heated to 60 °C while the bottle of oxidizer (water) was not heated, and the precursor and oxidizer manifolds were heated to 115 and 140 °C, respectively. Prior to deposition, the tubes and valves in the manifolds were degassed three times by performing a series of 30 pulses with the bottles manually closed. The edges of the ITO contacts were protected with Dupont's polyimide Kapton tape and then the substrates were inserted in the ALD chamber, which was

then evacuated. One ALD cycle consisted of consecutive purges of TDAT for 550 ms and water vapor for 200 ms, each followed by N<sub>2</sub> purges of 30 and 105 s, respectively, to ensure the complete removal of the precursors from the ALD chamber (final growth per cycle: 1.5 Å). Finally, 140 nm of ITO were deposited by Pulsed Laser Deposition technique (Solmates large area 200 mm PLD system) with a chamber pressure of 0.042 mbar and an O<sub>2</sub> partial pressure of 0.0076 mbar, controlled by a constant injection of an oxygen/argon gas mix, and at room temperature. This PLD tool is coupled to a N<sub>2</sub> glovebox, to minimize any detrimental effects from O<sub>2</sub> and moisture on the performance of the finally produced devices. A Lightmachinery IPEX-700 KrF excimer laser (λ = 248 nm) was employed, setting the repetition rate at 25 Hz and a fluence of 1.5–1.7 J cm<sup>-2</sup>. The source material for ITO deposition was a Sn:In<sub>2</sub>O<sub>3</sub> ceramic target with 2:98 wt%. The substrates were taped to shadow masks to obtain the final deposition layouts. Shadow masks were used during the ITO deposition to obtain a final active area of 6 mm<sup>2</sup>. To increase the conductivity of the ITO cathode, Au fingers of 50 nm were thermally evaporated at the side of the cathode without covering the active area of the cells. The final active area of the down side of the LEC is of 6 mm<sup>2</sup> while on the up side the active area measures 4.8 mm<sup>2</sup>. For the reference devices, 100 nm Al cathode was deposited via thermal evaporation using a shadow mask. The final active area of the cells was of 6 mm<sup>2</sup>. Samples on glass or glass/ITO substrates for photophysical and surface characterization followed exactly the same fabrication steps. The following samples were fabricated for the photophysical measures on glass/ITO substrates: PEDOT:PSS/Ir, PEDOT:PSS/Ir/SnO<sub>2</sub>, PEDOT:PSS/Ir/SnO<sub>2</sub>/ITO, and PEDOT:PSS/Ir/ITO.

**Photophysical Measurements:** The absorbance and transmittance were measured with an Avantes AvaLight-DS-S-BAL deuterium halogen light source and an Avantes AvaSpec-2048L spectrometer. While the photoluminescence was measured in an N-M01 integrated sphere and a FLS1000 Edinburg Spectrometer, the PL-lifetimes were measured with a Hamamatsu Quantaurus-Tau C11367 with an excitation LED light source of 365 nm and 1800 s measurement time in air.

**Atomic Force Microscopy:** AFM measurements were collected in a Multimode atomic force microscope (Veeco Instruments, Inc.). The images were obtained with a Si tip with frequency and K of ≈300 kHz and 40 N·m<sup>-1</sup>, respectively, using the tapping mode in air at room temperature. Images were recorded with a 0.5–1 Hz scan rate.

**X-Ray Photoelectron Spectroscopy:** The SnO<sub>2</sub> samples on glass substrates were analyzed with a Thermo Scientific K-alpha compact X-ray photoelectron spectrometer with a monochromatized Al K-alpha radiation of 1486.6 eV and a base pressure of 4 × 10<sup>-9</sup> mbar.

**Sheet Resistance Measurement:** A manual four point resistivity probe equipment (Signatone S-301-4 PWK) and a Keithley were employed.

**LECs Characterization:** The devices were measured by applying a pulsed current density of  $50 \text{ A m}^{-2}$  while monitoring the voltage and luminance versus time by using a True Color Sensor MAZeT (MTCSICT sensor) with a Botest OLT OLED Lifetime-Test system. The applied pulsed current consisted in block waves at a frequency of 1000 Hz with a duty cycle of 50%. As a result, the average current density and voltage were obtained by multiplying the values by the time-on (0.5 s) and dividing by the total cycle time (1 s). The sensor measured the average value of the luminance during the chosen duty cycle. The electroluminescence spectra were measured with an optical fiber connected to an Avantes AvaSpec-2048L spectrometer while driving the cell with a Botest OLT OLED Lifetime-Test system. The simultaneous photocurrent of the same pixel was recorded through two picoamperometers perpendicularly placed at the same distance from the pixel, while a constant current density of  $50 \text{ A m}^{-2}$  was applied with a Keithley. Thinner gold fingers were deposited on these devices to have the same active area from both dies. The LEC characterization was conducted under nitrogen atmosphere.

## Supporting Information

Supporting Information is available from the Wiley Online Library or from the author.

## Acknowledgements

The authors thank Jorge Ferrando for his technical support. The research leading to these results has received funding from the European Research Council (ERC) under the European Union's Horizon 2020 research and innovation programme (Grant agreement No. 834431), from Projects PCI2019-111829-2 and PID2021-126444OB-I00 funded by MCIN/AEI/10.13039/501100011033 and by the European Union, from Project CEX2019-000919-M funded by MCIN/AEI/10.13039/501100011033, and from Project PDC2021-121317-I00 funded by MCIN/AEI/10.13039/501100011033 and by the "European Union NextGenerationEU/PRTR". This work also received financial support from the Comunitat Valenciana (IDIFEDER/2018/061, CIGE/2021/027, and Prometeu/2020/077). K.P.S.Z. acknowledges funding from Comunitat Valenciana (APOSTD/2021/368). A.P. acknowledges his Grisolia grant from the Comunitat Valenciana (GRISOLIAP/2020/134).

## Conflict of Interest

The authors declare no conflict of interest.

## Data Availability Statement

The data that support the findings of this study are available from the corresponding author upon reasonable request.

## Keywords

atomic layer deposition, high transmittance, light-emitting electrochemical cells, pulsed laser deposition, transparent devices

Received: August 22, 2022  
Revised: September 8, 2022  
Published online:

- [1] C. S. Buga, J. C. Viana, *Adv. Mater. Technol.* **2021**, *6*, 2001016.
- [2] R. Pode, *Renewable Sustainable Energy Rev.* **2020**, *133*, 110043.
- [3] M. G. Song, K. S. Kim, H. I. Yang, S. K. Kim, J. H. Kim, C. W. Han, H. C. Choi, R. Pode, J. H. Kwon, *Org. Electron.* **2020**, *76*, 105418.
- [4] L. Liu, K. Cao, S. Chen, W. Huang, *Adv. Opt. Mater.* **2020**, *8*, 2001122.
- [5] M. Morales-Masis, S. De Wolf, R. Woods-Robinson, J. W. Ager, C. Ballif, *Adv. Electron. Mater.* **2017**, *3*, 1600529.
- [6] D. Li, W.-Y. Lai, Y.-Z. Zhang, W. Huang, *Adv. Mater.* **2018**, *30*, 1704738.
- [7] E. Aydin, C. Altinkaya, Y. Smirnov, M. A. Yaqin, K. P. S. Zanoni, A. Paliwal, Y. Firdaus, T. G. Allen, T. D. Anthopoulos, H. J. Bolink, M. Morales-Masis, S. De Wolf, *Matter* **2021**, *4*, 3549.
- [8] C. Y. Han, K. H. Lee, M. S. Kim, J. W. Shin, J. S. Kim, J. H. Hwang, T. Kim, M. S. Oh, J. Kim, Y. R. Do, H. Yang, *Org. Electron.* **2017**, *45*, 145.
- [9] J. H. Oh, J. W. Park, *Phys. Status Solidi RRL* **2020**, *14*, 1900707.
- [10] J. H. Oh, J. W. Park, *Org. Electron.* **2021**, *96*, 106252.
- [11] Y. Yasuda, S. Kobayashi, T. Uchida, Y. Hoshi, *Thin Solid Films* **2020**, *698*, 137868.
- [12] Y. J. Lee, J. H. Kim, J. N. Jang, I. H. Yang, S. N. Kwon, M. P. Hong, D. C. Kim, K. S. Oh, S. J. Yoo, B. J. Lee, W. G. Jang, *Thin Solid Films* **2009**, *517*, 4019.
- [13] W. Wang, H. Peng, S. Chen, *J. Mater. Chem. C* **2016**, *4*, 1838.
- [14] J. Xu, A. Sandström, E. M. Lindh, W. Yang, S. Tang, L. Edman, *ACS Appl. Mater. Interfaces* **2018**, *10*, 33380.
- [15] S. Kanagaraj, A. Puthanveedu, Y. Choe, *Adv. Funct. Mater.* **2020**, *30*, 1907126.
- [16] J. Gao, *ChemPlusChem* **2018**, *83*, 183.
- [17] A. Mishra, M. Alahbakhshi, R. Haroldson, L. D. Bastatas, Q. Gu, A. A. Zakhidov, J. D. Slinker, *Adv. Opt. Mater.* **2020**, *8*, 2000226.
- [18] J. Mindemark, L. Edman, *J. Mater. Chem. C* **2016**, *4*, 420.
- [19] M. H. Bowler, A. Mishra, A. C. Adams, C. L. D. Blangy, J. D. Slinker, *Adv. Funct. Mater.* **2020**, *30*, 1906715.
- [20] J. Mindemark, S. Tang, H. Li, L. Edman, *Adv. Funct. Mater.* **2018**, *28*, 1801295.
- [21] J. Mindemark, S. Tang, J. Wang, N. Kaihovirta, D. Brandell, L. Edman, *Chem. Mater.* **2016**, *28*, 2618.
- [22] L. Mardegan, C. Dreessen, M. Sessolo, D. Tordera, H. J. Bolink, *Adv. Funct. Mater.* **2021**, *31*, 2104249.
- [23] C. E. Housecroft, E. C. Constable, *Coord. Chem. Rev.* **2017**, *350*, 155.
- [24] C. Zhang, R. Liu, D. Zhang, L. Duan, *Adv. Funct. Mater.* **2020**, *30*, 1907156.
- [25] E. Auroux, A. Sandström, C. Larsen, P. Lundberg, T. Wågberg, L. Edman, *Org. Electron.* **2020**, *84*, 105812.
- [26] G. Qian, Y. Lin, G. Wantz, A. R. Davis, K. R. Carter, J. J. Watkins, *Adv. Funct. Mater.* **2014**, *24*, 4484.
- [27] J. D. Slinker, A. A. Gorodetsky, M. S. Lowry, J. Wang, S. Parker, R. Rohl, S. Bernhard, G. G. Malliaras, *J. Am. Chem. Soc.* **2004**, *126*, 2763.
- [28] K. P. S. Zanoni, A. Paliwal, M. A. Hernández-Fenollosa, P.-A. Repecaud, M. Morales-Masis, H. J. Bolink, *Adv. Mater. Technol.* **2022**, <https://doi.org/10.1002/admt.202101747>.
- [29] G. K. Dalapati, H. Sharma, A. Guchhait, N. Chakraborty, P. Bamola, Q. Liu, G. Saianand, A. M. Sai Krishna, S. Mukhopadhyay, A. Dey, T. K. S. Wong, S. Zhuk, S. Ghosh, S. Chakraborty, C. Mahata, S. Biring, A. Kumar, C. S. Ribeiro, S. Ramakrishna, A. K. Chakraborty, S. Krishnamurthy, P. Sonar, M. Sharma, *J. Mater. Chem. A* **2021**, *9*, 16621.
- [30] Q. Jiang, X. Zhang, J. You, *Small* **2018**, *14*, 1801154.
- [31] H. Wang, H. Yu, W. Xu, Z. Yuan, Z. Yan, C. Wang, X. Liu, M. Fahlman, J. M. Liu, X. K. Liu, F. Gao, *J. Mater. Chem. C* **2018**, *6*, 6996.
- [32] Y. Liu, S. Wei, G. Wang, J. Tong, J. Li, D. Pan, *Langmuir* **2020**, *36*, 6605.

- [33] M. N. Mullings, C. Hägglund, S. F. Bent, *J. Vac. Sci. Technol., A* **2013**, 31, 061503.
- [34] J. Heo, A. S. Hock, R. G. Gordon, *Chem. Mater.* **2010**, 22, 4964.
- [35] D. Choi, J.-S. Park, *Surf. Coat. Technol.* **2014**, 259, 238.
- [36] E. Bandiello, M. Sessolo, H. J. Bolink, *J. Mater. Chem. C* **2016**, 4, 10781.
- [37] J.-H. Lee, M. Yoo, D. Kang, H.-M. Lee, W. Choi, J. W. Park, Y. Yi, H. Y. Kim, J.-S. Park, *ACS Appl. Mater. Interfaces* **2018**, 10, 33335.
- [38] H. Kim, J. S. Horwitz, A. Piqué, C. M. Gilmore, D. B. Chrisey, *Appl. Phys. A: Mater. Sci. Process.* **1999**, 69, S447.
- [39] A. Khodorov, M. Piechowiak, M. J. M. Gomes, *Thin Solid Films* **2007**, 515, 7829.
- [40] R. Liang, J. Dai, L. Xu, J. He, S. Wang, Y. Peng, H. Wang, L. Ye, C. Chen, *IEEE Trans. Electron Devices* **2018**, 65, 2498.
- [41] J. Mei, M. S. Bradley, V. Bulović, *Phys. Rev. B* **2009**, 79, 235205.
- [42] V.-H. Tran, H. Park, S. H. Eom, S. C. Yoon, S.-H. Lee, *ACS Omega* **2018**, 3, 18398.
- [43] L. Yan, Q. Xue, M. Liu, Z. Zhu, J. Tian, Z. Li, Z. Chen, Z. Chen, H. Yan, H.-L. Yip, Y. Cao, *Adv. Mater.* **2018**, 30, 1802509.
- [44] J. M. Caruge, J. E. Halpert, V. Wood, V. Bulović, M. G. Bawendi, *Nat. Photonics* **2008**, 2, 247.
- [45] V. Wood, M. J. Panzer, J. E. Halpert, J.-M. Caruge, M. G. Bawendi, V. Bulović, *ACS Nano* **2009**, 3, 3581.

## PAPER

Cite this: *Dalton Trans.*, 2021, **50**, 17920**A counterion study of a series of [Cu(P<sup>^</sup>P)(N<sup>^</sup>N)][A] compounds with bis(phosphane) and 6-methyl and 6,6'-dimethyl-substituted 2,2'-bipyridine ligands for light-emitting electrochemical cells†**Marco Meyer,<sup>a</sup> Lorenzo Mardegan,<sup>b</sup> Daniel Tordera,<sup>a,b</sup> Alessandro Prescimone,<sup>a</sup> Michele Sessolo,<sup>b</sup> Henk J. Bolink,<sup>b</sup> Edwin C. Constable<sup>a</sup> and Catherine E. Housecroft<sup>a\*</sup>

The syntheses and characterisations of a series of heteroleptic copper(i) compounds [Cu(POP)(Me<sub>2</sub>bpy)][A], [Cu(POP)(Me<sub>2</sub>bpy)][A], [Cu(xantphos)(Me<sub>2</sub>bpy)][A] and [Cu(xantphos)(Me<sub>2</sub>bpy)][A] in which [A]<sup>-</sup> is [BF<sub>4</sub>]<sup>-</sup>, [PF<sub>6</sub>]<sup>-</sup>, [BPh<sub>4</sub>]<sup>-</sup> and [BAR<sup>F</sup><sub>4</sub>]<sup>-</sup> (Me<sub>2</sub>bpy = 6-methyl-2,2'-bipyridine, Me<sub>2</sub>bpy = 6,6'-dimethyl-2,2'-bipyridine, POP = oxydi(2,1-phenylene)bis(diphenylphosphane), xantphos = (9,9-dimethyl-9H-xanthene-4,5-diyl)bis(diphenylphosphane), [BAR<sup>F</sup><sub>4</sub>]<sup>-</sup> = tetrakis(3,5-bis(trifluoromethyl)phenyl)borate) are reported. Nine of the compounds have been characterised by single crystal X-ray crystallography, and the consequences of the different anions on the packing interactions in the solid state are discussed. The effects of the counterion on the photophysical properties of [Cu(POP)(N<sup>^</sup>N)][A] and [Cu(xantphos)(N<sup>^</sup>N)][A] (N<sup>^</sup>N = Me<sub>2</sub>bpy and Me<sub>2</sub>bpy) have been investigated. In the solid-state emission spectra, the highest energy emission maxima are for [Cu(xantphos)(Me<sub>2</sub>bpy)][BPh<sub>4</sub>]<sup>-</sup> and [Cu(xantphos)(Me<sub>2</sub>bpy)][BPh<sub>4</sub>]<sup>-</sup> ( $\lambda_{\text{max}}^{\text{em}}$  = 520 nm) whereas the lowest energy  $\lambda_{\text{max}}^{\text{em}}$  values occur for [Cu(POP)(Me<sub>2</sub>bpy)][PF<sub>6</sub>]<sup>-</sup> and [Cu(POP)(Me<sub>2</sub>bpy)][BPh<sub>4</sub>]<sup>-</sup> (565 nm and 563 nm, respectively). Photoluminescence quantum yields (PLQYs) are noticeably affected by the counterion; in the [Cu(xantphos)(Me<sub>2</sub>bpy)][A] series, solid-state PLQY values decrease from 62% for [PF<sub>6</sub>]<sup>-</sup>, to 44%, 35% and 27% for [BF<sub>4</sub>]<sup>-</sup>, [BPh<sub>4</sub>]<sup>-</sup> and [BAR<sup>F</sup><sub>4</sub>]<sup>-</sup>, respectively. This latter series of compounds was used as active electroluminescent materials on light-emitting electrochemical cells (LECs). The luminophores were mixed with ionic liquids (ILs) [EMIM][A] ([EMIM]<sup>+</sup> = [1-ethyl-3-methylimidazolium]<sup>+</sup>) containing the same or different counterions than the copper(i) complex. LECs containing [Cu(xantphos)(Me<sub>2</sub>bpy)][BPh<sub>4</sub>]<sup>-</sup> and [Cu(xantphos)(Me<sub>2</sub>bpy)][BAR<sup>F</sup><sub>4</sub>]<sup>-</sup> failed to turn on under the LEC operating conditions, whereas those with the smaller [PF<sub>6</sub>]<sup>-</sup> or [BF<sub>4</sub>]<sup>-</sup> counterions had rapid turn-on times and exhibited maximum luminances of 173 and 137 cd m<sup>-2</sup> and current efficiencies of 3.5 and 2.6 cd A<sup>-1</sup>, respectively, when the IL contained the same counterion as the luminophore. Mixing the counterions ([PF<sub>6</sub>]<sup>-</sup> and [BF<sub>4</sub>]<sup>-</sup>) of the active complex and the IL led to a reduction in all the figures of merit of the LECs.

Received 23rd September 2021.

Accepted 2nd November 2021

DOI: 10.1039/d1dt03239a

rsc.li/dalton

**Introduction**

Lighting is a principal user of the world's energy, accounting for around 15% of global energy consumption.<sup>1</sup> The move away from conventional light sources including incandescent lamps and fluorescent tubes is essential in terms of sustainability and conserving energy. Efficient solid-state lighting devices include both light-emitting diodes (LEDs) and organic light-emitting diodes (OLEDs) and, in Europe, these have largely superseded earlier technologies. Light-emitting electrochemical cells (LECs) are an alternative type of lighting device,<sup>2</sup> which can achieve high luminance and high power efficiency while being operated at low voltage.<sup>3–7</sup> Moreover, the architecture of LECs is less complex<sup>8</sup> and is simpler to fabri-

<sup>a</sup>Department of Chemistry, University of Basel, Mattenstrasse 24a, BPR 1096, 4058 Basel, Switzerland. E-mail: catherine.housecroft@unibas.ch

<sup>b</sup>Instituto de Ciencia Molecular (ICMol), Universidad de Valencia, Catedrático José Beltrán 2, 46980 Paterna, Spain. E-mail: daniel.tordera@uv.es

† Electronic supplementary information (ESI) available: Experimental details and analytical data for the copper(i) compounds; Fig. S1–S64: <sup>1</sup>H, HMQC and HMBC NMR spectra and mass spectra; Table S1: Crystallographic data; Fig. S65–74: Structural figures; Fig. S75–S78: Cyclic voltammograms; Table S2: PL properties of thin films and electroluminescence maxima for LECs; Fig. S79: Photography of powdered samples of [Cu(POP)(N<sup>^</sup>N)][A] complexes; Fig. S80: Current current efficiency of the best working LECs. CCDC 2081386–2081394. For ESI and crystallographic data in CIF or other electronic format see DOI: 10.1039/d1dt03239a

cate in comparison to state-of-the-art organic light-emitting diodes (OLEDs).<sup>4</sup>

The design of LECs allows the production of large-area lighting devices on substrates such as glass, metals and flexible materials including polymers, paper<sup>9</sup> and textile fibres.<sup>3,4,10–12</sup> LECs utilise mobile ionic species either as the luminophore or blended with the semiconductor within the same active layer.<sup>2,3,13–15</sup> This layer functions as an ionic conductor.<sup>5,16</sup> In its simplest implementation, the single-layer active composite is sandwiched between an air-stable cathode and anode.<sup>2</sup> LECs are relatively insensitive in terms of the active layer thickness.<sup>6,17,18</sup> Compared to OLEDs, less restriction is placed on the electrode materials because the use of low work-function metals is not required.<sup>19</sup> During device fabrication, coating of the active layer onto the electrode substrate can be carried out under ambient conditions by solution-based techniques such as spin coating,<sup>18,20,21</sup> spray sintering,<sup>3</sup> inkjet printing<sup>22,23</sup> and reel-to-reel<sup>17,18</sup> depositions.<sup>3</sup> Various types of compounds can be used as the emissive species, such as conjugated polymers,<sup>3,11,24–28</sup> small molecules,<sup>29–31</sup> quantum dots,<sup>32–34</sup> perovskites<sup>35–37</sup> and ionic transition metal complexes (iTMCs).<sup>38–44</sup>

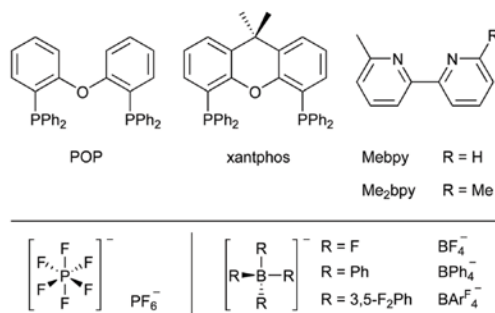
iTMC-LECs have the advantage that the properties of the emissive complexes can be tuned in terms of emission wavelength, excited-state lifetime and quantum yield.<sup>44,45</sup> LECs with iridium(III)-based emitters<sup>40,46–48</sup> have been shown to perform with high efficiencies, luminance values and lifetimes. More recently, Cu-iTMCs have proven to be promising emitting species.<sup>49,50</sup> In contrast to iridium which is among the rarest elements on Earth, copper is abundant and inexpensive which translates to lower production costs and lower consumption of less sustainable elements.<sup>51</sup> Among the most investigated types of copper(I)-based luminophores are  $[\text{Cu}(\text{P}^{\wedge}\text{P})(\text{N}^{\wedge}\text{N})]^+$  complexes where  $\text{P}^{\wedge}\text{P}$  is a chelating bisphosphane, usually a derivative of POP (POP = oxydi(2,1-phenylene)bis(diphenylphosphane)) or xantphos (xantphos = 9,9-dimethyl-9H-xanthene-4,5-diyl)bis(diphenylphosphane)) and  $\text{N}^{\wedge}\text{N}$  is typically a derivative of bpy (bpy = 2,2'-bipyridine) or phen (phen = 1,10-phenanthroline).<sup>13,21,50,52–54</sup>

$[\text{Cu}(\text{P}^{\wedge}\text{P})(\text{N}^{\wedge}\text{N})]^+$  complexes have the advantage of being suitable scaffolds for systematic investigations and tuning of energy levels of the frontier molecular orbitals.<sup>55–57</sup> The spatial localization of the highest occupied molecular orbital (HOMO) has been calculated to mostly reside on the copper centre and partially on the bidentate bis(phosphane) ligand. The lowest unoccupied molecular orbital (LUMO), however, is localized on the diimine ligand.<sup>55,58</sup> Thus, the two energy levels can be tailored independently depending on which of the two ligands is chemically modified. Ideally the two levels are attuned to facilitate charge injection as well as to enable recombination in the active layer.<sup>59</sup> In photoexcitation, where the singlet-singlet transition is spin-allowed, singlet excited states are mostly accessed. During electroluminescence, electrons and holes recombine, each having its own spin. Due to spin statistics, the recombination yields 25% singlet and 75% triplet excitons.<sup>60</sup>  $[\text{Cu}(\text{P}^{\wedge}\text{P})(\text{N}^{\wedge}\text{N})]^+$  complexes often exhibit thermally

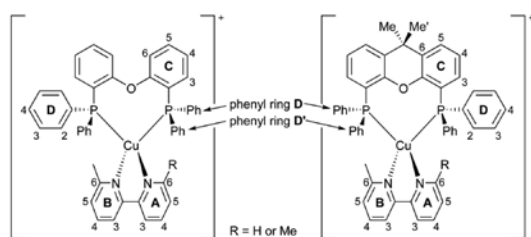
activated delayed fluorescence (TADF).<sup>61</sup> With TADF, harvesting of all spin states of excitons after recombination is, in theory, possible. This leads to theoretical internal quantum efficiency (IQE) values of up to 100%. In contrast, with purely fluorescent emitters only 25% of the excitons can afford photon emission.<sup>59,62</sup> We have previously demonstrated that  $[\text{Cu}(\text{POP})(\text{N}^{\wedge}\text{N})][\text{PF}_6]$  and  $[\text{Cu}(\text{xantphos})(\text{N}^{\wedge}\text{N})][\text{PF}_6]$  compounds, in which the  $\text{N}^{\wedge}\text{N}$  ligand is bpy or a methyl-substituted derivative, exhibit TADF.<sup>20,63</sup>

Currently the operational model of a LEC is described both by the electrochemical doping model (ECDM) and the electrodynamic model (EDM). Both theoretical mechanisms rely on mobile ions in the active layer. The two models are considered to coexist after comprehensive mathematical modelling of experimental data.<sup>14,18,64,65</sup> The ECDM describes the growth of doped regions towards the centre of the emissive layer as an electric potential is applied across the two electrodes. Between the p- and n-doped region, an undoped intrinsic region constitutes the p-i-n junction where recombination takes place.<sup>18,66</sup> The EDM depicts ions being attracted to the electrodes under the applied potential. The ions then form a double layer on the electrodes which shields the centre of the emissive layer from the electric field and facilitates charge injection. Injected charge carriers migrate into the centre where they recombine to form excitons and light is emitted.<sup>45,66</sup> The preferential electrochemical doping model (PECDM) describes the behaviour if only one type of doping occurs. In reality, a combination of the models is thought to be operative as electric double layers are formed before doping takes place.<sup>8,67,68</sup>

It follows from the combination of the two models that the operation of a LEC strongly relies on the mobility of the ions distributed in the active layer. In turn, the mobility depends on the chemical and physical properties of the iTMC as well as the ionic liquid (IL) which is added to the active layer to promote this phenomenon. In the present work, we report a series of  $[\text{Cu}(\text{P}^{\wedge}\text{P})(\text{N}^{\wedge}\text{N})][\text{A}]$  complexes in which  $[\text{A}]^-$  is either  $[\text{PF}_6]^-$ ,  $[\text{BF}_4]^-$ ,  $[\text{BPh}_4]^-$  or  $[\text{BAR}^{\text{F}}_4]^-$  ( $[\text{BAR}^{\text{F}}_4]^-$  = tetrakis(3,5-bis(trifluoromethyl)phenyl)borate) combined with different ionic liquids which are used in LECs. It has previously been reported that the choice of anion has a strong influence on the photophysical and structural characteristics of the Cu(I)-iTMCs.<sup>69–71</sup> In the solid-state, molecular packing has a remarkable effect on the emissive properties of a luminophore, and it has been reported that pairing the complex cations with different counter ions can substantially alter the photoluminescence quantum yield (PLQY) of the salt.<sup>71</sup> We were motivated to investigate the different characteristics and performances of the Cu(I)-complexes in different ILs within the LEC environment. The ILs were selected to have a consistent organic cation combined with anions that mimicked those in the Cu-iTMC. We report a family of 16 heteroleptic  $[\text{Cu}(\text{P}^{\wedge}\text{P})(\text{N}^{\wedge}\text{N})][\text{A}]$  complexes, subdivided into salts of four anions where  $\text{P}^{\wedge}\text{P}$  is either POP/xantphos and  $\text{N}^{\wedge}\text{N}$  represents either 6-methyl-2,2'-bipyridine (Meppy) or 6,6'-dimethyl-2,2'-bipyridine ( $\text{Me}_2\text{bpy}$ ) (Schemes 1 and 2).



**Scheme 1** Top: Structures of the POP and xantphos P<sup>^</sup>P ligands and the Mebpy and Me<sub>2</sub>bpy N<sup>^</sup>N ligands. Bottom: Structures of the [PF<sub>6</sub>]<sup>-</sup>, [BF<sub>4</sub>]<sup>-</sup>, [BPh<sub>4</sub>]<sup>-</sup> and [BARF<sub>4</sub>]<sup>-</sup> anions.



**Scheme 2** Structures of the [Cu(POP)(N<sup>^</sup>N)]<sup>+</sup> and [Cu(xantphos)(N<sup>^</sup>N)]<sup>+</sup> cations with ring and atom labelling for NMR spectroscopic data. When R = H, the rings are labelled A and B as shown. When R = Me, the pyridine rings are equivalent and are labelled B. Non-backbone phenyl rings in the P<sup>^</sup>P ligands are labelled D. The aromatic rings in the [BPh<sub>4</sub>]<sup>-</sup> or [BARF<sub>4</sub>]<sup>-</sup> anions are labelled E.

## Experimental

### General

Reactions under microwave conditions were carried out in a Biotage Initiator + microwave reactor. <sup>1</sup>H, <sup>11</sup>B{<sup>1</sup>H}, <sup>13</sup>C{<sup>1</sup>H}, <sup>19</sup>F{<sup>1</sup>H} and <sup>31</sup>P{<sup>1</sup>H} NMR spectra were recorded at ca. 295 K in acetone-*d*<sub>6</sub> using a Bruker Avance III-500 NMR spectrometer. <sup>1</sup>H and <sup>13</sup>C chemical shifts were referenced to residual solvent peaks (<sup>1</sup>H δ(acetone-*d*<sub>3</sub>) = 2.50 ppm, <sup>13</sup>C δ(acetone-*d*<sub>6</sub>) = 29.84 ppm). Absorption and emission spectra in solution were measured using a Shimadzu UV-2600 spectrophotometer and a Shimadzu RF-5301-PC spectrofluorometer, respectively. A Shimadzu LCMS-2020 instrument was used to record electro-spray (ESI) mass spectra. Quantum yields (dichloromethane (CH<sub>2</sub>Cl<sub>2</sub>) solution and powder) were measured using a Hamamatsu absolute photoluminescence (PL) quantum yield spectrometer C11347 Quantaaurus-QY. Powder emission spectra and excited state lifetimes were measured with a Hamamatsu Compact Fluorescence lifetime Spectrometer C11367 Quantaaurus-Tau using an LED light source (λ<sub>exc</sub> = 365 nm). Lifetimes were obtained by fitting the measured data to an exponential decay using MATLAB®; a biexponential fit was

used when a single exponential fit gave a poor fit. Where stated, the sample was degassed using argon bubbling for 20 min. PL spectra and PLQY measurements of the pure thin films were carried out using a Xe lamp and a monochromator as excitation source at 365 nm and an integrated sphere coupled to a spectrometer (Hamamatsu C9920-02 with a Hamamatsu PMA-11 optical detector). Electrochemical measurements used an Ametek VersaSTAT 3F potentiostat with [<sup>18</sup>Bu<sub>4</sub>N][PF<sub>6</sub>] (0.1 M) as supporting electrolyte and a scan rate of 0.1 V s<sup>-1</sup>; the solvent was dry propylene carbonate and solution concentrations were ca. 2 × 10<sup>-3</sup> mol dm<sup>-3</sup>. The solutions were constantly degassed with argon bubbling. The working electrode was glassy carbon, the reference electrode was a leakless Ag<sup>+</sup>/AgCl (eDAQ ET069-1, filling electrolyte aqueous KCl, conc. 3.4 mol L<sup>-1</sup>) and the counter-electrode was a platinum wire. Final potentials were internally referenced with respect to the Fc/Fc<sup>+</sup> couple.

[Cu(MeCN)<sub>4</sub>][PF<sub>6</sub>] was prepared according to the literature procedure.<sup>72</sup> Me<sub>2</sub>bpy was purchased from Fluorochem. 2-Pyridylzinc bromide, POP and xantphos were purchased from Acros Organics. 2-Chloro-6-methylpyridine and Na[BArF<sub>4</sub>] were bought from Apollo Scientific, Na[BPh<sub>4</sub>] from Fluka, and [Pd(PPh<sub>3</sub>)<sub>4</sub>], [EMIM][PF<sub>6</sub>] and [EMIM][BF<sub>4</sub>] from Sigma Aldrich. Mebpy was prepared by a Negishi coupling reaction following a microwave reactor adaption<sup>56</sup> of a literature method.<sup>73</sup> The NMR spectroscopic data were consistent with those reported.<sup>73</sup>

### Syntheses and characterization of all copper(i) compounds

Details of syntheses, <sup>1</sup>H, <sup>13</sup>C{<sup>1</sup>H}, <sup>11</sup>B{<sup>1</sup>H}, <sup>19</sup>F{<sup>1</sup>H}, and <sup>31</sup>P{<sup>1</sup>H} NMR characterization and assignments, electrospray mass spectrometric data, and elemental analyses are given in the ESI.†

### General procedures for [PF<sub>6</sub>]<sup>-</sup> and [BF<sub>4</sub>]<sup>-</sup> salts of the copper(i) complexes

POP-containing compounds were synthesized by the following procedure: POP (1.1 eq.) and [Cu(MeCN)<sub>4</sub>][PF<sub>6</sub>] or [Cu(MeCN)<sub>4</sub>][BF<sub>4</sub>] (1.0 eq.) were dissolved in CH<sub>2</sub>Cl<sub>2</sub> (20 mL) and the reaction mixture was stirred for 1.5 h. The desired N<sup>^</sup>N ligand (1.0 eq.) was added, followed by stirring of the mixture for 2 h. The solvent was then removed under reduced pressure. The residue was purified by precipitation from CH<sub>2</sub>Cl<sub>2</sub> with diethyl ether (Et<sub>2</sub>O), followed by centrifugation and decantation of the supernatant. This step was repeated four times. Then the product was washed with cyclohexane (100 mL).

Compounds containing xantphos were prepared according to the following procedure: a solution of the appropriate N<sup>^</sup>N ligand (1.0 eq.) and xantphos (1.1 eq.) in CH<sub>2</sub>Cl<sub>2</sub> (10 mL) was added dropwise to a CH<sub>2</sub>Cl<sub>2</sub> solution (10 mL) of [Cu(MeCN)<sub>4</sub>][PF<sub>6</sub>] or [Cu(MeCN)<sub>4</sub>][BF<sub>4</sub>] (1.0 eq.). The reaction mixture was then stirred for 2 h before the solvent was removed under reduced pressure. The residue was purified by precipitation from CH<sub>2</sub>Cl<sub>2</sub> with Et<sub>2</sub>O, followed by centrifugation and decantation of the supernatant. This step was repeated four times. Then the product was washed with cyclo-

hexane (100 mL) and dried under high vacuum. Detailed experimental conditions are given in the ESI.†

#### General procedures for [BPh<sub>4</sub>]<sup>-</sup> and [BAR<sup>F</sup><sub>4</sub>]<sup>-</sup> salts of the copper(i) complexes

The following procedure was adapted from a literature method.<sup>74</sup> To synthesise the [BPh<sub>4</sub>]<sup>-</sup> and [BAR<sup>F</sup><sub>4</sub>]<sup>-</sup> salts, an ion exchange was carried out starting with the appropriate [PF<sub>6</sub>]<sup>-</sup> salt.

The [PF<sub>6</sub>]<sup>-</sup> salt (1.0 eq.) of the desired complex was dissolved in a minimal amount of MeOH at 45 °C while sonicating. Then NaBPh<sub>4</sub> (1.3 eq.) or NaBAR<sup>F</sup><sub>4</sub> (1.3 eq.), respectively, was added to the warm solution. The mixture was sonicated and H<sub>2</sub>O (60 mL) was added to precipitate the product. The product was washed with H<sub>2</sub>O and dried under vacuum.

The products were purified as follows. The crude product was dissolved in CH<sub>2</sub>Cl<sub>2</sub> (20 mL) and water was added (15 mL). The mixture was vigorously shaken, centrifuged and the aqueous phase was removed. The organic phase was dried with MgSO<sub>4</sub>. The product was precipitated from CH<sub>2</sub>Cl<sub>2</sub> with Et<sub>2</sub>O, followed by centrifugation and decantation of the supernatant. This step was repeated three times. Then the product was washed with cyclohexane (100 mL) and dried under vacuum. Details of the conditions for each complex are given in the ESI.†

#### Crystallography

Crystallographic data for all the compounds are presented in Table S1.† Single crystal data were collected on a Bruker APEX-II diffractometer (CuKα radiation, see Table S1†) with data reduction, solution and refinement using the programs APEX,<sup>75</sup> ShelXT,<sup>76</sup> Olex2,<sup>77</sup> and ShelXL v. 2014/7,<sup>78</sup> or using a STOE StadiVari diffractometer equipped with a Pilatus300K detector and with a Metaljet D2 source (GaKα radiation, see Table S1†) and solving the structure using Superflip,<sup>79,80</sup> and Olex2.<sup>77</sup> The structural model was refined with ShelXL v. 2014/7.<sup>78</sup> Structure analysis used Mercury CSD v. 2021.1.0.<sup>81</sup>

In [Cu(xantphos)(Mebpy)][BF<sub>4</sub>]-CH<sub>2</sub>Cl<sub>2</sub>-Et<sub>2</sub>O, a solvent mask was used to treat the solvent region, and the removed electron density equated to one CH<sub>2</sub>Cl<sub>2</sub> and one Et<sub>2</sub>O molecule per Cu, which have been added to all the formulae and metrics. In [Cu(xantphos)(Me<sub>2</sub>bpy)][BF<sub>4</sub>]-0.5C<sub>6</sub>H<sub>12</sub>-0.8Me<sub>2</sub>CO, part of the solvent region was treated with a solvent mask and 0.8 molecules of acetone were added to the formula and relevant data.

In [Cu(POP)(Mebpy)][PF<sub>6</sub>]-0.5CH<sub>2</sub>Cl<sub>2</sub>-0.3Et<sub>2</sub>O, the region of the solvent contained disordered CH<sub>2</sub>Cl<sub>2</sub> and Et<sub>2</sub>O molecules which were modelled over two sites with partial occupancies 0.5 and 0.3, respectively. The dichloromethane molecules in [Cu(xantphos)(Mebpy)][PF<sub>6</sub>]-0.5CH<sub>2</sub>Cl<sub>2</sub>-Et<sub>2</sub>O were modelled with half occupancy sites. The anion in [Cu(xantphos)(Mebpy)][BF<sub>4</sub>]-CH<sub>2</sub>Cl<sub>2</sub>-Et<sub>2</sub>O was disordered and was modelled over two sites with a common B position, and F atoms in half-occupancy sites. In [Cu(POP)(Me<sub>2</sub>bpy)][BAR<sup>F</sup><sub>4</sub>], three CF<sub>3</sub> groups in the [BAR<sup>F</sup><sub>4</sub>]<sup>-</sup> anion were rotationally disordered; the CF<sub>3</sub> groups with F24 and F26, and with F19 and F29 were each modelled over two sites of equal occupancies, and the CF<sub>3</sub> group with F1, F20 and F31 was modelled over three sites of equal occupancies. In [Cu(POP)(Mebpy)][BAR<sup>F</sup><sub>4</sub>]-C<sub>6</sub>H<sub>12</sub>, the dis-

ordered Mebpy ligand was modelled over two, equal occupancy sites. In addition, three of the CF<sub>3</sub> groups in the [BAR<sup>F</sup><sub>4</sub>]<sup>-</sup> anion were rotationally disordered; the group containing F7 and F33 was modelled over sites with fractional occupancies of 0.65 and 0.35, respectively, and that with F14 and F34 was modelled over two equal occupancy sites, and the CF<sub>3</sub> group with F19, F25 and F28 was modelled over three sites with fractional occupancies of 0.4, 0.4 and 0.2, respectively.

#### Device preparation and characterization

Solutions of the copper(i) complexes were mixed in a molar ratio of 4:1 with an ionic liquid (IL) containing the same anion as the copper(i) compound. The ILs comprised [1-ethyl-3-methylimidazolium]<sup>+</sup> ([EMIM]<sup>+</sup>) with [PF<sub>6</sub>]<sup>-</sup>, [BF<sub>4</sub>]<sup>-</sup>, [BPh<sub>4</sub>]<sup>-</sup> and [BAR<sup>F</sup><sub>4</sub>]<sup>-</sup> counterions. The solutions of ILs were prepared in CH<sub>2</sub>Cl<sub>2</sub> at a concentration of 10 mg mL<sup>-1</sup>. Solutions of the [Cu(xantphos)(Me<sub>2</sub>bpy)]<sup>+</sup> series containing [Cu(xantphos)(Me<sub>2</sub>bpy)][PF<sub>6</sub>], [Cu(xantphos)(Me<sub>2</sub>bpy)][BF<sub>4</sub>], [Cu(xantphos)(Me<sub>2</sub>bpy)][BPh<sub>4</sub>] or [Cu(xantphos)(Me<sub>2</sub>bpy)][BAR<sup>F</sup><sub>4</sub>] were prepared in CH<sub>2</sub>Cl<sub>2</sub> to a final concentration of 15 mg mL<sup>-1</sup>. Dissolution in CH<sub>2</sub>Cl<sub>2</sub> of both the iTMC and ionic liquids as well as the final mixed solution was instantaneous and no further heating and stirring was needed. Pre-patterned indium tin oxide (ITO)-coated glass plates were used as transparent conductive substrates. They were subsequently cleaned ultrasonically in soapy-water, water, and propan-2-ol baths. After drying, the substrates were placed in an UV-ozone cleaner (Jelight 42-220) for 20 min. The ITO substrates were first coated with PEDOT:PSS (PEDOT = poly(3,4-ethylenedioxythiophene), PSS = polystyrenesulfonate) and iTMC-IL solutions. Thicknesses of 100 nm and 80 nm were obtained respectively. Before depositing the light-emitting layer, the PEDOT:PSS layers were annealed on a hotplate at 150 °C for 10 minutes. The copper(i) complex thin films were then annealed at 70 °C for 30 minutes. Devices were also prepared by changing the counter ion of the IL added to the copper complex to study the effect of the anion size on the device performance. This was done by mixing [Cu(xantphos)(Me<sub>2</sub>bpy)][PF<sub>6</sub>] with [EMIM][BF<sub>4</sub>] and [Cu(xantphos)(Me<sub>2</sub>bpy)][BF<sub>4</sub>], [Cu(xantphos)(Me<sub>2</sub>bpy)][BPh<sub>4</sub>] or [Cu(xantphos)(Me<sub>2</sub>bpy)][BAR<sup>F</sup><sub>4</sub>] with [EMIM][PF<sub>6</sub>]. Finally, an Al electrode (100 nm) was thermally evaporated on top of the active layer using a shadow mask under inert atmosphere. The final active area of the cells was 6 mm<sup>2</sup>. The thickness of the PEDOT:PSS and the active layer were determined with an Ambios XP-1 profilometer. The devices were measured by applying a pulsed current density of 50 A m<sup>-2</sup> while monitoring the voltage and luminance *versus* time by using a True Color Sensor MAZeT (MTCSiCT sensor) with a Botest OLT OLED Lifetime-Test system. The applied pulsed current consisted of block waves at a frequency of 1000 Hz with a duty cycle of 50%. Hence, the average current density and voltage were obtained by multiplying the values by the time-on (0.5 s) and dividing by the total cycle time (1 s). Electroluminescence (EL) spectra were recorded by driving the cells with the Botest OLT system and an optical fibre connected to the Avant spectrometer AvaSpec - 2048L.



## Results and discussion

### Synthesis of [Cu(P<sup>^</sup>P)(N<sup>^</sup>N)][PF<sub>6</sub>] and [Cu(P<sup>^</sup>P)(N<sup>^</sup>N)][BF<sub>4</sub>]

The different strategies for preparing heteroleptic [Cu(P<sup>^</sup>P)(N<sup>^</sup>N)][PF<sub>6</sub>] and [Cu(xantphos)(N<sup>^</sup>N)][BF<sub>4</sub>] complexes have been detailed previously.<sup>21,53,55,58</sup> The formation of heteroleptic complexes over the kinetically more favoured homoleptic [Cu(N<sup>^</sup>N)<sub>2</sub>][A] complexes was ensured by the following optimizations. To obtain the heteroleptic [Cu(POP)(N<sup>^</sup>N)][A] complexes, 1.1 equivalents of POP were added to [Cu(MeCN)<sub>4</sub>][A], followed by the addition of the N<sup>^</sup>N ligand after 2 hours. Residual excess POP was removed in the purification steps (see Experimental section). To obtain the heteroleptic [Cu(xantphos)(N<sup>^</sup>N)][A] complexes, a solution containing both the N<sup>^</sup>N ligand and xantphos were added to a solution of [Cu(MeCN)<sub>4</sub>][A]. These procedures were followed to afford the [Cu(POP)(N<sup>^</sup>N)][A] and [Cu(xantphos)(N<sup>^</sup>N)][A] complexes (P<sup>^</sup>P = POP or xantphos; N<sup>^</sup>N = Mebpy or Me<sub>2</sub>bpy; [A]<sup>-</sup> = [PF<sub>6</sub>]<sup>-</sup> or [BF<sub>4</sub>]<sup>-</sup>) as yellow solids in yields of 72–94%.

### Synthesis of [Cu(P<sup>^</sup>P)(N<sup>^</sup>N)][BPh<sub>4</sub>] and [Cu(P<sup>^</sup>P)(N<sup>^</sup>N)][BAR<sup>F</sup><sub>4</sub>]

The complexes containing [BPh<sub>4</sub>]<sup>-</sup> and [BAR<sup>F</sup><sub>4</sub>]<sup>-</sup> anions were prepared by anion exchange starting from the corresponding [PF<sub>6</sub>]<sup>-</sup> salt and adding an excess of NaBPh<sub>4</sub> or NaBAR<sup>F</sup><sub>4</sub>, respectively. For the [BPh<sub>4</sub>]<sup>-</sup> salts, the anion exchange was conducted in two steps to ensure complete replacement of [PF<sub>6</sub>]<sup>-</sup> ions. During the washing process, H<sub>2</sub>O was used to remove NaPF<sub>6</sub> or NaBF<sub>4</sub> generated in the ion exchange. In further purification steps, any remaining impurities were removed using Et<sub>2</sub>O and cyclohexane. [Cu(POP)(N<sup>^</sup>N)][A] and [Cu(xantphos)(N<sup>^</sup>N)][A] ([A]<sup>-</sup> = [BPh<sub>4</sub>]<sup>-</sup> or [BAR<sup>F</sup><sub>4</sub>]<sup>-</sup>) were obtained as yellow solids in yields of 72–84%.

### Characterisation of the copper(i) complexes

The positive mode electrospray mass spectrum of each compound exhibited peak envelopes arising from the [Cu(POP)(N<sup>^</sup>N)]<sup>+</sup> or [Cu(xantphos)(N<sup>^</sup>N)]<sup>+</sup> cations as well as from the [Cu(POP)]<sup>+</sup> or [Cu(xantphos)]<sup>+</sup> cation (see Experimental section in ESI<sup>†</sup>).

<sup>1</sup>H, <sup>13</sup>C{<sup>1</sup>H}, and, where appropriate, <sup>11</sup>B{<sup>1</sup>H}, <sup>19</sup>F{<sup>1</sup>H} and <sup>31</sup>P{<sup>1</sup>H} NMR spectra were recorded at room temperature in acetone-*d*<sub>6</sub> solutions. The <sup>1</sup>H and <sup>13</sup>C{<sup>1</sup>H} spectra were assigned using COSY, NOESY, HMQC and HMBC techniques; atom labelling used for NMR assignments are given in Scheme 2. Fig. 1 shows the aromatic regions of the <sup>1</sup>H NMR spectra of [Cu(POP)(Mebpy)][BF<sub>4</sub>], [Cu(POP)(Me<sub>2</sub>bpy)][BF<sub>4</sub>], [Cu(xantphos)(Mebpy)][BF<sub>4</sub>] and [Cu(xantphos)(Me<sub>2</sub>bpy)][BF<sub>4</sub>] as representative examples (see Fig. S1–S64<sup>†</sup> for <sup>1</sup>H, HMQC and HMBC NMR and ESI-MS spectra of all the complexes).

### Structural characterizations

X-ray quality single crystals of: [Cu(POP)(Mebpy)][PF<sub>6</sub>].0.5CH<sub>2</sub>Cl<sub>2</sub>.0.3Et<sub>2</sub>O, [Cu(xantphos)(Mebpy)][PF<sub>6</sub>].0.5CH<sub>2</sub>Cl<sub>2</sub>.Et<sub>2</sub>O, [Cu(xantphos)(Mebpy)][BF<sub>4</sub>].CH<sub>2</sub>Cl<sub>2</sub>.Et<sub>2</sub>O and [Cu(xantphos)(Me<sub>2</sub>bpy)][PF<sub>6</sub>] were grown by slow diffusion of Et<sub>2</sub>O into CH<sub>2</sub>Cl<sub>2</sub> solutions of the compounds.

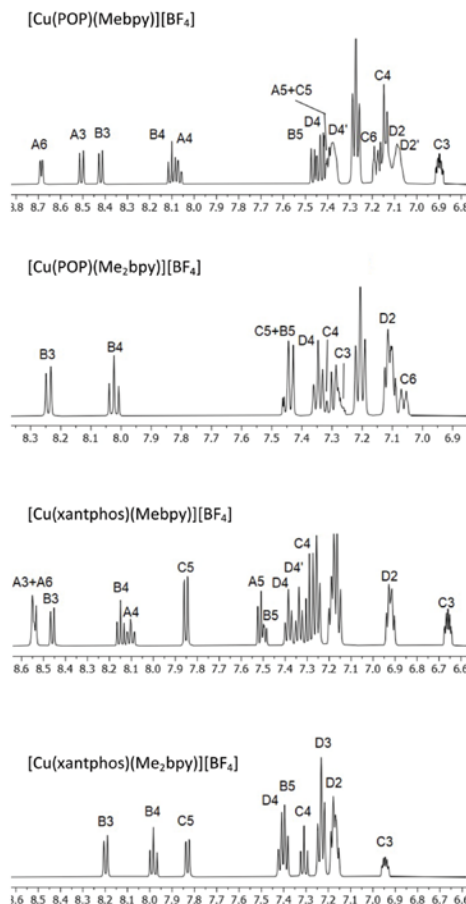


Fig. 1 Part of the 500 MHz <sup>1</sup>H NMR spectra of [Cu(POP)(Mebpy)][BF<sub>4</sub>], [Cu(POP)(Me<sub>2</sub>bpy)][BF<sub>4</sub>], [Cu(xantphos)(Mebpy)][BF<sub>4</sub>] and [Cu(xantphos)(Me<sub>2</sub>bpy)][BF<sub>4</sub>] in acetone-*d*<sub>6</sub>. Chemical shifts in δ/ppm. See Fig. S18–32<sup>†</sup> for the complete spectra. Atom labels are defined in Scheme 2.

Those of: [Cu(POP)(Mebpy)][BAR<sup>F</sup><sub>4</sub>].C<sub>6</sub>H<sub>12</sub>, [Cu(POP)(Me<sub>2</sub>bpy)][BAR<sup>F</sup><sub>4</sub>].0.5C<sub>6</sub>H<sub>12</sub>.0.8(CH<sub>3</sub>)<sub>2</sub>CO, [Cu(xantphos)(Me<sub>2</sub>bpy)][BF<sub>4</sub>].C<sub>6</sub>H<sub>12</sub>, [Cu(xantphos)(Me<sub>2</sub>bpy)][BPh<sub>4</sub>].0.7C<sub>3</sub>H<sub>6</sub>O and [Cu(xantphos)(Me<sub>2</sub>bpy)][BAR<sup>F</sup><sub>4</sub>] were grown by slow diffusion of cyclohexane into acetone solutions of the complexes.

Crystallographic data are summarized in Table S1,<sup>†</sup> and important angles and bond distances defining the copper(i) coordination sphere are summarized in Table 1 together with published data for the benchmark compounds [Cu(POP)(bpy)][PF<sub>6</sub>].CHCl<sub>3</sub><sup>13</sup> and [Cu(xantphos)(bpy)][PF<sub>6</sub>]<sup>55</sup> for comparison. The molecular structures of the complex cations are shown in Fig. S65–S74.<sup>†</sup> Most of the complexes crystallized in the triclinic space group *P* $\bar{1}$  with exceptions being [Cu(POP)(Mebpy)][PF<sub>6</sub>].0.5CH<sub>2</sub>Cl<sub>2</sub>.0.3Et<sub>2</sub>O (monoclinic *P*<sub>21</sub>/*n*), [Cu(POP)(Mebpy)][BAR<sup>F</sup><sub>4</sub>].C<sub>6</sub>H<sub>12</sub> (monoclinic *P*<sub>21</sub>/*n*), [Cu(xantphos)

(Me<sub>2</sub>bpy)]][PF<sub>6</sub>] (orthorhombic *P*2<sub>1</sub>2<sub>1</sub>2<sub>1</sub> with two crystallographically independent ion-pairs) and [Cu(xantphos)(Me<sub>2</sub>bpy)]][BPh<sub>4</sub>]-0.7Me<sub>2</sub>CO (orthorhombic *Pna*2<sub>1</sub> with two crystallographically independent ion-pairs). In [Cu(POP)(Me<sub>2</sub>bpy)]][BAR<sup>F</sup><sub>4</sub>], the Me<sub>2</sub>bpy ligand is disordered over two sites, each with 50% occupancy. The chiral space group of [Cu(xantphos)(Me<sub>2</sub>bpy)]][PF<sub>6</sub>] (*P*2<sub>1</sub>2<sub>1</sub>2<sub>1</sub>) with a Flack parameter of 0.370 (6) indicates a non-racemic mixture of the two enantiomers in the crystal lattice resulting from twinning by inversion. We have previously reported the structure of this compound (CSD Refcode GABVAJ),<sup>58</sup> but in this case, it crystallized in the triclinic space group *P*1̄. The structure determinations confirm the expected bidentate chelating mode of both the bisphosphane and diimine ligands (Fig. 2a). The copper(i) centres exhibit a tetrahedral coordination geometry with varying degrees of distortion. The angles between the N–Cu–N plane and the P–Cu–P plane range from almost orthogonal (89.49°) to moderate distortion (86.18°) (Table 1).

In both [Cu(xantphos)(Me<sub>2</sub>bpy)]][PF<sub>6</sub>] and [Cu(xantphos)(Me<sub>2</sub>bpy)]][BF<sub>4</sub>], the 6-methyl substituent points towards the 'bowl-shaped' xanthene unit of the P<sup>∧</sup>P ligand (Fig. 2b). The geometry of the bpy ligand is also characterized by the dihedral N–C–C–N torsional angle which ranges from a significant inter-ring torsion value of –17.7(4)° in [Cu(xantphos)(Me<sub>2</sub>bpy)]][BAR<sup>F</sup><sub>4</sub>] and 11.0(9)° in [Cu(POP)(Me<sub>2</sub>bpy)]][BAR<sup>F</sup><sub>4</sub>] to almost coplanar pyridine rings (torsion angle = 0.9(8)°) in [Cu(xantphos)(Me<sub>2</sub>bpy)]][BPh<sub>4</sub>]. The P–Cu–P chelating angles vary considerably from 111.54(3)° ([Cu(xantphos)(Me<sub>2</sub>bpy)]][BF<sub>4</sub>]) to 121.53(8)° ([Cu(xantphos)(Me<sub>2</sub>bpy)]][PF<sub>6</sub>]). As expected, the N–Cu–N chelating angles vary little, being in a range from 79.0(2)° ([Cu(xantphos)(Me<sub>2</sub>bpy)]][PF<sub>6</sub>]) to 81.4(3)° ([Cu(POP)(Me<sub>2</sub>bpy)]][BAR<sup>F</sup><sub>4</sub>]). The Cu–N and Cu–P distances all lie within a typical range of 1.983(6) to 2.163(6) Å and 2.2296(8) to 2.306(2) Å, respectively.

With the exception of [Cu(xantphos)(Me<sub>2</sub>bpy)]][PF<sub>6</sub>], all the xantphos-containing structures exhibit offset face-to-face

π-stacking interactions between phenyl rings of two different PPh<sub>2</sub> units (Fig. 2c). In [Cu(xantphos)(Me<sub>2</sub>bpy)]][PF<sub>6</sub>], the angle between the planes containing the π-stacked phenyl rings is 5.8°, the average of the two centroid...plane distances is 3.73 Å and the centroid...centroid distance is 3.84 Å. These parameters are 9.9°, 3.60 Å and 3.86 Å for [Cu(xantphos)(Me<sub>2</sub>bpy)]][BF<sub>4</sub>], 13.3°, 3.66 Å and 3.87 Å for [Cu(xantphos)(Me<sub>2</sub>bpy)]][BPh<sub>4</sub>], 17.3°, 4.05 Å and 4.17 Å for one of the crystallographically independent cations in [Cu(xantphos)(Me<sub>2</sub>bpy)]][BPh<sub>4</sub>] and 14.36°, 3.79 Å and 3.84 Å for [Cu(xantphos)(Me<sub>2</sub>bpy)]][BAR<sup>F</sup><sub>4</sub>]. These all comply with the definitions delineated by Janiak.<sup>82</sup> The first independent cation in [Cu(xantphos)(Me<sub>2</sub>bpy)]][BPh<sub>4</sub>] exhibits two C–H...π contacts between one phenyl ring of each PPh<sub>2</sub> group and the bpy domain (Fig. S74†) which are in agreement with Nishio.<sup>83</sup> The remaining two phenyl rings engage in a π-stacking interaction with each other. The second independent cation in [Cu(xantphos)(Me<sub>2</sub>bpy)]][BPh<sub>4</sub>] features a phenyl ring from one PPh<sub>2</sub>-unit π-stacked over the bpy domain (Fig. 2e). The angle between the least-squares planes containing the phenyl ring and the bpy is 8.6°, the average of the two centroid...plane distances is 3.37 Å and the centroid...centroid distance is 3.40 Å. The phenyl rings mentioned above, exhibiting π-stacking interactions in the first independent cation, show instead C–H...π – contacts in the second cation (Fig. 2d). This interaction is agreement with Nishio.<sup>83</sup> The structural feature of a phenyl ring from one PPh<sub>2</sub>-unit π-stacked over the bpy domain (Fig. 2e) is also seen in the two independent cations in [Cu(xantphos)(Me<sub>2</sub>bpy)]][PF<sub>6</sub>]. For these two cations, the angle between the least-squares planes containing the phenyl ring and the bpy-ligand is 17.56°, 18.92°, the average of the two centroid...plane distances is 3.52 Å, 3.51 Å and the centroid...centroid distance is 3.66 Å, 3.61 Å. In the initially reported structure of [Cu(xantphos)(Me<sub>2</sub>bpy)]][PF<sub>6</sub>], intramolecular π-stacking between phenyl rings was observed.<sup>58</sup>

**Table 1** Important structural parameters in the cations in [Cu(P<sup>∧</sup>P)(N<sup>∧</sup>N)][A]. Benchmark [Cu(P<sup>∧</sup>P)(bpy)]][PF<sub>6</sub>] complexes are included for comparison

Complex	P–Cu–P chelating angle /°	N–Cu–N chelating angle /°	P...P distance/Å	Angle between PCuP and NCuN planes/°	N–C–C–N torsion angle/°
[Cu(POP)(bpy)]][PF <sub>6</sub> ] <sup>a</sup>	115.00(3)	79.66(7)	3.790(1)	88.5	–2.8(3)
[Cu(POP)(Me <sub>2</sub> bpy)]][PF <sub>6</sub> ] <sup>b</sup>	112.93(3)	80.11(9)	3.773(1)	87.41	–8.0(4)
[Cu(POP)(Me <sub>2</sub> bpy)]][BAR <sup>F</sup> <sub>4</sub> ] <sup>c</sup> 1 (50%)	115.43(4)	79.1(2)	3.826(1)	88.66	8.8(9)
[Cu(POP)(Me <sub>2</sub> bpy)]][BAR <sup>F</sup> <sub>4</sub> ] <sup>c</sup> 2 (50%)	115.43(4)	81.4(3)	3.826(1)	89.49	11.0(9)
[Cu(POP)(Me <sub>2</sub> bpy)]][BAR <sup>F</sup> <sub>4</sub> ] <sup>d</sup>	115.92(3)	80.5(1)	3.855(6)	88.64	–2.6(4)
[Cu(xantphos)(bpy)]][PF <sub>6</sub> ] <sup>d</sup>	113.816(14)	79.32(5)	3.801(5)	79.6	20.5(2)
[Cu(xantphos)(Me <sub>2</sub> bpy)]][PF <sub>6</sub> ] <sup>b</sup>	113.44(3)	80.8(1)	3.777(1)	87.89	–1.9(5)
[Cu(xantphos)(Me <sub>2</sub> bpy)]][BF <sub>4</sub> ] <sup>b</sup>	113.34(3)	81.1(1)	3.778(1)	88.79	–1.0(5)
[Cu(xantphos)(Me <sub>2</sub> bpy)]][PF <sub>6</sub> ] <sup>e</sup> 1 <sup>e</sup>	121.53(8)	79.1(2)	4.016(3)	86.18	–10(1)
[Cu(xantphos)(Me <sub>2</sub> bpy)]][PF <sub>6</sub> ] <sup>e</sup> 2 <sup>e</sup>	117.77(8)	79.0(2)	3.926(3)	86.28	7(1)
[Cu(xantphos)(Me <sub>2</sub> bpy)]][BF <sub>4</sub> ] <sup>b</sup>	111.54(3)	79.60(9)	3.777(1)	89.16	2.6(4)
[Cu(xantphos)(Me <sub>2</sub> bpy)]][BPh <sub>4</sub> ] <sup>b</sup> 1 <sup>e</sup>	117.99(7)	79.3(2)	3.913(2)	88.21	0.9(8)
[Cu(xantphos)(Me <sub>2</sub> bpy)]][BPh <sub>4</sub> ] <sup>b</sup> 2 <sup>e</sup>	113.48(7)	78.9(2)	3.841(2)	86.92	–1.0(8)
[Cu(xantphos)(Me <sub>2</sub> bpy)]][BAR <sup>F</sup> <sub>4</sub> ] <sup>b</sup>	113.12(3)	79.02(9)	3.821(1)	88.88	–17.7(4)

<sup>a</sup> Data for [Cu(POP)(bpy)]][PF<sub>6</sub>]-CHCl<sub>3</sub>.<sup>13</sup> <sup>b</sup> Two different solvent molecules. <sup>c</sup> Me<sub>2</sub>bpy ligand is disordered over two orientations with 50% occupancy each. <sup>d</sup> Data for [Cu(xantphos)(bpy)]][PF<sub>6</sub>].<sup>55</sup> <sup>e</sup> Two crystallographically independent ion-pairs.

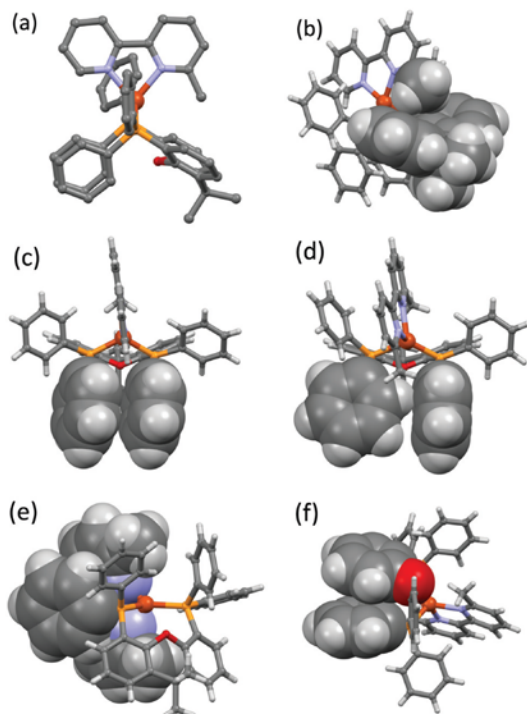


Fig. 2 Selected structural features of the  $[\text{Cu}(\text{P}^{\text{A}}\text{P})(\text{N}^{\text{A}}\text{N})]^+$  cations (H-atoms omitted for clarity): (a) perspective along the P–P vector perpendicular to the  $\text{Me}_2\text{bpy}$ -plane in  $[\text{Cu}(\text{xantphos})(\text{Me}_2\text{bpy})][\text{PF}_6]$ ; (b) accommodation of the 6-Me group of  $\text{Me}_2\text{bpy}$  within the xantphos 'cavity' in  $[\text{Cu}(\text{xantphos})(\text{Me}_2\text{bpy})][\text{PF}_6]$ ; (c) face-to-face  $\pi$ -stacking of two phenyl rings connected to the two different  $\text{PPh}_2$  units in  $[\text{Cu}(\text{xantphos})(\text{Me}_2\text{bpy})][\text{PF}_6]$ ; (d) interaction of two phenyl rings connected to the two different  $\text{PPh}_2$  units in  $[\text{Cu}(\text{xantphos})(\text{Me}_2\text{bpy})][\text{PF}_6]$ ; (e) offset  $\pi$ -stacking of one POP-phenyl ring with the  $\text{Me}_2\text{bpy}$  ligand in  $[\text{Cu}(\text{xantphos})(\text{Me}_2\text{bpy})][\text{PF}_6]$ ; (f) face-to-face  $\pi$ -stacking of one POP-phenyl ring with a POP backbone ring in  $[\text{Cu}(\text{POP})(\text{Me}_2\text{bpy})][\text{PF}_6]$ .

Two of the POP-containing structures feature a  $\pi$ -stacking interaction between one phenyl ring of a  $\text{PPh}_2$  unit and one arene ring of the POP backbone (Fig. 2f). The angle between the planes containing the  $\pi$ -stacked phenyl and arene rings is  $18.1^\circ$ , the average of the two centroid...plane distances is  $3.73 \text{ \AA}$  and the centroid...centroid distance is  $3.58 \text{ \AA}$  for  $[\text{Cu}(\text{POP})(\text{Me}_2\text{bpy})][\text{PF}_6]$ . The corresponding parameters are  $14.1^\circ$ ,  $3.58 \text{ \AA}$  and  $3.78 \text{ \AA}$  for  $[\text{Cu}(\text{POP})(\text{Me}_2\text{bpy})][\text{BARF}_4]$ .

The effect of altering the spatial requirements of the anion, and of introducing anions with the potential for  $\pi$ -stacking interactions can be assessed by considering one series in which the copper(i) cation remains constant. Fig. 3 compares the packing in the unit cells of  $[\text{Cu}(\text{xantphos})(\text{Me}_2\text{bpy})][\text{A}]$  where  $\text{A}^-$  is  $[\text{PF}_6]^-$  (Fig. 3a),  $[\text{BF}_4]^-$  (Fig. 3b),  $[\text{BPh}_4]^-$  (Fig. 3c), and  $[\text{BARF}_4]^-$  (Fig. 3d). It is clear from the figure that cation...cation interactions are essentially switched off in  $[\text{Cu}(\text{xantphos})(\text{Me}_2\text{bpy})][\text{BARF}_4]$  as a consequence of the steric demands

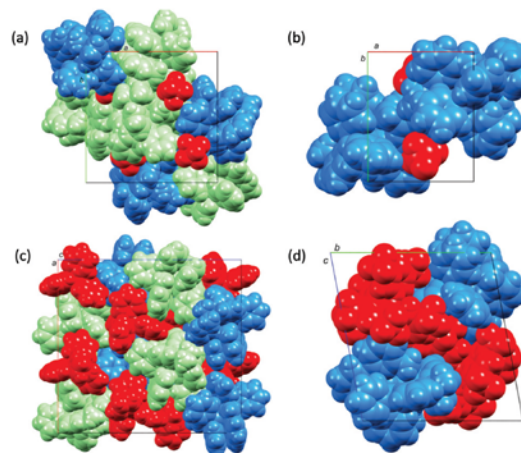


Fig. 3 Packing of cations (blue and green) and anions (red) in (a)  $[\text{Cu}(\text{xantphos})(\text{Me}_2\text{bpy})][\text{PF}_6]$  (two crystallographically independent ion-pairs), (b)  $[\text{Cu}(\text{xantphos})(\text{Me}_2\text{bpy})][\text{BF}_4]$ , (c)  $[\text{Cu}(\text{xantphos})(\text{Me}_2\text{bpy})][\text{BPh}_4]$  (two independent ion-pairs), and (d)  $[\text{Cu}(\text{xantphos})(\text{Me}_2\text{bpy})][\text{BARF}_4]$ . Solvent molecules have been omitted.

of the anions. In contrast, in  $[\text{Cu}(\text{xantphos})(\text{Me}_2\text{bpy})][\text{PF}_6]$  and  $[\text{Cu}(\text{xantphos})(\text{Me}_2\text{bpy})][\text{BF}_4]$ , cation...anion interactions comprise C–H...F contacts, but accommodation of the  $[\text{BF}_4]^-$  and  $[\text{PF}_6]^-$  anions in the lattices still permits cation...cation interactions (Fig. 4). In the  $[\text{BF}_4]^-$  salt, pairs of cations embrace across an inversion centre with multiple edge-to-face interactions (Fig. 4). In addition, one CH unit in the phenyl ring containing C19 engages in a CH... $\pi$  interaction with the phenyl ring containing C13<sup>i</sup> (symmetry code  $i = -x, 1 - y, 1 - z$ ; C–H...centroid =  $2.72 \text{ \AA}$ , angle C–H...centroid =  $147^\circ$ ). Finally, the  $\text{Me}_2\text{bpy}$  C4–H4 unit forms a CH... $\pi$  contact with the phenyl ring containing C19<sup>ii</sup> (symmetry code  $ii = 1 + x, y, z$ ; C–H...centroid =  $2.77 \text{ \AA}$ , angle C–H...centroid =  $132^\circ$ ).  $[\text{Cu}(\text{xantphos})(\text{Me}_2\text{bpy})][\text{PF}_6]$  contains two crystallographically independent cations which engage in an offset face-to-face  $\pi$ -stacking interaction between the phenyl ring containing C40

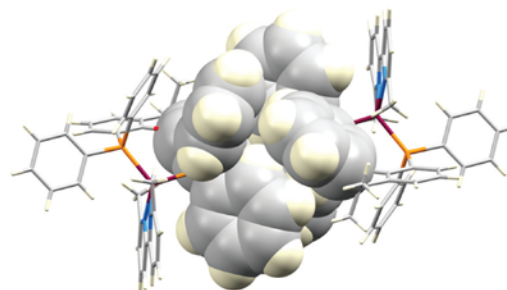


Fig. 4 Centrosymmetric embrace of two  $[\text{Cu}(\text{xantphos})(\text{Me}_2\text{bpy})]^+$  cations in  $[\text{Cu}(\text{xantphos})(\text{Me}_2\text{bpy})][\text{BF}_4]$ .

and the pyridine ring with N3 (see Fig. S70† for atom numbers). The distance between the ring centroids is 3.79 Å and angle between the ring planes is 14.6°. There are additional intermolecular CH... $\pi$  contacts. Adjacent CH units in the xantphos ligand containing C86 and C87 (see Fig. S70†) are directed towards the  $\pi$ -system of the phenyl ring with C64<sup>i</sup> (symmetry code  $i = 1 - x, 1/2 + y, 3/2 - z$ ); an analogous interaction involves xantphos units C34H34 and C35H35 and the phenyl ring containing C13<sup>ii</sup> (symmetry code  $ii = -x, 1/2 + y, 3/2 - z$ ).

### Electrochemistry

The redox properties of the complexes were investigated by cyclic voltammetry in dry propylene carbonate solution containing 0.1 mol dm<sup>-3</sup> [<sup>n</sup>Bu<sub>4</sub>N][PF<sub>6</sub>] as supporting electrolyte. The cyclic voltammograms of the complexes are presented in Fig. S75–S78.† Potentials were referenced internally to ferrocene. In each cyclic voltammogram (CV), the Cu<sup>+</sup>/Cu<sup>2+</sup> oxidation appears between  $E_{pa} = +0.81$  and +0.93 V and is typically an irreversible process (see Table 2). For the two families, the Cu<sup>+</sup>/Cu<sup>2+</sup> oxidation moves to a higher potential when going from the Mebpy to the Me<sub>2</sub>bpy complexes. As the copper centre is formally oxidized from Cu(I) to Cu(II), the coordination geometry changes from tetrahedral to square planar. This can be rationalized by the two methyl substituents in Me<sub>2</sub>bpy preventing flattening of the Cu coordination sphere, resulting in a higher oxidation potential for the Me<sub>2</sub>bpy-containing compounds. For compounds containing the [Cu(xantphos)(Mebpy)]<sup>+</sup> and [Cu(xantphos)(Me<sub>2</sub>bpy)]<sup>+</sup> cations, the Cu<sup>+</sup>/Cu<sup>2+</sup> process was partially reversible and  $E_{1/2}^{ox}$  values are given in Table 2. In all the complexes, one partially reversible ligand-centred reduction process was observed with  $E_{pc}$  between -2.1 and -2.7 V. The CVs of the [BPh<sub>4</sub>]<sup>-</sup> salts show an additional irreversible oxidation peak with  $E_{pa}$  between +0.48 and +0.60 V consistent with the [BPh<sub>4</sub>]<sup>-</sup> anion undergoing an oxidation process at low potentials.

### Photophysical properties

The absorption spectra of solutions of the complexes in CH<sub>2</sub>Cl<sub>2</sub> exhibit intense high-energy absorption bands below ca. 330 nm arising from ligand-centred and, in the case of the [BPh<sub>4</sub>]<sup>-</sup> and [BAr<sup>F</sup><sub>4</sub>]<sup>-</sup> salts, counterion-centred  $\pi^* \leftarrow \pi$  transitions. Additionally, each spectrum comprises a broad, lower intensity metal-to-ligand charge transfer (MLCT) band with  $\lambda_{max}$  in the range 373–385 nm for the POP-containing complexes and in the range 373–381 nm for the xantphos-containing complexes. The spectra are displayed in Fig. 5 and 6 and the absorption data are given in Table 3.

The MLCT absorption of the Me<sub>2</sub>bpy-containing complexes is shifted to higher energies compared to the analogous Mebpy-containing compounds (Table 3). This is consistent with the electron-donating methyl groups destabilizing the LUMO to a greater extent in the Me<sub>2</sub>bpy – compared to the Mebpy containing compounds, the LUMO being mainly located on the N<sup>^</sup>N ligand.

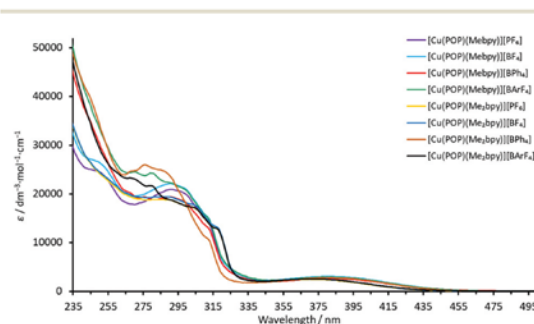


Fig. 5 Solution absorption spectra (CH<sub>2</sub>Cl<sub>2</sub>, 2.5 × 10<sup>-5</sup> mol dm<sup>-3</sup>) of the POP-containing heteroleptic copper(I) complexes.

**Table 2** Cyclic voltammetric data for [Cu(P<sup>^</sup>A)(N<sup>^</sup>N)]<sup>+</sup>[A]<sup>-</sup> in propylene carbonate (10<sup>-4</sup> to 10<sup>-5</sup> mol dm<sup>-3</sup>, vs. Fc/Fc<sup>+</sup>, [<sup>n</sup>Bu<sub>4</sub>N][PF<sub>6</sub>]) as supporting electrolyte, scan rate = 0.1 V s<sup>-1</sup>). When the oxidative process is reversible, both  $E_{1/2}^{ox}$  and  $E_{pa} - E_{pc}$  are given. In case of an irreversible oxidative process,  $E_{pa}$  is given

Complex	Oxidative process			BPh <sub>4</sub> oxidation $E_{pa}/V$ (irrev.)	Reductive process $E_{1/2}^{red}/V$
	$E_{1/2}^{ox}/V$	$E_{pa} - E_{pc}/mV$	$E_{pa}/V$		
[Cu(POP)(Mebpy)][PF <sub>6</sub> ]	—	—	+0.81	—	-2.08
[Cu(POP)(Mebpy)][BF <sub>4</sub> ]	—	—	+0.81	—	-2.10
[Cu(POP)(Mebpy)][BPh <sub>4</sub> ]	—	—	+0.82	+0.48	-2.13
[Cu(POP)(Mebpy)][BAr <sup>F</sup> <sub>4</sub> ]	—	—	+0.82	—	-2.10
[Cu(POP)(Me <sub>2</sub> bpy)][PF <sub>6</sub> ]	—	—	+0.93	—	-2.06
[Cu(POP)(Me <sub>2</sub> bpy)][BF <sub>4</sub> ]	—	—	+0.93	—	-2.07
[Cu(POP)(Me <sub>2</sub> bpy)][BPh <sub>4</sub> ]	—	—	+0.92	+0.60	-2.05
[Cu(POP)(Me <sub>2</sub> bpy)][BAr <sup>F</sup> <sub>4</sub> ]	—	—	+0.92	—	-2.07
[Cu(xantphos)(Mebpy)][PF <sub>6</sub> ]	—	—	+0.92	—	-2.11
[Cu(xantphos)(Mebpy)][BF <sub>4</sub> ]	—	—	+0.90	—	-2.05
[Cu(xantphos)(Mebpy)][BPh <sub>4</sub> ]	+0.85	13	+0.91	+0.46	-2.05
[Cu(xantphos)(Mebpy)][BAr <sup>F</sup> <sub>4</sub> ]	—	—	+0.90	—	-2.07
[Cu(xantphos)(Me <sub>2</sub> bpy)][PF <sub>6</sub> ]	—	—	+0.91	—	-2.06
[Cu(xantphos)(Me <sub>2</sub> bpy)][BF <sub>4</sub> ]	+0.84	14	+0.91	—	-2.08
[Cu(xantphos)(Me <sub>2</sub> bpy)][BPh <sub>4</sub> ]	+0.86	15	+0.93	+0.49	-2.07
[Cu(xantphos)(Me <sub>2</sub> bpy)][BAr <sup>F</sup> <sub>4</sub> ]	+0.84	17	+0.92	—	-2.09

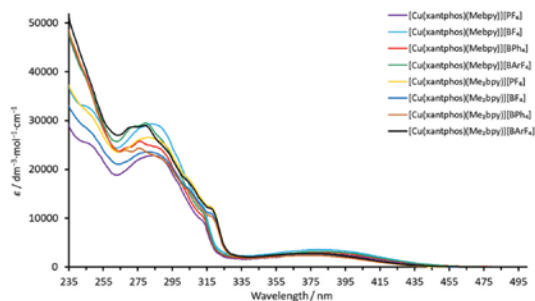


Fig. 6 Solution absorption spectra ( $\text{CH}_2\text{Cl}_2$ ,  $2.5 \times 10^{-5}$  mol  $\text{dm}^{-3}$ ) of the xantphos-containing heteroleptic copper(I) complexes.

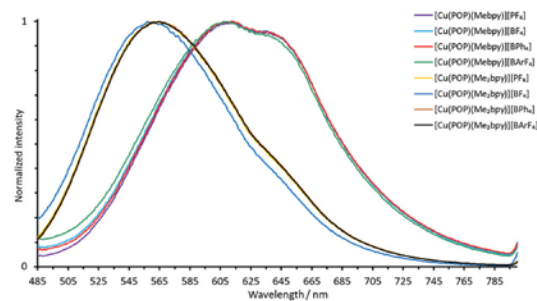


Fig. 7 Normalized solution emission spectra of the POP-containing heteroleptic copper(I) complexes (deaerated  $\text{CH}_2\text{Cl}_2$ ,  $1.0 \times 10^{-5}$  mol  $\text{dm}^{-3}$ ,  $\lambda_{\text{exc}} = 365$  nm).

The normalized solution emission spectra of the complexes in deaerated  $\text{CH}_2\text{Cl}_2$  solution with excitation wavelengths in the region of their MLCT band are displayed in Fig. 7 and 8. The solid-state (powder) emission spectra of the complexes are shown in Fig. 9 and 10, and photophysical data are summarized in Table 4. Solution emission spectra were measured with an excitation wavelength of  $\lambda_{\text{exc}} = 410$  nm to avoid overlapping of the second harmonic of the excitation peak with the broad emission band. Excitation at  $\lambda_{\text{exc}} = 365$  nm resulted in an identical emission band after normalization.

The solid-state emission maxima of the complexes lie between 520 and 565 nm and thus, the complexes are green to yellow emitters in powdered form. In solution, the emission maxima are red-shifted to a range between 560 and 636 nm which gives yellow to orange emission. This red-shift corresponds to previous observations for similar families of complexes.<sup>58</sup> Upon changing from complexes containing Mebpy to  $\text{Me}_2\text{bpy}$  for a given P^P ligand, the solution emission maxima are significantly blue-shifted in the range of 55–60 nm, caused by the increased steric stabilization of the coordination sphere. The previously reported solution emission maxima of

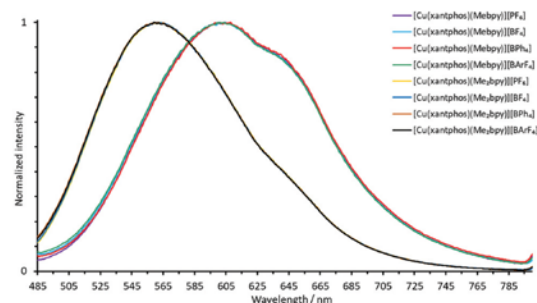


Fig. 8 Normalized solution emission spectra of the xantphos-containing heteroleptic copper(I) complexes (deaerated  $\text{CH}_2\text{Cl}_2$ ,  $1.0 \times 10^{-5}$  mol  $\text{dm}^{-3}$ ,  $\lambda_{\text{exc}} = 365$  nm).

$\lambda_{\text{em}}^{\text{max}} = 618, 649$  nm for  $[\text{Cu}(\text{POP})(\text{bpy})][\text{PF}_6]$  and  $\lambda_{\text{em}}^{\text{max}} = 620, 650$  nm for  $[\text{Cu}(\text{xantphos})(\text{bpy})][\text{PF}_6]$  are consistent with this.<sup>55</sup>

In the solid-state emission spectra, the highest energy emission maxima are for  $[\text{Cu}(\text{xantphos})(\text{Mebpy})][\text{BPh}_4]$  and

Table 3 Absorption maxima for  $\text{CH}_2\text{Cl}_2$  solutions of  $[\text{Cu}(\text{P}^{\wedge}\text{P})(\text{N}^{\wedge}\text{N})][\text{A}]$

Complex	$\lambda_{\text{max}}/\text{nm}$ ( $\epsilon_{\text{max}}/\text{dm}^3 \text{ mol}^{-1} \text{ cm}^{-1}$ )		MLCT
	$\pi^* \leftarrow \pi$		
$[\text{Cu}(\text{POP})(\text{Mebpy})][\text{PF}_6]$	252 sh (24 700), 292 (21 800), 301 sh (20 400), 313 sh (14 100)		385 (3300)
$[\text{Cu}(\text{POP})(\text{Mebpy})][\text{BF}_4]$	251 sh (26 200), 292 (22 200), 302 sh (19 900), 313 sh (14 500)		383 (3100)
$[\text{Cu}(\text{POP})(\text{Mebpy})][\text{BPh}_4]$	269 (19 700), 278 (19 000), 291 (19 300), 300 sh (18 000), 313 sh (12 500)		383 (2600)
$[\text{Cu}(\text{POP})(\text{Mebpy})][\text{BARf}_4]$	271 (24 000), 282 (23 500), 291 (21 800), 301 sh (19 900), 313 sh (14 200)		383 (3000)
$[\text{Cu}(\text{POP})(\text{Me}_2\text{bpy})][\text{PF}_6]$	290 (18 200), 305 (16 400), 318 sh (12 000)		374 (2410)
$[\text{Cu}(\text{POP})(\text{Me}_2\text{bpy})][\text{BF}_4]$	287 (18 000), 305 (16 000), 317 sh (11 500)		373 (2430)
$[\text{Cu}(\text{POP})(\text{Me}_2\text{bpy})][\text{BPh}_4]$	269 (26 800), 276 (25 100), 287 (23 800), 290 (23 200), 312 sh (10 300)		378 (2410)
$[\text{Cu}(\text{POP})(\text{Me}_2\text{bpy})][\text{BARf}_4]$	269 (22 800), 280 (21 000), 292 (18 300), 305 (16 600), 317 sh (12 800)		373 (2500)
$[\text{Cu}(\text{xantphos})(\text{Mebpy})][\text{PF}_6]$	247 sh (24 600), 275 (21 400), 285 (22 300), 289 (21 800), 313 sh (9400)		379 (2620)
$[\text{Cu}(\text{xantphos})(\text{Mebpy})][\text{BF}_4]$	247 sh (31 800), 275 (27 800), 284 (28 600), 292 (26 300), 313 sh (11 700)		380 (3260)
$[\text{Cu}(\text{xantphos})(\text{Mebpy})][\text{BPh}_4]$	269 (24 300), 276 (25 600), 287 (24 200), 312 sh (10 500)		380 (2820)
$[\text{Cu}(\text{xantphos})(\text{Mebpy})][\text{BARf}_4]$	271 (28 500), 281 (29 300), 288 (26 400), 312 sh (11 400)		381 (3080)
$[\text{Cu}(\text{xantphos})(\text{Me}_2\text{bpy})][\text{PF}_6]$	246 (31 700), 279 (26 700), 285 (26 500), 304 (18 200), 316 (12 200)		374 (2580)
$[\text{Cu}(\text{xantphos})(\text{Me}_2\text{bpy})][\text{BF}_4]$	248 sh (28 700), 276 (23 900), 282 (24 300), 292 (22 500), 305 sh (16 200), 318 sh (11 000)		375 (2630)
$[\text{Cu}(\text{xantphos})(\text{Me}_2\text{bpy})][\text{BPh}_4]$	267 (23 300), 276 (23 700), 284 (22 400), 290 (21 200), 304 sh (15 300), 319 sh (9500)		376 (2200)
$[\text{Cu}(\text{xantphos})(\text{Me}_2\text{bpy})][\text{BARf}_4]$	271 (28 100), 280 (28 400), 292 sh (23 400), 304 sh (17 300), 318 sh (11 600)		374 (2680)

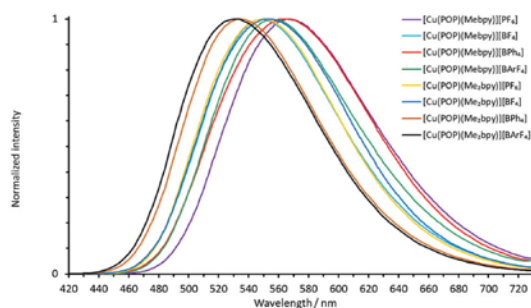


Fig. 9 Normalized emission spectra of powdered samples of the POP-containing heteroleptic copper(I) complexes ( $\lambda_{\text{exc}} = 365 \text{ nm}$ ).

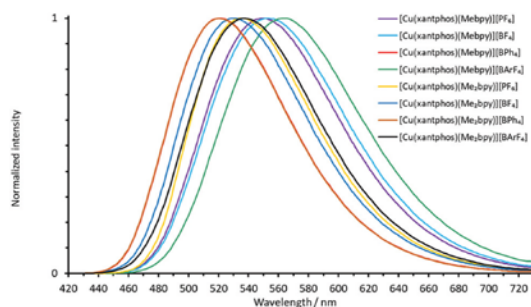


Fig. 10 Normalized emission spectra of powdered samples of the xantphos-containing heteroleptic copper(I) complexes ( $\lambda_{\text{exc}} = 365 \text{ nm}$ ).

[Cu(xantphos)(Me<sub>2</sub>bpy)][BPh<sub>4</sub>] ( $\lambda_{\text{max}}^{\text{em}} = 520 \text{ nm}$ ) whereas the lowest energy emission maxima are for [Cu(POP)(Me<sub>2</sub>bpy)][PF<sub>6</sub>] and [Cu(POP)(Me<sub>2</sub>bpy)][BPh<sub>4</sub>] with  $\lambda_{\text{max}}^{\text{em}} = 565 \text{ nm}$  and  $563 \text{ nm}$ ,

respectively. Upon going from complexes containing Me<sub>2</sub>bpy to Me<sub>2</sub>bpy for a given P<sup>^</sup>P ligand, the solid-state emission maxima undergo a blue-shift of 15–30 nm.

The appearance and luminescence of powdered samples of the [Cu(xantphos)(N<sup>^</sup>N)][A] and [Cu(POP)(N<sup>^</sup>N)][A] complexes are illustrated in Fig. 11 and Fig. S79,<sup>†</sup> respectively, with samples shown under daylight and under UV irradiation ( $\lambda_{\text{exc}} = 366 \text{ nm}$ ).

The emissive behaviour of the complexes is enhanced in the solid-state relative to deaerated solution. The solid-state PLQY values lie within the range of 10–62%, compared to solution values of 0.9–14% (Table 4). Salts of [Cu(POP)(Me<sub>2</sub>bpy)]<sup>+</sup> and [Cu(xantphos)(Me<sub>2</sub>bpy)]<sup>+</sup> have the highest PLQYs both in the solid state and solution which can be ascribed to the increased steric hindrance in the Cu(I) coordination sphere provided by the Me<sub>2</sub>bpy ligand. This impedes flattening of the tetrahedron upon excitation. This is consistent with the solid-state PLQY-values reported for the unsubstituted bpy containing complexes of 3.0% for [Cu(POP)(bpy)][PF<sub>6</sub>] and 1.7% for [Cu(xantphos)(bpy)][PF<sub>6</sub>].<sup>55</sup> Sterically protected copper centres are less accessible to, for example, solvent molecules. Exciton quenching by non-radiative intermolecular processes like collisional quenching, Förster resonance energy transfer<sup>84</sup> and Dexter electron transfer<sup>85</sup> are also expected to be reduced. In solution, salts of [Cu(POP)(Me<sub>2</sub>bpy)]<sup>+</sup> have the highest PLQYs (Table 4, average 13%). In contrast, in the solid state, salts of [Cu(xantphos)(Me<sub>2</sub>bpy)]<sup>+</sup> show the highest PLQY values with a range of 27–62% (Table 4). The solid-state PLQY of [Cu(POP)(Me<sub>2</sub>bpy)][PF<sub>6</sub>] of 12% is higher than the value we have previously reported (9.5%).<sup>21</sup> On the other hand, for [Cu(POP)(Me<sub>2</sub>bpy)][PF<sub>6</sub>], a lower solid-state PLQY of 34% was measured compared to the reported 38%.<sup>21</sup> There is also some variation when comparing the measured PLQY values of 62% for [Cu(xantphos)(Me<sub>2</sub>bpy)][PF<sub>6</sub>] to the reported value of 37%,

Table 4 Photophysical properties of the [Cu(P<sup>^</sup>P)(N<sup>^</sup>N)][A] complexes

Complex	Solution (CH <sub>2</sub> Cl <sub>2</sub> , de-aerated, $1.0 \times 10^{-5} \text{ mol dm}^{-3}$ )				Powder					
	$\lambda_{\text{exc}}/\text{nm}$	$\lambda_{\text{max}}^{\text{em}}/\text{nm}$	PLQY/%	$\tau/\mu\text{s}$	$\lambda_{\text{exc}}/\text{nm}$	$\lambda_{\text{max}}^{\text{em}}/\text{nm}$	PLQY/%	$\tau^a/\mu\text{s}$	$\tau(1)/\mu\text{s} (A_1)$	$\tau(2)/\mu\text{s} (A_2)$
[Cu(POP)(Me <sub>2</sub> bpy)][PF <sub>6</sub> ]	410	609, 637	1.1	0.37	365	565	12	2.9	0.6 (0.070)	3.1 (0.89)
[Cu(POP)(Me <sub>2</sub> bpy)][BF <sub>4</sub> ]	410	609, 637	1.2	0.37	365	549	21	8.0	2.8 (0.19)	9.4 (0.77)
[Cu(POP)(Me <sub>2</sub> bpy)][BPh <sub>4</sub> ]	410	609, 637	0.9	0.39	365	563	10	4.9	2.1 (0.34)	6.5 (0.57)
[Cu(POP)(Me <sub>2</sub> bpy)][BARF <sub>4</sub> ]	410	609, 637	1.5	0.42	365	555	6.6	3.3	1.7 (0.41)	4.7 (0.47)
[Cu(POP)(Me <sub>2</sub> bpy)][PF <sub>6</sub> ]	410	566, 620	13	4.5	365	549	34	8.7	2.5 (0.14)	9.8 (0.81)
[Cu(POP)(Me <sub>2</sub> bpy)][BF <sub>4</sub> ]	410	560, 616	12	4.1	365	553	28	8.7	2.6 (0.14)	9.7 (0.82)
[Cu(POP)(Me <sub>2</sub> bpy)][BPh <sub>4</sub> ]	410	566, 620	13	4.2	365	533	24	10.0	11.0 (0.84)	2.1 (0.11)
[Cu(POP)(Me <sub>2</sub> bpy)][BARF <sub>4</sub> ]	410	566, 620	14	4.5	365	532	24	8.4	3.0 (0.34)	11.4 (0.60)
[Cu(xantphos)(Me <sub>2</sub> bpy)][PF <sub>6</sub> ]	410	603, 636	1.3	0.72	365	550	33	10.5	11.2 (0.91)	1.6 (0.067)
[Cu(xantphos)(Me <sub>2</sub> bpy)][BF <sub>4</sub> ]	410	603, 636	1.3	0.82	365	552	20	7.5	2.0 (0.23)	9.3 (0.69)
[Cu(xantphos)(Me <sub>2</sub> bpy)][BPh <sub>4</sub> ]	410	603, 636	1.4	0.77	365	520	13	12.7	13.8 (0.87)	1.7 (0.095)
[Cu(xantphos)(Me <sub>2</sub> bpy)][BARF <sub>4</sub> ]	410	603, 636	1.5	0.83	365	562	13	5.2	1.9 (0.10)	5.6 (0.86)
[Cu(xantphos)(Me <sub>2</sub> bpy)][PF <sub>6</sub> ]	410	563, 631	8.3	3.3	365	535	62	14.7	15.1 (0.93)	0.99 (0.020)
[Cu(xantphos)(Me <sub>2</sub> bpy)][BF <sub>4</sub> ]	410	563, 631	9.1	3.1	365	530	44	8.7	1.6 (0.34)	13.1 (0.57)
[Cu(xantphos)(Me <sub>2</sub> bpy)][BPh <sub>4</sub> ]	410	563, 631	8.2	3.0	365	520	35	12.9	14.0 (0.88)	2.0 (0.083)
[Cu(xantphos)(Me <sub>2</sub> bpy)][BARF <sub>4</sub> ]	410	563, 631	8.3	3.7	365	536	27	8.5	3.1 (0.30)	11.1 (0.64)

<sup>a</sup> A biexponential fit to the lifetime delay was used because a single exponential gave a poor fit;  $\tau$  is calculated from the equation  $\sum A_i \tau_i / \sum A_i$  and  $A_i$  is the pre-exponential factor for the lifetime and values of  $\tau(1)$ ,  $\tau(2)$ ,  $A_1$  and  $A_2$  are also given. Deaeration was performed by bubbling a stream of argon through the solution.

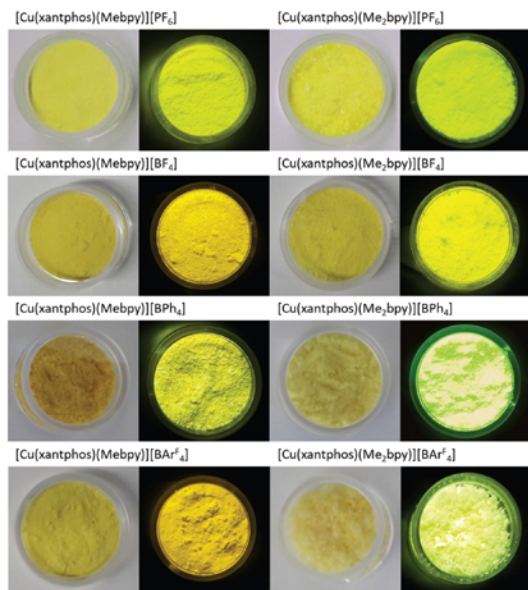


Fig. 11 Powder samples of  $[\text{Cu}(\text{xantphos})(\text{Me}_2\text{bpy})][\text{A}]$  complexes under ambient light (left) and under UV light ( $\lambda_{\text{exc}} = 366 \text{ nm}$ , right).

respectively.<sup>58</sup> The PLQYs in this work were recorded on the same instrument as the previously reported data and the most likely reason is the different morphology of the samples. Linfoot *et al.* have previously observed a similar phenomenon.<sup>86</sup> Both in solution and in solid-state, the  $\lambda_{\text{max}}^{\text{em}}$  of  $[\text{Cu}(\text{POP})(\text{Mebpy})][\text{PF}_6]$  and  $[\text{Cu}(\text{POP})(\text{Me}_2\text{bpy})][\text{PF}_6]$  are very close to the data reported by Keller *et al.*<sup>21</sup> In terms of the solid-state structures, two factors have been identified in the literature that may contribute to the solid-state PLQY. The first is the non-bonded  $\text{Cu}\cdots\text{O}$  distance, the O atom being in the POP or xantphos ligand,<sup>87</sup> and the second is the intra-cation  $\pi$ -stacking.<sup>88</sup> In the series of compounds described in this paper, it is difficult to see clear correlations between these structural factors and the solid-state PLQY values. It is also complicated by the introduction of aromatic groups in the  $[\text{BPh}_4]^-$  and  $[\text{BARF}_4]^-$  anions.

The excited state lifetimes  $\tau$  of the solid-state samples were determined using a biexponential fit;<sup>89</sup> the data for both solution and solid state are displayed in Table 4. The excited state lifetimes of the powder samples range from 2.9  $\mu\text{s}$  for  $[\text{Cu}(\text{POP})(\text{Mebpy})][\text{PF}_6]$  to 14.7  $\mu\text{s}$  for  $[\text{Cu}(\text{xantphos})(\text{Me}_2\text{bpy})][\text{PF}_6]$ . Between solutions of all salts, both  $\text{Me}_2\text{bpy}$  containing cations consistently exhibit increased excited state lifetimes compared to the  $\text{Mebpy}$  containing cations.

#### Device properties

We have previously reported the performances of LECs containing  $[\text{Cu}(\text{POP})(\text{Mebpy})][\text{PF}_6]$ ,  $[\text{Cu}(\text{POP})(\text{Me}_2\text{bpy})][\text{PF}_6]$ ,  $[\text{Cu}(\text{xantphos})(\text{Mebpy})][\text{PF}_6]$  and  $[\text{Cu}(\text{xantphos})(\text{Me}_2\text{bpy})][\text{PF}_6]$  in

their active layers, but under different device driving conditions.<sup>21,58</sup> These compounds exhibit some of the highest PLQY values of known  $[\text{Cu}(\text{P}^{\wedge}\text{P})(\text{N}^{\wedge}\text{N})]^+$  complexes and are, therefore, good candidates for LECs. In this work, we chose to focus on the series  $[\text{Cu}(\text{xantphos})(\text{Me}_2\text{bpy})][\text{PF}_6]$ ,  $[\text{Cu}(\text{xantphos})(\text{Me}_2\text{bpy})][\text{BF}_4]$ ,  $[\text{Cu}(\text{xantphos})(\text{Me}_2\text{bpy})][\text{BPh}_4]$  and  $[\text{Cu}(\text{xantphos})(\text{Me}_2\text{bpy})][\text{BARF}_4]$  to study their electroluminescence properties when used as active layers in LECs.

The thin-film PL spectra and PLQY of complexes were measured and are shown in Fig. 12 and Table 5. The PL spectra reveal that the four complexes do not have exactly the same PL maximum, consistent with the solution and powder PL spectra. Both  $[\text{Cu}(\text{xantphos})(\text{Me}_2\text{bpy})][\text{PF}_6]$  and  $[\text{Cu}(\text{xantphos})(\text{Me}_2\text{bpy})][\text{BF}_4]$  show a PL maximum at 563 nm whereas thin-films of  $[\text{Cu}(\text{xantphos})(\text{Me}_2\text{bpy})][\text{BPh}_4]$  and  $[\text{Cu}(\text{xantphos})(\text{Me}_2\text{bpy})][\text{BARF}_4]$  have values of  $\lambda_{\text{max}}^{\text{em}} = 548$  and 552 nm, respectively. This is possibly associated with the different cation...anion interactions discussed earlier (Fig. 3). The PLQYs of the thin films are 44, 45, 32 and 35%, respectively, for the  $[\text{PF}_6]^-$ ,  $[\text{BF}_4]^-$ ,  $[\text{BPh}_4]^-$  and  $[\text{BARF}_4]^-$  salts. The EL spectra of the LECs using the best performing complexes,  $[\text{Cu}(\text{xantphos})(\text{Me}_2\text{bpy})][\text{PF}_6]$  and  $[\text{Cu}(\text{xantphos})(\text{Me}_2\text{bpy})][\text{BF}_4]$ , were also measured with values of  $\lambda_{\text{max}}^{\text{em}}(\text{EL})$  of 546 and 550 nm, respectively (Fig. 13a). The EL is blue-shifted with respect to the PL in solution and red-shifted with respect to the PL in solid state.<sup>20</sup>

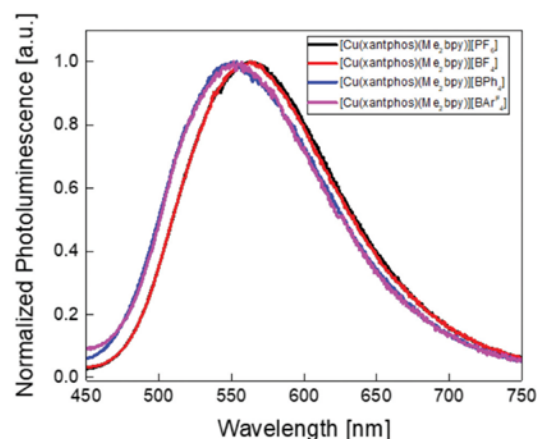
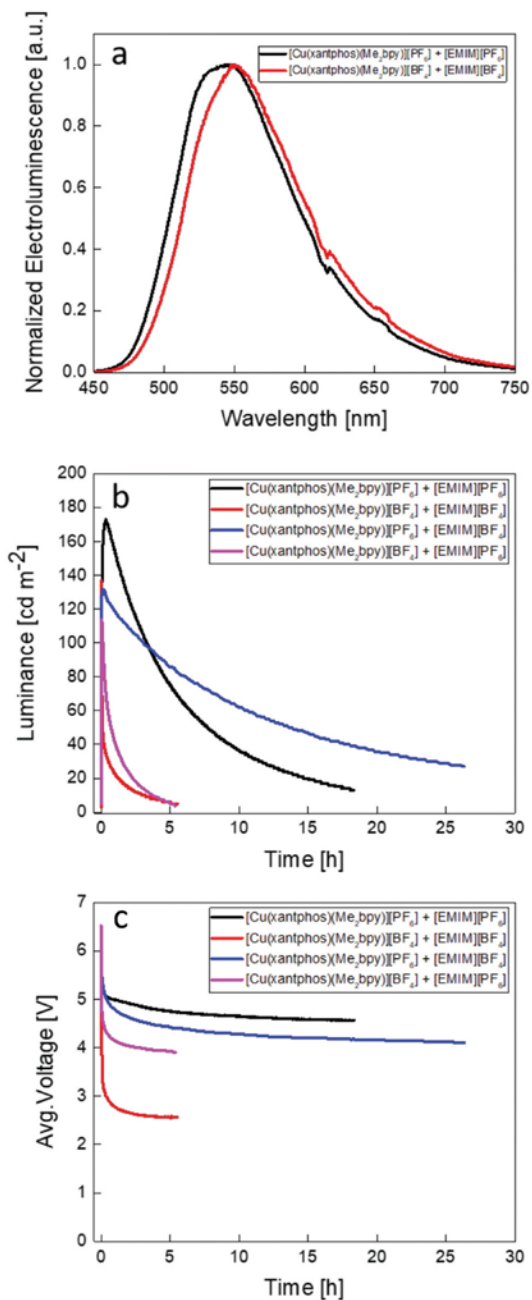


Fig. 12 Normalized thin-film photoluminescence spectra of the  $[\text{Cu}(\text{xantphos})(\text{Me}_2\text{bpy})]^+$  complexes with different counterions.

Table 5 Photoluminescence properties of thin films of the  $[\text{Cu}(\text{xantphos})(\text{Me}_2\text{bpy})]^+$  complexes with different counterions

Compound	$\lambda_{\text{max}}^{\text{em}}/\text{nm}$ ( $\lambda_{\text{exc}} = 365 \text{ nm}$ )	PLQY/%
$[\text{Cu}(\text{xantphos})(\text{Me}_2\text{bpy})][\text{PF}_6]$	563	44
$[\text{Cu}(\text{xantphos})(\text{Me}_2\text{bpy})][\text{BF}_4]$	563	45
$[\text{Cu}(\text{xantphos})(\text{Me}_2\text{bpy})][\text{BPh}_4]$	548	32
$[\text{Cu}(\text{xantphos})(\text{Me}_2\text{bpy})][\text{BARF}_4]$	552	35



**Fig. 13** (a) Normalized electroluminescence spectra of the two best performing complexes [Cu(xantphos)(Me<sub>2</sub>bpy)](PF<sub>6</sub>) and [Cu(xantphos)(Me<sub>2</sub>bpy)](BF<sub>4</sub>). (b) Luminance values and (c) voltage of [Cu(xantphos)(Me<sub>2</sub>bpy)](PF<sub>6</sub>) and [Cu(xantphos)(Me<sub>2</sub>bpy)](BF<sub>4</sub>) LECs driven at an average current density of 50 A m<sup>-2</sup> with different IL counterions.

Table 6 displays the active layers of the devices and LEC main figures of merit. As described in the Experimental section, the complexes were mixed with ILs (4 : 1 molar ratio complex : IL) containing the same and different counterions in order to study the behaviour of these complexes in LEC devices and the specific effect of the IL anion on the performance of the device. The cells were then driven under an average pulsed current of 50 A m<sup>-2</sup> while monitoring the luminance and voltage behaviour. Device performances of LECs containing [Cu(xantphos)(Me<sub>2</sub>bpy)](PF<sub>6</sub>) and [Cu(xantphos)(Me<sub>2</sub>bpy)](BF<sub>4</sub>) mixed with [EMIM]<sup>+</sup> ILs using the same counterion as the copper(i) complex can be seen in Fig. 13b (black and red curves, respectively). In both cases the cells have the typical LEC behaviour characterized by an initial high resistance and hence, a high initial voltage. As the electrochemical doping takes place over time, the film conductivity increases, and the voltage drops. The luminance increases following the electrochemical doping until a maximum value is reached. Then, a rapid loss of the EL intensity is observed, probably due to quenching caused by the growing doped zones as the voltage maintains a steady value, where smaller anions result in lower steady state voltage (Fig. 13c). Both devices show a fast turn-on time of 58 s and 15 s (the time to reach a luminance of 100 cd m<sup>-2</sup>) with a maximum luminance of 173 cd m<sup>-2</sup> and 137 cd m<sup>-2</sup> respectively. As expected from the anion sizes, [Cu(xantphos)(Me<sub>2</sub>bpy)](BF<sub>4</sub>) has a faster turn-on time, as the [BF<sub>4</sub>]<sup>-</sup> ion has smaller radius than [PF<sub>6</sub>]<sup>-</sup>, and thus is expected to have a higher mobility in the device. The LECs have a maximum current efficiency (CE) of 3.5 cd A<sup>-1</sup> and 2.7 cd A<sup>-1</sup>, respectively (Fig. 80†). Recent works explored the electroluminescent properties of copper complexes with similar P<sup>^</sup>P and N<sup>^</sup>N ligands: [Cu(xantphos)(4,5,6-Me<sub>3</sub>bpy)](PF<sub>6</sub>),<sup>20</sup> [Cu(xantphos)(Me<sub>2</sub>bpy)](PF<sub>6</sub>)<sup>58</sup> and [Cu(BnN-xantphos)(Me<sub>2</sub>bpy)](PF<sub>6</sub>).<sup>90</sup> When comparing the performances of these complexes with the LECs in the current investigation (Table 6) we notice similar luminance and current efficiencies (CE) with values of 190 cd m<sup>-2</sup> and 3.8 cd A<sup>-1</sup>, 90 cd m<sup>-2</sup> and 1.9 cd A<sup>-1</sup> and 179 cd m<sup>-2</sup> and 3.6 cd A<sup>-1</sup>, respectively, when operated under the same driving conditions. It is important to notice that the added IL was not always the same in all studies, and this can affect the performance of the device, as we show here. Additionally, the reported [Cu(xantphos)(Me<sub>2</sub>bpy)](PF<sub>6</sub>) was also previously studied<sup>58</sup> mixed with the IL [1-butyl-3-methylimidazolium](PF<sub>6</sub>) ([BMIM](PF<sub>6</sub>)). The devices show a slightly lower luminance of 145 cd m<sup>-2</sup> and CE of 3.0 cd A<sup>-1</sup>. The performances of devices using [Cu(xantphos)(Me<sub>2</sub>bpy)](PF<sub>6</sub>) and [Cu(xantphos)(Me<sub>2</sub>bpy)](BF<sub>4</sub>) with mixed counterions ([EMIM](BF<sub>4</sub>) and [EMIM](PF<sub>6</sub>)) can be seen in Fig. 13b (blue and purple curves, respectively) and in Table 5. The addition of the IL with a different counterion seems to affect the luminance and the turn-on time of the LEC. Both the luminance of LECs containing [Cu(xantphos)(Me<sub>2</sub>bpy)](BF<sub>4</sub>) and [Cu(xantphos)(Me<sub>2</sub>bpy)](PF<sub>6</sub>) decrease to 132 cd m<sup>-2</sup> and 114 cd m<sup>-2</sup> at a maximum CE of 2.6 cd A<sup>-1</sup> and 2.3 cd A<sup>-1</sup>, respectively. The turn-on time (time to reach 100 cd m<sup>-2</sup>) increases to 47 s for [Cu(xantphos)(Me<sub>2</sub>bpy)](BF<sub>4</sub>),



**Table 6** Performance of LECs with the [Cu(xantphos)(Me<sub>2</sub>bpy)]<sup>+</sup> series in the active layer; cell architecture ITO/PEDOT:PSS/[Cu(xantphos)(Me<sub>2</sub>bpy)]<sup>+</sup>[A]<sup>-</sup>: [EMIM][A] (4 : 1 molar ratio)/Al. LECs were measured using a pulsed current driving (average current density 50 A m<sup>-2</sup>, 1 kHz, 50% duty cycle, block wave)

Complex	Max luminance/cd m <sup>-2</sup>	Max current efficiency/cd A <sup>-1</sup>	Turn-on time <sup>a</sup> /s
[Cu(xantphos)(Me <sub>2</sub> bpy)] <sup>+</sup> [PF <sub>6</sub> ] <sup>-</sup> + [EMIM][PF <sub>6</sub> ]	173	3.5	58
[Cu(xantphos)(Me <sub>2</sub> bpy)] <sup>+</sup> [BF <sub>4</sub> ] <sup>-</sup> + [EMIM][BF <sub>4</sub> ]	137	2.7	15
[Cu(xantphos)(Me <sub>2</sub> bpy)] <sup>+</sup> [PF <sub>6</sub> ] <sup>-</sup> + [EMIM][BF <sub>4</sub> ]	132	2.6	61
[Cu(xantphos)(Me <sub>2</sub> bpy)] <sup>+</sup> [BF <sub>4</sub> ] <sup>-</sup> + [EMIM][PF <sub>6</sub> ]	114	2.3	47

<sup>a</sup> Turn-on-time is time to time to reach a luminance of 100 cd m<sup>-2</sup>.

while [Cu(xantphos)(Me<sub>2</sub>bpy)]<sup>+</sup>[PF<sub>6</sub>]<sup>-</sup> shows a similar turn-on time of 61 s (Table 5).

The two complexes with larger aryl-substituted anions, [Cu(xantphos)(Me<sub>2</sub>bpy)]<sup>+</sup>[BPh<sub>4</sub>]<sup>-</sup> and [Cu(xantphos)(Me<sub>2</sub>bpy)]<sup>+</sup>[BAR<sup>F</sup><sub>4</sub>]<sup>-</sup>, were also used in LECs. As before, two ILs with different anions were employed: one in which the anion in the IL ([EMIM][BPh<sub>4</sub>]<sup>-</sup> and [EMIM][BAR<sup>F</sup><sub>4</sub>]<sup>-</sup>) matched the anion in the complex, and another in which the anion in the IL is [PF<sub>6</sub>]<sup>-</sup> (IL = [EMIM][PF<sub>6</sub>]<sup>-</sup>). In both cases the devices maintained a high voltage value of 9 V (limit of our setup) and did not turn-on after several minutes even at higher driving current density (avg. 100 A m<sup>-2</sup> and 200 A m<sup>-2</sup>) and with higher IL concentrations (2 : 1, Cu : IL). The failure to turn on is an indication of low charge injection/transport efficiency within the thin film. In the case of large counterions, the charge injection might be less efficient due to the lower ionic mobility. These results indicate that mixing counterions is not likely to produce a beneficial change in performance, since it reduces all the figures of merit in LECs, as shown for [Cu(xantphos)(Me<sub>2</sub>bpy)]<sup>+</sup>[PF<sub>6</sub>]<sup>-</sup> and [Cu(xantphos)(Me<sub>2</sub>bpy)]<sup>+</sup>[BF<sub>4</sub>]<sup>-</sup> (Table 5). Moreover, using ILs with smaller counterions (*e.g.* [PF<sub>6</sub>]<sup>-</sup>) for devices using big aryl-substituted complexes, such as [Cu(xantphos)(Me<sub>2</sub>bpy)]<sup>+</sup>[BPh<sub>4</sub>]<sup>-</sup> and [Cu(xantphos)(Me<sub>2</sub>bpy)]<sup>+</sup>[BAR<sup>F</sup><sub>4</sub>]<sup>-</sup> is not sufficient to turn on these LECs.

## Conclusions

We have described the syntheses of [Cu(POP)(Mebpy)]<sup>+</sup>[A]<sup>-</sup>, [Cu(POP)(Me<sub>2</sub>bpy)]<sup>+</sup>[A]<sup>-</sup>, [Cu(xantphos)(Mebpy)]<sup>+</sup>[A]<sup>-</sup> and [Cu(xantphos)(Me<sub>2</sub>bpy)]<sup>+</sup>[A]<sup>-</sup> in which [A]<sup>-</sup> is [BF<sub>4</sub>]<sup>-</sup>, [PF<sub>6</sub>]<sup>-</sup>, [BPh<sub>4</sub>]<sup>-</sup> or [BAR<sup>F</sup><sub>4</sub>]<sup>-</sup>. The [PF<sub>6</sub>]<sup>-</sup> salts have previously been described,<sup>21,58</sup> but are reported here for comparative purposes. Nine [Cu(P<sup>^</sup>P)(N<sup>^</sup>N)]<sup>+</sup>[A]<sup>-</sup> salts were characterised by single crystal X-ray crystallography. As expected, a change from [BF<sub>4</sub>]<sup>-</sup> or [PF<sub>6</sub>]<sup>-</sup> to the more sterically demanding [BPh<sub>4</sub>]<sup>-</sup> or [BAR<sup>F</sup><sub>4</sub>]<sup>-</sup> counterions has a significant impact on the packing interactions in the solid state. Cation...cation interactions are effectively switched off in [Cu(xantphos)(Me<sub>2</sub>bpy)]<sup>+</sup>[BAR<sup>F</sup><sub>4</sub>]<sup>-</sup> as a result of the steric demands of the anions. In contrast, in [Cu(xantphos)(Me<sub>2</sub>bpy)]<sup>+</sup>[PF<sub>6</sub>]<sup>-</sup> and [Cu(xantphos)(Me<sub>2</sub>bpy)]<sup>+</sup>[BF<sub>4</sub>]<sup>-</sup>, there are extensive C-H...F contacts between cations and anions, but accommodation of the [BF<sub>4</sub>]<sup>-</sup> and [PF<sub>6</sub>]<sup>-</sup> anions in the lattices still allows cation...cation interactions.

We reported the effects of the counterion on the photo-physical properties of [Cu(POP)(N<sup>^</sup>N)]<sup>+</sup>[A]<sup>-</sup> and [Cu(xantphos)(N<sup>^</sup>N)]<sup>+</sup>[A]<sup>-</sup> (N<sup>^</sup>N = Mebpy and Me<sub>2</sub>bpy). While a change from Mebpy to Me<sub>2</sub>bpy has previously been explored,<sup>21,58</sup> the current investigation revealed an anion dependence on  $\lambda_{\text{max}}^{\text{em}}$  and PLQY. In the solid-state emission spectra, the highest energy  $\lambda_{\text{max}}^{\text{em}}$  values are for [Cu(xantphos)(Mebpy)]<sup>+</sup>[BPh<sub>4</sub>]<sup>-</sup> and [Cu(xantphos)(Me<sub>2</sub>bpy)]<sup>+</sup>[BPh<sub>4</sub>]<sup>-</sup> ( $\lambda_{\text{max}}^{\text{em}}$  = 520 nm) whereas the lowest energy  $\lambda_{\text{max}}^{\text{em}}$  values occur for [Cu(POP)(Mebpy)]<sup>+</sup>[PF<sub>6</sub>]<sup>-</sup> and [Cu(POP)(Mebpy)]<sup>+</sup>[BPh<sub>4</sub>]<sup>-</sup> (565 nm and 563 nm, respectively). Variation in PLQY is illustrated for the [Cu(xantphos)(Me<sub>2</sub>bpy)]<sup>+</sup>[A]<sup>-</sup> series, in which PLQYs decrease from 62% for [PF<sub>6</sub>]<sup>-</sup>, to 44%, 35% and 27% for [BF<sub>4</sub>]<sup>-</sup>, [BPh<sub>4</sub>]<sup>-</sup> and [BAR<sup>F</sup><sub>4</sub>]<sup>-</sup>, respectively. The [Cu(xantphos)(Me<sub>2</sub>bpy)]<sup>+</sup>[A]<sup>-</sup> compounds were incorporated into the active layers of LECs. The luminophores were mixed with [EMIM][A] ILs in which [A]<sup>-</sup> was the same or a different counterion than in the copper(i) complex. LECs containing [Cu(xantphos)(Me<sub>2</sub>bpy)]<sup>+</sup>[BPh<sub>4</sub>]<sup>-</sup> and [Cu(xantphos)(Me<sub>2</sub>bpy)]<sup>+</sup>[BAR<sup>F</sup><sub>4</sub>]<sup>-</sup> failed to turn on under the LEC operating conditions, whereas those with the smaller [PF<sub>6</sub>]<sup>-</sup> or [BF<sub>4</sub>]<sup>-</sup> counterions had rapid turn-on times and exhibited maximum luminances of 173 or 137 cd m<sup>-2</sup> and current efficiencies of 3.5 and 2.6 cd A<sup>-1</sup>, respectively, if the IL contained the same counterion as the luminophore. Mixing the counterions ([PF<sub>6</sub>]<sup>-</sup> and [BF<sub>4</sub>]<sup>-</sup>) in the active complex and the IL led to a reduction in all the figures of merit of the LECs.

## Conflicts of interest

There are no conflicts to declare.

## Acknowledgements

We thank the Swiss National Science Foundation (grant number 200020\_182000) and the University of Basel for support. We acknowledge support from the European Research Council (ERC) under the European Union's Horizon 2020 research and innovation program grant agreement no. 834431, the Spanish Ministry of Science, Innovation and Universities (RTI2018-095362-A-I00, EQC2018-004888-P and RYC-2016-21316) and the Comunitat Valenciana (IDIFEDER/2020/063 and PROMETEU/2020/077).

## Notes and references

- 1 United States Department of Energy, <https://www.energy.gov/articles/rise-and-shine-lighting-world-10-billion-led-bulbs>, (accessed 25.08.2021).
- 2 Q. Pei, G. Yu, C. Zhang, Y. Yang and A. J. Heeger, *Science*, 1995, **269**, 1086–1088.
- 3 S. Tang and L. Edman, *Top. Curr. Chem.*, 2016, **374**, 40.
- 4 S. Tang, A. Sandström, P. Lundberg, T. Lanz, C. Larsen, S. van Reenen, M. Kemerink and L. Edman, *Nat. Commun.*, 2017, **8**, 1190.
- 5 J. Gao, *ChemPlusChem*, 2018, **83**, 183–196.
- 6 E. Fresta and R. D. Costa, *J. Mater. Chem. C*, 2017, **5**, 5643–5675.
- 7 B. N. Bideh, H. Shahroosvand, A. Sousarai and J. Cabanillas-Gonzalez, *Sci. Rep.*, 2019, **9**, 228.
- 8 S. van Reenen, P. Matyba, A. Dzwilewski, R. A. J. Janssen, L. Edman and M. Kemerink, *J. Am. Chem. Soc.*, 2010, **132**, 13776–13781.
- 9 A. Asadpooravarsh, A. Sandström, C. Larsen, R. Bollström, M. Toivakka, R. Österbacka and L. Edman, *Adv. Funct. Mater.*, 2015, **25**, 3238–3245.
- 10 T. Lanz, A. Sandström, S. Tang, P. Chabreck, U. Sonderegger and L. Edman, *Flex. Print. Electron.*, 2016, **1**, 025004.
- 11 Z. Zhang, K. Guo, Y. Li, X. Li, G. Guan, H. Li, Y. Luo, F. Zhao, Q. Zhang, B. Wei, Q. Pei and H. Peng, *Nat. Photonics*, 2015, **9**, 233–238.
- 12 J. M. Moran-Mirabal, J. D. Slinker, J. A. DeFranco, S. S. Verbridge, R. Ilic, S. Flores-Torres, H. Abruña, G. G. Malliaras and H. G. Craighead, *Nano Lett.*, 2007, **7**, 458–463.
- 13 R. D. Costa, D. Tordera, E. Orti, H. J. Bolink, J. Schönle, S. Graber, C. E. Housecroft, E. C. Constable and J. A. Zampese, *J. Mater. Chem.*, 2011, **21**, 16108–16118.
- 14 Q. B. pei and Y. Yang, *J. Am. Chem. Soc.*, 1996, **118**, 7416–7417.
- 15 J. D. Slinker, J. Rivnay, J. S. Moskowitz, J. B. Parker, S. Bernhard, H. D. Abruña and G. G. Malliaras, *J. Mater. Chem.*, 2007, **17**, 2976–2988.
- 16 J. Slinker, D. Bernards, P. L. Houston, H. D. Abruña, S. Bernhard and G. G. Malliaras, *Chem. Commun.*, 2003, 2392–2399.
- 17 A. Sandström, H. F. Dam, F. C. Krebs and L. Edman, *Nat. Commun.*, 2012, **3**, 1002.
- 18 R. D. Costa, *Light-Emitting Electrochemical Cells: Concepts, Advances and Challenges*, Springer Nature, Cham, 1st edn, 2017.
- 19 J. Xu, A. Sandström, E. M. Lindh, W. Yang, S. Tang and L. Edman, *ACS Appl. Mater. Interfaces*, 2018, **10**, 33380–33389.
- 20 S. Keller, A. Prescimone, M.-G. La Placa, J. M. Junquera-Hernández, H. J. Bolink, E. C. Constable, M. Sessolo, E. Orti and C. E. Housecroft, *RSC Adv.*, 2020, **10**, 22631–22644.
- 21 S. Keller, E. C. Constable, C. E. Housecroft, M. Neuberger, A. Prescimone, G. Longo, A. Pertegàs, M. Sessolo and H. J. Bolink, *Dalton Trans.*, 2014, **43**, 16593–16596.
- 22 E. Fisslthaler, S. Sax, U. Scherf, G. Mauthner, E. Moderegger, K. Landfester and E. J. W. List, *Appl. Phys. Lett.*, 2008, **92**, 183305.
- 23 J. Huo, W. Zou, Y. Zhang, W. Chen, X. Hu, Q. Deng and D. Chen, *RSC Adv.*, 2019, **9**, 6163–6168.
- 24 J. Zimmermann, N. Jürgensen, A. J. Morfa, B. Wang, S. Tekoglu and G. Hernandez-Sosa, *ACS Sustainable Chem. Eng.*, 2016, **4**, 7050–7055.
- 25 J. Mindemark, S. Tang, J. Wang, N. Kaihovirta, D. Brandell and L. Edman, *Chem. Mater.*, 2016, **28**, 2618–2623.
- 26 Y. Nishikitani, D. Takizawa, H. Nishide, S. Uchida and S. Nishimura, *J. Phys. Chem. C*, 2015, **119**, 28701–28710.
- 27 G. Gozzi, L. D. Cagnani, R. M. Faria and L. F. Santos, *J. Solid State Electrochem.*, 2016, **20**, 2127–2133.
- 28 T. Sakanoue, F. Yonekawa, K. Albrecht, K. Yamamoto and T. Takenobu, *Chem. Mater.*, 2017, **29**, 6122–6129.
- 29 S. Jenatsch, L. Wang, N. Leclaire, E. Hack, R. Steim, S. B. Anantharaman, J. Heier, B. Ruhstaller, L. Penninck, F. Nüesch and R. Hany, *Org. Electron.*, 2017, **48**, 77–84.
- 30 K. Shanmugasundaram, R. K. Chitumalla, J. Jang and Y. Choe, *New J. Chem.*, 2017, **41**, 9668–9673.
- 31 K. Shanmugasundaram, M. S. Subeesh, C. D. Sunesh and Y. Choe, *RSC Adv.*, 2016, **6**, 28912–28918.
- 32 G. Qian, Y. Lin, G. Wantz, A. R. Davis, K. R. Carter and J. J. Watkins, *Adv. Funct. Mater.*, 2014, **24**, 4484–4490.
- 33 J. Frohleiks, F. Wepfer, S. Wepfer, A.-R. Hong, H. S. Jang and E. Nannen, *Adv. Mater. Technol.*, 2017, **2**, 1700154.
- 34 J. Frohleiks, S. Gellner, S. Wepfer, G. Bacher and E. Nannen, *ACS Appl. Mater. Interfaces*, 2018, **10**, 42637–42646.
- 35 M. Alahbakhshi, A. Mishra, R. Haroldson, A. Ishteev, J. Moon, Q. Gu, J. D. Slinker and A. A. Zakhidov, *ACS Energy Lett.*, 2019, **4**, 2922–2928.
- 36 M. F. Aygüler, M. D. Weber, B. M. D. Puscher, D. D. Medina, P. Docampo and R. D. Costa, *J. Phys. Chem. C*, 2015, **119**, 12047–12054.
- 37 C.-M. Wang, Y.-M. Su, T.-A. Shih, G.-Y. Chen, Y.-Z. Chen, C.-W. Lu, I.-S. Yu, Z.-P. Yang and H.-C. Su, *J. Mater. Chem. C*, 2018, **6**, 12808–12813.
- 38 Q. Zeng, F. Li, T. Guo, G. Shan and Z. Su, *Org. Electron.*, 2017, **42**, 303–308.
- 39 J. Wu, F. Li, Q. Zeng, C. Nie, P. C. Ooi, T. Guo, G. Shan and Z. Su, *Org. Electron.*, 2016, **28**, 314–318.
- 40 K. J. Suhr, L. D. Bastatas, Y. Shen, L. A. Mitchell, B. J. Holliday and J. D. Slinker, *ACS Appl. Mater. Interfaces*, 2016, **8**, 8888–8892.
- 41 D. A. W. Ross, P. A. Scattergood, A. Babaei, A. Pertegàs, H. J. Bolink and P. I. P. Elliott, *Dalton Trans.*, 2016, **45**, 7748–7757.
- 42 M. Lepeltier, B. Graff, J. Lalevée, G. Wantz, M. Ibrahim-Ouali, D. Gimes and F. Dumur, *Org. Electron.*, 2016, **37**, 24–34.
- 43 M. Di Marcantonio, J. E. Namanga, V. Smetana, N. Gerlitzki, F. Vollkommer, A. V. Mudring, G. Bacher and E. Nannen, *J. Mater. Chem. C*, 2017, **5**, 12062–12068.
- 44 C. E. Housecroft and E. C. Constable, *Coord. Chem. Rev.*, 2017, **350**, 155–177.

- 45 R. D. Costa, E. Ortí, H. J. Bolink, F. Monti, G. Accorsi and N. Armaroli, *Angew. Chem., Int. Ed.*, 2012, **51**, 8178–8211.
- 46 H. J. Bolink, E. Coronado, R. D. Costa, E. Ortí, M. Sessolo, S. Graber, K. Doyle, M. Neuburger, C. E. Housecroft and E. C. Constable, *Adv. Mater.*, 2008, **20**, 3910–3913.
- 47 R. D. Costa, E. Ortí, H. J. Bolink, S. Graber, C. E. Housecroft and E. C. Constable, *Adv. Funct. Mater.*, 2010, **20**, 1511–1520.
- 48 P. Dreyse, B. Loeb, M. Barrera and I. González, *J. Chil. Chem. Soc.*, 2014, **59**, 2628–2631.
- 49 S.-M. Kuang, D. G. Cuttall, D. R. McMillin, P. E. Fanwick and R. A. Walton, *Inorg. Chem.*, 2002, **41**, 3313–3322.
- 50 D. G. Cuttall, S.-M. Kuang, P. E. Fanwick, D. R. McMillin and R. A. Walton, *J. Am. Chem. Soc.*, 2002, **124**, 6–7.
- 51 A. A. Yaroshevsky, *Geochem. Int.*, 2006, **44**, 48–55.
- 52 N. Armaroli, G. Accorsi, M. Holler, O. Moudam, J.-F. Nierengarten, Z. Zhou, R. T. Wegh and R. Welter, *Adv. Mater.*, 2006, **18**, 1313–1316.
- 53 F. Brunner, S. Graber, Y. Baumgartner, D. Häussinger, A. Prescimone, E. C. Constable and C. E. Housecroft, *Dalton Trans.*, 2017, **46**, 6379–6391.
- 54 M. D. Weber, C. Garino, G. Volpi, E. Casamassa, M. Milanese, C. Barolo and R. D. Costa, *Dalton Trans.*, 2016, **45**, 8984–8993.
- 55 S. Keller, F. Brunner, J. M. Junquera-Hernández, A. Pertegás, M.-G. La-Placa, A. Prescimone, E. C. Constable, H. J. Bolink, E. Ortí and C. E. Housecroft, *ChemPlusChem*, 2018, **83**, 217–229.
- 56 F. Brunner, A. Babaei, A. Pertegás, J. M. Junquera-Hernández, A. Prescimone, E. C. Constable, H. J. Bolink, M. Sessolo, E. Ortí and C. E. Housecroft, *Dalton Trans.*, 2019, **48**, 446–460.
- 57 F. Brunner, L. Martínez-Sarti, S. Keller, A. Pertegás, A. Prescimone, E. C. Constable, H. J. Bolink and C. E. Housecroft, *Dalton Trans.*, 2016, **45**, 15180–15192.
- 58 S. Keller, A. Pertegás, G. Longo, L. Martínez, J. Cerdà, J. M. Junquera-Hernández, A. Prescimone, E. C. Constable, C. E. Housecroft, E. Ortí and H. J. Bolink, *J. Mater. Chem. C*, 2016, **4**, 3857–3871.
- 59 M. Y. Wong and E. Zysman-Colman, *Adv. Mater.*, 2017, **29**, 1605444.
- 60 M. A. Baldo, D. F. O'Brien, Y. You, A. Shoustikov, S. Sibley, M. E. Thompson and S. R. Forrest, *Nature*, 1998, **395**, 151–154.
- 61 R. Czerwieńiec, M. J. Leiti, H. H. H. Homeier and H. Yersin, *Coord. Chem. Rev.*, 2016, **325**, 2–28.
- 62 Z. Li, W. Li, C. Keum, E. Archer, B. Zhao, A. M. Z. Slawin, W. Huang, M. C. Gather, I. D. W. Samuel and E. Zysman-Colman, *J. Phys. Chem. C*, 2019, **123**, 24772–24785.
- 63 C. E. Housecroft and E. C. Constable, *J. Mater. Chem. C*, 2021, DOI: 10.1039/D1TC04028F, advance article.
- 64 J. Gao and J. Dane, *Appl. Phys. Lett.*, 2004, **84**, 2778–2780.
- 65 T. J. Mills and M. C. Lonergan, *Phys. Rev. B: Condens. Matter Mater. Phys.*, 2012, **85**, 035203.
- 66 E. Fresta and R. D. Costa, *Adv. Funct. Mater.*, 2020, **30**, 1908176.
- 67 S. B. Meier, S. van Reenen, B. Lefevre, D. Hartmann, H. J. Bolink, A. Winnacker, W. Sarfert and M. Kemerink, *Adv. Funct. Mater.*, 2013, **23**, 3531–3538.
- 68 M. Lenes, G. Garcia-Belmonte, D. Tordera, A. Pertegás, J. Bisquert and H. J. Bolink, *Adv. Funct. Mater.*, 2011, **21**, 1581–1586.
- 69 X.-N. Kuang, S. Lin, J.-M. Liu, H.-L. Han, M. Liu, X.-L. Xin, Y.-P. Yang, Z.-F. Li, Q.-H. Jin, S.-F. Li, Y.-X. Li and Y.-B. Feng, *Polyhedron*, 2019, **165**, 51–62.
- 70 Y.-R. Zhang, X. Yu, S. Lin, Q.-H. Jin, Y.-P. Yang, M. Liu, Z.-F. Li, C.-L. Zhang and X.-L. Xin, *Polyhedron*, 2017, **138**, 46–56.
- 71 T. Gneuß, M. J. Leiti, L. H. Finger, H. Yersin and J. Sundermeyer, *Dalton Trans.*, 2015, **44**, 20045–20055.
- 72 G. J. Kubas, B. Monzyk and A. L. Crumbliss, in *Inorg. Synth*, 1979, pp. 90–92.
- 73 S.-H. Kim and R. D. Rieke, *Tetrahedron*, 2010, **66**, 3135–3146.
- 74 C. S. Smith, C. W. Branham, B. J. Marquardt and K. R. Mann, *J. Am. Chem. Soc.*, 2010, **132**, 14079–14085.
- 75 Software for the Integration of CCD Detector System Bruker Analytical X-ray Systems, Bruker axs, Madison, WI, (after 2013).
- 76 G. Sheldrick, *Acta Crystallogr., Sect. A: Found. Adv.*, 2015, **71**, 3–8.
- 77 O. V. Dolomanov, L. J. Bourhis, R. J. Gildea, J. A. K. Howard and H. Puschmann, *J. Appl. Crystallogr.*, 2009, **42**, 339–341.
- 78 G. Sheldrick, *Acta Crystallogr., Sect. C: Struct. Chem.*, 2015, **71**, 3–8.
- 79 L. Palatinus and G. Chapuis, *J. Appl. Crystallogr.*, 2007, **40**, 786–790.
- 80 L. Palatinus, S. J. Prathapa and S. van Smaalen, *J. Appl. Crystallogr.*, 2012, **45**, 575–580.
- 81 C. F. Macrae, I. Sovago, S. J. Cottrell, P. T. A. Galek, P. McCabe, E. Pidcock, M. Platings, G. P. Shields, J. S. Stevens, M. Towler and P. A. Wood, *J. Appl. Crystallogr.*, 2020, **53**, 226–235.
- 82 C. Janiak, *Dalton Trans.*, 2000, 3885–3896.
- 83 M. Nishio, *CrystEngComm*, 2004, **6**, 130–158.
- 84 T. Förster, *Ann. Phys.*, 1948, **2**, 55–75.
- 85 D. L. Dexter, *J. Chem. Phys.*, 1953, **21**, 836–850.
- 86 C. L. Linfoot, M. J. Leiti, P. Richardson, A. F. Rausch, O. Chepelin, F. J. White, H. Yersin and N. Robertson, *Inorg. Chem.*, 2014, **53**, 10854–10861.
- 87 S. Keller, M. Alkan-Zambada, A. Prescimone, E. C. Constable and C. E. Housecroft, *Crystals*, 2020, **10**, 255.
- 88 E. Leoni, J. Mohanraj, M. Holler, M. Mohankumar, I. Nierengarten, F. Monti, A. Sournia-Saquet, B. Delavaux-Nicot, J.-F. Nierengarten and N. Armaroli, *Inorg. Chem.*, 2018, **57**, 15537–15549.
- 89 T. Hofbeck, U. Monkowius and H. Yersin, *J. Am. Chem. Soc.*, 2015, **137**, 399–404.
- 90 N. Arnosti, F. Brunner, I. Susic, S. Keller, J. M. Junquera-Hernández, A. Prescimone, H. J. Bolink, M. Sessolo, E. Ortí, C. E. Housecroft and E. C. Constable, *Adv. Opt. Mater.*, 2020, **8**, 1901689.

Cite this: *J. Mater. Chem. C*, 2022,  
10, 15491

## Green light-emitting electrochemical cells based on platinum(II) complexes with a carbazole-appended carbene ligand†‡

Sara Fuertes,<sup>a</sup> Lorenzo Mardegan,<sup>b</sup> Ignacio Martínez,<sup>a</sup> Silvia Ventura,<sup>a</sup> Irene Ara,<sup>a</sup> Daniel Tordera,<sup>b</sup> Henk J. Bolink<sup>b</sup> and Violeta Sicilia<sup>b\*</sup>

Platinum(II) complexes bearing new carbazole-appended cyclometallated N-heterocyclic carbenes such as [Pt(Cbz-C<sup>∧</sup>C<sup>\*</sup>)Cl(NCCH<sub>3</sub>)](**3**), [Pt(Cbz-C<sup>∧</sup>C<sup>\*</sup>)Cl(PPh<sub>3</sub>)](**4**), [Pt(Cbz-C<sup>∧</sup>C<sup>\*</sup>)(PPh<sub>3</sub>)(py)]PF<sub>6</sub> (py = pyridine, **5**), [Pt(Cbz-C<sup>∧</sup>C<sup>\*</sup>)(P<sup>∧</sup>N)]PF<sub>6</sub> (P<sup>∧</sup>N = 2-(2-(diphenylphosphino) ethyl) pyridine, **6**), and [Pt(Cbz-C<sup>∧</sup>C<sup>\*</sup>)(P<sup>∧</sup>P)]PF<sub>6</sub> (P<sup>∧</sup>P: 1,1-bis(diphenylphosphino)methane, dppm **7**; 1,2-bis(diphenylphosphino)ethane, dppe, **8**, 1,2-bis(diphenylphosphino) benzene, dppbz, **9**) have been prepared using a stepwise procedure from 9-(4-bromophenyl)-9H-carbazole, imidazole, [(Pt(μ-Cl)(η<sup>3</sup>-2-Me-C<sub>3</sub>H<sub>4</sub>))<sub>2</sub>] and the corresponding ancillary ligands. They have been fully characterized. Also, single-crystal X-ray structures, theoretical calculations and photophysical studies have been performed. These complexes have been employed as emitters in simple solution-processed light-emitting electrochemical cells (LECs). When driven under a pulsed current of 50 A m<sup>-2</sup>, devices based on **7–9** exhibited green emission, a luminance of 265 cd m<sup>-2</sup> and a current efficiency of 5.7 cd A<sup>-1</sup> (for the best performing emitter, **7**). As far as we know, these are the first examples of green-emitting Pt(II)-based LECs.

Received 17th June 2022.  
Accepted 16th September 2022

DOI: 10.1039/d2tc02539f

rsc.li/materials-c

## Introduction

Light-emitting electrochemical cells (LECs) celebrated their 25th anniversary in 2020.<sup>1,2</sup> Since the LEC technology was first discovered by Pei *et al.*,<sup>3</sup> it has become an excellent candidate and a viable alternative to traditional solid state light sources.<sup>4–7</sup> In its simplest form, it consists of a single layer of an ionic luminescent material sandwiched between two air-stable contact electrodes.<sup>8</sup> Generally, this material consists of either a conjugated light-emitting polymer (CP)<sup>9–12</sup> or an ionic transition-metal complex (iTMC).<sup>13</sup> The latter presents some advantages since the ionic metal complex can perform all the necessary roles for light generation: (a) charge injection

promoted by the mobile counterions, (b) transport of electrons and holes, and (c) generation of photons from triplet excited states.<sup>13–16</sup> In this context, iTMCs have been largely investigated,<sup>13,17–19</sup> in particular those based on Ir(III) complexes;<sup>18,20–22</sup> however, platinum-based LECs have seldom been explored, with just a few examples found in the literature.<sup>23–26</sup> Most of them are polynuclear complexes of Pt(II) with cyclometallated C<sup>∧</sup>N or N<sup>∧</sup>C<sup>∧</sup>N/N<sup>∧</sup>N<sup>∧</sup>C pincer ligands. All the cited materials exhibit emission in the red region of the visible spectrum with no examples of green or blue emitting Pt(II)-based LECs reported to date. In this regard, Pt(II) complexes with cyclometallated N-heterocyclic carbenes (NHCs; C<sup>∧</sup>C<sup>\*</sup>) have been proved to emit light in different colours (blue,<sup>27–32</sup> green-yellow,<sup>33,34</sup> and orange-red<sup>29,30,35,36</sup>) with elevated quantum efficiencies. The cycloplatinated C<sup>∧</sup>C<sup>\*</sup> ligands surpass the donor capability of C<sup>∧</sup>N-cyclometallated imines, increasing the energy of the empty d<sub>x<sup>2</sup>-y<sup>2</sup></sub> orbitals and preventing their photo- or thermal population, which would lead to severe distortions resulting in non-emissive deactivation.<sup>37</sup> In line with this, when designing a Pt(II) emitter, it is important to minimize the structural distortions upon excitation. These promote non-emissive decays due to the electron-vibrational coupling of the excited and ground states.<sup>38</sup> Thus, rigid or semi-rigid scaffolds with chelating coordination and strong donor atoms are desired structural features to improve emission quantum yields.

With this in mind, the 9H-carbazol-9-yl (Cbz) group possesses several advantages: an intrinsic rigid molecular structure, strong

<sup>a</sup> Departamento de Química Inorgánica, Facultad de Ciencias, Instituto de Síntesis Química y Catálisis Homogénea (ISQCH), CSIC – Universidad de Zaragoza, Pedro Cerbuna 12, 50009, Zaragoza, Spain. E-mail: s.fuertes@csic.es

<sup>b</sup> Instituto de Ciencia Molecular, Universidad de Valencia, C/J. Beltrán 2, 46980, Paterna, Spain. E-mail: daniel.tordera@uv.es

<sup>c</sup> Departamento de Química Inorgánica, Escuela de Ingeniería y Arquitectura de Zaragoza, Instituto de Síntesis Química y Catálisis Homogénea (ISQCH), CSIC – Universidad de Zaragoza, Campus Río Ebro, Edificio Torres Quevedo, 50018, Zaragoza, Spain. E-mail: sicilia@unizar.es

† Dedicated to Paul R. Raithby, celebrating a career in inorganic and organometallic chemistry, on the occasion of his 70th birthday.

‡ Electronic supplementary information (ESI) available. CCDC 2151291–2151294. For ESI and crystallographic data in CIF or other electronic format see DOI: <https://doi.org/10.1039/d2tc02539f>



electron-donating ability and hole transporting properties, which are appealing attributes for developing electroluminescent devices.<sup>39–43</sup> Therefore, incorporating the Cbz moiety into a molecular scaffold produces a situation where the HOMO and LUMO are localized separately over the molecule, leading to donor-acceptor conjugated systems. They exhibit excellent electronic properties through the induction of a highly efficient intramolecular charge transfer process.<sup>44,45</sup> Besides, the attachment of this bulky side-group can prevent stacking interactions of the molecules and reduce self-quenching effects, which are known limiting factors on the efficiency of LECs.<sup>46,47</sup> Additionally, the photophysical properties of the mononuclear Pt(II) complexes can be fine-tuned by modifying the cyclometallated and the ancillary ligands.<sup>48</sup> Incorporating electron-donating or -withdrawing substituents into the chromophoric cyclometallated fragment and into the auxiliary ligands strongly influences the energies of the frontier orbitals and consequently the MLCT/ILCT character of the lowest energy transition, thus altering the radiative energy and lifetime of the excited state.

Previous results for PhOLEDs using complexes bearing cyclometallated N-heterocyclic carbenes, such as [Pt(R-C<sup>+</sup>C\*)(dppbz)]PF<sub>6</sub> (R = H, CN), showed sky blue EL, but a poor performance. The rather deep HOMO in these complexes was considered the cause that could prevent efficient hole injection/transport processes.<sup>27</sup> With all the above in mind and considering our interesting results with the cyclometallated C<sup>+</sup>C\* complexes of Pt(II) applied in photo- and electroluminescent devices,<sup>27,29–31,33</sup> we explored the Pt(Cbz-C<sup>+</sup>C\*) system with a pendant electron-donating Cbz (Cbz-CH<sup>+</sup>C\* = 1-(4-(9H-Carbazol-9-yl)phenyl)-3-methyl-1H-imidazole) group that provides suitable steric and electronic properties for its application in iTMC-LECs. As a result, herein we report the synthesis and the structural properties of these cationic compounds with non-chelating, [Pt(Cbz-C<sup>+</sup>C\*)(PPh<sub>3</sub>)(py)]PF<sub>6</sub> (5), and chelating ancillary ligands, [Pt(Cbz-C<sup>+</sup>C\*)(P<sup>+</sup>N)]PF<sub>6</sub> (6) and [Pt(Cbz-C<sup>+</sup>C\*)(P<sup>+</sup>P)]PF<sub>6</sub> (P<sup>+</sup>P = dpmp, dppe, dppbz 9). Theoretical calculations and photophysical studies were also carried out on the ionic Pt(II) complexes 5–9. They showed high PL quantum yields, ranging from 47% to 83%, and were employed as emitters in simple solution-processed iTMC-LECs. The effect of different solvents was also studied showing that the solvent can have a great impact on the performance of the LECs. More importantly, the devices emit in the green region (7–9), which is, as far as we know, the first example of green-emitting Pt(II)-based LECs.

## Experimental section

Materials, instrumentation, and synthesis of 9-[4-(1H-imidazol-1-yl)phenyl]-9H-carbazole (1), 1-(4-(9H-carbazol-9-yl)phenyl)-3-methyl-1H-imidazolium iodide (2), [Pt(Cbz-C<sup>+</sup>C\*)Cl(NCCH<sub>3</sub>)] (3) and NMR spectroscopic data for 4–9 are included in the ESI.†

### Synthesis of [Pt(Cbz-C<sup>+</sup>C\*)(Cl)(PPh<sub>3</sub>)] (4)

Triphenylphosphine (66.3 mg, 0.253 mmol) was added to a suspension of 3 (150 mg, 0.253 mmol) in dichloromethane

(20 mL) at rt. After 90 min. of the reaction, the solution was filtered through Celite and evaporated to dryness. The residue was treated with methanol (5 mL) and filtered to give 4 as a yellow solid. Yield: 176.0 mg, 85.3%. Anal. calcd for C<sub>40</sub>H<sub>31</sub>ClN<sub>3</sub>Pt: C, 58.93; H, 3.83; N, 5.15. Found: C, 58.58; H, 3.66; N, 5.01. IR (ATR, cm<sup>-1</sup>): ν = 691 (s, PPh<sub>3</sub>). MS (MALDI<sup>+</sup>): m/z 779.2 [Pt(C<sup>+</sup>C\*)(PPh<sub>3</sub>)]<sup>+</sup>.

### Synthesis of [Pt(Cbz-C<sup>+</sup>C\*)(PPh<sub>3</sub>)(py)]PF<sub>6</sub> (5)

Pyridine (19.6 mg, 0.247 mmol) and KPF<sub>6</sub> (33.9 mg, 0.184 mmol) were added to a suspension of 4 (150 mg, 0.184 mmol) in a mixture of dichloromethane/acetone (10/20 mL) at rt. After 2 hours of the reaction, the solution was evaporated to dryness. Then, 15 mL of dichloromethane was added and the solution was filtered through Celite and evaporated to dryness again. The residue was treated with diethyl ether (5 mL) and filtered to give 5 as a yellow solid. Yield: 117.8 mg, 63.8%. Anal. calcd. for C<sub>45</sub>H<sub>36</sub>F<sub>6</sub>N<sub>4</sub>P<sub>2</sub>Pt·CH<sub>2</sub>Cl<sub>2</sub>: C, 50.75; H, 3.52; N, 5.15. Found: C, 50.57; H, 3.48; N, 5.23. IR (ATR, cm<sup>-1</sup>): ν = 833 (s, PF<sub>6</sub>), 697 (s, PPh<sub>3</sub>), 556 (s, PF<sub>6</sub>). MS (MALDI<sup>+</sup>): m/z 779.2 [Pt(C<sup>+</sup>C\*)(PPh<sub>3</sub>)]<sup>+</sup>. A<sub>M</sub> (5 × 10<sup>-4</sup> acetone): 100.7 Ω<sup>-1</sup> cm<sup>2</sup> mol<sup>-1</sup>.

### Synthesis of [Pt(Cbz-C<sup>+</sup>C\*)(P<sup>+</sup>N)]PF<sub>6</sub> (6)

2-(2-(Diphenylphosphino)ethyl)pyridine (40.1 mg, 0.138 mmol) and KPF<sub>6</sub> (25.3 mg, 0.138 mmol) were added to a suspension of 3 (81.7 mg, 0.138 mmol) in a mixture of dichloromethane/acetone (10/5 mL) at rt., under an argon atmosphere. After 2 hours of the reaction, the solution was evaporated to dryness. Then, 10 mL of dichloromethane was added and the solution was filtered through Celite and evaporated to dryness again. The residue was treated with diethyl ether (5 mL) and filtered. The solid was purified by dissolving in dichloromethane/methanol (2/2 mL) and then adding 20 mL of diethyl ether to precipitate 6 as a yellow solid. Yield: 91.6 mg, 69.8%. Anal. calcd. for C<sub>41</sub>H<sub>34</sub>F<sub>6</sub>N<sub>4</sub>P<sub>2</sub>Pt: C, 51.63; H, 3.59; N, 5.87. Found: C, 51.49; H, 3.44; N, 5.64. IR (ATR, cm<sup>-1</sup>): ν = 834 (s, PF<sub>6</sub>), 556 (s, PF<sub>6</sub>). MS (MALDI<sup>+</sup>): m/z 808.3 [Pt(C<sup>+</sup>C\*)(P<sup>+</sup>N)]<sup>+</sup>. A<sub>M</sub> (5 × 10<sup>-4</sup> acetone): 67.5 Ω<sup>-1</sup> cm<sup>2</sup> mol<sup>-1</sup>.

### Synthesis of [Pt(Cbz-C<sup>+</sup>C\*)(dppm)]PF<sub>6</sub> (7)

dppm (49 mg, 0.13 mmol) and KPF<sub>6</sub> (23 mg, 0.13 mmol) were added to a suspension of 3 (75 mg, 0.13 mmol) in acetone (25 mL). After 3 h of the reaction at room temperature, the mixture was evaporated to dryness. The residue was treated with dichloromethane (3 × 15 mL) and filtered through Celite. Then, the solution was evaporated to a volume of ca. 2 mL and the addition of diethyl ether (15 mL) rendered 7 as a pale-yellow solid. Yield: 90 mg, 68.2%. Anal. calcd. for C<sub>47</sub>H<sub>38</sub>N<sub>3</sub>P<sub>3</sub>F<sub>6</sub>Pt: C, 53.93; H, 3.66; N, 4.01. Found: C, 53.73; H, 3.70; N, 3.72. IR (ATR, cm<sup>-1</sup>): ν = 834 (s, PF<sub>6</sub>), 556 (s, PF<sub>6</sub>). MS (MALDI<sup>+</sup>): m/z 901.4 [Pt(C<sup>+</sup>C\*)(dppm)]<sup>+</sup>. A<sub>M</sub> (5 × 10<sup>-4</sup> M acetone) = 64.54 Ω<sup>-1</sup> cm<sup>2</sup> mol<sup>-1</sup>.

### Synthesis [Pt(Cbz-C<sup>+</sup>C\*)(dppe)]PF<sub>6</sub> (8)

It was prepared following the method described for 7. dppe (83 mg, 0.21 mmol), KPF<sub>6</sub> (38 mg, 0.21 mmol) and 3 (124 mg,



0.21 mmol). Compound **8** (159 mg, 72%). Anal. calcd for  $C_{48}H_{40}N_3P_3F_6Pt$ : C, 54.35; H, 3.80; N, 3.96. Found: C, 54.14; H, 3.84; N, 4.01. IR (ATR,  $cm^{-1}$ ):  $\nu = 835$  (s,  $PF_6$ ), 556 (s,  $PF_6$ ). MS (MALDI+):  $m/z$  915.1  $[Pt(C^{\wedge}C^*)(dppe)]^+$ .  $A_M$  ( $5 \times 10^{-4}$  M acetone) =  $64.37 \Omega^{-1} cm^2 mol^{-1}$ .

#### Synthesis of $[Pt(Cbz-C^{\wedge}C^*)(dppbz)]PF_6$ (**9**)

It was prepared following the method described for **7**. dppbz (83 mg, 0.18 mmol),  $KPF_6$  (34 mg, 0.18 mmol) and **3** (110 mg, 0.19 mmol). Compound **9** (178 mg, 86.3%). Anal. calcd for  $C_{52}H_{40}N_3P_3F_6Pt$ : C, 56.32; H, 3.64; N, 3.79. Found: C, 56.07; H, 3.69; N, 3.79. IR (ATR,  $cm^{-1}$ ):  $\nu = 833$  (s,  $PF_6$ ), 547 (s,  $PF_6$ ). MS (MALDI+):  $m/z$  963.6  $[Pt(C^{\wedge}C^*)(dppbz)]^+$ .  $A_M$  ( $5 \times 10^{-4}$  M acetone) =  $64.99 \Omega^{-1} cm^2 mol^{-1}$ .

## Results and discussion

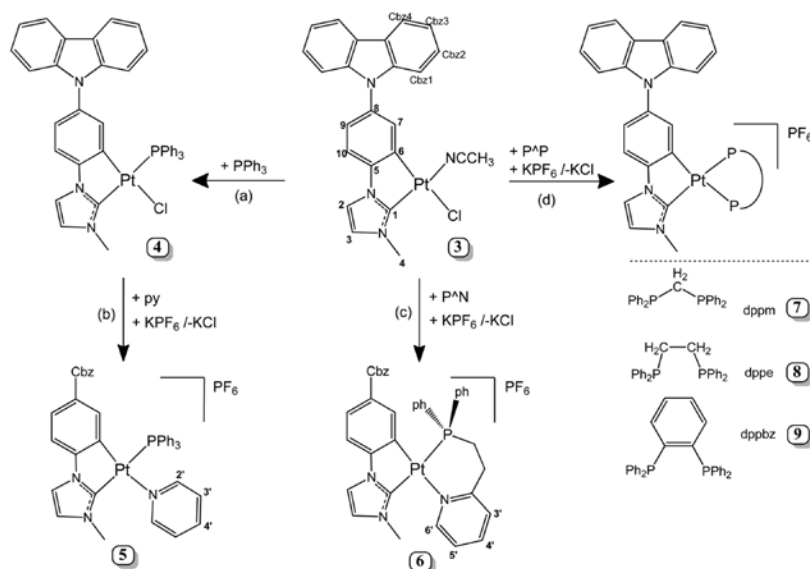
### Synthesis and characterization of platinum(II) complexes

The new Pt(II) complex with a cyclometallated N-heterocyclic carbene (NHC) containing an appended carbazole, **3**, was synthesized following a procedure similar to a previously reported one<sup>29,33,49</sup> (see the ESI† part 1.6 and Fig. S1–S3 for the NMR spectra) and it was used as the starting material to synthesize new complexes containing the  $Pt(Cbz-C^{\wedge}C^*)$  fragment. As shown in Scheme 1, compound **4** (path a) was prepared by adding  $PPh_3$  to a suspension of **3** in dichloromethane at room temperature. After the reaction work-up, a yellow solid was obtained in a very good yield (85%). Compound **5** was obtained as a yellow solid by reacting **4** with pyridine and  $KPF_6$  in a mixture of acetone and dichloromethane at rt

(Scheme 1, path b). On the other hand, compounds **6–9** were obtained directly from compound **3**,  $KPF_6$  and the corresponding chelating phosphine (see Scheme 1, paths c and d).

Regarding structural characterization, multinuclear NMR spectra (Fig. S4–S9, ESI† and Table 1) provided the most significant information, which revealed that only one isomer was obtained for compounds **4–6**, the *trans*-( $C_1$ , P). Their  $^{31}P\{^1H\}$  resonances appear flanked by  $^{195}Pt$  satellites with Pt–P coupling constants around 2900 Hz, according to the P atom being located *trans* to the N-heterocyclic carbene ( $C_1$ ).<sup>50</sup> Compared to the diphosphine complexes, the two inequivalent P atoms appear as an AB system for the dppm derivative (**7**) or as two doublets for **8** and **9**.  $^{31}P$  and  $^{195}Pt$  chemical shifts and the  $J_{Pt,P}$  values are similar to those found in the related compounds  $[Pt(R-C^{\wedge}C^*)(PPh_3)(py)]PF_6$  ( $R = -CN, -CO_2Et$ )<sup>31</sup> and  $[Pt(R-C^{\wedge}C^*)(P^{\wedge}P)]PF_6$  ( $R = -H,^{27} -CN,^{27}$  and  $-CO_2Et^{29}$ ). Also, it deserves to be noted that the H4 resonance appears more shielded ( $\delta \sim 2.9$ – $3.2$  ppm) in **5–9** than that in compound **4** ( $\delta = 4.3$  ppm) due to the anisotropic shielding effect caused by the proximity in space of the aromatic ring current of the pyridine or phenyl rings.

The structures of **5–7** and **9** were confirmed by X-ray diffraction (Fig. 1 and Fig. S10 and Tables S1 and S2, ESI†). In **5** and **6**, the asymmetric unit contains two molecules (Pt01 and Pt02) with very similar structural details; thus, only one set of data (Pt01) is included in Table S2 (ESI†) for discussion. As expected, they are mononuclear complexes with the platinum(II) center in a distorted square-planar environment due to the small bite angle of the  $C^{\wedge}C^*$  ligand, which is under  $80^\circ$  in all cases.  $PPh_3$  and pyridine complete the coordination sphere of the metal center in **5**, whereas in the rest these positions are filled in by



Scheme 1 Synthesis of compounds **4–9**. The numerical scheme for NMR purposes.





Paper

**Table 1** Relevant  $^{31}\text{P}\{^1\text{H}\}^a$  and  $^{195}\text{Pt}\{^1\text{H}\}^b$  NMR data ( $\delta$  (ppm),  $J$  (Hz))

Compounds	$\delta$ Pt	$J_{\text{Pt,trans-C1}}$	$J_{\text{Pt,trans-C6}}$	$\delta$ P <sub>trans-C1</sub>	$\delta$ P <sub>trans-C6</sub>	$J_{\text{P,P}}$
5	-4271	2914.2		29.0		
6	-4208	2896.5		19.2		
7	-4384	2374.9	1559.7	-38.8 $\nu_A$	-39.4 $\nu_B$	42
8	-4983	2699.9	1964.2	50.4	43.4	6.3
9	-4917	2661.4	1956.2	47.0	39.8	4.4

<sup>a</sup> 162 MHz, CD<sub>2</sub>Cl<sub>2</sub>. <sup>b</sup> 86 MHz, CD<sub>2</sub>Cl<sub>2</sub>.

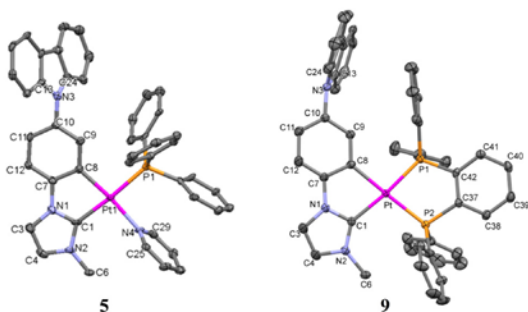


**Fig. 1** Molecular structures of the cationic complexes **5** and **9**. Thermal ellipsoids are drawn at the 50% probability level. Hydrogen atoms, solvent molecules and PF<sub>6</sub><sup>-</sup> have been omitted for clarity.

the P and X (N (**6**) and P (**7**, **9**)) atoms from the chelating phosphine ligands. Comparing the bite angle of these chelate ligands (P–Pt–X), it can be observed that it is lower for compound **7** (71.37(10)°), which forms a four-membered ring, than those observed for **6** and **9**, with six- and five-membered rings.

Bond distances and angles (Table S2, ESI†) are similar to those observed in other complexes with the same kinds of ligands.<sup>27,29,31,50</sup> The Cbz moiety (N3 and C13–C24) appears twisted with respect to the platinum coordination plane forming dihedral angles of 59.21(3)° for **5**, 61.47(2)° for **6**, 54.39(17)° for **7** and 75.76(4)° for **9**. In **5**, the interplanar angle between the platinum coordination plane and that of the pyridine is 79.8(2)°, while it is somewhat lower (53.7(1)°) for the complex with the chelate ligand, **6**. As commented before, this orientation of the pyridine ring has a great influence on the H<sub>4</sub> signal in the <sup>1</sup>H NMR spectra. Also, in their supramolecular structure, there are no close intermolecular Pt···Pt or  $\pi$ – $\pi$  interactions between the adjacent molecules, probably due to the great steric demand of the Cbz and phosphine groups.

**Photophysical properties and theoretical calculations**

The photophysical properties of the ionic compounds **5–9** have been investigated. Their absorption spectra in CH<sub>2</sub>Cl<sub>2</sub> solution are depicted in Fig. 2 and their data are listed in Table S3 (ESI†). They exhibit very similar absorption profiles with relatively intense bands around 290–350 nm that are normally attributed to intraligand transitions of the NHC ligand. Additionally, they show rather weak absorptions at  $\lambda > 370$  nm that appear slightly redshifted for the diphosphine derivatives (see the inset

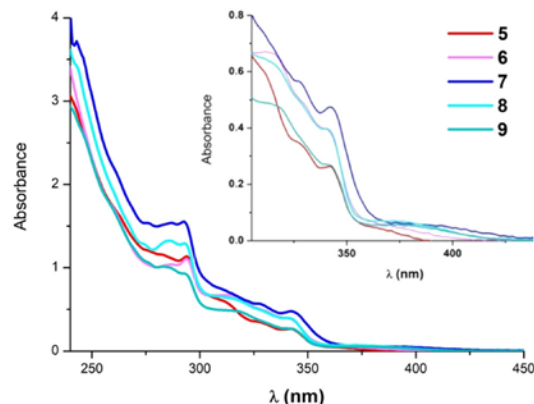


**Fig. 2** UV-Vis spectra of **5–9** in CH<sub>2</sub>Cl<sub>2</sub> at  $5 \times 10^{-5}$  M. Inset: close-up for the 350–450 nm range.

of Fig. 2). These bands do not experience any significant wavelength shift with solvent polarity (Fig. S11, ESI† for **9**).

A concentration dependence study of **5** and **7** in CH<sub>2</sub>Cl<sub>2</sub> showed that no significant ground state aggregation takes place in the concentration range from  $10^{-6}$  to  $10^{-3}$  M (see Fig. S12 and S13, ESI†). Therefore, the low energy absorptions at  $\lambda > 370$  nm are originated from electronic transitions within the mononuclear species. Besides, when comparing compounds with the same ancillary ligands but different C<sup>\*</sup>C<sup>\*</sup> groups [Pt(R–C<sup>\*</sup>C<sup>\*</sup>)(PPh<sub>3</sub>(py))PF<sub>6</sub>], (R = –CN, –CO<sub>2</sub>Et)<sup>31</sup> and [(R–C<sup>\*</sup>C<sup>\*</sup>–Pt(P<sup>\*</sup>P))PF<sub>6</sub>], (R = –H, –CN, –CO<sub>2</sub>Et),<sup>27,29</sup> the absorption bands appear shifted to lower energies in these electron donating carbazolyl derivatives (**5** and **7–9**). Thus, these observations are indicating a great participation of the C<sup>\*</sup>C<sup>\*</sup> fragment in the electronic transitions.

To gain further knowledge on this matter, theoretical calculations (density functional theory (DFT) and time dependent density functional theory (TD-DFT)) were carried out for **5**, **7** and **9** in CH<sub>2</sub>Cl<sub>2</sub> (Tables S4 and S5, ESI†). Considering that the computational results of the diphosphine derivatives are very similar, those corresponding to **9** are available in the ESI†. As shown in Fig. 3, the lowest energy calculated absorption (S<sub>1</sub>) fits well with the experimental one and its main contribution is the HOMO → LUMO transition (69% **5** and 92% **7**, see Fig. 3). The assignment of these electronic transitions is based on the analysis of the frontier orbitals (Table S5, ESI†).

For both complexes, the HOMO is centered on the NHC ligand (99%), essentially on the Cbz fragment whereas the LUMO is distributed over the ancillary ligands (50% **5** and 28% **7**), the NHC (32% **5** and 43% **7**) and the Pt center (18% **5** and 29% **7**), with no participation of the Cbz fragment. Thus, the lowest energy absorption for both is attributed to a mixed transition LL'/CT [ $\pi$ (NHC) →  $\pi^*$ (L')]/ILCT [(NHC)] and LMCT [ $\pi$ (NHC) → d(Pt)], with the latter having a greater contribution in **7**.

The photoluminescence properties were examined in poly(methyl methacrylate) (PMMA) films at a 5 wt% doping

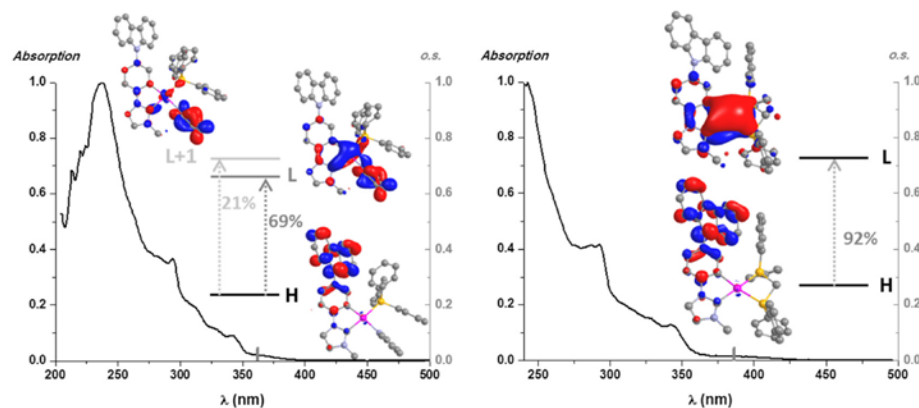


Fig. 3 UV-Vis absorption spectra,  $S_1$  calculated transitions in  $\text{CH}_2\text{Cl}_2$  (bars) and molecular orbital plots (isovalue 0.03) of compounds **5** (left) and **7** (right).

Table 2 Photophysical data for **5–9** in 5 wt % PMMA films with  $\lambda_{\text{exc}} = 340$  nm

Comp.	$\lambda_{\text{em}}(\text{nm})$	$\tau(\mu\text{s})^a$	$\Phi_{\text{Ar}}/\Phi_{\text{Air}}$	$k_r^a$	$k_{\text{nr}}^a$
<b>5</b>	461, 481 <sub>max</sub>	22.6	0.47/0.39	$1.7 \times 10^4$	$2.7 \times 10^4$
<b>6</b>	467, 484 <sub>max</sub>	18.1	0.49/0.35	$1.9 \times 10^4$	$3.6 \times 10^4$
<b>7</b>	492 <sub>shr</sub> , 522 <sub>max</sub>	22.1	0.76/0.55	$2.5 \times 10^4$	$2.0 \times 10^4$
<b>8</b>	487 <sub>shr</sub> , 507 <sub>max</sub>	26.6	0.77/0.50	$1.8 \times 10^4$	$1.8 \times 10^4$
<b>9</b>	478 <sub>shr</sub> , 509 <sub>max</sub>	23.1	0.83/0.63	$2.7 \times 10^4$	$1.6 \times 10^4$

<sup>a</sup> In air;  $k_r = \Phi/\tau_{\text{exp}}$  and  $k_{\text{nr}} = (1 - \Phi)/\tau_{\text{exp}}$ .

concentration of the Pt compound (Table 2). As shown in Fig. 4, compounds **5** and **6** show blue emissions whereas the diphosphine derivatives (**7–9**) display green ones. Their emission lifetime decays fit to one rather long component ( $\sim 20$   $\mu\text{s}$ ) and their quantum yield (QY) measurements reach very high values under an Ar atmosphere, in particular those corresponding to the P<sup>^</sup>P derivatives (QY > 0.75). The excitation

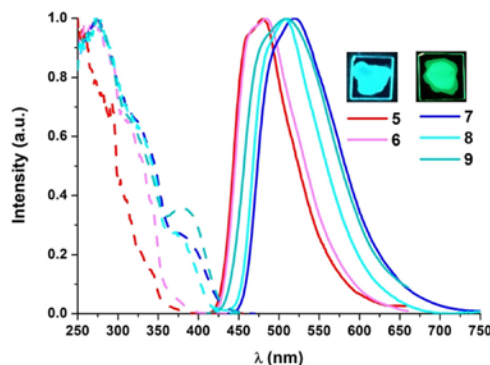


Fig. 4 Normalized excitation (—) and emission (---) spectra of **5–9** in 5 wt% PMMA films (right;  $\lambda_{\text{exc}} = 340$  nm). Pictures of **5** and **7** were taken under 365 nm light.

spectra match the absorption ones, even though there is a remarkable increase in the intensity of the lowest energy band.

To assist in the photoluminescence discussion, the lowest energy triplet states for the optimized structures at the ground state have been calculated by TD-DFT in  $\text{CH}_2\text{Cl}_2$  (see Tables S4 and S5, the ESI<sup>†</sup>) for the three lowest ones:  $T_1$ ,  $T_2$  and  $T_3$ . In all cases,  $T_1$  energies are considerably lower than those for  $T_2$  (0.16 eV for **5**, 0.28 eV for **7** and 0.17 eV for **9**); thus, there are no close low-lying triplets. The calculated wavelengths of these  $T_1$  states follow the trend observed for the experimental phosphorescence data (calculated 429 **5**, 449 **7**, and 431 nm **9** vs. experimental 481 **5**, 522 **7**, and 509 nm **9**). Also, the geometry optimizations of the  $T_1$  states were carried out and their spin-density distributions calculated (Fig. S15, ESI<sup>†</sup>). They are mainly located on the C<sup>^</sup>C\* ligand (1.803 **5**, 1.712 **7**, and 1.753 **9**) and to a minor extent on the Pt center (0.150 **5**, 0.166 **7**, and 0.155 **9**) and the ancillary ligands (0.047 **5**, 0.122 **7**, and 0.092 **9**). This great contribution of C<sup>^</sup>C\* to the emissive state  $T_1$  agrees with the obtained  $K_r$  values ( $10^4$  order, Table 2).<sup>51</sup>

Therefore, the emission for all complexes would be attributed mainly to metal-perturbed  $^3\text{IL}$  [NHC] transitions with some contribution of LL'/CT [ $\pi(\text{NHC}) \rightarrow \pi^*(\text{L}')$ ]. Similar to what occurs in the UV-vis absorptions, the emissions of **5** ( $\lambda_{\text{max}} = 481$  nm) and **7–9** ( $\lambda_{\text{max}} = 522$ – $507$  nm) appear shifted to lower energies in relation to those bearing different substituents in the C<sup>^</sup>C\* ligand [Pt(R-C<sup>^</sup>C\*)(py)(PPh<sub>3</sub>)PF<sub>6</sub> (R = -CN, -CO<sub>2</sub>Et;  $\lambda_{\text{max}} \sim 470$  nm)<sup>31</sup> and [(R-C<sup>^</sup>C\*)Pt(P<sup>^</sup>P)]PF<sub>6</sub> (R = -H, -CN, -CO<sub>2</sub>Et;  $\lambda_{\text{max}} \sim 490$ – $476$  nm).<sup>27,29</sup> Thus, based on these spectroscopic observations and on the DFT calculations, the presence of an electron donating group (R = Cbz) in the C<sup>^</sup>C\* skeleton increases the energy of the HOMO and results in a red-shift in the emission bands.

#### Light-emitting electrochemical cells

Light-emitting electrochemical cells using complexes **5–9** as active materials were fabricated. Complexes were mixed with





the ionic liquid (IL) 1-butyl-3-methyl-imidazolium-hexafluorophosphate (BMIM<sup>+</sup>PF<sub>6</sub><sup>-</sup>) in a molar ratio of 4 to 1 (iTMC:IL). In the case of complexes **7**, **8** and **9**, they were dissolved in two different solvents, acetonitrile (ACN) and dichloromethane (DCM). Due to their low solubility in these solvents, complexes **5** and **6** were tested in dichloroethane (DCE) solutions. The active layers (iTMC:IL) were characterized by means of photoluminescence (PL) and quantum yield (PLQY). Devices were then fabricated from the solutions adopting the archetypical stack configuration: ITO/PEDOT:PSS (80 nm)/iTMC + IL (90–120 nm)/Al (100 nm) (where ITO is indium tin oxide and PEDOT:PSS is poly(3,4-ethylenedioxythiophene):poly(styrenesulfonate)). The details of the processing can be found in the Experimental Section of the ESI.† Devices were tested by measuring their performance over time and their electroluminescence (EL) spectra were recorded.

We will start the discussion focusing on the emitters **7**, **8** and **9**. The principal figures of merit are collected in Table 3. First, the PL and PLQY of the active layers prepared from ACN and DCM solutions of **7**, **8** and **9** were measured ( $\lambda_{\text{ex}} = 340 \text{ nm}$ ), showing no significant solvent effect on either  $\lambda_{\text{em}}$  or PLQY (Fig. S16, ESI† and Table 3). These PLQY values are far lower than the ones obtained in PMMA, most probably due to the higher concentration of iTMC in the active layer. In fact, a self-quenching process is often observed, taking place in highly concentrated iTMC thin films.<sup>52</sup> These results are in agreement with the lower PLQYs of the solid samples of compounds **7–9** (Table S6, ESI†) compared to those obtained in PMMA. The QY values are generally a good indicator of the luminance performance of iTMCs when employed in a light-emitting device. In view of these results, a similar peak luminance is expected regardless of the solvent used.

The LEC devices were operated under a pulsed current driving with an average current density of  $50 \text{ A m}^{-2}$  (1000 Hz block-wave, 50% duty cycle with a peak current of  $100 \text{ A m}^{-2}$ ) and, in contrast to what was expected from the PLQY results, they behaved quite differently depending on the solvent used to process the active layers (Fig. 5).

Devices made from ACN solutions (Fig. 5a) showed in general lower efficiency with maximum luminance values of about  $60 \text{ cd m}^{-2}$ , current efficiency (CE) values of around  $1.2 \text{ cd A}^{-1}$  and power efficiency (PE) values of around  $0.6 \text{ lm W}^{-1}$ . When devices were fabricated from DCM instead, a three- to four-fold increase of the luminance and efficiency values was

observed, achieving luminance values of  $265 \text{ cd m}^{-2}$ ,  $187 \text{ cd m}^{-2}$  and  $180 \text{ cd m}^{-2}$  with peak CEs of  $5.7 \text{ cd A}^{-1}$ ,  $3.7 \text{ cd A}^{-1}$  and  $3.6 \text{ cd A}^{-1}$  and peak PEs of  $2.2 \text{ lm W}^{-1}$ ,  $1.3 \text{ lm W}^{-1}$  and  $1.1 \text{ lm W}^{-1}$  for compound **7**, **8** and **9**, respectively. These effects were also reflected in the external quantum efficiency (EQE), as expected since it depends directly on the CE (see Table 3). When compared with the theoretical maximum EQEs of these devices extracted from eqn S1 and shown in Table S7 (ESI†), we notice that the EQE derived from the EL data is substantially lower than the calculated EQE. The main reason behind this could be a quench of the emitter during the device operation. A possible cause for this phenomenon can be an unbalanced current injection because of the impartial screening by the mobile ions accumulated at the electrodes.<sup>53,54</sup> Another reason, as discussed above, is the effect of the concentration that eventually leads to a self-quenching of the emission.

Lower driving currents have been shown to improve the LEC device efficiency.<sup>55</sup> We biased devices fabricated from DCM and using emitter **7** with a pulsed current driving with average current densities of 25 and  $12.5 \text{ A m}^{-2}$  (Fig. S17a and b, ESI†). The results show that, even using these lower biases, the efficiencies remain very similar, with peak efficiencies of  $4.7$  and  $5.2 \text{ cd A}^{-1}$  for current densities of 25 and  $12.5 \text{ A m}^{-2}$ , respectively, which indicates that phenomena such as self-heating of the device is not the limiting factor on the efficiency in these devices, at least in the current density range studied.<sup>56</sup> A similar trend was observed when biasing devices fabricated from ACN (using emitter **7**) with average current densities of 25 and  $12.5 \text{ A m}^{-2}$  (Fig. S17c and d, ESI†). Generally, the half-luminance lifetime ( $t_{50}$ ) value is defined as the time needed to reach 50% of the peak luminance and it is used to determine the stability of a device over time, albeit it is also dependent on the driving conditions. In this case, devices made from ACN have  $t_{50}$  values of 13, 35 and 43 minutes, for emitters **7**, **8** and **9**, respectively, while those from DCM have  $t_{50}$  values of 15, 13 and 17 minutes, respectively. The increase in luminance together with the reduced  $t_{50}$  for DCM devices, despite the same PLQY values, could be explained by two main factors. The first point to take into consideration is the difference in the boiling point of the two solvents,  $\sim 81 \text{ }^\circ\text{C}$  for ACN and  $\sim 40 \text{ }^\circ\text{C}$  for DCM and the temperature at which the films were annealed before the cathode vacuum deposition,  $70 \text{ }^\circ\text{C}$  for 15 min. These annealing conditions could allow all the DCM to evaporate and escape from the samples but in the case of the ACN residual solvent

Table 3 Figures of merits of the devices obtained from **7**, **8** and **9** in ACN and DCM

Emitter in ACN	PL $\lambda_{\text{em}}$ [nm]	PLQY [%]	EL [nm]	Peak Lum. [ $\text{cd m}^{-2}$ ]	$t_{50}$ [min]	CE [ $\text{cd A}^{-1}$ ]	PE [ $\text{lm W}^{-1}$ ]	EQE [%]
<b>7</b>	531	11	523	61	13	1.2	0.61	0.34
<b>8</b>	516	8	528	60	35	1.2	0.61	0.33
<b>9</b>	521	14	519	57	43	1.1	0.58	0.32
Emitter in DCM	PL $\lambda_{\text{em}}$ [nm]	PLQY [%]	EL [nm]	Peak Lum. [ $\text{cd m}^{-2}$ ]	$t_{50}$ [min]	CE [ $\text{cd A}^{-1}$ ]	PE [ $\text{lm W}^{-1}$ ]	EQE [%]
<b>7</b>	525	12	542	265	15	5.7	2.24	1.46
<b>8</b>	517	6	535	187	13	3.7	1.26	0.97
<b>9</b>	517	11	528	180	17	3.6	1.13	1.00



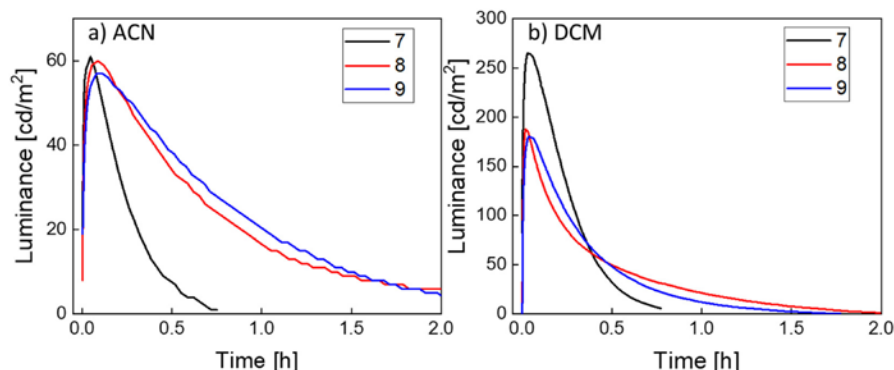


Fig. 5 Time-dependence of the luminance [ $\text{cd m}^{-2}$ ] of LECs ITO/PEDOT:PSS/iTMC:IL(4:1)/Al (iTMC: **7** (black), **8** (red) and **9** (blue)) with the active layer prepared from solutions in ACN (a) and DCM (b). All the devices shown were driven with a pulsed current with an average current density of  $50 \text{ A m}^{-2}$ .

could remain in the active films. The effect of retained solvents has been reported in the past as detrimental for the devices as it can lead to degradation pathways or quenching.<sup>57</sup> In view of this, and once the stability of the emitters was checked by NMR in  $\text{MeCN-}d_3$  at  $70^\circ\text{C}$  for at least 1 hour (Fig. S18, ESI<sup>†</sup> for **7**), we increased the annealing conditions of devices prepared from ACN in terms of time and temperature. To do this, we prepared a device using emitter **7** with a longer annealing time (4 h) at the same temperature ( $70^\circ\text{C}$ ) and a device using emitter **9** with a higher temperature annealing process ( $90^\circ\text{C}$ ) and a longer time (1 h). The performance of the device processed at  $70^\circ\text{C}$  for 4 h slightly improved with a maximum luminance of  $75 \text{ cd m}^{-2}$  (vs.  $61 \text{ cd m}^{-2}$ ), a CE of  $1.5 \text{ cd A}^{-1}$  (vs.  $1.2 \text{ cd A}^{-1}$ ) and a  $t_{50}$  of 11 min (vs. 13 min) (Fig. S19a, ESI<sup>†</sup>). On the other hand, the device processed at higher annealing temperature not only did not improve but it decreased, showing a maximum luminance of  $48 \text{ cd m}^{-2}$  (vs.  $57 \text{ cd m}^{-2}$ ), a CE of  $0.96 \text{ cd A}^{-1}$  (vs.  $1.1 \text{ cd A}^{-1}$ ) and a  $t_{50}$  of 7 min (vs. 43 min) (Fig. S19b, ESI<sup>†</sup>). These results, in particular the much lower  $t_{50}$ , could be an indication that the harsher annealing conditions are inducing a degradation of the emitter. The second aspect to be pointed out is the voltage during operation (Fig. S20, ESI<sup>†</sup>). When compared, the voltage of the devices prepared from ACN is significantly lower than the DCM, with values between 3 V and 3.5 V for ACN and values between 4 V and 5 V for DCM. The origin of this effect can also be related to the residual solvent present on the active layer, where it has been seen that the presence of a solvent decreases the resistance of the film, resulting in a lower turn-on voltage.<sup>57</sup> Lower voltages notoriously allow for longer lifetimes, and therefore higher  $t_{50}$ , but at the expense of lower luminance levels. All in all, these results point that the origin of the difference in the performance of devices processed from ACN and from DCM might reside in their different morphology. Indeed, in previous works, it has been seen that morphology can affect the performance of LEC devices.<sup>58–60</sup> However, atomic force microscopy (AFM) images show no significant differences between active films using emitter **7** processed from different solvents (Fig. S21, ESI<sup>†</sup>). Both layers are very flat and

homogeneous with no apparent phase separation or aggregation and with just small differences in the root mean square (RMS) roughness of the films (0.5 nm and 0.3 nm for ACN and DCM, respectively).

Finally, the EL spectra were characterized in both ACN and DCM (Fig. 6a, b and Table 3). In ACN, the EL peaks of **7**, **8** and **9** are centered at 523 nm, 528 nm and 519 nm while in DCM at 542 nm, 535 nm and 528 nm, respectively. The slight difference on the EL peaks between ACN- and DCM-processed devices is ascribed to optical effects arising from the differences in the thicknesses of the active layers (90 and 120 nm, respectively). The EL is very similar to the PL of the active layer films. In some cases, **8** from ACN and **7**, **8** and **9** from DCM, a slight red-shift of the EL can be observed. The red-shift of the EL of iTMCs can be common and was also previously observed in LECs based on Ir(III) and Cu(I) complexes.<sup>61,62</sup> The corresponding emission colours, expressed as CIE (Commission Internationale de l'Éclairage) coordinates, are shown in Fig. S22 (ESI<sup>†</sup>) and compiled in Table S8 (ESI<sup>†</sup>). The EL was also measured over time (for devices made from emitter **7**), down to their  $t_{50}$ , in order to observe the EL evolution during the degradation (Fig. S23, ESI<sup>†</sup>). The  $\lambda_{\text{max}}$  of the EL remains constant for devices processed from ACN and only slightly changes for devices processed from DCM (from 542 to 549 nm), an indication of the high stability of the EL over the lifetime of the device. Notably, as seen by the EL spectra and the CIE coordinates, the three devices emit in the green region. To our knowledge, these are the first reported green-emitting Pt(II)-based LECs.

In spite of their simplicity, iTMC-LECs fabricated from DCM solutions of the carbazole-appended compounds, **7–9**, showed an improved performance than PhOLEDs based on similar complexes bearing  $\text{R-C}^*\text{C}^*$  ( $\text{R} = \text{H}, \text{CN}$ ), since the optimal OLED, based on compound  $[\text{Pt}(\text{H-C}^*\text{C}^*)(\text{dppbz})]\text{PF}_6$  achieved a maximum luminance of  $200 \text{ cd m}^{-2}$  with a peak CE of 0.4, at  $10 \text{ V}$ .<sup>27</sup>

Similarly, devices made from compounds **5** and **6** were also fabricated. The active layers (iTMC:IL) showed very low PLQYs with values of 1% for both emitters. Devices made with **5** and **6**



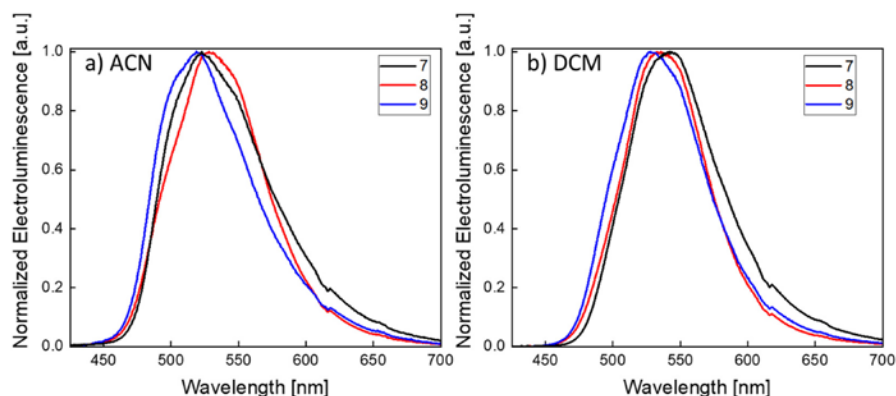


Fig. 6 Normalized electroluminescence spectra of LEC devices ITO/PEDOT:PSS/iTMC:IL(4 : 1)/Al, (iTMC: **7** (black), **8** (red) and **9** (blue)) with the active layer prepared from solutions in ACN (a) and DCM (b).

turned-on, showing the classic voltage evolution over time of a LEC (Fig. S24, ESI<sup>†</sup>); however their performance was extremely poor. For emitter **6**, the maximum observed luminance was  $4 \text{ cd m}^{-2}$  (Fig. S24b, ESI<sup>†</sup>) while for emitter **5** the luminance was lower than the sensitivity of our LEC lifetime characterization setup (less than *ca.*  $1 \text{ cd m}^{-2}$ ). For emitter **6**, it was also possible to measure the EL spectra, which showed a blue emission centered at 491 nm (CIE 0.2343, 0.4776). The very low QY of emitters **5** and **6** somewhat predicts the very low EL observed on these devices.

## Conclusions

Platinum(II) complexes bearing new carbazole-appended cyclometallated N-heterocyclic carbenes such as [Pt(Cbz-C<sup>∧</sup>C<sup>\*</sup>)Cl(NCCH<sub>3</sub>)<sub>3</sub>](**3**), [Pt(Cbz-C<sup>∧</sup>C<sup>\*</sup>)Cl(PPh<sub>3</sub>)<sub>3</sub>](**4**), [Pt(Cbz-C<sup>∧</sup>C<sup>\*</sup>)(PPh<sub>3</sub>)(py)]PF<sub>6</sub> (**5**), [Pt(Cbz-C<sup>∧</sup>C<sup>\*</sup>)(P<sup>∧</sup>N)]PF<sub>6</sub> (**6**), and [Pt(Cbz-C<sup>∧</sup>C<sup>\*</sup>)(P<sup>∧</sup>P)]PF<sub>6</sub> (P<sup>∧</sup>P: dppm **7**; dppe, **8**; dppbz, **9**) have been prepared by a stepwise procedure from 9-(4-bromo-phenyl)-9H-carbazole, imidazole, [{Pt(μ-Cl)(η<sup>3</sup>-2-Me-C<sub>3</sub>H<sub>4</sub>)<sub>2</sub>}] and the corresponding ancillary ligands and then exhaustively characterized. The presence of an electron donating group (R = Cbz) in the R-C<sup>∧</sup>C<sup>\*</sup> skeleton of these complexes increases the energy of the HOMO compared with those of similar complexes bearing R-C<sup>∧</sup>C<sup>\*</sup> (R = H, CN, and CO<sub>2</sub>Et), shifting their emissions from blue to green. In spite of the simplicity, iTMC-LECs fabricated from the DCM solutions of the carbazole-appended compounds, **7–9**, operate at a 4–5 V voltage, and achieve luminance values of 265, 187 and  $180 \text{ cd m}^{-2}$  with peak CEs of 5.7, 3.7 and  $3.6 \text{ cd A}^{-1}$ , respectively. Thus, we have tactically brought together the strong electron-donating abilities and good hole transporting properties from Pt(C<sup>∧</sup>C<sup>\*</sup>) and Cbz groups to prepare the first green-emitting iTMC-LECs based on mononuclear Pt(II) complexes.

## Conflicts of interest

The authors declare no competing financial interest.

## Acknowledgements

This work was supported by the “Ministerio de Ciencia Innovación y Universidades”/FEDER (Project PGC2018-094749-B-I00) and the Gobierno de Aragón (Grupo E17\_20R: Química Inorgánica y de los Compuestos Organometálicos). The authors thank the Centro de Supercomputación de Galicia (CESGA) for generous allocation of computational resources. The authors acknowledge support from Comunitat Valenciana (IDIFEDER/2020/063, PROMETEU/2020/077 and CIGE/2021/027), the European Research Council (ERC) under the European Union’s Horizon 2020 research and innovation program Grant agreement No. 834431 and the Spanish Ministry of Science, Innovation and Universities (MICIU) (RTI2018-095362-A-I00 and EQC2018-004888-P).

## References

- 1 K. Schlingman, Y. Chen, R. S. Carmichael and T. B. Carmichael, *Adv. Mater.*, 2021, **33**, 2006863.
- 2 Q. B. Pei and R. D. Costa, *Adv. Funct. Mater.*, 2020, **30**.
- 3 Q. B. Pei, G. Yu, C. Zhang, Y. Yang and A. J. Heeger, *Science*, 1995, **269**, 1086–1088.
- 4 E. Frezza and R. D. Costa, *Adv. Funct. Mater.*, 2020, **30**, 1908176.
- 5 K. Youssef, Y. Li, S. O’Keeffe, L. K. Li and Q. Pei, *Adv. Funct. Mater.*, 2020, **30**, 1909102.
- 6 S. B. Meier, D. Tordera, A. Pertegas, C. Roldan-Carmona, E. Orti and H. J. Bolink, *Mater. Today*, 2014, **17**, 217–223.
- 7 S. Tang, A. Sandström, P. Lundberg, T. Lanz, C. Larsen, S. van Reenen, M. Kemerink and L. Edman, *Nat. Commun.*, 2017, **8**, 1190.
- 8 Q. J. Sun, Y. F. Li and Q. B. Pei, *J. Disp. Technol.*, 2007, **3**, 211–224.
- 9 T. Lanz, E. M. Lindh and L. Edman, *J. Mater. Chem. C*, 2017, **5**, 4706–4715.



- 10 E. M. Lindh, P. Lundberg, T. Lanz and L. Edman, *Sci. Rep.*, 2019, **9**, 10433.
- 11 J. Ràfols-Ribé, X. Zhang, C. Larsen, P. Lundberg, E. M. Lindh, C. T. Mai, J. Mindemark, E. Gracia-Espino and L. Edman, *Adv. Mater.*, 2022, **34**, 2107849.
- 12 L. Edman, *Electrochim. Acta*, 2005, **50**, 3878–3885.
- 13 R. D. Costa, E. Orti, H. J. Bolink, F. Monti, G. Accorsi and N. Armadori, *Angew. Chem., Int. Ed.*, 2012, **51**, 8178–8211.
- 14 A. F. Henwood and E. Zysman-Colman, *Top. Curr. Chem.*, 2016, **374**, 36.
- 15 C. H. Lyons, E. D. Abbas, J. K. Lee and M. F. Rubner, *J. Am. Chem. Soc.*, 1998, **120**, 12100–12107.
- 16 G. U. Mahoro, J. Fernandez-Cestau, J.-L. Renaud, P. B. Coto, R. D. Costa and S. Gaillard, *Adv. Opt. Mater.*, 2020, **8**, 2000260.
- 17 K. Matsuki, J. Pu and T. Takenobu, *Adv. Funct. Mater.*, 2020, **30**, 1908641.
- 18 R. B. Bai, X. W. Meng, X. X. Wang and L. He, *Adv. Funct. Mater.*, 2020, **30**, 1907169.
- 19 S. Keller, A. Pertegas, G. Longo, L. Martinez, J. Cerda, J. M. Junquera-Hernandez, A. Prescimone, E. C. Constable, C. E. Housecroft, E. Orti and H. J. Bolink, *J. Mater. Chem. C*, 2016, **4**, 3857–3871.
- 20 Q. Zeng, F. Li, Z. Chen, K. Yang, Y. Liu, T. Guo, G.-G. Shan and Z. Su, *ACS Appl. Mater. Interfaces*, 2020, **12**, 4649–4658.
- 21 A. F. Henwood and E. Zysman-Colman, *A Comprehensive Review of Luminescent Iridium Complexes Used in Light-Emitting Electrochemical Cells (LEECs)*, 2017.
- 22 C. E. Housecroft and E. C. Constable, *Coord. Chem. Rev.*, 2017, **350**, 155–177.
- 23 W. Lu, M. C. W. Chan, N. Y. Zhu, C. M. Che, C. N. Li and Z. Hui, *J. Am. Chem. Soc.*, 2004, **126**, 7639–7651.
- 24 K. T. Weber, K. Karikis, M. D. Weber, P. B. Coto, A. Charisiadis, D. Charitaki, G. Charalambidis, P. Angaridis, A. G. Coutsolelos and R. D. Costa, *Dalton Trans.*, 2016, **45**, 13284–13288.
- 25 M. Z. Shafikov, S. Tang, C. Larsen, M. Bodensteiner, V. N. Kozhevnikov and L. Edman, *J. Mater. Chem. C*, 2019, **7**, 10672–10682.
- 26 L. M. Cinninger, L. D. Bastatas, Y. L. Shen, B. J. Holliday and J. D. Slinker, *Dalton Trans.*, 2019, **48**, 9684–9691.
- 27 V. Sicilia, L. Arnal, A. J. Chueca, S. Fuertes, A. Babaei, A. M. Igual Munoz, M. Sessolo and H. J. Bolink, *Inorg. Chem.*, 2020, **59**, 1145–1152.
- 28 S. Fuertes, A. J. Chueca, A. Martín and V. Sicilia, *J. Organomet. Chem.*, 2019, **889**, 53–61.
- 29 V. Sicilia, S. Fuertes, A. J. Chueca, L. Arnal, A. Martín, M. Perálvarez, C. Botta and U. Giovannella, *J. Mater. Chem. C*, 2019, **7**, 4509–4516.
- 30 S. Fuertes, A. J. Chueca, M. Perálvarez, P. Borja, M. Torrell, J. Carreras and V. Sicilia, *ACS Appl. Mater. Interfaces*, 2016, **8**, 16160–16169.
- 31 S. Fuertes, A. J. Chueca, L. Arnal, A. Martín, U. Giovannella, C. Botta and V. Sicilia, *Inorg. Chem.*, 2017, **56**, 4829–4839.
- 32 S. Stipurin and T. Strassner, *Inorg. Chem.*, 2021, **60**, 11200–11205.
- 33 S. Fuertes, H. Garcia, M. Perálvarez, W. Hertog, J. Carreras and V. Sicilia, *Chem. – Eur. J.*, 2015, **21**, 1620–1631.
- 34 H. Leopold, M. Tenne, A. Tronnier, S. Metz, I. Munster, G. Wagenblast and T. Strassner, *Angew. Chem., Int. Ed.*, 2016, **55**, 15779–15782.
- 35 P. Pinter, J. Soellner and T. Strassner, *Eur. J. Inorg. Chem.*, 2021, 3104–3107.
- 36 P. Pinter, J. Soellner and T. Strassner, *Organometallics*, 2021, **40**, 557–563.
- 37 A. F. Rausch, L. Murphy, J. A. G. Williams and H. Yersin, *Inorg. Chem.*, 2012, **51**, 312–319.
- 38 H. Yersin, A. F. Rausch, R. Czerwieńiec, T. Hofbeck and T. Fischer, *Coord. Chem. Rev.*, 2011, **255**, 2622–2652.
- 39 Z. Yang, Z. Mao, Z. Y. Xie, Y. Zhang, S. Liu, J. F. Zhao, J. Xu, Z. Chi and M. P. Aldred, *Chem. Soc. Rev.*, 2017, **46**, 915–1016.
- 40 W.-J. Xu, S.-J. Liu, T.-C. Ma, Q. Zhao, A. Pertegas, D. Tordera, H. J. Bolink, S.-H. Ye, X.-M. Liu, S. Sun and W. Huang, *J. Mater. Chem.*, 2011, **21**, 13999–14007.
- 41 A. Chan, M. Ng, Y.-C. Wong, M.-Y. Chan, W.-T. Wong and V. W.-W. Yam, *J. Am. Chem. Soc.*, 2017, **139**, 10750–10761.
- 42 F. K.-W. Kong, M.-C. Tang, Y.-C. Wong, M.-Y. Chan and V. W.-W. Yam, *J. Am. Chem. Soc.*, 2016, **138**, 6281–6291.
- 43 L. K. Li, W. K. Kwok, M. C. Tang, W. L. Cheung, S. L. Lai, M. Ng, M. Y. Chan and V. W. W. Yam, *Chem. Sci.*, 2021, **12**, 14833–14844.
- 44 A. P. Kulkarni, C. J. Tonzola, A. Babel and S. A. Jenekhe, *Chem. Mater.*, 2004, **16**, 4556–4573.
- 45 F. S. Kim, X. G. Guo, M. D. Watson and S. A. Jenekhe, *Adv. Mater.*, 2010, **22**, 478.
- 46 D. Tordera, A. Pertegas, N. M. Shavaleev, R. Scopelliti, E. Orti, H. J. Bolink, E. Baranoff, M. Grätzel and M. K. Nazeeruddin, *J. Mater. Chem.*, 2012, **22**, 19264–19268.
- 47 H.-C. Su, F.-C. Fang, T.-Y. Hwu, H.-H. Hsieh, H.-F. Chen, G.-H. Lee, S.-M. Peng, K.-T. Wong and C.-C. Wu, *Adv. Funct. Mater.*, 2007, **17**, 1019–1027.
- 48 J. a G. Williams, *Photochemistry and Photophysics of Coordination Compounds: Platinum*, Springer, Berlin, 2007.
- 49 S. Jaime, L. Arnal, V. Sicilia and S. Fuertes, *Organometallics*, 2020, **39**, 3695–3704.
- 50 S. Fuertes, A. J. Chueca and V. Sicilia, *Inorg. Chem.*, 2015, **54**, 9885–9895.
- 51 T. Ogawa, W. M. C. Sameera, D. Saito, M. Yoshida, A. Kobayashi and M. Kato, *Inorg. Chem.*, 2018, **57**, 14086–14096.
- 52 J. D. Slinker, J. Rivnay, J. S. Moskowitz, J. B. Parker, S. Bernhard, H. D. Abruna and G. G. Malliaras, *J. Mater. Chem.*, 2007, **17**, 2976–2988.
- 53 H. J. Bolink, E. Coronado, R. D. Costa, N. Lardies and E. Orti, *Inorg. Chem.*, 2008, **47**, 9149–9151.
- 54 J. D. Slinker, J. A. DeFranco, M. J. Jaquith, W. R. Silveira, Y.-W. Zhong, J. M. Moran-Mirabal, H. G. Craighead, H. D. Abruña, J. A. Marohn and G. G. Malliaras, *Nat. Mater.*, 2007, **6**, 894–899.
- 55 D. Tordera, J. Frey, D. Vonlanthen, E. Constable, A. Pertegas, E. Orti, H. J. Bolink, E. Baranoff and M. K. Nazeeruddin, *Adv. Energy Mater.*, 2013, **3**, 1338–1343.



- 56 J. Ràfols-Ribé, N. D. Robinson, C. Larsen, S. Tang, M. Top, A. Sandström and L. Edman, *Adv. Funct. Mater.*, 2020, **30**, 1908649.
- 57 W. Zhao, C. Y. Liu, Q. Wang, J. M. White and A. J. Bard, *Chem. Mater.*, 2005, **17**, 6403–6406.
- 58 Y. Cao, Q. Pei, M. R. Andersson, G. Yu and A. J. Heeger, *J. Electrochem. Soc.*, 1997, **144**, L317–L320.
- 59 L. Edman, B. Liu, M. Vehse, J. Swensen, G. C. Bazan and A. J. Heeger, *J. Appl. Phys.*, 2005, **98**, 044502.
- 60 M. L. D. Weber, E. Fresta, M. Elie, M. E. Miehlich, J.-L. Renaud, K. Meyer, S. Gaillard and R. D. Costa, *Adv. Funct. Mater.*, 2018, **28**, 1707423.
- 61 H. J. Bolink, L. Cappelli, S. Cheylan, E. Coronado, R. D. Costa, N. Lardies, M. K. Nazeeruddin and E. Orti, *J. Mater. Chem.*, 2007, **17**, 5032–5041.
- 62 M. Meyer, L. Mardegan, D. Tordera, A. Prescimone, M. Sessolo, H. J. Bolink, E. C. Constable and C. E. Housecroft, *Dalton Trans.*, 2021, **50**, 17920–17934.



